# TUDelft

Delft University of Technology

## Biopolymer nanocomposites: lessons from structure-property relationships

Pereira Espíndola, S.

**Important note**
To cite this publication, please use the final published version (if applicable).
Please check the document version above.

# Biopolymer nanocomposites:

lessons from structure-property relationships

# Biopolymer nanocomposites:

## lessons from structure-property relationships

Proefschrift

ter verkrijging van de graad van doctor

aan de Technische Universiteit Delft,

opgezag van de Rector Magnificus, Prof.dr.ir. T.H.J.J. van der Hagen,

voorzitter van het College voor Promoties,

in het openbaar te verdedigen op maandag 02 Oktober 2023 om 17:30 uur.

door

**Suellen PEREIRA ESPÍNDOLA**

Master of Science in Water Technology,

Wageningen University, Netherlands,

geboren te Uberlândia, Brazil.

Dit proefschrift is goedgekeurd door de

Samenstelling promotiecommissie:

| | |
|---|---|
| Rector magnificus, | Voorzitter |
| Prof.dr. S.J. Picken, | Technische Universiteit Delft, promotor |
| dr.ir. J Zlopasa, | Technische Universiteit Delft, copromotor |
| Prof.dr.ir. M.C.M. van Loosdrecht, | Technische Universiteit Delft, promotor |

*Onafhankelijke leden:*

| | |
|---|---|
| Prof.dr. M.M.G. Kamperman, | Rijksuniversiteit Groningen |
| Prof.dr.ir. J. van der Gucht, | Wageningen University & Research |
| Prof.dr. D. Bonn, | Universiteit van Amsterdam |
| em.Prof.dr.ir. S. van der Zwaag, | Technische Universiteit Delft |

*Reservelid:*

| | |
|---|---|
| Prof.dr. J.H. van Esch, | Technische Universiteit Delft |

*To my inner child*

# Contents

# Summary

The urgent need to address sustainability within material science, driven by global environmental concerns over pollution, climate change, and resource scarcity, has led to a growing interest in bio-based materials. This thesis explores the potential of biopolymers as alternatives to non-renewable resources, specifically the ones derived from renewable and residual sources. The biomacromolecules can be harvested from plants, algae, microorganisms, and animal products; or extracted from the process waste of agricultural and urban cycles. In particular, the high stiffness (Young's modulus) exhibited by certain biopolymers, often surpassing that of standard engineering polymers, motivates this investigation. The biopolymers' uncontrolled chemical structure and morphology still inhibit their application in many industries. Inspired by the unique structures, properties, and functions found in biological systems, this research aimed to develop (solid-state) structure-property relationships for relevant biopolymer systems aiming at predicting final material properties (physicochemical, thermal, mechanical, barrier). The focus on structure-property guidelines is brought about by systematic investigations of the intricate architecture and interactions found in biopolymers and bioinspired nanocomposites. The ultimate goal is to design bio-based materials with superior performance, such as lightweight, high stiffness and strength, and functionality, while at a competitive cost and sustainability.

**Chapter 1** gives a general background to biopolymers, bioinspired (nano)composites, and a recent circular economy approach for recovering biopolymers from wastewater treatment facilities. We discuss the state-of-the-art of biopolymer properties (from biomass and urban waste) and the motivation to develop high-performance materials using bioinspired principles. The outline of this thesis is presented.

The polysaccharide alginate is examined in Chapters 2 and 3 to establish structure-property relationships, generating insights into many other biopolymer materials. **Chapter 2** investigates biopolymer film plasticization through the effect on the glass transition temperature ($Tg$). A case-study of Na-alginate-(polyol) mixtures is given, focusing on understanding the role of structural composition and plasticizer size. A new thermodynamic model was developed to describe heterogeneous polymer mixtures (using plasticizers, blends, and co-polymers) and describe $Tg$ variations in (bio)polymer systems, including cases of anti-plasticization. The linearized Generalized Mean model (*GML*) was tested for its versatility and ability to fit several cases of (heterogeneous) polymeric mixtures. It can describe many complex systems by one model constant that can represent partitioning ($k_{GM}$). Last but not least, there is a clear tendency for biopolymer materials toughened by additives or blends to present heterogeneous morphological structures. **Chapter 3** explores different methods of ion-crosslinking alginates, analyzing the behavior and solid-state properties of ion-crosslinked alginates with various cations (alkali, alkaline earth, transition). We briefly discuss the effectiveness of ion-exchange methods: film solvent exchange, acid gel neutralization, and dialysis. The study primarily investigates storage modulus, water diffusion, and the sol-gel transition of alginate films, providing indirect insights into the structural changes induced by

ion crosslinking and its influence on material performance. Through structure-property relations, we discuss the hypothesis of forming (large) ionic aggregates from specific ion binding. That would lead to a transition from a polyelectrolyte to ionomer behavior in charged biopolymers like alginates. In general, monovalent alginates exhibit the typical behavior of a polyelectrolyte, while most polyvalent alginates and, indeed, alginic acid form ionomer-like hydrogels. By fitting the *GML* model to this *Tg* data, we find that plasticized films of alginates exhibit higher morphological heterogeneity with clustering phenomena, showing a trend of transition metal > alkaline earth metal > alkali metal for the studied alginate composition. The water vapor transport properties indicate a moisture-induced alginate chain relaxation, in which a delay was observed in crosslinked systems due to restricted regions formed by ion aggregates. Hence, specific interactions in ionomer-like alginate films lead to different dynamics and structure-property relationships.

In Chapters 4 and 5, the focus was on fabrication strategies and properties of highly-ordered bioinspired nanocomposites, taking as a key example the case of gelatin/montmorillonite (gelatin/MMT). Unlike most bioinspired composite works, selecting specific materials was not the focus but rather to comprehensively explore the mechanisms for 2D material exfoliation and alignment. **Chapter 4** presents a theoretical basis for characterizing nacre-like nanostructures in 2D platelet/sheet composites. It is well-established that nanoparticle exfoliation is imperative to give ultimate anisotropic properties, *e.g.*, thermal, mechanical, and barrier properties. The study explores strategies for exfoliating 2D materials through fast hydrogelation and investigates possible positional order-disorder transitions with increasing nanofiller incorporation. We present an easily attainable strategy for exfoliating 2D materials using a hydrogel matrix with rapid network formation, offering controlled all-exfoliated systems across a wide loading range (0.4 to 64% MMT volume fraction). The high exfoliation of clay platelets enables precise tuning of sample d-spacing through a volumetric rule analogous to colloidal swelling. Controlled hydrogelation emerges as a promising alternative to laborious processes, such as multilayer deposition and in situ polymerization. However, achieving sufficient particle immobilization during the drying phase is essential. System properties also depend on initial polymer-particle compatibility, polymer-penetration energy, and interfacial interactions. Notably, our investigation uncovers particle order-disorder transitions within these nanostructures. We examined the correlation and domain length at high filler loadings, from 33 to 64% MMT volume fraction, finding highly ordered phases and crystallite sizes of approximately 200 Å. **Chapter 5** examines the ordering mechanism in bioinspired nanocomposites with great detail via nanostructure analysis, application of orientation distribution functions, and effect on the properties. We give an overview of current nacre-like fabrication methods and the (in-plane) orientational order mechanisms that are possible to occur. We conclude that most waterborne methods seem to utilize either mean-field self-assembly or, more frequently, a network affine deformation. We investigated a nacre-like nanocomposite system (gelatin/MMT) for achieving the alignment of nanoplatelets. The orientation distribution functions were fitted to spectroscopy data to show the predominance of the alignment method. We found that this system's ordering indeed follows the modified affine deformation model. Through a comprehensive characterization, we establish relationships between alignment mechanism, structure, thermomechanical properties, and barrier properties as a function of MMT loading, orientational order, and effective aspect ratio. Remarkably, we achieve a high degree of compression ($\lambda_z$) and

orientational order (average $<P_2>$ order parameter oscillates around 0.7) up to 64 vol.% filler, indicating the efficiency of the hydrogel strategy in immobilizing 2D-materials without stacking. The study emphasizes the importance of orientational order for obtaining high performance. The resulting nanocomposites exhibited enhanced stiffness, even at high relative humidity, and showed indications of increased heat resistance and lower gas permeability. However, the influence of platelet wrinkling on the effective aspect ratio and reinforcement efficiency requires further investigation. The water vapor diffusion studies revealed reduced sorption kinetics and diffusion coefficients with increasing filler loading, although interactions with the clay component altered the matrix diffusion coefficient. We propose that the affine deformation mechanism offers a promising approach for designing nacre-inspired nanocomposites (1D or 2D particle morphology), even at very high nanofiller level, with controlled orientational order, alignment, and optimized properties, facilitated by the scalability of hydrogel affine deformation method.

The utilization of biomass from agricultural and organic urban waste has gained momentum in the fabrication of biodegradable and circular materials. In Chapters 6 and 7, we integrate the lessons learned from biopolymers and bionanocomposites with recovering resources from urban waste (wastewater). **Chapter 6** focuses on the study of Kaumera˚, a biopolymer extracted from wastewater sludge, for sustainable polymer applications. Characterizing the extracted exopolymer substances (EPS) from sludge biofilms poses several challenges due to its complex composition based on (glyco)proteins, polysaccharides, lipids, nucleotides, and humic substances. Analyzing the composition and structure of Kaumera˚, derived from EPS in aerobic granular sludge, is particularly difficult. Therefore, a black box approach focusing on desired properties was preferred for material development. The research encompassed Kaumera˚ biopolymer(s) physicochemical (predominant functional groups, polyampholyte behavior, solubility) and charge characterization (cationic to anionic charge reversal and possible complex coacervation), film formation through plasticization and blending, and the development of nacre-like MMT nanocomposites and derivative materials. We discuss the high potential to develop competitive high-end materials with lightweight characteristics, exceptional stiffness, strength, functionality, affordability, and environmental sustainability. These materials are derived from bio-based sources, rendering them biodegradable and somewhat biocompatible. Through material formulations and processing strategies, the fabrication of films, fibers, foams, absorbers, binders, and coatings should be within close reach. Understanding structure-property relationships in Kaumera˚ nanocomposites, influenced by polymer structure, nanofiller quantity and type, and intermolecular interactions, will guide the selection of commercially-viable polymer characteristics and enable the development of nature-inspired designer products from wastewater. **Chapter 7** investigates the recovery of cellulose and nanocellulose from wastewater, specifically exploring the extraction of secondary raw cellulose from toilet paper. A facile procedure for cellulose extraction and determination of cellulose content in wastewater solids or sludge is demonstrated based on alkaline and bleaching treatments. The method shows high specificity to the source and can yield pulp with cellulose fractions exceeding 86 wt.%. Controlled acid hydrolysis is employed to isolate Cellulose NanoCrystals (CNC) from toilet paper and wastewater-derived cellulose, with a feasible process yielding CNC at or above 30% based on cellulosic pulp. The CNC suspensions exhibit visible flow birefringence and possess rod-like shapes with dimensions around 130 nm in length and 10 nm in width, exhibiting comparable

crystallinity (62-68%) to commercial standards. Solvent-cast bio-nanocomposites using wastewater-CNC and Na-alginate as a matrix demonstrate high stiffness (18 to 22 GPa), with the addition of toilet paper or wastewater-CNC resulting in a remarkable increment in stiffness, similar to the commercial product (58%). These findings suggest that the aspect ratio, morphology, chemical structure, crystallinity, and reinforcement of wastewater-CNC samples closely resemble the current commercial standard, indicating the potential of wastewater as a resource for fabricating high-end and circular products. These efforts shown in Chapters 6 and 7 contribute to developing nature-inspired designer products derived from wastewater and allow establishing structure-property relationships, even if from bio-based materials from dynamic sources.

**Chapter 8** provides the outlook and concluding remarks of this thesis. Results from the previous chapters are summarized, and recommendations for future advanced biopolymer-based material research are given from the physical chemistry and polymer science perspectives.

The significance of structure-property relationships in tailored material design is underscored in this thesis. Such relationships have been successfully explored across various scales, encompassing molecular morphology nuances (**Chapters 2 and 3**) as well as the micro- and mesostructures within composites (**Chapters 4 to 7**). Collectively, attaining a certain degree of control over structure-property associations holds the potential to stimulate the utilization of biopolymers in high-performance material applications. The study of bionanocomposites highlighted the feasibility of designing lightweight and high-performance materials using biopolymers, non-toxic fillers, and additives. Substantial enhancements in thermal, mechanical, and barrier properties can be achieved by incorporating mechanisms and nanostructures inspired by biological systems, which have undergone refinement over millions of years of evolution. This demonstrates the potential for developing advanced materials with improved performance characteristics based on nature-inspired design principles. The integration of resource recovery from wastewater highlights the importance of circular economy principles in material science. Future research should continue to investigate novel processing techniques, the nano-, and microstructures of bio-based polymers and composites, expand understanding of structure-property relationships, and explore new avenues for sustainable material development from waste resources.

# Samenvatting

De dringende behoefte om duurzaamheid aan te pakken binnen de materiaalwetenschappen, gedreven door wereldwijde milieuzorgen over vervuiling, klimaatverandering en schaarste aan hulpbronnen, heeft geleid tot een groeiende interesse in bio-gebaseerde materialen. Dit proefschrift onderzoekt het potentieel van biopolymeren als alternatieven voor niet-hernieuwbare hulpbronnen, met name die afkomstig zijn uit hernieuwbare en reststromen. De biomacromoleculen kunnen worden gewonnen uit planten, algen, micro-organismen en dierlijke producten; of geëxtraheerd uit het procesafval van landbouw- en stedelijke kringlopen. Met name de hoge stijfheid (Young's modulus) die door bepaalde biopolymeren wordt vertoond, vaak hoger dan die van standaard technische polymeren, motiveert dit onderzoek. De ongecontroleerde chemische structuur en morfologie van biopolymeren belemmeren echter nog steeds hun toepassing in veel industrieën. Geïnspireerd door de unieke structuren, eigenschappen en functies die worden gevonden in biologische systemen, heeft dit onderzoek tot doel (vaste-stof) structuur-eigenschaprelaties te ontwikkelen voor relevante biopolymeersystemen met het oog op uiteindelijke materiaaleigenschappen (fysisch-chemisch, thermisch, mechanisch, barrière). De focus op richtlijnen voor structuur-eigenschap wordt tot stand gebracht door systematisch onderzoek van de complexe architectuur en interacties die worden aangetroffen in biopolymeren en bio-geïnspireerde nanocomposieten. Het uiteindelijke doel is het ontwerpen van bio-gebaseerde materialen met superieure prestaties, zoals lichtgewicht, hoge stijfheid en sterkte, en functionaliteit, tegen een concurrerende prijs en duurzaamheid.

**Hoofdstuk 1** geeft een algemene achtergrond van biopolymeren, bio-geïnspireerde (nano)composieten, en een recente benadering van de circulaire economie voor het terugwinnen van biopolymeren uit afvalwaterzuiveringsinstallaties. We bespreken de stand van zaken van de eigenschappen van biopolymeren (uit biomassa en stedelijk afval) en de motivatie om hoogwaardige materialen te ontwikkelen met behulp van bio-geïnspireerde principes. De opzet van dit proefschrift wordt uiteengezet.

Het polysaccharide alginaat wordt onderzocht in Hoofdstukken 2 en 3 om structuur-eigenschaprelaties vast te stellen en inzichten te genereren in vele andere biopolymeermaterialen. **Hoofdstuk 2** onderzoekt het week maken van biopolymeerfilms door het effect op de glasovergangstemperatuur ($Tg$). Er wordt een casestudy gegeven van Na-alginaat-(polyol) mengsels, waarbij de nadruk ligt op het begrijpen van de rol van structurele samenstelling en plastificeermiddelgrootte. Er is een nieuw thermodynamisch model

ontwikkeld om heterogene polymeermengsels (met behulp van plastificeermiddelen, mengsels en copolymeren) te beschrijven en *Tg*-variaties in (bio)polymeersystemen te beschrijven, inclusief gevallen van anti-plasticization. Het lineaire Generalized Mean-model (*GML*) is getest op zijn veelzijdigheid en vermogen om verschillende gevallen van (heterogene) polymeermengsels te beschrijven. Het kan veel complexe systemen beschrijven met behulp van één modelconstante die de partitionering ($k_{GM}$) kan vertegenwoordigen. Ten slotte was er een duidelijke neiging voor biopolymeermaterialen, die versterkt zijn met additieven of bestaan uit mengsels, om heterogene morfologische structuren te vertonen. **Hoofdstuk 3** onderzoekt verschillende methoden voor ionische crosslinking van alginaten en analyseert het gedrag en de vaste-stofeigenschappen van ionisch vernette alginaten met daarin verschillende kationen (alkali, aardalkali, overgangsmetaal). We bespreken kort de effectiviteit van ionenuitwisselingsmethoden: uitwisseling van oplosmiddel voor de film, neutralisatie van zuurgel en dialyse. De studie onderzoekt voornamelijk de opslagmodulus, waterdiffusie en de sol-gelovergang van alginaatfilms, en geeft indirect inzicht in de structurele veranderingen die worden veroorzaakt door ionische vernetting en de invloed ervan op de materiaaleigenschappen. Op basis van structuur-eigenschaprelaties bespreken we de hypothese van het vormen van (grote) ionische aggregaten door specifieke ionbinding. Dit zou leiden tot een overgang van polyelektrolytgedrag naar ionomeergedrag in geladen biopolymeren zoals alginaten. Over het algemeen vertoonden mono-valente alginaten het typische gedrag van een polyelektrolyt, terwijl de meeste poly-valente alginaten en inderdaad algininezuur ionomeerachtige hydrogels vormden. Door het *GML*-model aan te passen aan *Tg*-gegevens, ontdekten we dat geplastificeerde films van alginaten een hogere morfologische heterogeniteit vertonen met clustering, waarbij een trend wordt waargenomen van overgangsmetaal > aardalkaliemetaal > alkaliemetaal voor de bestudeerde samenstelling van alginaat. De eigenschappen van waterdamptransport duiden op een vochtgeïnduceerde relaxatie van de alginaatketen, waarbij een vertraging wordt waargenomen in gecrosslinkede systemen als gevolg van beperkte gebieden gevormd door ion-aggregaten. Daarom leiden specifieke interacties in ionomeerachtige alginaatfilms tot verschillende dynamiek en structuur-eigenschaprelaties.

In hoofdstukken 4 en 5 ligt de focus op fabricatiestrategieën en eigenschappen van sterk geordende bio-geïnspireerde nanocomposieten, waarbij gelatine/montmorilloniet (gelatine/MMT) als sleutelvoorbeeld is genomen. In tegenstelling tot het meeste onderzoek met bio-geïnspireerde composieten ligt de nadruk niet op het selecteren van specifieke materialen, maar eerder op het bestuderen van de mechanismen voor het exfoliëren en uitlijnen van 2D-materialen. **Hoofdstuk 4** geeft een theoretische basis voor het karakteriseren van parelmoer-achtige nanostructuren in 2D-plaatcomposieten. Het is algemeen bekend dat het exfoliëren van plaatvormige nanodeeltjes essentieel is voor het verkrijgen van uiteindelijke anisotrope eigenschappen, zoals thermische, mechanische en barrière-eigenschappen. Het

onderzoek verkent strategieën voor het exfoliëren van 2D-materialen door middel van snelle hydrogelvorming en onderzoekt de mogelijke overgangen van positiële orde naar wanorde bij toenemende incorporatie van de nanodeeltjes. We presenteren een eenvoudige strategie voor het exfoliëren van 2D-materialen met behulp van een hydrogelmatrix met snelle netwerkvorming, die gecontroleerde volledig geëxfolieerde systemen mogelijk maakt over een breed bereik aan samenstelling (0,4 tot 64% MMT-volumefractie). Het hoge exfoliatiegehalte van klei-plaatjes maakte een nauwkeurige afstemming van de d-spacing van de monster mogelijk via een volumetrische mengregel die analoog is aan colloïdaal zwellen. Gecontroleerde hydrogelvorming komt naar voren als een veelbelovend alternatief voor arbeidsintensieve processen zoals meerlaagse depositie en in-situ polymerisatie. Het is echter essentieel om voldoende immobilisatie van de deeltjes tijdens het droogproces te bereiken. De eigenschappen van het systeem zijn ook afhankelijk van de aanvankelijke polymeer endeeltjes compatibiliteit, de polymeer-penetratie-energie en de grensvlakinteracties. Opmerkelijk genoeg bracht ons onderzoek orde naar wanorde overgangen van de nanodeeltjes aan het licht binnen deze nanostructuren. We onderzochten de correlatie en domeinlengte bij hoge vulstofbeladingen, van 33 tot 64% MMT-volumefractie, waarbij sterk geordende fasen en kristallietgroottes van ongeveer 200 Å werden gevonden. **Hoofdstuk 5** beschrijft het ordeningmechanisme in bio-geïnspireerde nanocomposieten met grote nauwkeurigheid via nanostructuuranalyse, toepassing van oriëntatieverdelingsfuncties en het effect op de eigenschappen. We geven een overzicht van de huidige fabricatiemethoden van parelmoer-achtige structuren en de (in-vlak) mechanismen voor oriëntatie ontwikkeling die mogelijk zijn. We concluderen dat de meeste watergedragen methoden ofwel gemiddeld-veld zelfassemblage of – nog vaker – een affiene netwerk vervorming gebruiken. We onderzochten een parelmoer-achtig nanocomposietsysteem (gelatine/MMT) om de uitlijning van plaatvormige nanodeeltjes te bereiken. De oriëntatieverdelingsfuncties werden aangepast aan diffractiegegevens om de overheersende uitlijningsmethode aan te tonen. We constateerden dat de ordening in dit systeem inderdaad het gemodificeerde affiene vervormingsmodel volgt. Door een uitgebreide karakterisering hebben we verbanden vastgesteld tussen uitlijningsmechanisme, structuur, thermomechanische eigenschappen en barrière-eigenschappen als functie van MMT-belading, oriëntatievolgorde en effectieve asverhouding. Opmerkelijk genoeg bereiken we een hoge mate van compressie ($\lambda_z$) en oriëntatiegraad (de <$P_2$>-ordeparameter oscilleert rond de 0,7) tot 64 vol.% vulstof, wat duidt op een hoge efficiëntie van de hydrogelstrategie voor het immobiliseren van 2D-materialen zonder stapeling van de plaatjes. Het onderzoek benadrukt het belang van oriëntatie om een hoge performance te bereiken. De resulterende nanocomposieten vertonen verbeterde stijfheid, zelfs bij hoge relatieve vochtigheid, en ern zijn aanwijzingen voor voor verbeterde hittebestendigheid en lagere gasdoorlaatbaarheid. De invloed van het rimpelen van de plaatjes op de effectieve asverhouding en het versterkingsrendement vereist echter verder onderzoek.

Bovendien toonden waterdampdiffusiestudies verminderde sorptiekinetiek en lagere diffusiecoëfficiënten bij toenemende vulstofbelading, hoewel interacties met het kleibestanddeel de diffusiecoëfficiënt van de matrix veranderen. We stellen voor dat het affiene vervormingsmechanisme een veelbelovende benadering biedt voor het ontwerpen van op parelmoer geïnspireerde nanocomposieten (1D of 2D-deeltjesmorfologie), zelfs bij zeer hoge vulgraden, met gecontroleerde oriëntatie, uitlijning en geoptimaliseerde eigenschappen, vergemakkelijkt door de schaalbaarheid van de hydrogel affiene vervormingsmethode.

Het gebruik van biomassa uit landbouw- en organisch stedelijk afval heeft aan kracht gewonnen bij de fabricage van biologisch afbreekbare en circulaire materialen. In hoofdstukken 6 en 7 worden de geleerde lessen uit biopolymeren en bionanocomposieten geïntegreerd met het terugwinnen van hulpbronnen uit stedelijk afval (afvalwater). **Hoofdstuk 6** richt zich op de studie van Kaumera˚, een biopolymeer dat wordt gewonnen uit afvalwaterslib, voor duurzame toepassingen. Het karakteriseren van de geëxtraheerde exopolymeerstoffen (EPS) uit slibbiofilms brengt verschillende uitdagingen met zich mee vanwege de complexe samenstelling op basis van (glyco)proteïnen, polysacchariden, lipiden, nucleotiden en humusstoffen. Het analyseren van de samenstelling en structuur van Kaumera˚, afgeleid van EPS in aeroob korrelig slib, is bijzonder moeilijk. Daarom werd gekozen voor een black box-benadering die zich richt op gewenste eigenschappen voor materiaalontwikkeling. Het onderzoek omvatte fysisch-chemische eigenschappen van Kaumera˚ biopolymeer(s) (dominante functionele groepen, polyamfolytisch gedrag, oplosbaarheid) en ladingkarakterisering (kationisch naar anionisch ladingomkering en mogelijk complexe coacervatie), filmvorming door weekmaken en blending, en de ontwikkeling van parelmoer-achtige MMT-nanocomposieten en daaruit afgeleide materialen. We bespreken het grote potentieel om concurrerende hoogwaardige materialen te ontwikkelen met lichtgewicht eigenschappen, uitzonderlijke stijfheid, sterkte, functionaliteit, betaalbaarheid en duurzaamheid. Deze materialen zijn afkomstig van bio-gebaseerde bronnen, waardoor ze biologisch afbreekbaar en enigszins biocompatibel zijn. Door middel van materiaalformuleringen en verwerkingsstrategieën zou de fabricage van films, vezels, schuimen, absorbers, bindmiddelen en coatings binnen handbereik moeten liggen. Het begrijpen van de structuur-eigenschaprelaties in Kaumera˚-nanocomposieten, beïnvloed door polymeerstructuur, hoeveelheid en type nanovuller, en intermoleculaire interacties, zal de selectie van commercieel haalbare polymeerkarakteristieken en de ontwikkeling van natuur-geïnspireerde ontwerpproducten uit afvalwater mogelijk maken. **Hoofdstuk 7** beschrijft de productie van cellulose en nanocellulose uit afvalwater, waarbij specifiek de extractie van secundaire ruwe cellulose uit toiletpapier is onderzocht. Een eenvoudige procedure voor cellulose-extractie en bepaling van het cellulosegehalte in afvalwater vaste stoffen of slib wordt gedemonstreerd op basis van alkalische en bleekbehandelingen. De methode vertoont een hoge specificiteit voor de bron en kan pulp opleveren met cellulosefracties van meer dan 86

gew.%. Gecontroleerde zuurhydrolyse wordt toegepast om Cellulose NanoKristallen (CNC) te isoleren uit toiletpapier en uit afvalwater afkomstige cellulose, waarbij een haalbaar proces CNC oplevert met opbrengsten van 30% of meer gebaseerd op de cellulosepulp fractie. De CNC-suspensies vertonen zichtbare stromingsdubbelebreking en bevatten staafachtige deeltjes met afmetingen van ongeveer 130 nm lengte en 10 nm breedte, waarbij ze vergelijkbare kristalliniteit (62-68%) vertonen als de huidige commerciële producten. Vanuit oplosmiddel verwerkte bio-nanocomposieten met daarin afvalwater-CNC en Na-alginaat als matrix vertonen een hoge stijfheid (18 tot 22 GPa), waarbij de toevoeging van toiletpapier of afvalwater-CNC resulteert in een opmerkelijke toename in stijfheid, vergelijkbaar met het commerciële product (58%). Deze bevindingen suggereren dat de asverhouding, morfologie, chemische structuur, kristalliniteit en versterking door middel afvalwater-CNC-monsters sterk lijkt op de huidige commerciële standaard, dit bewijst het potentieel van afvalwater als bron van grondstoffen voor de fabricage van hoogwaardige en circulaire producten. Deze resulaten, zoals beschreven in hoofdstukken 6 en 7, dragen bij aan de ontwikkeling van op de natuur geïnspireerde producten afgeleid van afvalwater en het daarbij vaststellen van structuur-eigenschaprelaties, zelfs als het gaat om bio-gebaseerde materialen uit dynamische bronnen.

**Hoofdstuk 8** biedt een overzicht en afsluitende opmerkingen van dit proefschrift. Resultaten uit de voorgaande hoofdstukken worden samengevat en aanbevelingen voor toekomstig geavanceerd onderzoek naar biopolymeergebaseerde materialen worden gegeven vanuit het perspectief van de fysische chemie en polymeerwetenschap.

De betekenis van structuur-eigenschaprelaties in op maat gemaakte materiaalontwerp wordt benadrukt in dit proefschrift. Dergelijke relaties zijn succesvol onderzocht op verschillende schaalniveaus, waarbij nuances in moleculaire morfologie (**hoofdstukken 2 en 3**) evenals micro- en mesostructuren binnen composieten (**hoofdstukken 4 tot 7**) zijn meegenomen. Het verkrijgen van een zekere mate van controle over structuur-eigenschap relaties biedt perpectief om het gebruik van biopolymeren in hoogwaardige materiaaltoepassingen te bevorderen. Het onderzoek naar bionanocomposieten benadrukt de haalbaarheid van het ontwerpen van lichtgewicht en hoogwaardige materialen met behulp van biopolymeren, niet-giftige vulstoffen en additieven. Aanzienlijke verbeteringen in thermische, mechanische en barrière-eigenschappen konden worden bereikt door mechanismen en nanostructuren te incorporeren die geïnspireerd zijn op biologische systemen, die gedurende miljoenen jaren van evolutie verfijnd zijn. Dit toont het potentieel voor de ontwikkeling van geavanceerde materialen met verbeterde prestatiekenmerken op basis van ontwerpprincipes geïnspireerd door de natuur. De integratie van hulpbrongericht herstel uit afvalwater benadrukt het belang van circulaire economieprincipes in de materiaalwetenschappen. Toekomstig onderzoek moet doorgaan met het onderzoeken van nieuwe verwerkingstechnieken, de nano- en

microstructuren van bio-gebaseerde polymeren en composieten, het uitbreiden van het begrip van structuur-eigenschaprelaties en het verkennen van nieuwe mogelijkheden voor duurzame materiaalontwikkeling uit afvalbronnen.

# 1

# Introduction

## 1.1. Background

The globally intensifying environmental concerns over pollution, climate change, and resource scarcity became the main drives for addressing sustainability within material science.[1] This thesis adds to this purpose by exploring the potential of a few bio-based materials as an alternative to non-renewable resources. Biomacromolecules, complex polymers naturally synthesized by living organisms, offer interesting solutions for developing advanced and sustainable materials. The biopolymers can be extracted from renewable sources, such as plants, algae, microorganisms, and animal product waste. Alongside these advantages comes the general interest in understanding the evolutionary mechanisms present in the design of natural materials. The unique structures, properties, and functions found in biological systems like nacre, silk, or the human skin has served as inspiration for many decades.[2,3] More recently, the use of biomass from agricultural and organic urban wastes has also increased to fabricate biodegradable and circular materials.[4–6] Therefore, the nature and processing of bio-based polymers are the subjects of our systematic investigations aiming at structure-property relationships. These links are fundamental in designing and tailoring (bio)polymeric materials to advanced physical, chemical, and mechanical properties.

### 1.1.1. The complex nature of biopolymers

The *abundance* of biomacromolecules, such as proteins, nucleic acids, and polysaccharides found in biomass, offers an extraordinary opportunity to tap into nature's repertoire and establish *renewable* material supply chains. Moreover, the inherent *biodegradability* of bio-based materials ensures a reduced accumulation of non-recyclable waste, paving the way for circular and sustainable economies and minimizing the environmental burden.

As a signature of evolution, bio-based molecules are versatile and present unique features, such as supramolecular structures, self-assembly, responsiveness to stimuli, and high mechanical stiffness and strength relative to synthetic polymers. This has enabled a wide range of applications across diverse industries like food, cosmetics, medical, packaging, and even automotive.[7] In the field of medicine, owing to their biocompatibility, bio-based and semi-synthetic materials have revolutionized drug delivery systems, tissue engineering, and regenerative medicine.[8] Similarly, the packaging, textile, and engineering fiber industries have long witnessed advancements with the integration of

bio-based materials.[7,9,10] Additionally, sustainable fabrics incorporating bio-based materials like cotton, hemp, and flax present improved durability, paving the way for eco-conscious fashion. Nevertheless, it is noteworthy that the industrial applications of biomacromolecules are far from new, and there is only a comeback, *e.g.*, gelatin in combination with silver halide has been used in photographic films since the 1920s or gramophone vinyl discs that used to made from shellac gum of lac bugs (Figure 1.1). Nowadays, it is the emerging need for sustainable products that has been escalating in the market. The European Commission estimates a compounded annual growth rate of around 20% in bio-based sales in the upcoming years, supported by global and local subsidies.[11]



**(a)** Gelatin silver print   **(b)** Shellac vinyl
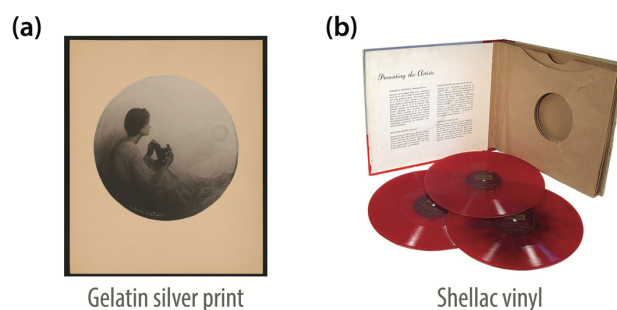
**Figure 1.1.** Industrial bio-based materials that have been commercialized during the early twentieth century. (a) Black and white photograph enabled by using the gelatin silver print process of Kodak. The image is developed by exposing a photosensitive paper coated with gelatin containing light-sensitive silver halide salts to light. Image credits to photographer Brigman, Anne, 1869-1950, Public Domain, H116457 U.S. Copyright Office. (b) Red shellac vinyl discs were widely used until the late 1950s as a medium for commercial music recordings. Shellac is a natural resin secreted by female lac bugs and harvested from tree branches. Public domain image.

An extensive but incomplete list of natural biopolymers includes cellulose and starch (amylopectin and amylose) from plants; Arabic gum and shellac resins, respectively, from tree and bug exudates; alginate and carrageenan from algae and seaweeds; pectin from fruit peels and skin; zein proteins from corn; chitosan from the shells of mollusks, fish, fungi and insects; casein and whey proteins extracted from milk; collagen, gelatin, and keratin from animal bones and skin; mucin secreted from snails and hagfish; RNA/DNA from living organisms, etc. Furthermore, a category of bio-based materials that is usually separated are the so-called bioplastics, which are those that can be thermally processed.

## Introduction

Examples include synthetic polylactic acid, semi-synthetic polymers like cellulose triacetate and modified starch, polyhydroxyalkanoates (PHB and PHBV) produced via microbial biotechnology, and the natural shellac resin. Even though bioplastics derived from biomolecules, *e.g.,* lactic acid, exhibit reduced carbon footprints and decreased reliance on petroleum-based polymers, it is important to account that they are not always biodegradable (end decay products are $CO_2$ and water). This is another reason for synthetic routes to become undesirable and applications restricted. Overall, biopolymers and derivatives are present everywhere. However, biomass resources tend to have limited availability, depending on harvesting or extraction from residual sources.

Despite the tremendous potential of bio-based materials, several challenges persist on the path to widespread adoption. Hence, the high price and availability have often limited the investigation of biopolymers for material applications. The present challenges are achieving high extraction and processing yields at a reasonably low cost per unit. Scaling up production, ensuring consistent quality, and optimizing performance are crucial aspects that require interdisciplinary collaborations and technological advancements.[12] The development of frameworks and supportive policies is essential to incentivize the adoption of bio-based materials and promote their integration across industries. Continued research and development efforts, bridging academia, industry, and policymakers, are vital to address these challenges and progress towards bio-based materials for sustainable material science.

In line with the goals of better processing and quality, it is vital that we develop ways to overcome the complex physical and chemical nature of biopolymers, allowing us to predict and measure properties for materials science. If we consider the example of natural biopolymers, high-end analysis of monomer composition becomes easily out of hand. Polysaccharides can have various kinds of (modifiable) monomers. The sugar code of polysaccharides consists of more than 50 monomers, each of which can have different derivatives and multiple reactive sites for polymerization. For instance, the ubiquitous cellulose polymer can be naturally or synthetically modified by replacing the hydroxyl (-OH) groups on the glucose units and alter the polymer backbone structures. Proteins and nucleotides are more tangible to identify, respectively, with only 22 amino-acids and four possible bases. Adding to this complexity, the functional groups, degree of chain branching, molecular weight distribution, chirality, and crystallinity can considerably challenge the interpretation of high-throughput analytical results. In addition, single molecules (or mixtures thereof) combining sugars, peptides, and lipids are the very basis of many biological systems. Fortunately, the interpretation of many physical and

chemical phenomena linked to cohesive material properties can often be simplified. One way to estimate properties is by employing principles from polymer science and a simplified picture of functionalities, chemical and electrostatic interactions, and conformational arrangements. Leveraging these attributes and working on structure-property relationships, researchers can engineer biopolymer-based materials with tailored functionalities for a range of applications.

## 1.1.2. Structure-property relationships for bio-based materials

In the field of polymer science, structure-property relationships play a fundamental role in designing and tailoring macromolecular materials with desired properties. The molecular structure of a polymer, including the type and arrangement of monomers, molecular weight, branching, and tacticity, influences its macroscopic properties. For example, the crystallinity of a polymer, which is determined by the arrangement of polymer chains, directly affects its thermomechanical properties. Experimental techniques, such as X-ray diffraction, microscopy, spectroscopy, and thermal analysis, are employed to characterize the structure-property of macromolecules at broad length scales. Computational modeling and simulations are also used to elucidate the relationships between structure and properties. Investigating structure-property relationships in macromolecules provides a foundation for tailoring materials with specific properties, guiding the design of innovative technologies in materials science, polymer chemistry, and engineering.

The structure-property relationships of many synthetic polymers and composites have already been elucidated.[13] By systematically studying and manipulating the structure of macromolecules, researchers can gain insights into how specific molecular characteristics (chemical structure, chirality, molecular weight, supramolecular arrangement, crosslinking, crystallinity) translate into material properties. This knowledge is often based on properties depending on the materials' cohesive energy. It allows for the rational design of polymeric materials with multiple functions like improved mechanical stiffness, strength, and thermal stability. This theoretical background has also been applied to some biopolymer and derivative systems, largely in the fields of packaging, food technology, and biomedicine.[14,15] To the limit of our knowledge, increasing accounts on the design of bio-based advanced materials using structure-property relationships have been scarce and limited to the past decade.[16–18] Especially, there is an increasing need for structure-property relations of complex hybrid biopolymer materials and their integration to yield

multiple desired functions. These relationships are crucial for understanding and predicting the behavior and performance of materials based on biomacromolecules.

### 1.1.3. Bioinspired hierarchical design in (bio)polymer nanocomposites

The course of millions of years of evolution has shaped all living creatures, resulting in the development of unique structures and specialized functions that enable them to thrive in their respective environments. Nature's diverse species exhibit captivating interfacial phenomena, including vivid iridescent colors, distinctive light-response behavior, and mechanical and transport properties, among others (Figure 1.2).[19–23] These natural examples serve as remarkable inspirations for the creation of artificial nano-materials and -composites that can emulate similar functionalities. By manipulating chemistry and interfacial interactions based on insights from nature, researchers could fabricate bioinspired and biomimetic materials with tailored properties. So far, numerous bioinspired structures have been successfully engineered, exhibiting exceptional properties and functions that can even surpass their natural counterparts.[24] Important examples include the outstanding mechanical, surface, transport, and optical properties observed in plants, trees, bone, nacre, gecko feet, spider silk, butterfly wings, beetle chitin, human skin, tooth enamel, and a large set of other biological systems.[25] As a result, these nature-inspired systems have encouraged research efforts to understand the underlying mechanisms across multiple length scales (nano to macro) and to propose new advanced materials for emerging applications (optical devices, harvesting solar energy, electrodes, oil-water separation, antifouling surfaces, adhesives, etc.).

In a way, these bioinspired principles are also a set of structure-property relationships. Indeed, naturally produced structural materials are durable and can exhibit exceptional mechanical properties, combining strength, toughness, and lightweight characteristics through intricate hierarchical architectures.[16,26] In composites, the properties of individual components can be largely improved by incorporating the exceptional features of rigid high aspect-ratio materials. For instance, the brick-and-mortar structure of 2D aragonite tablets in nacre can impart the normally excluding properties like exceptional stiffness and toughness into the composite.[17,26] Pioneering studies have reported the tensile strength and modulus of nacre along the lamellar direction, revealing impressive values of 80-130 MPa and 60-70 GPa, respectively.[16] This is extraordinary because nacre

structures are fabricated at ambient temperature with minimal energy requirements. By mimicry or inspiration, several nacre-like materials have been engineered, showing similar or enhanced structure-property profiles, altogether with some tunability.[23,24] For example, our previous works on nacre-like alginate nanocomposites have yielded excellent stiffness and reduced water permeability, *i.e.,* an elastic modulus of 26 and 35 GPa, respectively, for 50 wt.% montmorillonite and 25 wt.% graphene oxide.[27,28] Though composite bioinspiration and performance have risen, biopolymer-particle interactions and nanostructures have yet to be extensively studied. Thus, this topic is open for research and innovations, where sophisticated methods and precise manufacturing techniques are immediately needed to achieve hierarchical structures down to the nanoscale.

The synthetic interplay of soft and hard matter found in natural composites is incredibly laborious to replicate in detail. Despite that, these materials often comprise common subunits like proteins, polysaccharides, and minerals that can be produced in situ, such as calcite and aragonites.[17] This is encouraging for materials engineering since many biopolymers can be readily available for modification and application, *e.g.,* cellulose, alginate, chitosan, gelatin, milk proteins, etc. Nanomaterials can now be synthesized in a standardized fashion and are also commercially available. The field of nanotechnology has been growing rapidly for the last 20 years. Depending on composition and fabrication, the desired nanomorphology can be spheres, whiskers, platelets, and sheets. On bionanocomposites, there have been many reports on the synergisms between biopolymers and nanoparticles based on clay (montmorillonite, laponite, hectorite, aragonite, boehmite, gibbsite, etc.) or cellulose (fibers, crystals, TEMPO-oxidized, phosphorylated, etc.).[29,30] There are, of course, other natural and semi-synthetic nanofillers available, to name a few: carbon black, expanded graphite, graphene, and (reduced) graphene oxides. At last, the chemical palette of polymers and nanofillers that can be harvested from biomass, natural or waste sources is enormous, and, although limited by availability, we can expect bionanocomposites to offer many of the required materials needed for a sustainable transition.
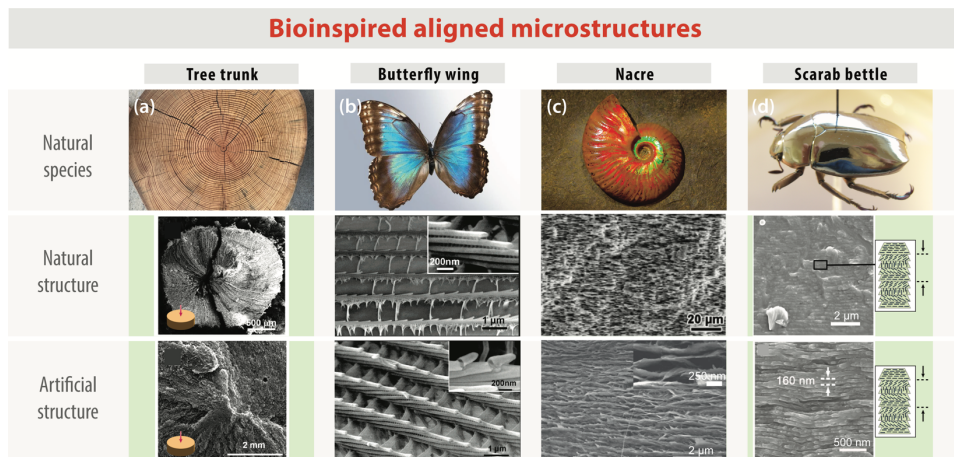
**Figure 1.2.** A few important examples of aligned microstructures in natural and bioinspired or biomimetic artificial materials. (a) Tree trunk shows radial alignment and growth rings. Conifer tree trunk cross-sectional microstructure has radially aligned channels. A freeze-casted aerogel composite of graphene oxide and boron nitride shows radial and centrosymmetric cross-sectional morphology.[19] Microscopy images reproduced with permission from ref. 19. Copyright (2020) American Chemical Society. (b) The wings of butterfly *Morpho peleides* display blue structural coloring. The wings have a lamellar microstructure with uniformly tilted multilayer nanostructures (Bragg stacks) that create a photonic band gap. The replica material is made from alumina via atomic layer deposition to create an artificial photonic band gap of similar size.[20] Microscopy images reprinted from ref. 20. Copyright (2006) American Chemical Society. (c) The fossil shell of the mollusk ammonite[31] has high stiffness and toughness and shows typical nacre iridescence. A similar mollusk shell is that of the nautilus organism, showing the nacre's brick-and-mortar microstructure[21]. Microscopy image reprinted from ref. 21. Copyright (2021) American Chemical Society. Artificial nacre composites can be made from the effective dispersion of mineral clays in a polymer matrix. The figure shows polyvinyl alcohol and laponite composite with the typical multiscale hierarchical layered structures[23]. Microscopy image reprinted from ref. 23. Copyright (2015) Springer Nature Limited. (d) A scarabaeid beetle showing an iridescent cuticle or elytra[32]. The fibers in the beetle cuticle have a helical Bouligand structure, developing a pitch of the aligned layer rotation, and hence reflect differently with circularly polarized light. Man-made chiral photonic crystals and structures can be made from mineral oxide nanowires, allowing for programmable structure-color control[22]. Microscopy images reproduced from ref. 22. Copyright (2019) John Wiley and Sons.

## 1.1.4. High-performance nanocomposites from wastewater-recovered biopolymers: towards a circular economy

Wastewater treatment plants serve the dual purpose of environmental protection and water reclamation. However, a major challenge lies in the substantial generation of waste streams, such as sludge biomass requiring proper disposal via incineration or land-filling.[5,33] From a circular economy perspective, wastewater treatment should be integrated with resource recovery from the waste compounds found in sewage, closing the loop in urban areas between waste and raw material.[5] In the future, wastewater treatment plants are expected to become resource factories. This means facilities will not only treat wastewaters to meet legal standards, producing water and energy but will also simultaneously recover commercial resources in a cost-efficient manner.[5] Recent strategies in the Netherlands have been focusing on the recovery of biogas, fertilizers, volatile fatty acids, cellulose, and the microbially produced polymers: polyhydroxyalkanoates (PHAs) and exopolymer substances (EPS).[5,33,34] However, the endeavor on circularity needs more than policy and strategy and so relies on scientific explorations over the raw material quality and process towards sustainable applications.

A revolutionary and energy-efficient biological wastewater treatment process employing granular sludge, known as the Nereda® technology, has emerged as the new standard for sewage treatment. The Nereda® technology[1], commercialized worldwide, has already reached the important milestone of 100 full-scale granular sludge wastewater treatment plants across six continents.[35–37] A distinctive characteristic of Nereda® granular sludge biofilms is its significant production of gel forming exocellular biopolymers by the selected microorganisms. Remarkably, the waste sludge obtained from this technology can be benefited for the extraction of structural biopolymers in EPS. In this case, the EPS is extracted in a multi-step process of thickening, hot alkaline solubilization reaction, and acid-precipitation (Figure 1.3). The gel-like product has been recently named Kaumera®, and a considerable amount can be recovered from the sludge (approximately 25-35% of granular sludge dry weight).

Early studies have identified Kaumera® to have some similar properties to the polysaccharide alginate[38,39], for instance, based on its ability to crosslink with divalent counterions. From this viewpoint, one important objective has been to explore potential applications for the Kaumera® biopolymer. The extracted EPS is also expected to have competitive pricing. This is attributed to the negative value of the raw resource, i.e., the

---

[1] Nereda® is a trademark owned by Royal HaskoningDHV.

# Introduction

excess sludge from Nereda* installations. The annual production of Kaumera* from a single intermediate-sized wastewater treatment plant utilizing Nereda* technology is estimated to reach 2000 tons annually. Consequently, the anticipated exopolymer production is substantially larger, far surpassing the global alginate market (44,481 tons/year in 2021[40]). Since 2019, there are already two Kaumera* plants in the Netherlands (Zutphen and Epe factories), with a combined capacity to produce 450 tons/year of this biopolymer.[41] Previous interdisciplinary research with biotechnology has unraveled unexpected properties of Kaumera*, paving the way for the production and application of novel bio-based materials in a circular economy. For instance, initial investigations indicate that Kaumera* can be employed as a surface coating material for paper to confer water resistance, as a barrier layer on curing concrete to enhance its service life, and as a flame-retardant nanocomposite film.[27,38,42] In addition, several promising applications for the raw material are already being developed, targeting the agriculture, construction, textile, and paper industries.[43] Thus, the potential to recover Kaumera* and utilize it as a resource for developing commercially-viable and high-performance materials is immense.

Establishing structure-property relationships for biopolymer materials shall give valuable insights into the requisite polymer characteristics for various Kaumera-based applications. The polymer structure significantly influences the properties of the final (nanocomposite) material, *e.g.*, stiffness, strength, and toughness, enabling more innovative technological applications. In this sense, one of the main challenges is to sufficiently characterize the extracted EPS[44] while overcoming the influence of the sludge composition as a dynamic substrate. EPS is considered to be a complex mixture of multiple compounds, including (glyco)proteins, polysaccharides, lipids, nucleotides, and humic substances. This pool of possible monomers makes the analysis of actual Kaumera* composition and structure very challenging.[39] Therefore, the preferred approach for material development is a black box, in which we focus on the final desired properties. With this rationale, there are hopes not only to valorize the waste sludge but also to create a space for advanced material properties by defining and tuning its unique functionalities. In addition, the properties of Kaumera* nanocomposites should be influenced by parameters such as polymer structure, nanofiller quantity and type, and intermolecular interactions. The elucidation of structure-property relationships in these bio-based materials will also guide the selection of commercially-viable polymer characteristics, facilitating the development of nature-inspired designer products derived from wastewater.
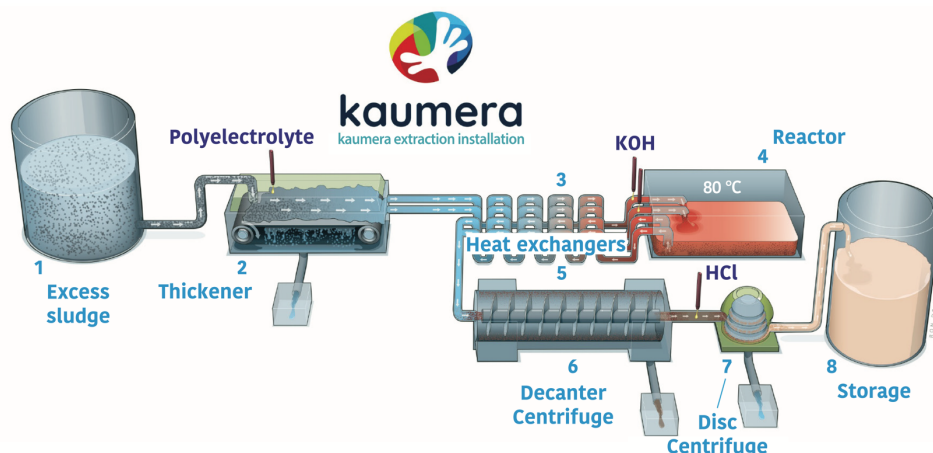
**Figure 1.3.** The process line of Kaumera® biopolymer extraction factory in Zutphen, the Netherlands. (1) A buffer tank stocks excess sludge from the aerobic granular sludge technology; (2) the sludge is passed through a conveyor belt thickener after a polyelectrolyte flocculant addition; (3) the thickened sludge is heated to 80 °C by heat exchangers, and afterward base is added until pH 9-11; (4) in the extraction reactor, the alkaline mixture is digested for about 2 hours; (5) the sludge is cooled down to room temperature; (6) a decanter centrifuge separates de alkaline soluble and insoluble phases and acid is added to the solution until pH 2-4; (7) a disc centrifuge is used to collect the acidic gel product; (8) the H-Kaumera® gel is stored in silo prior to distribution. Figure based on an illustration by Ron de Haer (2019) and made available at Kaumera® official website[41,45].

## 1.2. Central theme and objective of the thesis

The background information above underlines the importance of systematic investigations of biopolymer and bionanocomposite structure-property relationships. The main goal of this thesis is to develop structure-property links for widely and commercially available biopolymers and derivatives. This should also prove useful for wastewater-recovered polymers, such as the Kaumera® EPS.

Another important aspect of the thesis is the particular focus on the solid state of biopolymers and composites, as this state has not been underexplored using modern techniques. It is essential to provide insights into the control for thermal, mechanical, and barrier properties. In fact, the high Youngs modulus of a subset of biopolymers motivates this work. We have noticed that charged polymers, such as alginates, can attain moduli up to 13 GPa, surpassing standard engineering polymers typically at 3 GPa without

additives. In addition, due to the above-mentioned uncontrolled structure of biopolymers, our focus was on global structural changes in composition and their correlation with final material properties.

In essence, this thesis addresses the missing links to the design of ultimate material properties using bio-based and natural components. This should allow for understanding and tuning of bionanocomposites, for instance, with respect to the actual nanostructures, mechanics, and permeability.

Moreover, our investigation extends to the development of advanced materials derived from waste streams, particularly focusing on exploring the properties of biopolymers recovered from wastewater aerobic granular sludge (Kaumera® EPS) and their potential applications in bionanocomposite materials. The indications are that competitive high materials performance can be obtained, making use of detailed insight into macromolecule physics, control of interactions, and explicit use of non-equilibrium structure formation processes. We aim at competitive high-end materials that are lightweight, with high stiffness and strength, functional, low-cost, and environmentally friendly (bio-based, bio-compatible, bio-degradable). Promising avenues for fabrication include films, fibers, foams, absorbers, binders, and coatings through an intelligent design of material formulations and processing strategies.

## 1.3. Thesis outline

**Chapters 2 and 3.** In these chapters, the polysaccharide alginate is explored for structure-property relations. Chapter **2** provides data on film plasticization via the casting of Na-alginate-(polyol). We explore how the Na-alginate property of glass transition ($Tg$) changes with material composition and increasing size of plasticizer molecule. This study is expanded to several (bio)polymer systems, considering common plasticizer incorporation or (co)-polymer blending cases. A novel model to describe and, at times, predict the variations in $Tg$ with the composition of the mixture is developed. A short review of significant cases for $Tg$ modeling is given. Interestingly, there are systems in which anti-plasticization occurs, and a transition to the plasticized regime appears only at higher concentrations. This work highlights the importance of heterogenous structures in materials made with biopolymers. Alginate is well-known for showing a crosslinking phenomenon with polyvalent cations. Chapter **3** explores diverse methods for counterion exchange in alginates, such as solvent exchange, neutralization, and dialysis. The focus is

on the behavior and solid-state properties of ion-crosslinked alginates. Series of cations of monovalent alkali metals and di/trivalent alkaline-earth and transition metals are compared. The properties of storage modulus and water diffusion are discussed. In addition, glycerol-plasticized films are studied for plasticizing profile via $Tg$. The alginate sol/gel transition is described from the viewpoint of a shift from soluble polyelectrolyte to an ionomer-type of hydrogel, where the clustering of ionic pairs is the major structural feature. The presence of these ionic aggregates reflects on the solid-state performance of neat and plasticized alginates.

**Chapters 4 and 5.** In these chapters, bioinspired composites composed of gelatin/montmorillonite are investigated. Unlike most bioinspired works, materials screening and chemical composition are not the focus. Here, the main aim is to explore strategies and methods for attaining multiscale (nano to macro) and highly ordered nacre-like nanostructures in (bio)nanocomposites. In Chapter **4**, gives a theoretical framework, elucidating all the possible 2D nanostructures combining orientational and positional order in platelet/sheet composites. A strategy to promote 2D material exfoliation by fast hydrogelation is investigated through X-ray diffraction of gelatin/montmorillonite samples. Remarkably, these samples show nearly perfect exfoliation, following a volumetric rule or colloidal swelling with nanoparticle loading. We report the possibility of incorporating high filler loadings by rapid hydrogelation, studied up to 64% volume fraction. In addition, particle order-disorder transitions were found in sample nanostructures with increasing nanofiller incorporation. Thus, the correlation or domain length in high filler loadings is investigated. Chapter **5** takes this study further by looking at the alignment mechanism and resulting properties in nacre-like gelatin/montmorillonite samples. Again, we systematically explore a method that influences nanostructuring by performing a case study. Common composite fabrication processes are discussed over the development of orientational order, as this is crucial to obtain high performance. The central hypothesis tested is whether an affine deformation mechanism can be tuned to result in highly-ordered nanostructures in 2D material composites prepared via solvent evaporation. Orientation distribution functions are explained and fitted to spectroscopy data to show the predominance of the alignment method. The level of in-plane orientation is monitored through the calculated order parameter. A high level of order was present for the wide filler concentration regime ranging from 0.4 to 64 vol.%. This motivated us to investigate the mechanical and water vapor barrier properties in these composites, with the additional goal of indirectly monitoring the nanoparticle aspect ratio. Finally, the affine deformation method is

discussed for developing next-generation advanced materials with tailored properties even at (very) high filler loadings.

**Chapters 6 and 7.** In these chapters, materials science and examples of urban waste resource recovery are integrated. In Chapter **6**, a novel biopolymer material that can be extracted from wastewater sludge, Kaumera˚, is studied for sustainable applications. The study is subdivided into multiple assays over (i) physicochemical and charge characterization, (ii) film plasticization and blending, (iii) nacre-like nanocomposites, and (iv) outlook towards applications. In general, the complex polymer mixture is briefly examined - from the perspective of a black box - for functionalities, polyelectrolyte/polyampholyte behavior, solubility and coacervation, and composite assembly and nanostructure alignment. In Chapter **7**, wastewater is investigated for cellulose and nanocellulose resource recovery. Secondary raw cellulose originating from toilet paper can be mined from wastewater sieving solids, return sludge, or excess sludge. A cellulose extraction method is developed and used to monitor the relative yield of cellulose in each wastewater stream. Based on the high quality of recovered fiber, closely resembling pristine cellulose, the wastewater-derived fibrous material is analyzed to synthesize cellulose nanocrystals. A synthetic hydrolysis route for producing nanocellulose from the recovered fibers is given. The yield and quality of the cellulose nanocrystals isolated from recovered fibers are investigated through various techniques. The incorporation of recovered nanorods is tested in bionanocomposites using Na-alginate as a matrix. To conclude, we discuss the fabrication of high-end and circular products from wastewater.

**Chapter 8.** This chapter aims to give a general outlook on biopolymer and bionanocomposite structure-property relations from the point of view of physical chemistry and polymer science.

# References

(1)     Rosenboom, J.-G.; Langer, R.; Traverso, G. Bioplastics for a Circular Economy. *Nat Rev Mater* **2022**, *7* (2), 117–137. https://doi.org/10.1038/s41578-021-00407-8.

(2)     Barthelat, F. Biomimetics for next Generation Materials. *Phil. Trans. R. Soc. A.* **2007**, *365* (1861), 2907–2919. https://doi.org/10.1098/rsta.2007.0006.

(3)     Tang, Z.; Kotov, N. A.; Magonov, S.; Ozturk, B. Nanostructured Artificial Nacre. *Nature Materials* **2003**, *2* (6), 413–418. https://doi.org/10.1038/nmat906.

(4)     Rajinipriya, M.; Nagalakshmaiah, M.; Robert, M.; Elkoun, S. Importance of Agricultural and Industrial Waste in the Field of Nanocellulose and Recent Industrial Developments of Wood Based Nanocellulose: A Review. *ACS Sustainable Chemistry and Engineering* **2018**, *6* (3), 2807–2828. https://doi.org/10.1021/acssuschemeng.7b03437.

(5)     Kehrein, P. A. Towards Water Resource Factories: Designing and Planning Sustainable Circular Wastewater Treatment Processes, *Delft University of Technology*, 2021. https://doi.org/10.4233/UUID:227A498C-52EE-4848-9E98-74FE0E7D2453.

(6)     Estévez-Alonso, Á.; Pei, R.; van Loosdrecht, M. C. M.; Kleerebezem, R.; Werker, A. Scaling-up Microbial Community-Based Polyhydroxyalkanoate Production: Status and Challenges. *Bioresource Technology* **2021**, *327*, 124790. https://doi.org/10.1016/j.biortech.2021.124790.

(7)     Aaliya, B.; Sunooj, K. V.; Lackner, M. Biopolymer Composites: A Review. *International Journal of Biobased Plastics* **2021**, *3* (1), 40–84. https://doi.org/10.1080/24759651.2021.1881214.

(8)     Koyyada, A.; Orsu, P. Natural Gum Polysaccharides as Efficient Tissue Engineering and Drug Delivery Biopolymers. *Journal of Drug Delivery Science and Technology* **2021**, *63*, 102431. https://doi.org/10.1016/j.jddst.2021.102431.

(9)     Babu, R. P.; O'connor, K.; Seeram, R. Current Progress on Bio-Based Polymers and Their Future Trends. *Progress in biomaterials* **2013**, *2*, 1–16.

(10)    Pandit, P.; Nadathur, G. T.; Maiti, S.; Regubalan, B. Functionality and Properties of Bio-Based Materials. *Bio-based materials for food packaging: Green and sustainable advanced packaging materials* **2018**, 81–103.

(11)    European Commission, D.-G. for I. M., Industry, Entrepreneurship and SMEs. *Bio-based products*. Internal Market, Industry, Entrepreneurship and SMEs. https://single-market-economy.ec.europa.eu/sectors/biotechnology/bio-based-products_en (accessed 2023-05-27).

(12)    Joseph, T. M.; Unni, A. B.; Joshy, K.; Kar Mahapatra, D.; Haponiuk, J.; Thomas, S. Emerging Bio-Based Polymers from Lab to Market: Current Strategies, Market Dynamics and Research Trends. *C* **2023**, *9* (1), 30.

(13)    Jancar, J.; Douglas, J. F.; Starr, F. W.; Kumar, S. K.; Cassagnau, P.; Lesser, A. J.; Sternstein, S. S.; Buehler, M. J. Current Issues in Research on Structure–Property Relationships in Polymer Nanocomposites. *Polymer* **2010**, *51* (15), 3321–3343. https://doi.org/10.1016/j.polymer.2010.04.074.

(14)    Klemm, D.; Heublein, B.; Fink, H.; Bohn, A. Cellulose: Fascinating Biopolymer and Sustainable Raw Material. *Angewandte chemie international edition* **2005**, *44* (22), 3358–3393.

(15)    Zhu, F. Barley Starch: Composition, Structure, Properties, and Modifications. *Comprehensive Reviews in Food Science and Food Safety* **2017**, *16* (4), 558–579.

(16)    Wijerathne, B.; Liao, T.; Ostrikov, K. (Ken); Sun, Z. Bioinspired Robust Mechanical Properties for Advanced Materials. *Small Structures* **2022**, *3* (9), 2100228. https://doi.org/10.1002/sstr.202100228.

(17)    Wegst, U. G. K.; Bai, H.; Saiz, E.; Tomsia, A. P.; Ritchie, R. O. Bioinspired Structural Materials. *Nat. Mater.* **2015**, *14* (1), 23–36. https://doi.org/10.1038/NMAT4089.

(18)    Chen, K.; Zhang, S.; Li, A.; Tang, X.; Li, L.; Guo, L. Bioinspired Interfacial Chelating-like Reinforcement Strategy toward Mechanically Enhanced Lamellar Materials. *ACS Nano* **2018**, *12* (5), 4269–4279. https://doi.org/10.1021/acsnano.7b08671.

(19)    Liu, D.; Lei, C.; Wu, K.; Fu, Q. A Multidirectionally Thermoconductive Phase Change Material Enables High and Durable Electricity *via* Real-Environment Solar–Thermal–Electric Conversion. *ACS Nano* **2020**, *14* (11), 15738–15747. https://doi.org/10.1021/acsnano.0c06680.

(20)    Huang, J.; Wang, X.; Wang, Z. L. Controlled Replication of Butterfly Wings for Achieving Tunable Photonic Properties. *Nano Lett.* **2006**, *6* (10), 2325–2331. https://doi.org/10.1021/nl061851t.

(21)    Liang, S.-M.; Ji, H.-M.; Li, Y.-Y.; Li, X.-W. An Ingenious Microstructure Arrangement in Deep-Sea *Nautilus* Shell against the Harsh Environment. *ACS Biomater. Sci. Eng.* **2021**, *7* (10), 4819–4827. https://doi.org/10.1021/acsbiomaterials.1c00956.

(22)    Lv, J.; Ding, D.; Yang, X.; Hou, K.; Miao, X.; Wang, D.; Kou, B.; Huang, L.; Tang, Z. Biomimetic Chiral Photonic Crystals. *Angewandte Chemie International Edition* **2019**, *58* (23), 7783–7787. https://doi.org/10.1002/anie.201903264.

(23)    Das, P.; Malho, J.-M.; Rahimi, K.; Schacher, F. H.; Wang, B.; Demco, D. E.; Walther, A. Nacre-Mimetics with Synthetic Nanoclays up to Ultrahigh Aspect Ratios. *Nat Commun* **2015**, *6* (1), 5967. https://doi.org/10.1038/ncomms6967.

(24)     He, H.; Guan, L.; Le Ferrand, H. Controlled Local Orientation of 2D Nanomaterials in 3D Devices: Methods and Prospects for Multifunctional Designs and Enhanced Performance. *J. Mater. Chem. A* **2022**, *10* (37), 19129–19168. https://doi.org/10.1039/d2ta01926d.

(25)     Zhang, Y.; Mei, J.; Yan, C.; Liao, T.; Bell, J.; Sun, Z. Bioinspired 2D Nanomaterials for Sustainable Applications. *Advanced Materials* **2020**, *32* (18), 1902806.

(26)     Munch, E.; Launey, M. E.; Alsem, D. H.; Saiz, E.; Tomsia, A. P.; Ritchie, R. O. Tough, Bio-Inspired Hybrid Materials. *Science* **2008**, *322* (5907), 1516–1520. https://doi.org/10.1126/science.1164865.

(27)     Zlopaša, J. Exploring the Structure, Properties, and Applications of Highly Ordered Bionanocomposites. *Delft University of Technology* **2017**. https://doi.org/10.4233/uuid:e47bfa54-4d58-4c82-829f-3cb2ceb6cfc7.

(28)     Vilcinskas, K.; Norder, B.; Goubitz, K.; Mulder, F. M.; Koper, G. J. M.; Picken, S. J. Tunable Order in Alginate/Graphene Biopolymer Nanocomposites. *Macromolecules* **2015**, *48* (22), 8323–8330. https://doi.org/10.1021/acs.macromol.5b01380.

(29)     Kim, J. H.; Shim, B. S.; Kim, H. S.; Lee, Y. J.; Min, S. K.; Jang, D.; Abas, Z.; Kim, J. Review of Nanocellulose for Sustainable Future Materials. *International Journal of Precision Engineering and Manufacturing - Green Technology* **2015**, *2* (2), 197–213. https://doi.org/10.1007/s40684-015-0024-9.

(30)     Lossada, F.; Hoenders, D.; Guo, J.; Jiao, D.; Walther, A. Self-Assembled Bioinspired Nanocomposites. *Acc. Chem. Res.* **2020**, *53* (11), 2622–2635. https://doi.org/10.1021/acs.accounts.0c00448.

(31)     Ed. *Jurasic Iridescent Ammonite*. https://www.flickr.com/photos/47134714@N04/29558096455 (accessed 2023-05-27).

(32)     Notafly. *Chrysina limbata*. https://commons.wikimedia.org/wiki/File:Chrysinasp..JPG (accessed 2023-05-27).

(33)     Leeuwen, K. V. The Energy & Raw Materials Factory : Role and Potential Contribution to the Circular Economy of the Netherlands. *Environmental Management* **2018**, 786–795. https://doi.org/10.1007/s00267-018-0995-8.

(34)     Energie- en Grondstoffenfabriek. *Efgf.nl. De Energie- & Grondstoffenfabriek.* Producten. https://www.efgf.nl/producten (accessed 2023-05-27).

(35)     Pronk, M.; de Kreuk, M. K.; de Bruin, B.; Kamminga, P.; Kleerebezem, R.; van Loosdrecht, M. C. M. Full Scale Performance of the Aerobic Granular Sludge Process for Sewage Treatment. *Water Research* **2015**, *84*, 207–217. https://doi.org/10.1016/j.watres.2015.07.011.

(36)     Aerobic Granular Sludge. In *Biological Wastewater Treatment: Principles, Modeling and Design*; Pronk, M., van Dijk, E. J. H., van Loosdrecht, M. C. M., Chen, G., Ekama, G. A., van Loosdrecht, M. C. M., Brdjanovic, D., Eds.; IWA Publishing, **2020**; p 0. https://doi.org/10.2166/9781789060362_0497.

(37)     Nereda® - RoyalHaskoningDHV. *Nereda®'s 100th Project: From Breakthrough Technology to Global Player*. https://nereda.royalhaskoningdhv.com/en/projects/how-nereda-helps-wastewater-treatment-adapt-to-change (accessed 2023-05-27).

(38)     Lin, Y.; de Kreuk, M.; van Loosdrecht, M. C. M.; Adin, A. Characterization of Alginate-like Exopolysaccharides Isolated from Aerobic Granular Sludge in Pilot-Plant. *Water Research* **2010**, *44* (11), 3355–3364. https://doi.org/10.1016/J.WATRES.2010.03.019.

(39)     Felz, S. Structural Extracellular Polymeric Substances from Aerobic Granular Sludge. *Delft University of Technology* **2019**, 115–115. https://doi.org/10.4233/uuid:93e702d1-92b2-4025-ab57-6d2c141ed14d10.4233/uuid:93e702d1-92b2-4025-ab57-6d2c141ed14d.

(40)     Grand View Research. *Alginate Market Size, Share & Trends Analysis Report By Type (High M, High G), By Product (Sodium, Propylene Glycol), By Application (Pharmaceutical, Industrial), By Region, And Segment Forecasts, 2021 - 2028. Report ID: GVR-2-68038-244-0.* https://www.grandviewresearch.com/industry-analysis/alginate-market (accessed 2023-05-27).

(41)     The Rhine and IJssel Water Authority, the Vallei and Veluwe Water Authority, Delft University of Technology, RoyalHaskoningDHV and the Dutch Foundation for Applied Research in Water Management (STOWA(stichting onderzoek waterschappen)). *Kaumera*. https://kaumera.com/english/kaumera/ (accessed 2023-05-05).

(42)     Kim, N. K.; Mao, N.; Lin, R.; Bhattacharyya, D.; van Loosdrecht, M. C. M.; Lin, Y. Flame Retardant Property of Flax Fabrics Coated by Extracellular Polymeric Substances Recovered from Both Activated Sludge and Aerobic Granular Sludge. *Water Research* **2020**, *170*, 115344–115344. https://doi.org/10.1016/j.watres.2019.115344.

(43)     Bahgat, N. T.; Wilfert, P.; Korving, L.; Van Loosdrecht, M. Integrated Resource Recovery from Aerobic Granular Sludge Plants. *Water Research* **2023**, *234*, 119819. https://doi.org/10.1016/j.watres.2023.119819.

(44)     Seviour, T.; Derlon, N.; Dueholm, M. S.; Flemming, H.-C.; Girbal-Neuhauser, E.; Horn, H.; Kjelleberg, S.; van Loosdrecht, M. C. M.; Lotti, T.; Malpei, M. F.; Nerenberg, R.; Neu, T. R.; Paul, E.; Yu, H.; Lin, Y. Extracellular Polymeric Substances of Biofilms: Suffering from an Identity Crisis. *Water Research* **2019**, *151*, 1–7. https://doi.org/10.1016/j.watres.2018.11.020.

(45)     The Rhine and IJssel Water Authority, the Vallei and Veluwe Water Authority, Delft University of Technology, RoyalHaskoningDHV and the Dutch Foundation for Applied Research in Water Management

(STOWA(stichting onderzoek waterschappen)). *Kaumera. The extraction process.* https://kaumera.com/technologie/kaumera-extractieproces/ (accessed 2023-05-27).

(46)  Sing, C. E.; Perry, S. L. Recent Progress in the Science of Complex Coacervation. *Soft Matter* **2020**, *16* (12), 2885–2914. https://doi.org/10.1039/d0sm00001a.

(47)  Kudaibergenov, S. E.; Nuraje, N. Intra-and Interpolyelectrolyte Complexes of Polyampholytes. *Polymers* **2018**, *10* (10), 1146.

(48)  Liu, G.; Parsons, D.; Craig, V. S. J. Re-Entrant Swelling and Redissolution of Polyelectrolytes Arises from an Increased Electrostatic Decay Length at High Salt Concentrations. *Journal of Colloid and Interface Science* **2020**, *579*, 369–378. https://doi.org/10.1016/j.jcis.2020.06.072.

(49)  Maity, H.; Baidya, L.; Reddy, G. Salt-Induced Transitions in the Conformational Ensembles of Intrinsically Disordered Proteins. *J. Phys. Chem. B* **2022**, *126* (32), 5959–5971. https://doi.org/10.1021/acs.jpcb.2c03476.

(50)  Gao, M.; Gawel, K.; Stokke, B. T. Polyelectrolyte and Antipolyelectrolyte Effects in Swelling of Polyampholyte and Polyzwitterionic Charge Balanced and Charge Offset Hydrogels. *European Polymer Journal* **2014**, *53*, 65–74. https://doi.org/10.1016/j.eurpolymj.2014.01.014.

(51)  Choi, W.; Park, S.; Kwon, J.-S.; Jang, E.-Y.; Kim, J.-Y.; Heo, J.; Hwang, Y.; Kim, B.-S.; Moon, J.-H.; Jung, S.; Choi, S.-H.; Lee, H.; Ahn, H.-W.; Hong, J. Reverse Actuation of Polyelectrolyte Effect for *In Vivo* Antifouling. *ACS Nano* **2021**, *15* (4), 6811–6828. https://doi.org/10.1021/acsnano.0c10431.

(52)  Pignataro, M. F.; Herrera, M. G.; Dodero, V. I. Evaluation of Peptide/Protein Self-Assembly and Aggregation by Spectroscopic Methods. *Molecules* **2020**, *25* (20), 4854. https://doi.org/10.3390/molecules25204854.

(53)  Lyu, X.; Clark, B.; Peterson, A. M. Thermal Transitions in and Structures of Dried Polyelectrolytes and Polyelectrolyte Complexes. *J. Polym. Sci. Part B: Polym. Phys.* **2017**, *55* (8), 684–691. https://doi.org/10.1002/polb.24319.

(54)  Nolte, A. J.; Treat, N. D.; Cohen, R. E.; Rubner, M. F. Effect of Relative Humidity on the Young's Modulus of Polyelectrolyte Multilayer Films and Related Nonionic Polymers. *Macromolecules* **2008**, *41* (15), 5793–5798. https://doi.org/10.1021/ma800732j.

(55)  Lalwani, S. M.; Batys, P.; Sammalkorpi, M.; Lutkenhaus, J. L. Relaxation Times of Solid-like Polyelectrolyte Complexes of Varying PH and Water Content. *Macromolecules* **2021**, *54* (17), 7765–7776. https://doi.org/10.1021/acs.macromol.1c00940.

(56)  Pfaff, N. M.; Dijksman, J. A.; Kemperman, A. J. B.; van Loosdrecht, M. C. M.; Kleijn, J. M. Rheological Characterisation of Alginate-like Exopolymer Gels Crosslinked with Calcium. *Water Research* **2021**, *207* (October), 117835–117835. https://doi.org/10.1016/j.watres.2021.117835.

(57)  Felz, S.; Kleikamp, H.; Zlopasa, J.; van Loosdrecht, M. C. M.; Lin, Y. Impact of Metal Ions on Structural EPS Hydrogels from Aerobic Granular Sludge. *Biofilm* **2020**, *2*, 100011. https://doi.org/10.1016/j.bioflm.2019.100011.

(58)  Collins, K. D. Ion Hydration: Implications for Cellular Function, Polyelectrolytes, and Protein Crystallization. *Biophysical Chemistry* **2006**, *119* (3), 271–281. https://doi.org/10.1016/j.bpc.2005.08.010.

(59)  Ni, J.; Tai, Q.; Lu, H.; Hu, Y.; Song, L. Microencapsulated Ammonium Polyphosphate with Polyurethane Shell: Preparation, Characterization, and Its Flame Retardance in Polyurethane. *Polymers for Advanced Technologies* **2010**, *21* (6), 392–400.

(60)  UL, O. 94-Tests for Flammability of Plastic Materials for Parts in Devices and Appliances. *Underwriters Laboratories Inc* **1996**.

(61)  Zhang, L.; Huang, Y.; Sun, P.; Hai, Y.; Jiang, S. A Self-Healing, Recyclable, and Degradable Fire-Retardant Gelatin-Based Biogel Coating for Green Buildings. *Soft Matter* **2021**, *17* (20), 5231–5239. https://doi.org/10.1039/D1SM00435B.

(62)  Amsterdam Institute for Advanced Metropolitan Solutions. *COMPRO: Creating a fully circular and bio-based building material from wastewater resources.* Ams-Institute. https://www.ams-institute.org/urban-challenges/circularity-urban-regions/compro-composite-building-material-wastewater-resources/ (accessed 2023-05-05).

(63)  Spinnewijn, O. Sustainable Binders for the Creation of a Dredge-Based Tile, Utrecht University, 2021. https://studenttheses.uu.nl/handle/20.500.12932/191 (accessed 2023-05-05).

# Introduction

# 2

# The glass transition temperature of heterogeneous biopolymer systems

*"We are not to tell nature what she's gotta be...*

*She's always got better imagination than we have."*

*– Richard P. Feynman*

# Abstract

*Biopolymers are abundant, renewable, and biodegradable resources. However, bio-based materials often require toughening additives, like (co)polymers or small plasticizing molecules. Plasticisation is monitored via the glass transition temperature versus diluent content. To describe this, several thermodynamic models exist; nevertheless, most expressions are phenomenological and lead to over-parametrisation. They also fail to describe the influence of sample history and the degree of miscibility via structure-property relationships. We propose a new model to deal with semi-compatible systems: the Generalised Mean model, which can classify diluent segregation or partitioning. When the constant $k_{GM}$ is below unity, the addition of plasticisers has hardly any effect, and in some cases, even anti-plasticisation is observed. On the other hand, when $k_{GM}$ is above unity, the system is highly plasticised even for a small addition of the plasticiser compound, which indicates the plasticiser locally has a higher concentration. To showcase the model, we studied Na-Alginate films with increasing sizes of sugar alcohols. Our $k_{GM}$ analysis showed blends have properties that depend on specific polymer interactions and morphological size effects. Finally, we also modelled other plasticised (bio)polymer systems from literature, concluding they all tend to have heterogeneous nature.*
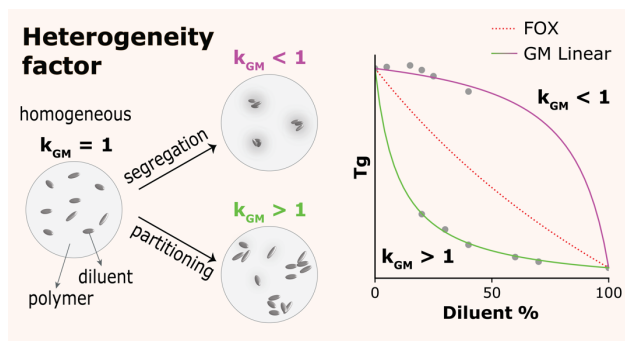
## 2.1. Introduction

Global concerns over climate change, plastic pollution, and scarcity of resources have made several industries actively look for alternative and sustainable materials sources. Biopolymers are a great alternative with many applications already developed in food, agriculture, biomedical, and composite fields[1–3]. However, solid-state materials consisting of polysaccharides and proteins are often too brittle and not workable[4]. This is a classical materials design dilemma, where films are either (too) stiff and brittle or tough and (too) ductile. A common alternative for toughening polymeric materials is blending them with a diluent[5–7]. This includes both (co)polymers and small non-volatile molecules, which can be added to decrease the polymer's glass transition temperature ($Tg$). Therefore, further exploring our understanding of polymer-polymer and polymer-diluent systems is fundamental for developing improved biodegradable and sustainable biopolymer-based applications.

Biopolymer blends are frequently required because they can combine the specific properties of different materials in one. Often small molecules are applied to plasticise the biopolymer, which provides better toughness and avoids catastrophic brittle failure. The ideal plasticiser for such biopolymer-based materials must be non-toxic, biodegradable, and preferably derived from natural sources[4]. For instance, there are many reports of materials composed of polyols, oligosaccharides, citrates, lactates, vegetable oils, and tannins as natural additives[8–10]. Even though the literature using bio-based materials and plasticiser agents is growing, their application is often investigated by trial and error. Furthermore, very few research studies exist on how to select a plasticiser, with most of them being phenomenological and case-specific. In addition, sample history, miscibility, and the extent of (local) phase separation are ignored. Therefore, how component compatibility affects the barrier, thermal and mechanical properties of biopolymers is poorly addressed. As a side note, it is probably fair to say that living tissues, materials in nature with structural and mechanical functions, such as teeth, bones, wood, wool, and silk, obtain their sometimes excellent properties by virtue of components that bring about the required amount of mobility.

## Glass transition model proposal

Polymer blend miscibility is often studied via the determination of $Tg$, in which a single measured transition temperature identifies compatible systems[11]. In truth, due to chain connectivity, even in miscible systems the components will effectively experience distinct

21

levels of mobility or relaxation times associated to a glass transition[12]. For binary systems, several thermodynamical models for predicting the averaged *Tg* have been proposed, for instance, using the Gordon-Taylor and Couchman-Karasz expressions[7,13–15]. In product engineering, the Fox equation[6] is frequently applied, which also appears as a limiting form of the Couchman-Karasz expression. Nevertheless, it is seldom mentioned that these theories are only intended for the case of full compatibility. This is far from the general case of (bio)polymer mixtures, which may have a complex chemical composition, might show multiple conformations, and variable levels of polydispersity. Due to this molecular complexity, the nanostructures that evolve from mixing biomacromolecules and diluents are expected to be locally heterogeneous in composition. On a supramolecular scale, there is a local organization of mixed components, i.e., a certain level of segregation or partitioning may be recognised (Chart 2.1). Experimentally, the *Tg* of such heterogeneous blends is identified by one broad transition. The prediction of the *Tg,* even in binary systems, will also be difficult due to possible component interactions[16]. As a result of concentration fluctuations[17] and specific interactions, data can show negative or positive deviations from the usual rule of mixing for *Tg*.

Not surprisingly, there have been plenty of reports on how models based on the Couchman-Karasz expression fail to describe systems lacking true miscibility[15,18,19]. Consequently, data from inhomogeneous mixtures are usually fitted by including additional correction terms to these equations. This leads to phenomenological expressions and over-parameterisation. To work with semi-compatible systems, we propose an alternative working model, the Generalised Mean (Linear) or *GM(L)*. Within this framework, the conventional Fox equation becomes a particular case of our model, that of a homogeneous miscible system. It is based on the rather obvious idea that *Tg* is connected to interactions (enthalpy) and degrees of freedom (entropy) using a second-order phase transition-like framework, where the enthalpy and entropy type terms are averaged as a function of composition.

**Chart 2.1.** The morphology classification of polymer systems we propose for glass transition ($Tg$) modelling, based on the degree of miscibility. Images inside boxes and circles relate to the microscale and nanoscale, respectively
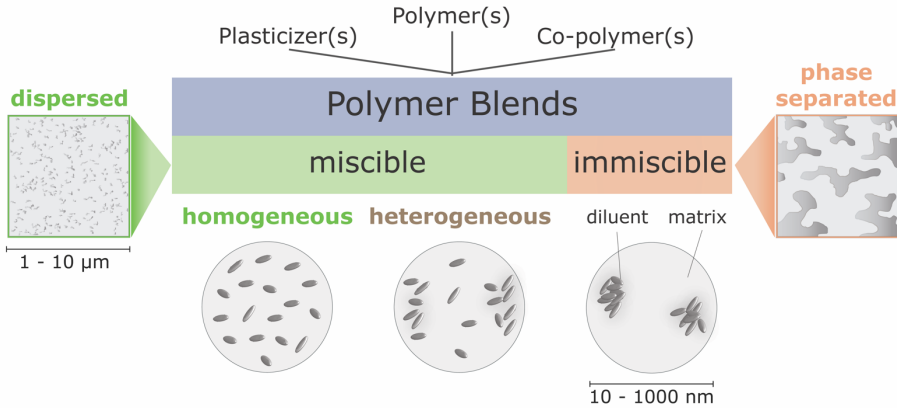


## Model case study with alginate-polyols

To showcase the use of the *GM(L)* model, we have performed a systematic study on the general plasticisation effects of Na-Alginate with polyols. We have selected sugar alcohols as polyols because they provide for a series of increasing H-bonded interactions and sizes. Then, we investigated if a single master curve of plasticisation occurs based on a plasticiser's mass fraction or molar density of the interacting functional group. Additionally, we used this system to investigate interactions and the degree of miscibility based on our *Tg* modelling.

Finally, we demonstrate how the *GM(L)* model can be applied to an extensive list of *Tg* datasets from the literature. We explore the general understanding of static heterogeneity in (bio)polymer mixtures by evaluating the model's constant $k_{GM}$. Special attention is given to complex, multicomponent biopolymer systems since we believe the current theoretical background on *Tg* for this class of materials has yet to be adequately addressed.

## 2.2. Materials and Methods

### 2.2.1. Materials

Sodium alginate (high ratio of mannuronic: guluronic acid, Mw ~12-40 kDa), Ethylene glycol, Glycerol, meso-Erythritol, D-(+)-Arabitol, D-Mannitol, and D-Sorbitol were purchased from Sigma–Aldrich.

### 2.2.2. Methods for Na-alginate-(sugar alcohol) films

#### Plasticisation and film casting

The alginate-polyol films were prepared by the solution-casting method. Different sugar alcohols ($(CHOH)_nH_2$, where $n$ is varying) with increasing chain length were tested to investigate the plasticising effect on the developed films. Namely, Ethylene glycol ($C_2$), Glycerol ($C_3$), Erythritol ($C_4$), Arabitol ($C_5$), Sorbitol ($C_6$), and Mannitol ($C_6$) were used as plasticisers. The film preparation procedure is described as follows: a 5 wt % stock solution of Na-alginate in demineralised water was prepared. Afterwards, an appropriate amount of dissolved plasticiser (5 wt %, in demineralised water) was added into separate film-forming solutions at a final dry mass of 0 to 50 wt % plasticiser (alginate basis, pH 8). The film-forming solutions with different plasticiser content were carefully homogenised with a glass rod, avoiding bubble formation until uniform blending, and cast into polystyrene petri-dishes. The exact weight was calculated separately for each plasticiser to result in films with a thickness of about 0.15 mm. The freshly cast films were placed in ambient conditions (at 50 RH and RT), and different drying environments were tested. After around 3 to 5 days of drying, the free-standing films were peeled from the casting surfaces for analysis. Water is a natural plasticiser for hygroscopic alginate films, and sorption/desorption phenomena occur depending on the ambient conditions. Hence, to evaluate only the effects of polyol addition to the films, the cut film specimens were vacuum dried for one day at 40 °C and kept in a desiccator containing silica gel until immediately before analysis. For glycerol and sorbitol, the humid films (ambient, ~50% RH) were also analysed for comparison.

#### Thermogravimetric analysis (TGA)

It was possible to add $C_2$ to alginate and cast thin films. However, vacuum drying also removed part of this plasticiser from the matrix since it is too volatile. Hence, to measure

the exact $C_2$ content in the dried films, Thermogravimetric Analysis (TGA) was carried out on a PerkinElmer TGA 8000. The measurements were performed on samples of about 5 mg, placed in a corundum crucible, from 30 – 300 °C at a heating rate of 5 °C min$^{-1}$, under a nitrogen atmosphere, with an isothermal step at 90 °C for 30 min. TGA was also used for determining the water content in films of $C_3$ and $C_6$ equilibrated to ambient relative humidity using similar scans.

## Dynamic mechanical thermal analysis (DMTA)

Dynamic Mechanical Thermal Analysis (DMTA) was performed on a PerkinElmer DMA-7e. DMTA experiments on the plasticised films were performed in a tensile mode at a frequency of 1 Hz from -100 to 180 °C temperature range at a heat rate of 5 °C min$^{-1}$, with film dimensions of roughly 20.0 x 3.0 x 0.1 mm. The thickness of the films was measured with the aid of a digital micrometer. The resulting glass transition was observed by the abrupt change in storage modulus slope and corresponding loss modulus maximum. This event is often called a polymer's alpha relaxation. When possible, $Tg$ was estimated from duplicate measurements.

## Glass transition modelling

To this experimental data, models were applied based on a $Tg$ rule of mixing of polymer and plasticiser contributions. For convention, $Tg$ 1 and $Tg$ 2 are expressed as polymer and diluent components, respectively, with high and low $Tg$ values. We chose to fit the often-applied Fox model[6]:

$$\frac{1}{Tg} = \frac{x_1}{Tg_1} + \frac{x_2}{Tg_2} \quad (2.1)$$

where $x_i$ and $Tg_i$ denote the molar fraction and glass transition of components 1 and 2, respectively.

Further, we also fitted our model of interest, the Generalised Mean Linear (*GM(L)*):

$$\frac{1}{Tg} = \frac{\frac{\phi_1}{Tg_1} + \frac{\phi_2 k_{GM}}{Tg_2}}{\phi_1 + \phi_2 k_{GM}} \quad (2.2)$$

where $\phi_i$ and $Tg_i$ denote the volume fraction and glass transition of components 1 and 2, respectively, and $k_{GM}$ denotes the model constant. A full description of the Fox model and the *GM(L)* models we propose here can be found in Appendix A (Supporting Information). Curve fitting using nonlinear least squares was performed for all the studied plasticisers using a Python code and the function *scipy.optimise.curve_fit*, which employs a trust region reflective algorithm[20]. The *Tg* values for alginate-polyol were optimised case by case but allowed to range from -200 to 200 °C. In addition, the *Tg* of alginate was not initially constrained to be the same in all systems. No initialisation values were given. The goodness-of-fit of models was evaluated by the total sum of squares (TSS), p-value, and standard error of the regression, S.

## 2.2.3. Modelling (bio)polymer mixtures from literature

Fox and *GM(L)* models, eqs 2.1 and 2.2, were also tested to an extended dataset of (bio)polymer blends carefully gathered from the literature. For completion, the full *GM* model was also investigated, with alpha and beta values set to be positive (Supporting Information, Figure S2.1, and Table S2.2), as this constraint on the exponents is required to ensure convergence.

## 2.3. Results and Discussion

### 2.3.1. Blends of Na-alginate-(sugar alcohol)

The glass transition temperature is a dynamic property with great current interest, since it is tied to thermal, mechanical, and vibrational properties. For instance, it is used not only to determine operational and processing temperature ranges but also influences mechanical properties like stiffness, tensile strength, toughness, hardness, and impact resistance[4,5]. Besides standard thermomechanical factors, it has been related to materials' adhesive and healing mechanisms [21–23]. Indirectly, *Tg* will also affect electrical, optical, diffusion and barrier properties, physical ageing, and environmental stability. The *Tg* of polymers can conventionally be assessed through thermal analysis, i.e., evaluating the

dependence of specific volume, jump in heat capacity, or change in modulus over temperature.

We chose to study the *Tg* of alginate-polyols by DMTA due to the high sensitivity of this method to polymer relaxations. The onset of the primary relaxation (alpha) corresponds to the mobility of the main chain, which happens only at *Tg*. Figure 2.1 shows examples of alpha relaxation identification from highly plasticised alginate films. In a polymer blend, the presence of one major relaxation is a sign of miscibility. DMTA showed primarily one main relaxation for dried samples, while samples left to ambient relative humidity resulted in the appearance of additional relaxations (Supporting Information). After the *Tg* event, the magnitude of the rubber plateau in alginate blends varied with the type and size of added sugar alcohol.
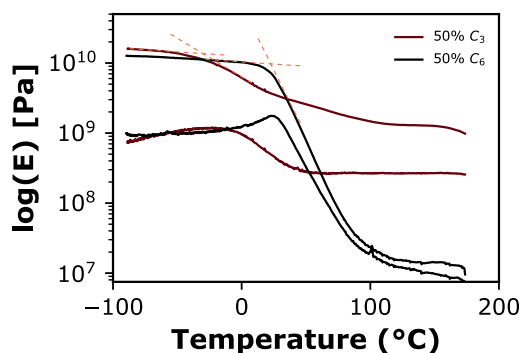


**Figure 2.1.** DMTA analysis of Na-alginate-(sugar alcohol) films containing 50 wt % glycerol ($C_3$) or sorbitol ($C_6$). The higher and lower curves show respectively the temperature dependence of storage (E') and loss (E'') modulus. The dashed lines demonstrate how to estimate the temperature of a glass transition relaxation on a logarithmic modulus scale.

In Figure 2.2, the obtained *Tg* values of dry blends are plotted against the diluent's mass or equivalent molar fractions. Irrespective of the way the plasticiser content is evaluated, one cannot find a master curve of *Tg* versus plasticiser. This is surprising since sugar alcohols have the same generic chemical formula: $(CHOH)_nH_2$. Even if we reduce all polyol concentrations to [CHOH] equivalents, as shown in the inset graph of Figure 2B, there is no obvious universal *Tg* pattern. This strong argument supports that, even though miscible, the sugar alcohols do not interact in the same way with the alginate chains.

# The glass transition temperature of heterogeneous biopolymer systems

Similar findings of a plasticiser-dependent interaction and compatibility limit have previously been reported for the systems of alginate and $C_3$ and $C_6$ polyols[24,25].
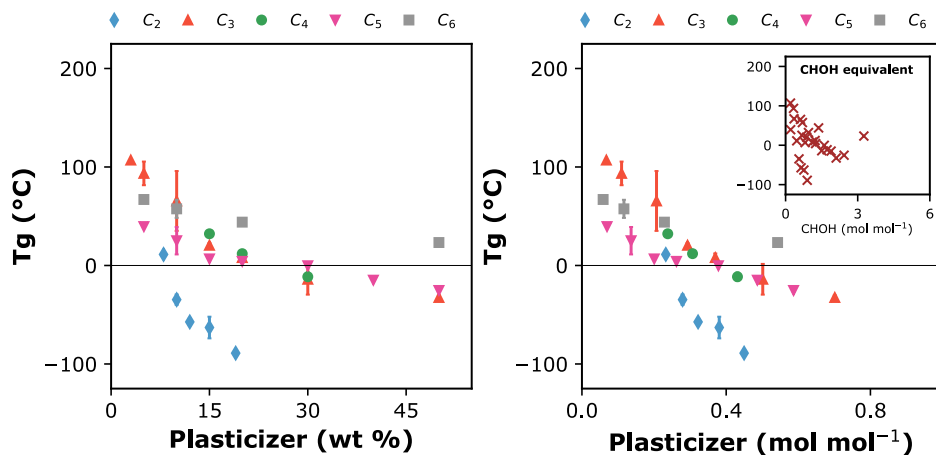


**Figure 2.2.** Glass transition temperature ($Tg$) of mixtures of Na-alginate and sugar alcohol plasticisers in mass (A) or molar (B) fractions. The sugar alcohols are depicted from $C_2$ to $C_6$, based on the general formula $(CHOH)_nH_2$. Inset: $Tg$ over plasticiser fractions translated to CHOH molar equivalents. Error bars indicate standard deviation.

We have performed model curve fitting to evaluate this $Tg$ data (Figure 2.3). The widely applied Fox model is a simple harmonic mean of $Tg$ contributions. We observe that this model does not fit the data of most sugar alcohol mixtures well. Even though the data fit for $C_3$ and $C_5$ are statistically accurate ($p < 0.05$, $S < 31$ °C), the values of $Tg$ are poorly predicted (Table 2.1). Alternatively, the linearization of the generalised mean model, *GML*, shows an excellent prediction of datasets ($p < 0.01$, $S < 15$ °C). In addition, the *GML* goodness-of-fit is equivalent to that obtained via the analogous Gordon-Taylor equation. However, when possible, the $Tg$ of individual components should also be experimentally obtained prior to model fitting. Hence, Table 2.1 values are to be taken as a likelihood of $Tg$ within the mixture. We also note that setting appropriate boundary conditions for the individual $Tg$ contributions was necessary for a good quality *GML* fit.
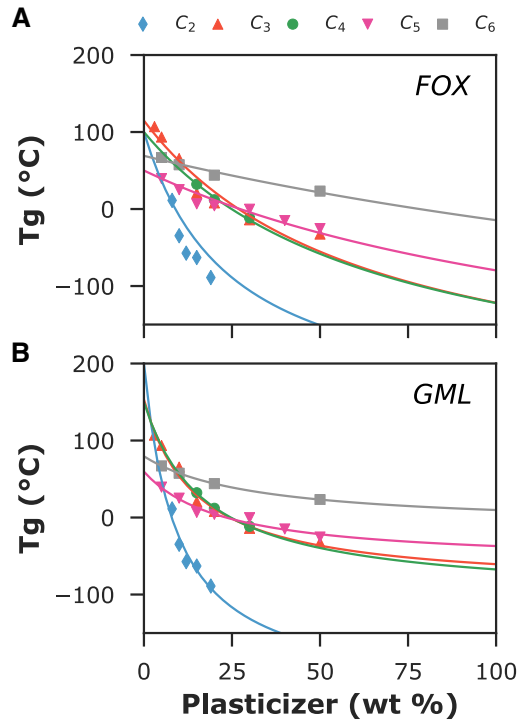
**Figure 2.3.** Experimental and calculated values of glass transition temperature (*Tg*) for Na-alginate-(sugar alcohols). A) Fox model (FOX); B) Generalised Mean Linear model (*GML*). Curve-fitting was allowed using appropriate boundary values for the individual *Tg* parameters.

**Table 2.1.** Glass transition parameters and statistics obtained from curve fitting Fox or Generalised Mean Linear (*GML*) model to Na-alginate-(sugar alcohol) datasets

| Polyol | Model | *Tg* 1 (°C) | *Tg* 2 (°C) | Model constant, k (fit ± st. error) | TSS | P-value | S (°C) |
|--------|-------|-------------|-------------|-------------------------------------|------|---------|--------|
| $C_2$ | Fox | 100* | -200* | 1 | 7781 | 0.0173 | 31.27 |
|  | GML | 200* | -196 | 1.93 ± 8.08 | 5665 | 0.0071 | 14.64 |
| $C_3$ | Fox | 115 | -122 | 1 | 17436 | 0.0006 | 16.30 |
|  | GML | 153 | -61 | 3.92 ± 1.31 | 17432 | 0.0002 | 8.31 |
| $C_4$ | Fox | 100* | -122 | 1 | 954 | 0.0374 | 4.25 |
|  | GML | 150* | -67 | 3.30 ± N/A | 954 | N/A | N/A |
| $C_5$ | Fox | 50* | -80 | 1 | 2944 | 0.0009 | 8.10 |
|  | GML | 60 | -37 | 3.75 ± 2.01 | 2944 | 0.0008 | 5.19 |
| $C_6$ | Fox | 69 | -14 | 1 | 1077 | 0.0252 | 4.12 |
|  | GML | 79 | 10 | 3.32 ± 0.00 | 1077 | 1.96E-14 | 6.62E-13 |

TSS: total sum of squares from the regression model
S: standard error of regression coefficient
N/A: not applicable due to zero degree of freedom
* Value corresponded to the used boundaries for the parameter

Another advantage of *Tg* models is that they can be used to indirectly determine the (virtual) transition of a glassy polymer by extrapolation to zero diluent concentration. Like many biopolymers[26], the *Tg* of pristine Na-alginate cannot be determined since thermal decomposition is observed before the transition. From Figure 2.3, all alginate-polyol datasets point towards a virtual Na-alginate *Tg*, or *Tg* 1, between 60 to 180 °C. Russo et al.[27] have previously reported a *Tg* of 133 °C for Na-alginate based on differential scanning calorimetry of relatively dry specimens. This seems a reasonable estimate of M-rich alginate with remaining tightly bound water. We can use this as a unified value for the Na-alginate-(sugar alcohols) data and retrofit it to the *GML* model (Figure 2.4). The approximated value of 133 °C does seem to fit well with most datasets except for $C_6$ (p > 0.05). That can be explained by the fact that the estimated *Tg* of Na-Alginate is not an actual material property but an apparent one, with a plasticiser changing the internal structure. For $C_5$ and $C_6$ polyols, both studied models result in a lower *Tg* estimated for the neat alginate. It might be that the addition of a larger H-bonding plasticiser partially

disrupted the semi-crystallinity of this block-copolymer. Evidence of semi-crystallinity was also found in powder XRD, haziness of alginate-polyol films, and a high modulus rubber plateau in DMTA results (Supporting Information). Additionally, the plasticiser itself also showed a tendency to crystallise, as in the case of films with high content of $C_4$ or another $C_6$ compound (mannitol).

Nevertheless, the new *GML* fits described all datasets well as a physical model (S < 25 °C) (Table 2.2). The fit values obtained for polyol *Tg* were in good agreement with literature (Supporting Information, Table S2.1). The retrofit allows us to appropriately compare the alginate *Tg* over increasing plasticiser fraction. For small-size polyols, $C_2$ and $C_3$, the *Tg* of the blend decreases rapidly with more polyol until a plateau is reached. For larger polyols, $C_5$ and $C_6$, we observe a *Tg* plateau already at a relatively lower polyol fraction. The *GML* model introduces a new constant, $k_{GM}$, which can be interpreted to arise from the static partitioning of the polymer/plasticiser fractions. From Table 2.2, the positive $k_{GM}$ values for all Na-Alginate-(sugar alcohols) indicate a substantial deviation from the case of miscibility ($k_{GM} = 1$, analogous to the Fox model). This $k_{GM}$ value > 1 means that the effective plasticiser concentration appears to be higher than expected, resulting in lower *Tg* at lower plasticiser content due to partitioning. The most significant deviations were observed for $C_5$ and $C_6$ alcohols, which might be explained by their size, causing substantial steric interaction-driven partitioning in a semi-crystalline matrix. We envision that a smaller plasticiser, such as $C_2$ polyol, would better penetrate and fill the free volume of the amorphous domains in contrast to $C_5$ and $C_6$ (Figure 2.4B), which would not be able to penetrate into the amorphous phase adjacent to the crystalline regions. In fact, it should be noticed that a certain level of semi-crystallinity will always result in $k_{GM}$ > 1, as the concentration of diluent in the amorphous matrix regions will effectively be higher than expected from the overall composition because the crystalline regions are not (or much less) available.

The actual extent of semi-crystalline/amorphous fractions and domain sizes is experimentally challenging to be obtained. In theory, it might have been resolved by X-ray scattering and analysis of the crystalline peak width using the Scherrer equation. For the case of alginate semi-crystallinity, the measured crystalline degree would also serve to estimate the amorphous phase that is available for the plasticizer. Thus, this amorphous space would be equivalent to the length of heterogeneity. This rationale obviously assumes the plasticizer to be amorphous in the resulting mixture. Nevertheless, getting good information on this from scattering techniques is very challenging and would constitute an entire additional study. One advantage of the *GML* model is that the

quantification of any crystalline or immobile fraction is not necessary to fit $Tg$ data over composition and identify levels of heterogeneity, therefore, it might serve to better determine heterogeneity from structural analysis as it provides an expectation value.

Indeed, only the *GML* model the *GML* model resulted in good descriptive curves for the $Tg$ of alginate-(sugar alcohols). We believe this can only be due to partial miscibility or, to put it in another way, local heterogeneity of polymer and plasticiser distribution in such blends. In some cases, the components' specific interactions might cause this phenomenon, i.e., semi-crystallinity, H-bonding, and chirality. In fact, H-bonds are well known to affect the final semi-crystallinity of polymers[28–30]. Another influence might be the chirality of $C_4$ to $C_6$ sugar alcohols, causing preferential sites in the plasticiser distribution. In general, the case of alginate blends is a good example that specific interaction contributions and partitioning need to be considered. The Fox model neglects such interactions, as it is based solely on the entropic contributions of components in a fully miscible blend. However, fully and partially miscible blends can be described with *GML*, where the constant $k_{GM}$ acts as a factor representing the heterogeneity. Regarding thermodynamics, $k_{GM}$ can also be interpreted as a convoluted factor of both (second order) enthalpic and entropic contributions.
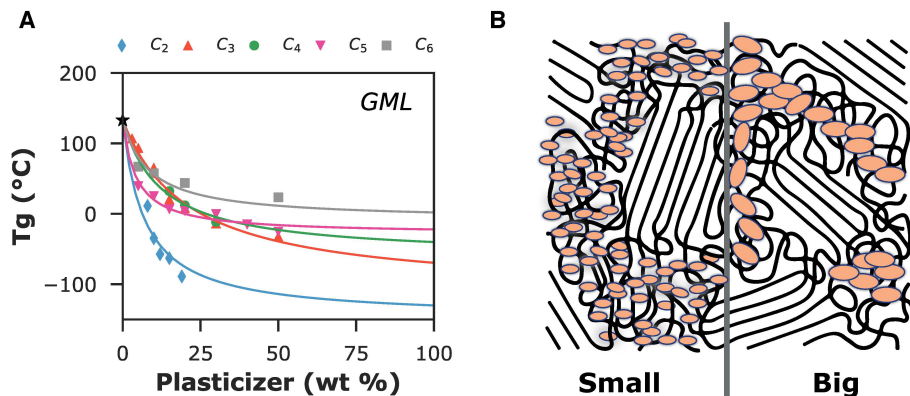
**Figure 2.4.** A) Experimental and calculated values of glass transition temperature (*Tg*) for Na-alginate-(sugar alcohols). Generalised Mean Linear (*GML*) model was fitted by assuming a fixed glassy polymer *Tg* (star) and appropriate boundary values for the plasticiser *Tg*. B) Illustration showing the difference in steric partitioning of a small or big plasticiser in a semi-crystalline polymer.

**Table 2.2.** Glass transition parameters and statistics obtained after curve fitting Generalised Mean Linear (*GML*) model on Na-alginate-(sugar alcohol) datasets using a unified *Tg* for the glassy polymer

| Polyol | *Tg* 1 (°C) | *Tg* 2 (°C) | Boundaries *Tg* 2 (°C) | $k_{GM}$ (fit ± st. error) | TSS | P-value | S (°C) |
|--------|-------------|-------------|------------------------|----------------------------|-----|---------|--------|
| $C_2$ | 133* | -130 | -100 ± 30 | 5.37 ± 42.85 | 5675 | 0.0432 | 24.96 |
| $C_3$ | 133* | -70 | -79 ± 30 | 2.83 ± 1.23 | 17439 | 0.0005 | 10.06 |
| $C_4$ | 133* | -40 | -10 ± 30 | 5.19 ± N/A | 956 | N/A | N/A |
| $C_5$ | 133* | -22 | -22 ± 30 | 14.90 ± 14.65 | 2945 | 0.0003 | 7.89 |
| $C_6$ | 133* | 2 | -28 ± 30 | 8.71 ± 20.26 | 1109 | 0.2949 | 20.84 |

TSS: total sum of squares from the regression model
S: standard error of regression coefficient
N/A: not applicable due to zero degree of freedom
* Assumed value for neat Na-alginate as found by Russo and co-workers[27]

## 2.3.2. Heterogeneity constant

Other situations can cause static heterogeneity ($k_{GM} \neq 1$) of a diluent distribution within a glassy polymer matrix. A link to the $Tg$ property can easily be interpreted if coupled with the free volume theory. For comparison purposes, one could classify heterogeneous blends resulting in $k_{GM}$ below or above unity, as illustrated in Chart 2.2. Both semi-crystallinity and crosslinking density variations can result in $Tg$ values lower than predicted by the Fox model ($k_{GM} > 1$). In the first case, as shown here with alginate-(polyols), steric partitioning effects can happen if the glassy matrix forms some crystalline or densely packed domains. With regards to crosslinking, a densely packed polymer-polymer network can also effectively create irregular boundaries to plasticiser clusters[7], even though crosslinking generically increases $Tg$ the plasticiser would be at a higher concentration in the available regions (Chart 2.2).

A few examples, usually in a low diluent content regime, can lead to $Tg$ values higher than predicted by the Fox model ($0 < k_{GM} < 1$). For instance, often at lower volume fractions, a plasticiser with a tendency for segregation can result in the free volume cavities of the polymer being filled with plasticiser, e.g., the anti-plasticisation effect. It can also happen that interactions between diluent/plasticiser and stiff polymer chains will enhance the level of polymer packing[31]. This is analogous to the anti-solvent polymer packing effect[32].

In both cases, further diluent clustering will frequently lead to microscopic phase separation of a blend, which is often observed in the form of opacity and coarsening of the phase-separated structure. Further, the diluent phase will either exudate out of the solid matrix, forming a binary or ternary-phased system, or even locally crystallise, thereby removing plasticiser from the polymer matrix entirely. These two events are macroscopic. From a thermodynamic perspective, the $k_{GM}$ factor can also characterise blends from miscible to immiscible states as it deviates away from unity.

It is interesting to note that the proposed local heterogeneity is not necessarily an undesirable phenomenon on a micro- or nanoscopic level. Heterogeneous plasticisation will create zones of local plasticisation and lubrication of amorphous polymer chains, resulting in mobility, pliability, and increased toughness. Simultaneously, the material's structural integrity or tenacity is still provided by the regions of low plasticiser content, preventing creep and flow. In other words, good plasticisers should not be too compatible with the polymer. It should be enough to mobilise but without solubilising the whole system.

Within the context of binary polymer blends, it might be helpful to consider the self-concentration approach proposed by Lodge and McLeish (2000) for blends with large $Tg_i$ difference[12]. The theory states that the average composition of the local environment around a certain component must be enriched by itself, because of chain connectivity. Therefore, even for homogeneous blends, each polymer will effectively experience its own composition dependent dynamics and effective $Tg$. This unavoidable segregation happens at the level of the chain Kuhn length and can get further exacerbated by the above-mentioned specific interactions and clustering/segregation phenomena. The $k_{GM}$ constant is obtained assuming a mixture's single or averaged $Tg$, where the product $k_{GM}\phi_2$ is an estimation of the (anti)plasticiser phase. Therefore, $k_{GM}$ is also a convoluted expression of local heterogeneity from multiple length scales: at chain segment and cluster levels. A theoretical relationship between the effective self-concentrations of a polymer/diluent in a blend and the $GM(L)$ model constant is still lacking, which shall be considered in future work.

2

**Chart 2.2.** Illustrations of a homogeneously distributed ($k_{GM} = 1$) or partitioned diluent ($k_{GM} \neq 1$) in a glassy polymer host. Boxes: microscale; circles: nanoscale
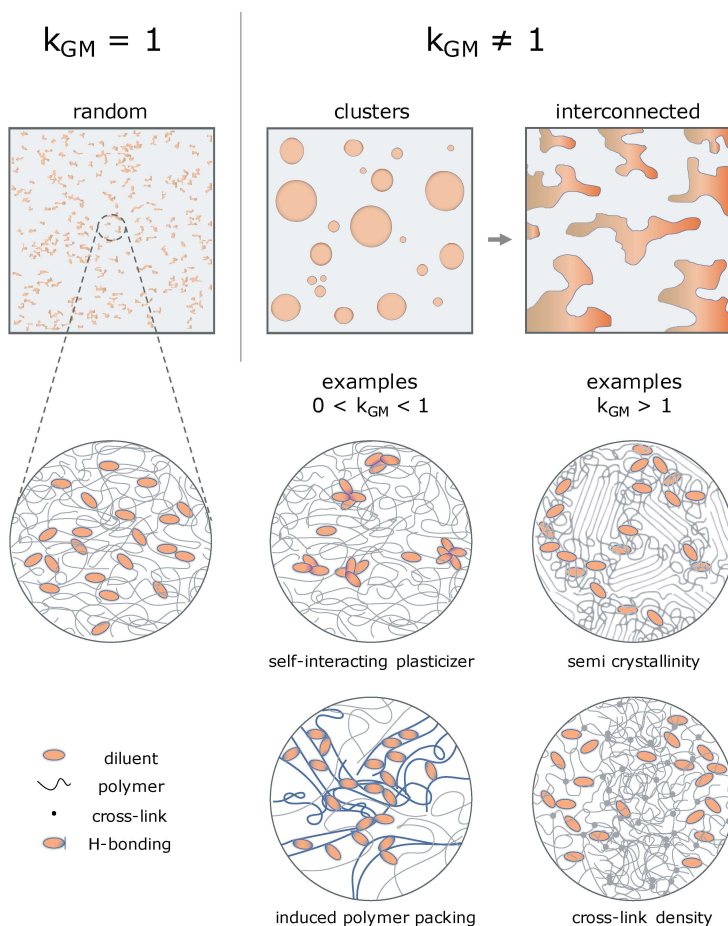


## 2.3.3. General application to heterogeneous mixtures

In this section, we demonstrate the versatility of the *GML* model for polymer blends of synthetic and biological origin. The goal is to show via partitioning factor $k_{GM}$ how easily systems fall outside true miscibility and simple rule of mixing theory, especially when biopolymers are used. These peculiar states of miscibility can arise from strong specific molecular interactions, steric effects, and conformational changes (morphology), depending strongly on sample history. It also makes sense to present this data compilation to connect our current work to general plasticisation and anti-plasticisation phenomena.

Figure 2.5 displays datasets with a greater decrease of $Tg$ with diluent content ($k_{GM} > 1$) in contrast to what was predicted by Fox's theory. We can interpret those results with the main rationale that the effective diluent volumetric fraction in a polymer matrix is higher than initially expected. In Figure 2.5A, the synthetic polymer blend of Phenoxy resin, or poly(hydroxy ether of bisphenol-A), with an aliphatic polyester of succinate (PDPS), shows decreased $Tg$ values in comparison with those predicted by entropic contributions (Fox theory)[31]. It is common knowledge in polymer processing that a physical blending of polymers needs strong specific interactions to result in miscibility. In this case, H-bonding between carbonyl groups of succinate ester and hydroxyl of Phenoxy should overcome intramolecular cohesion and favour miscibility. However, the $Tg$ curve gives us additional information that there must be competing energetic interactions since $k_{GM}$ > 1. We speculate this makes sense, since while Phenoxy is a blocky and amphiphilic polymer, the succinate polyester is polar, which might cause a more loosely packed structure, thus, affecting the free volume of the blend.

The plasticised mixture of tapioca starch-(glycerol/water) also follows a $k_{GM}$ > 1 trend (Figure 2.5). The difference between Fox and *GML* curves is subtle, as seen in Table 2.3. However, this becomes relevant if we know that the films formed a semi-crystalline matrix upon drying[33], possibly resulting in plasticiser partitioning. In starches, the recrystallisation of amylose and sometimes amylopectin can fundamentally influence properties, e.g., water vapour permeability and toughness. Water from moisture can further change $Tg$ considerably[34,35]. Consequently, the effect of water in crystalline biopolymer blends should always be evaluated or excluded.

Continuing on Figure 2.5B, the system of maltodextrin-glucose[15] is interesting because the polymer is a polydisperse derivative of starch. The maltodextrin analysed did not show crystallite sites; nevertheless, again, we find that $k_{GM}$ > 1. This can maybe be explained by the strong H-bonding interactions between glucose and maltodextrin, creating plasticiser-polymer and polymer-polymer domains with possible steric effects[15]. One could consider evaluating the extent of blending steric effects by systematically increasing the plasticiser size, for instance, from smaller polyols to different chain length polyethylene glycols[36].

Complexes of guest-host chemistry and crosslinking will also impact $Tg$ values and trends. In Figure 2.5B, a blend between a methylated polymer of β-cyclodextrin (polyβ-cyclodextrin) and mannitol[37] shows a significant divergence from Fox's prediction. The polymer cyclodextrin can form hydrophobic-core inclusion complexes for drug delivery.

# The glass transition temperature of heterogeneous biopolymer systems

The degree of di-ester crosslinking of the polymer with citrate is also essential to this application and $Tg$ determination. The 36 wt.% crosslinked and plasticised material was produced via a melting process. We could relate the $Tg$ divergence from the ideal rule of mixing theory to the increased free volume of heterogeneous crosslinking of the sample, influencing molecular packing, along with mannitol's resistance to filling in the hydrophilic core of cyclodextrin inclusions.
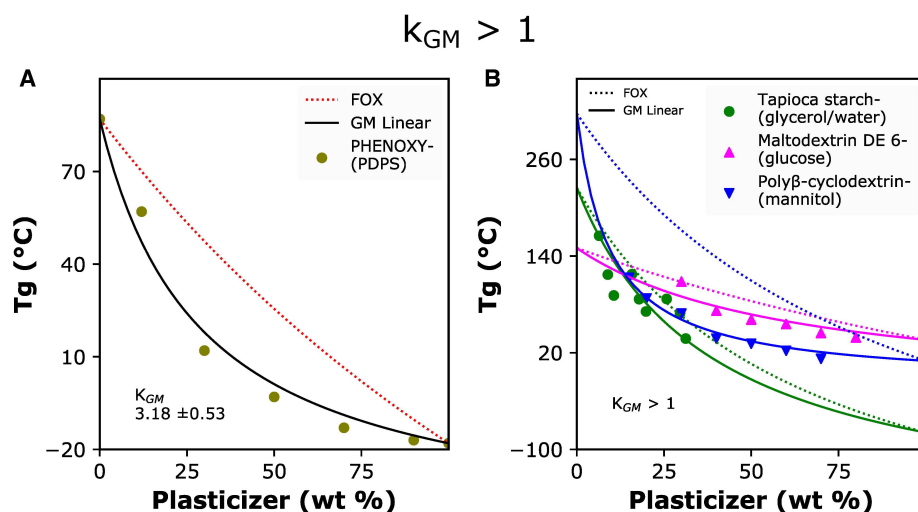
**Figure 2.5.** Experimental and calculated values of glass transition temperature ($Tg$) for several datasets displaying a greater-than-expected decrease with a plasticiser (or $k_{GM} > 1$). A) Synthetic polymer blend of Polyhydroxyether of bisphenol A (PHENOXY) and Poly(2,2-dimethyl-1,3-propylene succinate) (PDPS). B) Biopolymer-(plasticiser) mixtures. FOX: Fox model (dotted lines); GM Linear: Generalised Mean Linear model (solid lines). Curve-fitting was performed using fixed values for the individual $Tg$ parameters for demonstrative purposes. Data from Schneider, 1997[31]; Chang, 2006[33]; Linnenkugel et al., 2021[15]; Tabary et al., 2016[37].

A good plasticiser will result in pliable and durable materials that are easy to process by increasing the mixture's free volume or lowering the $Tg$. In turn, the mixed material should be tougher than the initial glassy polymer. In Figure 2.6, datasets show an increase of $Tg$ with polymer or plasticiser content. This increase deviates completely from Fox theory; for $GML$, it represents the case of $0 < k_{GM} < 1$ (Table 2.3). In fact, the synthetic blend of polybenzimidazole with commercial polyetherimide (Ultem)[31] resulted in anti-

plasticisation. This phenomenon happens when we observe an increase in overall specific density with diluent addition[5]. In extreme cases, even phase separation can occur. Within the partial miscibility region, anti-plasticisation can be desired if a material's performance needs to be improved. However, a slowly decreasing $Tg$ or even a plateau with increasing diluent content often seems counterintuitive. Polybenzimidazoles (PBIAz) are high-performance engineering thermoplastics with a very stiff aromatic polymer core and high $Tg$ values (> 400 °C). In Figure 2.6A, we propose that the strong H-bonding interaction of PBIAz with Ultem via amine groups may cause additional stiffness via chain confinement. Hence, in this case, the favourable interactions between the chains cause the $Tg$ to hardly decreases, giving rise to anti-plasticisation.

For sugar palm starch-(glycerol) plasticised films, data in Figure 2.6B, strong H-bonding interactions between glycerol and amylose/amylopectin resulted in high $Tg$ values[38,39]. In particular for starches, processing can be crucial. Starch samples often must be gelatinised at high temperatures (> 130 °C) to obtain thermoplastic behaviour. This could result in plasticiser affecting the formation of crystalline domains from starch moieties. Similarly, systems of chitosan-polyols can also show significantly different properties depending on the strength of H-bonding interaction with the polymer backbone and overall moisture content (Figure 2.6). The chitosan data shown is with respect to hydroxyl groups of sugar alcohols[40]. It is important to note that with further diluent addition, ageing, or the increment of water from moisture, systems can dramatically move from the anti-plasticised to plasticised regime[41–43]. This can be observed both in $Tg$ and in mechanical performance. The plasticisation shift will depend on how strong the energetic interactions (enthalpy-driven) are and how favourable the increase of free volume (entropy-driven) is. In polymer blends and plasticized systems with large $\Delta Tg_i$, this has been early on reported as a break (or cusp) in $Tg$-composition curves[11,44]. The phenomena have mostly been attributed to a critical temperature, where a change in (strong) specific interactions with diluent fraction is observed.

Trends in multicomponent systems can also be interpreted similarly via $k_{GM}$. A 1:1 starch/chitosan blend was produced by micro-fluidization[45]. This blend was plasticised by glycerol and water, showing high anti-plasticisation ($0 < k_{GM} < 1$) through strong H-bonding between plasticiser and macromolecules. Previous works have only presented explicit thermodynamic solutions for multicomponent systems of polysaccharides, polyols, and water[8,15]; by working with Flory Huggins's free volume theory and extending the Couchman-Karasz expression for $Tg$.

## The glass transition temperature of heterogeneous biopolymer systems

Locally heterogenous mixtures are ubiquitous in materials based on (bio)polymers, showing complex thermodynamic behaviour. We have observed that $k_{GM}$ can be a helpful tool to investigate (bio)polymer-diluent miscibility and possibly derive insights into structure-property relationships. We note that the linearised *GML* model is intended only for systems in a continuum, i.e., with no phase separation, crystallisation, or phase inversion. Alternatively, the original *GM* model can adopt complex shapes (Supporting Information, Figure S2.1). Yet we do not recommend modelling immiscible systems instead of splitting the developed phases. Overall, this study is another example that the topic of glass transition is a complicated part of polymer science[46]. For example, it is often very challenging to determine the *Tg* of neat and biopolymers mixtures because the thermal transitions are found above degradation, increasing with the strength of electrostatic interactions, crosslinks, and branching. Nowadays, this topic has become even more relevant with the rapid pursuit of tailored biodegradable and sustainable materials.
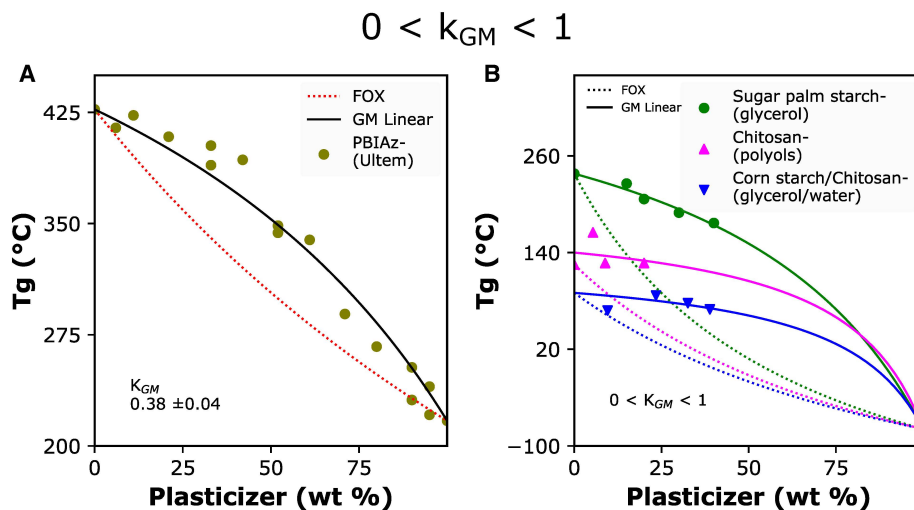
**Figure 2.6.** Experimental and calculated values of glass transition temperature (*Tg*) for several datasets displaying lower than expected decrease with a plasticiser (or $0 < k_{GM} < 1$). A) Synthetic polymer blend of Polybenzimidazole (PBIAz) and Ultem Polyetherimide (Ultem). B) Biopolymer-(plasticiser) mixtures. FOX: Fox model (dotted lines); GM Linear: Generalised Mean Linear model (solid lines). Curve-fitting was performed using fixed values for the individual *Tg* parameters for demonstration purposes. Data from Schneider 1997[31]; Sahari et al., 2013[38]; Ma et al., 2019[40]; Liu et al., 2013[45].

**Table 2.3.** Glass transition parameters and statistics obtained from curve fitting Fox and Generalised Mean Linear (*GML*) model for datasets showing deviations from the rule of mixing

| System | *Tg* 1 (°C) | *Tg* 2 (°C) | Model | Model constant, *k* (fit ± st. error) | TSS | P-value | S (°C) | References |
|---|---|---|---|---|---|---|---|---|
| PHENOXY - (PDPS) | 87* | -18* | Fox | 1 | 11167 | N/A | 18.92 | Schneider, 1997[31] |
| | | | GML | 3.18 ± 0.53 | 10183 | 2.52E-6 | 5.31 | |
| Tapioca starch - (glycerol/water) | 225** | -79** | Fox | 1 | 15759 | N/A | 28.57 | Chang, 2006[33] |
| | | | GML | 1.41 ± 0.19 | 10615 | 0.0009 | 24.24 | |
| Maltodextrin DE 6 - (glucose) | 150** | 36* | Fox | 1 | 5107 | N/A | 13.07 | Linnenkugel et al., 2021[15] |
| | | | GML | 1.91 ± 0.72 | 3779 | 0.0024 | 9.44 | |
| Poly-cyclodextrin - (mannitol) | 317* | 10* | Fox | 1 | 61190 | N/A | 67.79 | Tabary et al., 2016[37] |
| | | | GML | 5.60 ± 0.57 | 9984 | 6.95E-7 | 5.56 | |
| PBIAz - (ULTEM) | 427* | 217* | Fox | 1 | 112615 | N/A | 30.08 | Schneider 1997[31] |
| | | | GML | 0.38 ± 0.04 | 98908 | 6.04E-13 | 12.88 | |
| Sugar palm starch - (glycerol) | 238* | -79** | Fox | 1 | 41787 | N/A | 96.51 | Sahari et al., 2013[3838] |
| | | | GML | 0.14 ± 0.01 | 2526 | 0.0005 | 4.96 | |
| Chitosan - (polyols) | 125* | -79** | Fox | 1 | 8196 | N/A | 54.83 | Ma et al., 2019[40] |
| | | | GML | 0.09 ± 48.92 | 1124 | 0.7109 | 18.82 | |
| Corn starch/Chitosan - (glycerol/water) | 90** | -79** | Fox | 1 | 10514 | N/A | 52.92 | Liu et al., 2013[45] |
| | | | GML | 0.11 ± 0.19 | 250 | 0.3069 | 11.35 | |

\* Values used to fit models were extracted from the original data source
\*\* Values used to fit models were absent and, thus, estimated by this study for illustrative purposes

## 2.4. Summary and Conclusions

The Generalised Mean Linear model, *GML*, works as a versatile model for studying the glass transition of polymer blends and plasticised systems. The model can be seen as a natural extension of the widely used Fox model (1956). In *GML*, if the constant $k_{GM}$ is not 1, the system is not fully homogeneous - or Fox-like - and there is obvious evidence of heterogeneity or local de-mixing on a nanoscale. This can be explored via systematic

studies to reveal structure-property relationships of blends and to elect a suitable and stable plasticiser for a specific application. To deal with strong interactions and heterogeneity, previous models have been proposed and modified, like Couchman-Karasz equations. However, the adopted solutions are often case-specific, phenomenological, and lead to over-parametrisation, failing to describe the overall picture of (partial) miscibility.

This study showcases our *GML* model applied to predict the *Tg* of Na-alginate and polyols as plasticising molecules. The experimental data on *Tg* clearly does not follow the Fox equation, while only the *GML* model can fit the results. This indicates that heterogeneity is important in alginate-polyol, as is also substantiated by the observed size effect of the type of polyol on *Tg* curves. This proposed heterogeneity indeed becomes apparent at higher plasticiser content from the overall sample appearance and via microscopy. Hence, sample processing history also becomes important. This heterogeneous plasticiser distribution is presumably caused by regio-specific interactions in the alginate-polyol system, such as the semi-crystallinity of the polymer matrix and steric effects in amorphous domains, as is apparent from our results. In addition, the *GML* model can easily describe the heterogeneity present in a wide range of diverse (bio)polymer blends, demonstrating its utility in analysing complex polymer materials and even anti-plasticisation phenomena.

Based on the above and considering the heterogeneous nature of biopolymers, research on bio-based systems can benefit from the *GML* approach. Living organisms produce biopolymers that are designed to be complex in structure and interactions, containing chiral macromolecular arrangements taking the form of helices, sheets, or even showing semi-crystallinity. The already present structural heterogeneity is often amplified by extraction and (re)processing conditions. In the case of solvent-based processes, the scale of heterogeneity can be large, especially, if elevated temperatures are used. The chemical structure, therefore, is not so well controlled. In addition, electrostatic interactions are nearly always present, which adds additional specific interactions not customarily found in fossil-based polymers. In summary, one could say the molecular morphology of materials based on biopolymers and natural plasticisers is intrinsically heterogeneous. Hence, such systems should nearly always fall outside the commonly used rules of mixing for the thermal properties of polymer blends.

## Supporting information

The complete supporting information is available at DOI: 10.1021/acs.biomac.2c01356

## Appendix A

In this section, we give a short summary of the glass transition theory of mixtures and show how the Generalised Mean model can be derived from a quasi-second order thermodynamic transition.

### Glass transition modelling

Couchman and Karasz (1978) demonstrated an interesting model for the effect of the composition of binary mixtures on $Tg$[13]. The model was successful for compatible polymer-polymers blends and also polymer-diluent systems[7,15]. The model derivation was based on writing that $Tg$ is not a first-order thermodynamic transition; more specifically, on the property of continuity of a system's specific entropy at $Tg$. Hence, the integration of $\Delta c_p$ of a polymer blend results in the following simplified expression:

$$x_1 \int_{Tg_1}^{Tg} (c_{p1}^l - c_{p1}^g) d\ln T + x_2 \int_{Tg_2}^{Tg} (c_{p2}^l - c_{p2}^g) d\ln T + \Delta_{mix}S = 0 \qquad \text{(S2.1)}$$

where $x$, $Tg$, $c_p$, $l$, $g$ denote molar (or volume) fraction, glass transition, specific heat, supercooled liquid and glassy states of pure components 1 and 2, respectively. Originally, the authors were also careful to mention that the commonly neglected entropic terms just above and below the transition ($\Delta_{mix}S = \Delta S_{mix}^l - \Delta S_{mix}^g$), should be included if there are excess entropy changes upon mixing (conformational, thermal, etc.). From the perspective of Gibbs free energy, it is true that an enthalpic relationship of eq S2.1 also holds. Irrespective of the form (entropy or volume continuity conditions), note that for most systems the $c_p$ property of components undergoes a finite discontinuity at the transition.

All models derived from eq S2.1 have the activation or mobility of chain units as a fundamental principle, corrected through $\Delta c_p$ values. Another ubiquitous $Tg$ model is the expression earlier proposed by Gordon and Taylor (1953)[14], which can also be rearranged into another simplification of eq S2.1. To derive this relationship, we must rewrite $\Delta c_{p2}/\Delta c_{p1}$ into a constant, $k_{GT}$, so that:

$$Tg = \frac{x_1 Tg_1 + k_{\text{GT}} x_2 Tg_2}{x_1 + k_{\text{GT}} x_2} \qquad (S2.2)$$

In fact, the thermodynamic parameter $k_{GT}$ is related to a constant coefficient of expansion (volume) during the transition. However, this phenomenological solution was conceived for ideally mixed copolymers. Thus, a simplification ($k_{GT} = 1$) results in a linear averaging of the *Tg,* which to our knowledge never occurs.

The most frequently used equation for the change in *Tg* is the phenomenological Fox (1956) expression[6,30,47,48]:

$$\frac{1}{Tg} = \frac{x_1}{Tg_1} + \frac{x_2}{Tg_2} \qquad (S2.3)$$

From equation (S1), it assumes that $\Delta c_{p2} {}^* Tg_1 / \Delta c_{p1}$ is a constant. This way, the predicted *Tg* becomes a simple rule of mixing of the entropic contributions of the pure components. Hence, simply put, it assumes no effect from enthalpic interactions upon mixing.

However, when we analyse *Tg* changes with an $x_2$ component, a large portion of experimental results show large deviations from those ideal mixture predictions. The most used forms of the discussed models either neglect excess thermodynamic property from mixing or make it elusive to work around such values since $\Delta c_p$ corrections are not straightforward to interpret. Several other models have been proposed to tackle this, such as the models of Kwei (1984)[49], additional terms expanding Couchman-Karasz (eq 3)[15,19,50,51], and models based on virial coefficients[31]. Yet most of these approaches can easily result in over-parameterisation, and outcomes are hard to interpret.

## Generalised mean model

Inspired by the simple harmonic mean expression proposed by Fox, we have developed a new working model for the *Tg* property in blends. Similar to previous studies, we assume *Tg* is a quasi-second-order transition according to the Ehrenfest classification. Thus, it can be written as $T_g = \frac{\Delta_s \partial H}{\Delta_s \partial S}$, where $\partial H$ and $\partial S$ are, respectively, second or $n$th-term partial derivatives of enthalpy and entropy at transition. If we further expand on this equality, we can take the relation in thermodynamic properties to be weighted in the form of a generalised or power mean instead of the Fox-like harmonic mean. It follows that the Generalised Mean (GM) model becomes:

$$Tg = \frac{\Delta_s \partial H}{\Delta_s \partial S} = \frac{(\phi_1 \Delta_s \partial H_1{}^\beta + \phi_2 \Delta_s \partial H_2{}^\beta)^{1/\beta}}{(\phi_1 \Delta_s \partial S_1{}^\alpha + \phi_2 \Delta_s \partial S_2{}^\alpha)^{1/\alpha}} \qquad \text{(S2.4)}$$

where $\phi_i$, $\alpha$, $\beta$ are volume or mass fraction of components 1 or 2, entropy exponential, and enthalpy exponential, respectively.

The expression S2.4 can be further arranged if we couple some of the partial derivative terms into a constant, $k_{GM}$. For convenience, $k_{GM}$ is obtained by substituting the ratio of partial derivative enthalpies $\partial H$ of components ($\Delta_s \partial H_i$). However, a similar output could have been obtained by using $\partial S$. Considering that the Tg of each component is $\Delta_s \partial H_i / \Delta_s \partial S_i$ and that $k_{GM}$ can be expressed as $\Delta_s \partial H_2 / \Delta_s \partial H_1$, the full GM equation can be manipulated into the applicable form:

$$Tg = \frac{(\phi_1 Tg_1{}^\beta + \phi_2 (Tg_1 k_{GM})^\beta)^{1/\beta}}{(\phi_1 + \phi_2 (\frac{Tg_1 k_{GM}}{Tg_2})^\alpha)^{1/\alpha}} \qquad \text{(S2.4a)}$$

where $\phi_i$, $Tg_i$, $k_{GM}$, $\alpha$, $\beta$ are volume or mass fraction of components 1 or 2, glass transition of components 1 or 2, model constant, entropy exponential, and enthalpy exponential, respectively. This model has five degrees of freedom and can resolve into nontrivial parabola or S-shaped curves by tuning the $\alpha$ and $\beta$ exponents. Previously, such S-shaped data have been previously modelled using virial $Tg$ models, e.g., for tetramethyl bisphenol-A polycarbonate-(polystyrene) blend[31]. Nevertheless, we noticed that most data take a simple form, and we can do a linearisation ($\alpha$, $\beta$ = 1). Hence, the linearised Generalised Mean model (*GML*) becomes:

$$\frac{1}{Tg} = \frac{\frac{\phi_1}{Tg_1} + \frac{\phi_2 k_{GM}}{Tg_2}}{\phi_1 + \phi_2 k_{GM}} \qquad \text{(S2.5)}$$

From this form, the model can also revert to the Fox equation (eq S2.3) if $k_{GM}$ is 1, which explains our choice for defining $k_{GM}$ from the enthalpy ratio. The constant $k_{GM}$ can also be interpreted as a partitioning factor correcting the volume fraction of diluent ($\phi_2$). Hence, it is a static measure of system partitioning or heterogeneity. The *GML* version resolves most nonlinear cases and is mathematically analogous to the Gordon-Taylor model (appears from assuming a ratio of partial derivative entropies $\partial S$). Moreover, *GML* is useful because excess property and possible structural changes can be easily monitored with one factor, $k_{GM}$.

The values and morphological states implied from fitting the *GM(L)* model are heavily influenced by sample history. Hence, drying and cooling rates will likely influence the assessed diluent partitioning. In particular, the cooling rate effect on sample history

should be accounted for, since quenching can suppress the difference in $Tg$(s). It is also worth underlining that sensible experimental kinetic rates should be used for determining the thermal transition. The experiment observation times should obviously be probing the relaxation times of system components. Furthermore, the $Tg$ property is known to broaden and increase logarithmically with the quench rate[52]. Although the time-dependent effects are not explored, the model is able to fit accordingly the $Tg$ curves over composition, irrespective of the studied fabrication method or experimental rates employed.

Reliable $Tg$ measurements are crucial for the findings of $GML$ model fit to be valid. This should be ensured by selecting a sensitive enough technique, for instance DMTA, dielectric spectroscopy and modulated differential scanning calorimetry. These methods are less affected by broadening effects at transition[17]. Yet $Tg$ variations among methodologies as high as 20 °C are normally expected. In addition, adequate machine calibration and experimental conditions (environment, rate, strain, oscillatory parameters) need to be explored. Lastly, the data analysis step should be well reported for there are multiple standard ways to obtain $Tg$.

## Summary of thermodynamic relations

The Gibbs energy $G(T, P, \{n\})$ is a continuous function of its natural variables temperature $T$, pressure $P$, and composition, $\{n\}$, and has as derivatives over temperature entropy $S = -\frac{\partial G}{\partial T}$ and enthalpy $H = -T^2 \frac{\partial G/T}{\partial T}$. In the Ehrenfest sense, at a first-order transition, the Gibbs function is continuously differentiable everywhere except at the phase transition temperature, where the slope changes, so that $S$ and $H$ have jump-values, $\Delta S$ and $\Delta H$, respectively. The jump values differ by a factor equal to the transition temperature, i.e.: $T_t = \frac{\Delta_t H}{\Delta_t S}$, where the subscript $t$ denotes that the values are to be taken at the transition.

The entropy and enthalpy are continuous, except at first-order phase transitions, and their derivatives with temperature are related to the specific heat as: $\frac{\partial S}{\partial T} = \frac{c_p}{T}$ and $\frac{\partial H}{\partial T} = c_p$.

At a second order transition, the enthalpy and entropy are continuously differentiable everywhere except at the phase transition, where the slope changes so that the heat capacity has a jump value such that: $T_s = \frac{\Delta_s \frac{\partial H}{\partial T}}{\Delta_s \frac{\partial S}{\partial T}}$, where the subscript $s$ denotes that the

values are to be taken at the secondary transition. If a material's glass transition is assumed to be a (pseudo) second order phase transition, the same relation should apply to the jump-values of $\partial H$ and $\partial S$. Nevertheless, the relationships mentioned above do not work for systems with $c_p$ close to infinity at transition, i.e., lambda transitions, as is the case of systems with order-disorder evolution.

The blending of components will also involve thermodynamic mixing functions, i.e., the entropy of mixing $\Delta_{mix}S$ and enthalpy of mixing $\Delta_{mix}H$. For ideal miscible mixtures, the enthalpy of mixing is zero, and the entropy of mixing is positive from increased disorder. We can imagine entropy as the main driving force arising from the dispersion of components. Real mixtures often contain excess interaction of any of the pairs of components. This specific interaction(s) might result in enthalpy changes or additional entropy upon mixing, for instance, from molecular clustering. Depending on the magnitude of the enthalpy step from energetic interactions or adverse entropy, the total Gibbs energy becomes positive, and the system phase separates spontaneously. This would cause miscibility up to a certain composition (partial miscibility) or full immiscibly in a polymer blend. Excess functions can be calculated as the difference between $\Delta_{mix}S$ (or $\Delta_{mix}H$) of real and ideal solutions to investigate nonideal cases.

## Supporting Figures and Tables

### Sugar alcohol glass transition temperature

**Table S2.1.** Sugar alcohol glass transition temperature from literature and comparison to values from curve fitting Generalised Mean Linear (*GML*) model using a unified *Tg* for the glassy polymer

| Polyol | Literature Tg 2 (°C) | Reference | Tg 1 (°C) | Boundaries Tg 2 (°C) | GML Tg 2 (°C) | \|ΔTg 2\| (°C) |
|---|---|---|---|---|---|---|
| $C_2$ | -113 | Nagoe and Oguni (2008)[53] | 133* | -100 ± 30 | -130 | 17 |
| $C_3$ | -84 | Huang et al. (2018)[54] | 133* | -79 ± 30 | -70 | 14 |
| $C_4$ | -60 | Fujii et al. (2015)[55] | 133* | -10 ± 30 | -40 | 20 |
| $C_5$ | -13 | Huang et al. (2018)[54] | 133* | -22 ± 30 | -22 | 9 |
| $C_6$ | -4 | Huang et al. (2018)[54] | 133* | -28 ± 30 | 2 | 6 |

* Assumed value for neat Na-alginate as found by Russo and co-workers[27]
\|ΔTg 2\|: absolute difference between literature and curve-fit values of *Tg 2*

## Full GM model applied to datasets from literature
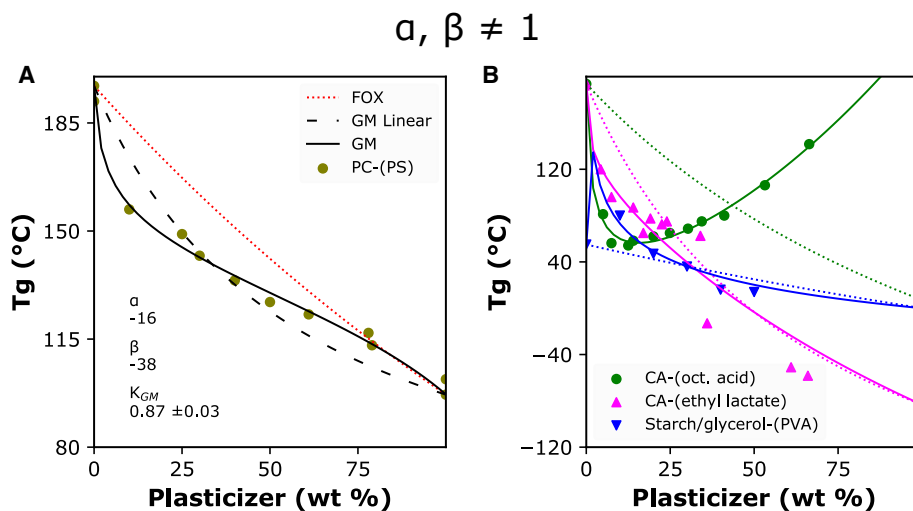


**Figure S2.1.** Experimental and calculated values of glass transition temperature (Tg) for several datasets displaying complex deviations from rules of mixing (or $\alpha_{GM}$, $\beta_{GM} \neq 1$ in eq S2.4a). A) A synthetic polymer blend of Polycarbonate (PC) and Polystyrene (PS). B) Biopolymer-(plasticizer) mixtures of cellulose acetate (CA) and a blend of plasticized Starch/PVA. FOX: Fox model (dotted lines); GML: Generalised Mean Linear model (dot-dashed line); GM: Generalised Mean model (solid lines). For demonstrative purposes, FOX and GML curve-fitting was performed using fixed values for the individual Tg parameters. Data from Schneider 1997[31]; Decroix et al. 2020[30]; Kahvand et al., 2019[56].

**Table S2.2.** Glass transition parameters and statistics obtained after curve fitting a Fox model and Generalised Mean models for datasets showing complex immiscibility

| System | $Tg\,1$ (°C) | $Tg\,2$ (°C) | Model | Model constant, $k$ (fit ± st. error) | $\alpha$ (fit ± st. error) | $\beta$ (fit ± st. error) | TSS | P-value | S (°C) | Ref. |
|---|---|---|---|---|---|---|---|---|---|---|
| PC - (PS) | 197 | 97 | Fox | 1 | 1 | 1 | 12195 | N/A | 9.33 | Schneider 1997[31] |
| | 197 | 97 | GM | 0.87 ± 0.03 | -15.94 ± 17.62 | -37.59 ± 24.26 | 11297 | 3.53E-12 | 2.87 | |
| CA - (octanoic acid) | 194 | 7* | Fox | 1 | 1 | 1 | 41492 | N/A | 63.14 | Decroix et al., 2020[30] |
| | 194 | 241 | GM | 2.25 ± 0.21 | 7.68 ± 2.70 | 2.94 ± 0.82 | 19264 | 2.12E-12 | 4.19 | |
| CA - (ethyl lactate) | 194 | -83* | Fox | 1 | 1 | 1 | 61010 | N/A | 32.81 | Decroix et al., 2020[30] |
| | 194 | -83 | GM | 0.78 ± 0.15 | -1.03 ± 0.82 | -30.87 ± 66.74 | 55949 | 4.07E-7 | 20.93 | |
| Starch/ glycerol- (PVA) | 55 | 0 | Fox | 1 | 1 | 1 | 4296 | N/A | 15.19 | Kahvand et al., 2019[56] |
| | 55 | 0 | GM | 89.13 ± 264056215.16 | 3.91 ± 2611662.85 | 6.54 ± 7315596.32 | 4271 | 6.27E-5 | 6.30 | |

* Values used to fit models were estimated by this study for illustrative purposes

# References

(1)　　Zhang, Y.; Han, J. H. Mechanical and Thermal Characteristics of Pea Starch Films Plasticized with Monosaccharides and Polyols. *J Food Sci* **2006**, *71* (2), E109–E118. https://doi.org/10.1111/j.1365-2621.2006.tb08891.x.

(2)　　Tavassoli-Kafrani, E.; Shekarchizadeh, H.; Masoudpour-Behabadi, M. Development of Edible Films and Coatings from Alginates and Carrageenans. *Carbohydr Polym* **2016**, *137*, 360–374. https://doi.org/10.1016/j.carbpol.2015.10.074.

(3)　　Area, M. R.; Montero, B.; Rico, M.; Barral, L.; Bouza, R.; López, J. Isosorbide Plasticized Corn Starch Filled with Poly(3-Hydroxybutyrate-Co-3-Hydroxyvalerate) Microparticles: Properties and Behavior under Environmental Factors. *Int J Biol Macromol* **2022**, *202*, 345–353. https://doi.org/10.1016/j.ijbiomac.2022.01.032.

(4)　　Vieira, M. G. A.; da Silva, M. A.; dos Santos, L. O.; Beppu, M. M. Natural-Based Plasticizers and Biopolymer Films: A Review. *Eur Polym J* **2011**, *47* (3), 254–263. https://doi.org/10.1016/j.eurpolymj.2010.12.011.

(5)　　Stukalin, E. B.; Douglas, J. F.; Freed, K. F. Plasticization and Antiplasticization of Polymer Melts Diluted by Low Molar Mass Species. *J Chem Phys* **2010**, *132* (8), 084504. https://doi.org/10.1063/1.3304738.

(6)　　Fox, T. G. Influence of Diluent and of Copolymer Composition on the Glass Temperature of a Polymer System. *Bull. Am. Phys. Soc.* **1956**, *1*, 123.

(7)　　Brinke, G. ten; Karasz, F. E.; Ellis, T. S. Depression of Glass Transition Temperatures of Polymer Networks by Diluents. *Macromolecules* **1983**, *16* (2), 244–249. https://doi.org/10.1021/ma00236a017.

(8)　　van der Sman, R. G. M. Phase Separation, Antiplasticization and Moisture Sorption in Ternary Systems Containing Polysaccharides and Polyols. *Food Hydrocoll* **2019**, *87* (August 2018), 360–370. https://doi.org/10.1016/j.foodhyd.2018.07.051.

(9)　　Bocqué, M.; Voirin, C.; Lapinte, V.; Caillol, S.; Robin, J. J. Petro-Based and Bio-Based Plasticizers: Chemical Structures to Plasticizing Properties. *J Polym Sci A Polym Chem* **2016**, *54* (1), 11–33. https://doi.org/10.1002/pola.27917.

(10)　　Wang, N.; Feng, X.; Pei, J.; Cui, Q.; Li, Y.; Liu, H.; Zhang, X. Biobased Reversible Cross-Linking Enables Self-Healing and Reprocessing of Epoxy Resins. *ACS Sustain Chem Eng* **2022**, *10* (11), 3604–3613. https://doi.org/10.1021/acssuschemeng.1c08378.

(11)　　Prud'Homme, R. E. Polymeric Plasticizers for PVC. *J. Vinyl Technol.* **1989**, *11* (1), 6–8. https://doi.org/10.1002/vnl.730110104.

(12)　　Lodge, T. P.; McLeish, T. C. B. Self-Concentrations and Effective Glass Transition Temperatures in Polymer Blends. *Macromolecules* **2000**, *33* (14), 5278–5284. https://doi.org/10.1021/ma9921706.

(13)　　Couchman, P. R.; Karasz, F. E. A Classical Thermodynamic Discussion of the Effect of Composition on Glass-Transition Temperatures. *Macromolecules* **1978**, *11* (1), 117–119. https://doi.org/10.1021/ma60061a021.

(14)　　Gordon, M.; Taylor, J. S. Ideal Copolymers and the Second-Order Transitions of Synthetic Rubbers. I. Noncrystalline Copolymers. *Rubber Chem Technol* **1953**, *26* (2), 323–335. https://doi.org/10.5254/1.3539818.

(15)　　Linnenkugel, S.; Paterson, A. H. J.; Huffman, L. M.; Bronlund, J. E. Prediction of the Glass Transition Temperature of Low Molecular Weight Components and Polysaccharide Mixtures. *J Food Eng* **2021**, *292* (June 2020), 110345. https://doi.org/10.1016/j.jfoodeng.2020.110345.

(16)　　Huang, C. C.; Du, M. X.; Zhang, B. Q.; Liu, C. Y. Glass Transition Temperatures of Copolymers: Molecular Origins of Deviation from the Linear Relation. *Macromolecules* **2022**, *55* (8), 3189–3200. https://doi.org/10.1021/acs.macromol.1c02287.

(17)　　Zetsche, A.; Fischer, E. W. Dielectric Studies of the A-relaxation in Miscible Polymer Blends and Its Relation to Concentration Fluctuations. *Acta Polym* **1994**, *45* (3), 168–175. https://doi.org/10.1002/actp.1994.010450306.

(18)　　Mayhew, E. J.; Neal, C. H.; Lee, S. Y.; Schmidt, S. J. Glass Transition Prediction Strategies Based on the Couchman-Karasz Equation in Model Confectionary Systems. *J Food Eng* **2017**, *214*, 287–302. https://doi.org/10.1016/j.jfoodeng.2017.07.007.

(19)　　Pinal, R. Entropy of Mixing and the Glass Transition of Amorphous Mixtures. *Entropy* **2008**, *10* (3), 207–223. https://doi.org/10.3390/entropy-e10030207.

(20)　　Virtanen, P.; Gommers, R.; Oliphant, T. E.; Haberland, M.; Reddy, T.; Cournapeau, D.; Burovski, E.; Peterson, P.; Weckesser, W.; Bright, J. SciPy 1.0: Fundamental Algorithms for Scientific Computing in Python. *Nat Methods* **2020**, *17* (3), 261–272.

(21)　　Boiko, Y. M.; Guérin, G.; Marikhin, V. A.; Prud'homme, R. E. Healing of Interfaces of Amorphous and Semi-Crystalline Poly (Ethylene Terephthalate) in the Vicinity of the Glass Transition Temperature. *Polymer* **2001**, *42* (21), 8695–8702.

(22)　　Ji, G.; Zhang, P.; Nji, J.; John, M.; Li, G. Shape Memory Polymer-Based Self-Healing Composites. In *Recent Advances in Smart Self-healing Polymers and Composites*; Elsevier Ltd, **2015**; pp 293–363. https://doi.org/10.1016/B978-1-78242-280-8.00011-X.

(23)　　Gately, T. J.; Li, W.; Mostafavi, S. H.; Bardeen, C. J. Reversible Adhesion Switching Using Spiropyran Photoisomerization in a High Glass Transition Temperature Polymer. *Macromolecules* **2021**, *54* (20), 9319–9326. https://doi.org/10.1021/acs.macromol.1c01262.

(24)     Gao, C.; Pollet, E.; Avérous, L. Innovative Plasticized Alginate Obtained by Thermo-Mechanical Mixing: Effect of Different Biobased Polyols Systems. *Carbohydr Polym* **2017**, *157*, 669–676. https://doi.org/10.1016/j.carbpol.2016.10.037.

(25)     Gao, C.; Pollet, E.; Avérous, L. Properties of Glycerol-Plasticized Alginate Films Obtained by Thermo-Mechanical Mixing. *Food Hydrocoll* **2017**, *63*, 414–420. https://doi.org/10.1016/j.foodhyd.2016.09.023.

(26)     Gatsiou, C. A.; Bick, A.; Krokidis, X.; Economou, I. G. Atomistic and Coarse-Grained Simulations of Bulk Amorphous Amylose above and below the Glass Transition. *Macromolecules* **2022**, *55* (8), 2999–3010. https://doi.org/10.1021/acs.macromol.1c01925.

(27)     Russo, R.; Malinconico, M.; Santagata, G. Effect of Cross-Linking with Calcium Ions on the Physical Properties of Alginate Films. *Biomacromolecules* **2007**, *8* (10), 3193–3197. https://doi.org/10.1021/bm700565h.

(28)     Domján, A.; Bajdik, J.; Pintye-Hódi, K. Understanding of the Plasticizing Effects of Glycerol and PEG 400 on Chitosan Films Using Solid-State NMR Spectroscopy. *Macromolecules* **2009**, *42* (13), 4667–4673. https://doi.org/10.1021/ma8021234.

(29)     Anglès, M. N.; Dufresne, A. Plasticized Starch/Tunicin Whiskers Nanocomposite Materials. 2: Mechanical Behavior. *Macromolecules* **2001**, *34* (9), 2921–2931. https://doi.org/10.1021/ma001555h.

(30)     Decroix, C.; Chalamet, Y.; Sudre, G.; Caroll, V. Thermo-Mechanical Properties and Blend Behaviour of Cellulose Acetate/Lactates and Acid Systems: Natural-Based Plasticizers. *Carbohydr Polym* **2020**, *237* (February), 116072. https://doi.org/10.1016/j.carbpol.2020.116072.

(31)     Schneider, H. A. Conformational Entropy Contributions to the Glass Temperature of Blends of Miscible Polymers. *J Res Natl Inst Stand Technol* **1997**, *102* (2), 229. https://doi.org/10.6028/jres.102.018.

(32)     Flory, P. J. *Principles of Polymer Chemistry*; Cornell university press, 1953.

(33)     Chang, Y. P.; Abd Karim, A.; Seow, C. C. Interactive Plasticizing-Antiplasticizing Effects of Water and Glycerol on the Tensile Properties of Tapioca Starch Films. *Food Hydrocoll* **2006**, *20* (1), 1–8. https://doi.org/10.1016/j.foodhyd.2005.02.004.

(34)     Li, W.; Yun, L.; Zhao, Y.; Zhi, Z.; Muhindo, E. M.; Geng, X.; Liu, R.; Wu, T.; Sui, W.; Zhang, M. Effect of Water Sorption on Glass Transition and Microstructural Variation of Dextran & Sugar Mixtures. *Carbohydr Polym* **2022**, *290*, 119505. https://doi.org/10.1016/j.carbpol.2022.119505.

(35)     Stępień, A.; Grzyb, K. Comparison of Critical Storage Parameters of the Powders Containing Soy Protein Isolate and Inulin, Based on the Concepts: Water Activity and Temperature of Glass Transition. *Int J Biol Macromol* **2023**, *230*, 123174. https://doi.org/10.1016/j.ijbiomac.2023.123174.

(36)     Pasini Cabello, S. D.; Takara, E. A.; Marchese, J.; Ochoa, N. A. Influence of Plasticizers in Pectin Films: Microstructural Changes. *Mater Chem Phys* **2015**, *162*, 491–497. https://doi.org/10.1016/j.matchemphys.2015.06.019.

(37)     Tabary, N.; Garcia-Fernandez, M. J.; Danède, F.; Descamps, M.; Martel, B.; Willart, J. F. Determination of the Glass Transition Temperature of Cyclodextrin Polymers. *Carbohydr Polym* **2016**, *148*, 172–180. https://doi.org/10.1016/j.carbpol.2016.04.032.

(38)     Sahari, J.; Sapuan, S. M.; Zainudin, E. S.; Maleque, M. A. Thermo-Mechanical Behaviors of Thermoplastic Starch Derived from Sugar Palm Tree (Arenga Pinnata). *Carbohydr Polym* **2013**, *92* (2), 1711–1716. https://doi.org/10.1016/j.carbpol.2012.11.031.

(39)     Sanyang, M. L.; Sapuan, S. M.; Jawaid, M.; Ishak, M. R.; Sahari, J. Effect of Plasticizer Type and Concentration on Tensile, Thermal and Barrier Properties of Biodegradable Films Based on Sugar Palm (Arenga Pinnata) Starch. *Polymers (Basel, Switz.)* **2015**, *7* (6), 1106–1124. https://doi.org/10.3390/polym7061106.

(40)     Ma, X.; Qiao, C.; Wang, X.; Yao, J.; Xu, J. Structural Characterization and Properties of Polyols Plasticized Chitosan Films. *Int J Biol Macromol* **2019**, *135*, 240–245. https://doi.org/10.1016/j.ijbiomac.2019.05.158.

(41)     Zhao, Y.; Liu, J.; Li, X.; Lu, Y.; Wang, S. Q. How and Why Polymer Glasses Lose Their Ductility Due to Plasticizers. *Macromolecules* **2017**, *50* (5), 2024–2032. https://doi.org/10.1021/acs.macromol.6b02158.

(42)     Lourdin, D.; Bizot, H.; Colonna, P. "Antiplasticization" in Starch-Glycerol Films? *J Appl Polym Sci* **1997**, *63* (8), 1047–1053. https://doi.org/10.1002/(sici)1097-4628(19970222)63:8<1047::aid-app11>3.0.co;2-3.

(43)     Mascia, L.; Kouparitsas, Y.; Nocita, D.; Bao, X. Antiplasticization of Polymer Materials: Structural Aspects and Effects on Mechanical and Diffusion-Controlled Properties. *Polymers (Basel, Swtiz.)* **2020**, *12* (4), 769. https://doi.org/10.3390/POLYM12040769.

(44)     Aubin, M.; Prud'homme, R. E. Analysis of the Glass Transition Temperature of Miscible Polymer Blends. *Macromolecules* **1988**, *21*(10), 2945–2948.

(45)     Liu, H.; Adhikari, R.; Guo, Q.; Adhikari, B. Preparation and Characterization of Glycerol Plasticized (High-Amylose) Starch-Chitosan Films. *J Food Eng* **2013**, *116* (2), 588–597. https://doi.org/10.1016/j.jfoodeng.2012.12.037.

(46)     Lapuk, S. E.; Ponomareva, M. A.; Galukhin, A. v.; Mukhametzyanov, T. A.; Schick, C.; Gerasimov, A. v. Glass Transition Kinetics and Physical Aging of Polyvinylpyrrolidones with Different Molecular Masses. *Macromolecules* **2022**, *55* (11), 4516–4522. https://doi.org/10.1021/acs.macromol.2c00547.

(47)     Guvendiren, M.; McSwain, R. L.; Mates, T. E.; Shull, K. R. Welding Kinetics in a Miscible Blend of High-Tg and Low-T g Polymers. *Macromolecules* **2010**, *43* (7), 3392–3398. https://doi.org/10.1021/ma902679u.

(48)     Su, S. Prediction of the Miscibility of Pbat/Pla Blends. *Polymers (Basel)* **2021**, *13* (14). https://doi.org/10.3390/polym13142339.

(49)      Kwei, T. K. The Effect of Hydrogen Bonding on the Glass Transition Temperatures of Polymer Mixtures. *Journal of Polymer Science: Polymer Letters Edition* **1984**, *22* (6), 307–313. https://doi.org/10.1002/pol.1984.130220603.

(50)      Brostow, W.; Chiu, R.; Kalogeras, I. M.; Vassilikou-Dova, A. Prediction of Glass Transition Temperatures: Binary Blends and Copolymers. *Mater Lett* **2008**, *62* (17–18), 3152–3155. https://doi.org/10.1016/j.matlet.2008.02.008.

(51)      Lu, X.; Weiss, R. A. Relationship between the Glass Transition Temperature and the Interaction Parameter of Miscible Binary Polymer Blends. *Macromolecules* **1992**, *25* (12), 3242–3246.

(52)      Trachenko, K.; Brazhkin, V. v. Heat Capacity at the Glass Transition. *Phys Rev B Condens Matter Mater Phys* **2011**, *83* (1), 014201. https://doi.org/10.1103/PhysRevB.83.014201.

(53)      Nagoe, A.; Oguni, M. Glass Transition Behaviors of Ethylene Glycol - Water Solutions Confined within Nano-Pores of Silica Gel. *AIP Conf Proc* **2008**, *982* (February 2008), 185–188. https://doi.org/10.1063/1.2897779.

(54)      Huang, C.; Chen, Z.; Gui, Y.; Shi, C.; Zhang, G. G. Z.; Yu, L. Crystal Nucleation Rates in Glass-Forming Molecular Liquids: D-Sorbitol, D-Arabitol, D-Xylitol, and Glycerol. *J. Chem. Phys.* **2018**, *149* (5). https://doi.org/10.1063/1.5042112.

(55)      Fujii, K.; Izutsu, K. I.; Kume, M.; Yoshino, T.; Yoshihashi, Y.; Sugano, K.; Terada, K. Physical Characterization of Meso-Erythritol as a Crystalline Bulking Agent for Freeze-Dried Formulations. *Chem Pharm Bull (Tokyo)* **2015**, *63* (5), 311–317. https://doi.org/10.1248/cpb.c14-00692.

(56)      Kahvand, F.; Fasihi, M. Plasticizing and Anti-Plasticizing Effects of Polyvinyl Alcohol in Blend with Thermoplastic Starch. *Int J Biol Macromol* **2019**, *140*, 775–781. https://doi.org/10.1016/j.ijbiomac.2019.08.185.

**2**

# 3

# Physical properties of ionomeric alginate films

*"If in the first act you have hung a pistol on the wall,*

*then in the following one it should be fired.*

*Otherwise, don't put it there."*

*– Anton Chekhov*

# Abstract

*The alginate sol/gel transition can be described as a shift from soluble polyelectrolyte to an ionomer-type of hydrogel. This gelation is apparently cation dependent. This work investigates how the solid-state properties of alginate systems are influenced by the counterion inclusion. Several cation-alginate films were fabricated via solvent ion-exchange, neutralization, and dialysis methods. Furthermore, the influence of plasticizer addition was investigated. Monovalent alginates exhibit the behavior of a polyelectrolyte, whereas most polyvalent alginates and indeed alginic acid form ionomer-like hydrogels. This means that the physical properties of crosslinked alginates can be discussed based on clustering of ionic pairs. The elastic modulus (E') decreases with crosslinking, a phenomenon not fully understood but likely related to a lower effective charge density due to ionic aggregation. For the plasticized films, the glass transition temperature data also show a higher morphological heterogeneity according to the clustering sequence: transition metal > alkaline earth metal > alkali metal. In comparison, the modulus of polyelectrolyte alginates can be resolved to effects in ionic radius (Li+ >> Cs+), however, the trend is not monotonic. The water uptake behavior in these monovalent alginates is gradual and kinetics scale with radius. For both types of alginate films, the water transport properties exhibit a moisture-induced chain relaxation. However, this is largely delayed in the crosslinked systems due to restricted regions formed by the ion aggregates. The additional specific interactions in ionomer-like alginate films might elucidate the different observed dynamics and structure-property relationships.*
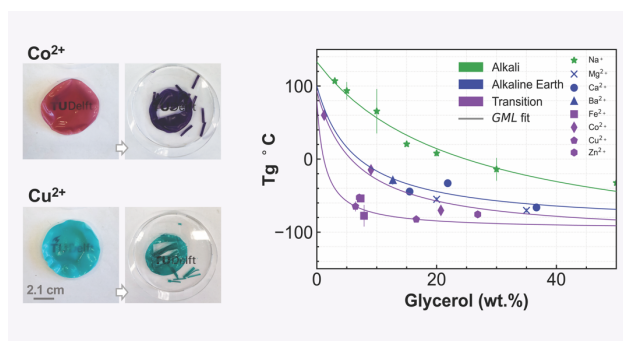
## 3.1. Introduction

In the recent years, there has been increased demand for the implementation and tuning of materials derived from biomass, particularly, in the EU.[1] Alginate is a widely commercial polysaccharide containing a high fraction of anionic pendant groups, which can be extracted from the cell wall of brown algae or bacterial biofilms.[2] Many applications have been developed based on the gelling properties of alginates, such as in drug delivery, food technology, liquid absorbing media, 3D-printing, textile industry, sensors and microelectronics, etc.[2–5] The chemical structure of the alginate is based on a linear block-copolymer of $\beta$-(1–4)-linked uronic acids: mannuronic acid (M-residue) and guluronic acid (G-residue). The ratio and sequence of M/G blocks is source dependent and can significantly modify the polymer physiochemical properties, e.g., solubility and viscosity.[2] Alginates can form physically crosslinked hydrogels by lowering of pH below the pKa of uronic acids or by metal-ions binding to the carboxylic anions in neighboring chains, an effect usually observed by polyvalent cations.[6] It has been shown that both the amount and length of G-units are predominantly responsible for the cooperative interactions with cations; working as ionic bridges between the alginate chains.[4,7]

The ionically crosslinked systems are composed of ion-pair aggregates which form due to strong cooperative associations between the multivalent cations and chain segments. Many theories have been used to describe the specific binding in cation-alginates, such as the formation of "egg-box" chain associations through G-blocks for Ca-alginate, lateral associations, or the concept of ionic junction zones.[4,8] These are all possible and clearly dependent on the specific block-copolymer structure, but it remains rather unclear how the counterion type and interactions play a role. Different cation-polyelectrolyte affinity has been reported, for instance, via calorimetric and mechanical tests. However, there is large variation between the reported binding strengths and apparent network morphology for similar alginates (low or high in G-residues).[2,7–9] Furthermore, the actual degree of ion coordination, complexation and possible chelation with the macromolecule is hardly ever investigated.

The alginate sol/gel transition can be described as a temperature-independent macromolecular shift from soluble polyelectrolyte to an ionomer-type of hydrogel. This gelation transition is apparently dependent on the nature of the counterion.[6] In general, polymers containing ionic groups can be classified as ionomers or polyelectrolytes. Polyelectrolytes are known for the (long-range) Coulombic forces that operate between

covalently attached ionically charged functional groups and counterions, in which omni-directional electrostatic interactions will govern the material properties.[10] In contrast, ionomers are polymers where the bulk properties are defined by the ionic interactions that occur in discrete regions or localized clusters.[10] The aggregation of the ion-pairs, strengthened by dipole-dipole interactions[11], happens largely due to the lower dielectric constant with respect to the solvent. This ionic aggregation makes the material more heterogenous, since segment mobility can be restricted by (higher-order) stiff zones.[12] Therefore, the ionomer-like alginate gels should have a distinct polymer morphology and should reveal the associated heterogenous dynamics.[8,13,14]

The precise effect of a certain alginate metal counterion appears to depend on the ligand formation. It is thus of fundamental interest to design ion-exchange experiments on the properties of alginate containing different counterions and valences.

The goal of this study was to explore how the solid-state physical properties (thermomechanical and transport properties) of alginate transition from polyelectrolyte to ionomer-like systems as a function of counterion inclusion. The effect of ions on gel formation and apparent degree of crosslinking, film mechanics, plasticization, and water vapor sorption are of interest for systematic investigation. With this research, we aim to better understand how the cation radius, the valency and the type of interactions will influence the physical properties of alginate materials.

## 3.2. Materials and Methods

### 3.2.1. Materials

Chemical grade Sodium Alginate (high ratio of mannuronic: guluronic acid, Mw ~12-40 kDa, Sigma Aldrich), Glycerol (Sigma Aldrich), Lithium hydroxide (Sigma Aldrich), Sodium hydroxide (Fluka), Potassium hydroxide (Fluka), Rubidium hydroxide (Sigma Aldrich), Cesium hydroxide (Sigma Aldrich), Ammonium hydroxide (Sigma Aldrich), Guanidinium chloride (Sigma Aldrich), Magnesium(II) sulfate heptahydrate (Fluka), Calcium(II) chloride (Sigma Aldrich), Barium(II) chloride (Sigma Aldrich), Iron(II) sulfate heptahydrate (Sigma Aldrich), Cobalt(II) chloride anhydrous (Sigma Aldrich), Copper(II) sulfate (Sigma Aldrich), Zinc(II) nitrate hexahydrate (Sigma Aldrich), Aluminum(III) nitrate nonahydrate (Sigma Aldrich), Iron(III) chloride (Sigma Aldrich), and Hydrochloric acid (Sigma Aldrich) were purchased and used as received.

## 3.2.2. Ion-exchange methods and film fabrication

First, the possibility and conditions for hydrogelation of alginate starting with a 3 wt.% solution in the sodium-form were tested. This was done at a 1:1 volumetric ratio with concentrated metal salt solutions, starting from 100 mM, which were designed to be at least twice the necessary molar equivalent for the counterion-exchange reaction in water (Table S3.1). Next, metal-alginate films were fabricated using different strategies, such as: (i) solution ion-exchange of Na-alginate film, (ii) synthesis from alginic acid and alkaline base, and (iii) dialysis of Na-alginate solution.

For method (i), Na-alginate films of thickness in range of 150 μm were prepared by solvent-casting from a 3 wt.% aqueous solution. Similar films were produced containing a percentage of glycerol as plasticizer (20 or 50 wt.% on an alginate basis). The Na-alginate films were immersed into a bath containing the dissolved concentrated metal salt (Table S3.1) and allowed to exchange for a studied amount of reaction time. To reduce swelling of the alginate hydrogels crosslinked with multivalent ions, either ethanol or glycerol were added as a co-solvent. It was necessary to carefully investigate the time of exchange reaction, solvent quality (balance between salt dissolution and polymer swelling) and rinsing step. In general, it took about 4h to 12h for hydrogel exchange to happen in a 25 v/v% ethanol: water solvent mixture (dielectric constant of 66). Method (i) was used to fabricate ionic alginates composed of $Ca^{2+}$, $Ba^{2+}$, $Cu^{2+}$, $Co^{2+}$, $Fe^{2+/3+}$, $Zn^{2+}$, $Al^{3+}$ counterions. The neutral form alginic acid was also studied by film solvent-exchange with 1N hydrochloric acid (HCl). The rising step was done with Milli-Q ultrapure water and the hydrogel films were set to dry under ambient conditions. To improve the flatness of the films, aluminum clamps were custom-made to keep the hydrogel films flat during exchange and drying steps (Supporting Text S3.2, Figure S3.1). Method (i) was also used to form glycerol plasticized alginate films of the respective metal-ions: $Ca^{2+}$, $Ba^{2+}$, $Mg^{2+}$, $Cu^{2+}$, $Co^{2+}$, $Fe^{2+/3+}$, $Zn^{2+}$, $Al^{3+}$.

Synthesis based on alginic acid was possible via neutralization, method (ii), using the hydroxide of $Li^+$, $K^+$, $Rb^+$, $Cs^+$, $NH_4^+$. A Na-alginate solution was acid-precipitated (HCl) and washed with ultrapure water to avoid excess inorganic salt formation. The corresponding monovalent base was slowly added to the acidified polymer until pH 9 to 11 was reached. The monovalent cation alginate films were obtained by solvent-casting the prepared 3 wt.% solution.

Dialysis of Na-alginate solution, method (iii), was possible with the use of cellulose membranes (10kDa molecular weight cut-off, Sigma-Aldrich). A 3 wt.% Na-alginate solution was dialyzed against optimized amounts of $MgSO_4$ or Guanidinium Chloride salt solutions for 3-4 days. The final step was a dialysis against ultrapure water. The Mg-alginate and Guanidium-alginate films were solvent-cast to produce thin films.

All these ion-exchange procedures were optimized for reaction time, solvents, and the used metal salt solutions (Supporting Texts S3.1 and S3.2). The successful film specimens are discussed and reported in the complete supporting information. From these films, rectangular specimens were cut and vacuum dried for one day at 40 °C and kept in a desiccator containing silica gel until immediately before analysis.

## 3.2.3. Characterization analyses

### Scanning electron microscopy - Energy-dispersive X-ray spectroscopy (SEM-EDS)

Surface morphology of the exchanged alginate films was examined with a JSM-6010LA JEOL (JEOL Ltd, Tokyo, Japan) scanning electron microscope (SEM) coupled with X-ray energy dispersive spectroscopy (SD detector with a 133 eV @ MnKα resolution). For EDS detection, the analysis of uncoated samples was performed in low vacuum mode (40 Pa) with an accelerating voltage of 20 kV.

### Thermogravimetric analysis (TGA)

Thermogravimetric analysis (TGA) was carried out using a Perkin-Elmer TGA 8000 (Perkin-Elmer, USA). The measurements were performed on cut-out samples of about 3 to 5 mg, placed in corundum crucibles, from 30 – 950 °C, at nominal heating rate of 10 °C min$^{-1}$ and oxidative atmosphere (air, 40 mL/min). To remove water, an isothermal step at 105 °C for 30 min was used as a programmed pre-step. Another isothermal was set at 250 °C in order to monitor the end of glycerol decomposition step in the plasticized films as a means of quantification.

## Dynamic mechanical thermal analysis (DMTA)

Dynamic Mechanical Thermal Analysis (DMTA) was performed on a PerkinElmer DMA-7e (Perkin-Elmer, USA). DMTA experiments of the ion-exchanged films were performed in a tensile mode at a frequency of 1 Hz from -100 to 180 °C temperature range at a heat rate of 5 °C min$^{-1}$, with film dimensions of roughly 10.0 x 3.0 x 0.1 mm. For the films containing glycerol, the glass transition was observed by the abrupt change in storage modulus slope and corresponding loss modulus maximum (alpha relaxation). If identified, the *Tg* was estimated from duplicate measurements by calculating the onset of the storage modulus decline (log scale).

Further analysis of Na$^+$, Co$^{2+}$, and Al$^{3+}$ ion-exchanged samples, dynamic mechanical analysis was also performed at constant temperature (30 °C) but with varying relative humidity, using a DMA Q800 (TA Instruments, USA) with a controlled humidity chamber accessory (HumiSys, InstruQuest Inc., USA). This allowed to monitor the moduli of alginates at different frequencies and varying water activity, $a_w$ = 0.01 to 0.80.

## Dynamic water vapor sorption (DVS)

The effect of ion-exchange on water vapor capacity and kinetics of alginate films were studied by dynamic water vapor sorption (DVS). Only the films without plasticizer were evaluated. DVS was performed in a TA Instruments Q5000 SA (TA Instruments, USA) by measuring the increment in mass from water vapor of the alginate films. The methods were designed to slowly saturate the initially dry films by applying a constant relative humidity of 80% RH until a plateau is reached.

## 3.3. Results and Discussion

### 3.3.1. Thermomechanical properties

Figure 3.1 displays the obtained mechanical properties for all studied alginate systems. In general, the DMTA analysis was very challenging without plasticizer due to excessive sample thickness, curvature, and embrittlement. The storage modulus (*E'*) of alginic acid, the neutral form of the polymer, was measured 6.3 GPa. For the charged alginates, the effect of counterion radius and valency on *E'* is not straightforward (Figure 3.1a). For monovalent ions, we expected a clear trend in the storage modulus with changing ionic radii. This property fundamentally scales with the effective charge density in the material,

since charged units will impose an omni-directional Coulombic force to the material, thus, resisting material deformation. In theory, the ionic radius is inversely proportional to the Coulombic electrostatic potential ($U_e$) experienced by the material. So, one should expect the $E'$ values in monovalent alginates to decrease with increasing ionic radius. However, the monovalent data shows that even though there is some global trend ($E'$ of Li-alginate $\gg$ Guanidinium-alginate), there must be other factors coming into play (coordinated interactions, steric effects on ionic affinity, semi-crystallinity, polymorphism, ion shell compressibility, etc.). In fact, the unexpected $E'$ sequence of $Na^+$ > $Li^+$ > $K^+$ does match the XPS-resolved affinity for $-COO^-$ ligand formation in amino-acids and acetates.[15] In these compounds, $Na^+$ outperforms because it matches best the hydration enthalpy of $-COO^-$ (aq). This steric affinity effect might play a role in alkali alginates. Meanwhile, for polyvalent ions the effect of radius is spread widely and seems ill-defined. If we interpret most ionically crosslinked systems to be fully ionomer-like, a lower radius should also increase $E'$ from stronger dipole-dipole interactions (Keesom energy). It is important to realize that although alginate semi-crystallinity should change with counterions, in the case of the elastic storage modulus below $Tg$ this cannot explain the large differences obtained.

Altogether, the di/trivalent cation alginates show a general decrease in modulus in contrast to the monovalent ones. This result is curious from a physical perspective, since more crosslinking points should make for higher resistance to deformation due to decreased network mobility. However, this is in agreement with previously reported values of Young's modulus for ionically crosslinked alginates.[7,16] The ability of each counterion to form multiple ligand structures with the carboxylic groups in alginate might partially explain these results. To estimate possible additional interactions of cations, we have also plotted $E'$ over the coordination number of acetate salts, as they can serve as reference for interaction with a carboxyl group (Figure 3.1b). This coordination number reflects the number of probable (poly)atomic neighbors. Unfortunately, there is no obvious trend with acetate-based coordination numbers, $i.e.$, there can be as much as $\Delta E' = 5$ GPa within alkaline earth and transition metal ions for a six-ligand coordination. However, this interpretation excludes specific binding (complex formation) and the ability of cations to form H-bonds with alginate chains, a feature expected for transition metal ions like $Cu^{2+}$ and $Co^{2+}$. Ca-alginate might also be a particular case due to the formation of lateral associations of M-blocks and rod-like nanostructures[4,8]. Resolving the actual coordination states formed in each metal-ion alginate would require demanding small-angle X-ray experiments and possibly computer modelling[2,4,8].

Specific binding in the form of complexation or chelation of the counterion is expected to be present for the ionomer-like alginates. With the rationale that $E'$ modulus primarily scales with the effective charge density in the charged polymer material, we speculate on the effect of specific binding to the acting Coulombic forces. Based on a force field perspective, the $E'$ should scale according to the effective pairs of Coulombic interactions which is governed by the electrostatic potential, $U_e$. However, if these charges are complexed or chelated, we propose that this might create nanostructures that will not have a major influence on the $E'$, analogous to the (series) contribution of spatially confined spheres or inclusions in composite materials (Figure 3.2). This tertiary structure from metal-coordination could develop from specific binding complexation and steric hindrance (related to the size of the oppositely charged species). Previous research using molecular dynamics has elucidated some of the probable nano and micro-structural aspects[8], however, to date there is no consensus or validation on the mechanisms of counter-ion association, i.e., egg-box model, dimerization, zipper mechanism, etc.[4] It is also uncertain how blockyness of the copolymer would influence such (meta)structures in the hydrogel or solid states. We propose this concept of complex formation could be further verified by systematic investiation of polyM and polyG homo-polymers, where gel particle size (hydrodynamic radius from light scattering) and solid-state structure (small angle X-ray scattering) could be better resolved.

From a fundamental perspective, the effective charge density should be modulated by specific coordination through $U_e$. The intensity of Coulombic force in soft matter is not the same as in ionic crystals. The potential $U_e$ is less far reaching due to screening from neutral organic matter. This decreases the modulus exponentially as charges get "deactivated", effectively, it is as if the charge density decreased. Ionomeric coordinated clusters in the extreme case will then give the effect of a neutral salt filler. These filler particles will not contribute to the Coulombic potential experienced by the material during mechanical loading. According to the Born-Landé lattice expression (second term of eq S3.1, Supporting Text S3.1), the attractive and repulsive terms in $U_e$ will be changing, respectively, via the Madelung constant and the Born exponent. One would expect a lower influence of the Born exponent for soft matter, as the ions will get closer together under deformation but the neutral organic material surrounding ions will screen repulsive interactions. The Madelung constant, however, is roughly a measure of the short- and long-range geometrical facets comprising the attractive forces between interacting ions. For polymers, this is quite relevant since short-range interactions can include π-π interactions, H-bonding, and van der Waals interactions. The clustering of

ions in the unit cell, with specific ion-pairing or coordination (closely packed ions), could lower this constant considerably. For organic salts, a tightly bound ion pair that behaves in isolation among a large neutral cloud from neighboring pairs can have a low Madelung constant that approximates to 1.[17] Similarly, this constant changes with structural factors, i.e., the locally different arrangement of the "point-like" charges. Nevertheless, a dedicated overview of the influence of ionic macromolecular structure to a Madelung-like constant and the resulting electrostatic potential is required.

From DMTA, we could also obtain the glass transition temperature ($Tg$) of some of the plasticized metal-alginates (Figure 3.1d). The $Tg$ values for divalent metal-alginates were relatively lower than that of the monovalent Na-alginate. This is unusual since crosslinked polymers often have decreased mobility and therefore a slightly elevated $Tg$. The changes in alginate physical properties can be to some extent linked to an increase in free volume upon ionomer-like crosslinking.[7] The relationship of $Tg$ with plasticizer concentration was modelled using the Generalized Mean model ($GML$).[18] We observe that the trends from divalent metal-alginates show plasticizer partitioning (heterogeneity constant $k_{GM} > 1$), indicating that they have a heterogenous structure. Higher heterogeneity constant was found in the order: transition > alkaline earth > alkali metals. Although data is limited, we also observe a decrease in $Tg$ trends with higher valency (alkali vs. alkaline earth) and coordination states (alkaline earth vs. transition). This is also substantiated by the higher ability of alkaline earth films to retain glycerol (Figure 3.1c), in contrast to transition metal alginates. These findings support the idea of ionomer-like systems, containing fractions of stiff ionic aggregates and flexible regions of unrestricted mobility.[11] Indeed, multiple sources provide evidence of rigid nano- and microstructures to occur in crosslinked alginates, *e.g.*, Ouwerx et al. (1998) described Cu-alginate as a rough association of independent microgels, and Agulhon et al. (2012) showed a type of alginic acid consisting of large aggregates (50 Å).[8,16]

Eisenberg (1970) has described three distinct regions within ionomers: multiplets or aggregates of ions; non mobile or restricted regions near the multiplets; and nonrestricted regions sufficiently far from the multiplets.[12] Only the latter will participate in the hydrogel dynamics and glass transition phenomena. Additionally, a significant decrease in polarity will induce the ion-pair associations, forming permanent dipoles, and likely a progressive aggregation of the surrounding pairs. This phenomenon can also be linked to the Oosawa/Manning theory of charge condensation[13], where the formation of condensed ion pairs lowers the electrostatic potential and effective charge density of the

system at the penalty of translational entropy. In sum, both theories seem fitting for the case of ionomer-like alginates.
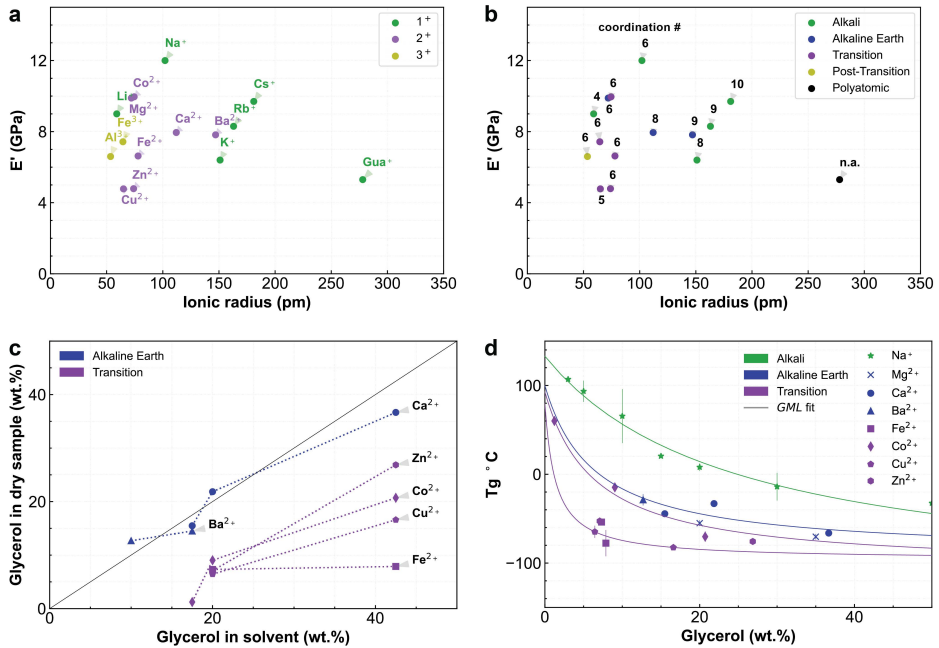


**Figure 3.1.** Storage modulus, *E'*, of ethanol solvent-exchanged alginate films versus counter-ion ionic radius (a.b). The ions can be clustered by valency (a) or assumed coordination state based on acetate salts (b). (c) The glycerol plasticizer uptake in solvent-exchanged alginate films. (d) The glass transition temperature (*Tg*) over plasticizer concentration for the viable ion-exchanged films, to which the predictive model Generalized Mean Linear (*GML*) was fitted. The glycerol content of samples $Fe^{3+}$, and $Al^{3+}$ was not estimated due to possible sample hydrolysis (pH < 3.5).
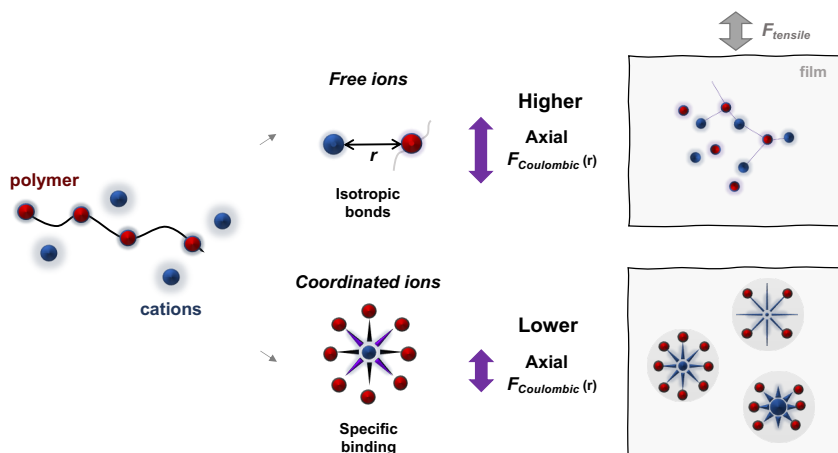
**Figure 3.2.** A proposed scheme of possible polymer and cation interactions leading to free bonds or coordinated complexed states. The coordinated ions form an ionomer-type system, in which specific binding of ions (e.g., from geometric factors) changes the range of Coulombic interactions. This ionomer inclusion effect on available Coulombic force (from the total electrostatic potential) is indirectly measured by a mechanical test (tensile force). The micro-inclusions can form from multiple ion-pairs and behave as particulate material in a composite and their contribution to modulus will be analogous to a series model like average of the soluble polymer (matrix) and the inclusion sphere (filler).

## 3.3.2. Water diffusion properties

The results on water vapor sorption also point towards ion-specific cases (Figure 3.3). The film water uptake capacity should scale with the alginate film free volume. All else being equal, *e.g.,* the degree of semi-crystallinity, we can assume the free volume in polyelectrolyte-like samples to systematically change with the counterion radius. For the monovalent alginates, we see that water capacity increased with the ionic radius of monovalent ions ($Li^+ > Cs^+$) (Figure 3.3c). This interpretation also holds if using the actual hydrodynamic or Stokes radius; and is the reason why Mg-alginate also showed high water capacity. For the remaining multivalent cations, this percentage is likely scaling with the marked change in free volume from crosslinking. This is also true for the neutral form, alginic acid, which had 15% water uptake. In fact, the uptake capacity is in concert with the findings in $Tg$, where higher heterogeneity from ionic aggregates was found for alginate bound to transition metal counterions.

The water diffusion isotherms are more difficult to compare since they cover a large humidity variation, from 1 to 80% RH (Figure 3.3a and b). For instance, note that they show a two-stage behavior for the multivalent and neutral systems. A model was derived to fit these kinetic curves of alginate films (eq S3.5, Supporting Text S3.3). The Penetrating Shell model (*Pen. Model*) deals with the diffusion case where a hydration shell is advancing at constant velocity towards a dry particle core. For monovalent alginates this model gave excellent description of the diffusion profiles (Efron's pseudo $R^2 > 0.99$) (Figure 3.3a). Thus, we observe a gradual water uptake for the monovalent systems, as expected from polyelectrolyte behavior. The uptake velocity in these films was analogously increasing with radius (lower electrostatic interaction) (Figure 3.3d). The ionomer type of alginates shows distinct two-stage water vapor sorption kinetics (Figure 3.3b). Hence, the *Pen. Model* could only be fitted until a time equivalent to half of total mass uptake ($t_{50}$) (Efron's pseudo $R^2 > 0.97$). Theoretically, the ionomer-like alginates could form systems of multiplets and higher-order aggregates. Water works as a plasticizer and facilitates the mobilization step of the flexible regions within the heterogenous structure. The higher the degree of ionomer-like complexation, the more regions of restricted mobility would compose the material until sufficient moisture-induced plasticization is achieved. Thus, the first kinetic event corresponds to water adsorption (Langmuir or multiple hydrogen bonding) and it is followed by network plasticization and saturation, which shows a non-Fickian diffusion.

Interestingly, an apparent increase in sorption is observed at different times for each counterion system. This is easier observed using the first derivative of sorption curves (Figure 3.4a and b). The kinetic event could be interpreted as chain relaxation phenomena, such as a glass transition induced by moisture. This relaxation was observed for the complex coordinated Al-alginate via dynamic mechanical analysis using a controlled humidity chamber (Figure 3.4c). A similar relaxation time ($\tau_{rel}$) was also found for Co-alginate. For comparison, the time to relaxation of Na-alginate was much smaller ($\tau_{rel} = 4000$ s). As a rule, we propose this relaxation transition is revealing how strongly bound the ionomer-polymer system is. This would mean that the transient crosslinks are (partially) loosened during the transition, however this needs further investigation. Even so, in our case, $\tau_{rel}$ indicates that the linear alginate seems to be specifically binding according to $Zn^{2+} < Co^{2+} = Al^{3+} < Ca^{2+} < Ba^{2+} <$ Acid. The same diffusion series is also observed with the *Pen. Model* via the calculated membrane uptake velocity (Figure 3.3d). The diffusion velocity in (non-ionic) alginic acid was 5e-9 m/s.
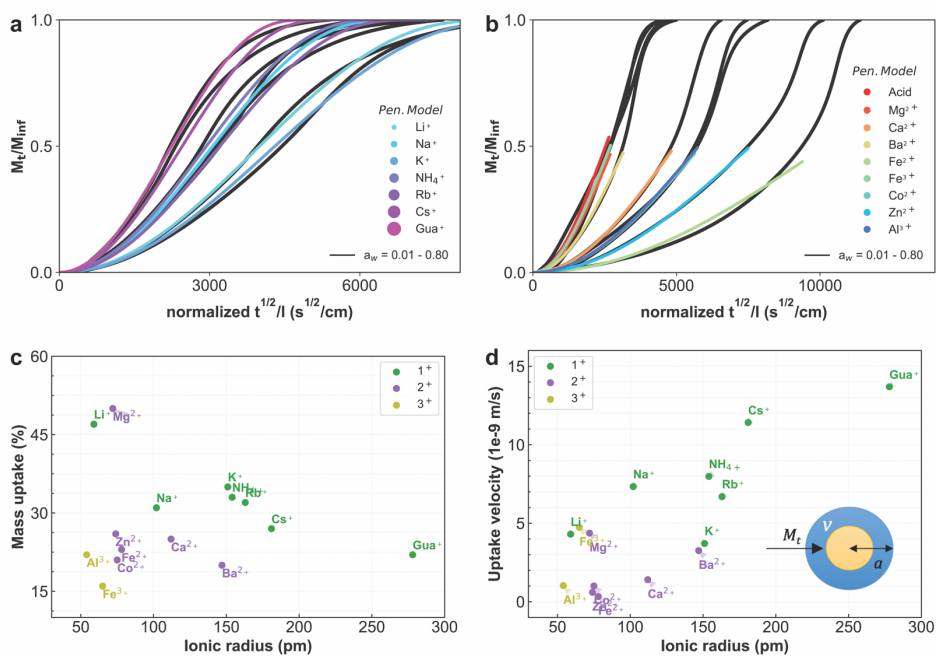
**Figure 3.3.** Water vapor sorption kinetics of films of alginate salts with monovalent charge and increasing ionic radii (a) and multiple valency and/or coordination states (b) at 25 °C, under atmospheric conditions, from 1 to 80% humidity. A kinetic model assuming a Penetrating Shell (Pen. Model) was fitted to the curves in the appropriate region. The model can describe the monovalent salts profile (a) but is limited to the first phase of likely complex coordinated alginate salts (b). The equilibrium water uptake capacity versus ionic radius (c). The Pen. model velocities from curve-fitting for each salt data (d).
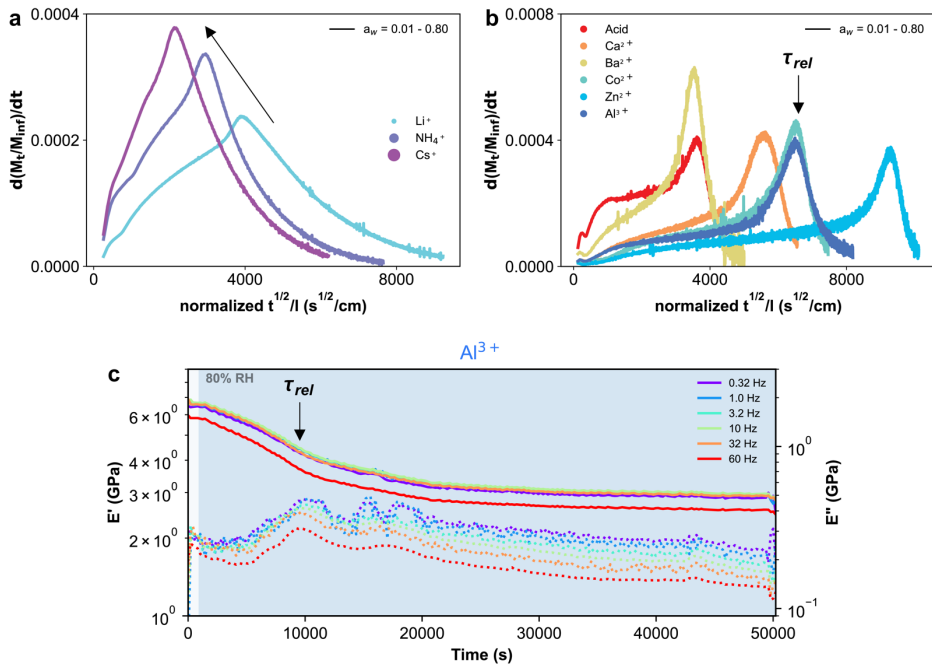
**Figure 3.4.** First derivative of water vapor sorption kinetics of films of alginate salts with monovalent charge and increasing ionic radii (a) and multiple valency and/or coordination states (b) at 25 °C, under atmospheric conditions, from 1 to 80% humidity. The derivative is assumed to correlate with the system relaxation time. For the $Al^{3+}$ alginate salt, the dynamic mechanical analysis at 30 °C and similar humidity profile (c) also shows a relaxation transition step for multiple frequencies.

## 3.4. Conclusions

As many ionically crosslinked alginate materials are being engineered, the current understanding on network structural binding and linked properties needs a comprehensive approach. Experimental efforts have been extensive but different findings in properties and diverging theories add complexity to the effective alginate state. In this study, the physical crosslinking phenomena attributed to alginates and counter-ion ligands is systematically investigated for its effect on the solid-state properties.

The alginate gelation can generically be viewed as a transitional shift from the polyelectrolyte state to ionomer-like state. Monovalent alginates behave as soluble polyelectrolytes, whereas most polyvalent alginates form insoluble hydrogels that are ionomeric.

## Physical properties of ionomeric alginate films

For polyelectrolytes, the mechanical property of elastic modulus, $E'$, showed good correlation with the electrostatic potential energy. In general, we observe that the storage modulus decreases with ionic radii (Li-alginate >> Cs-alginate). However, there is no $E'$ decreasing series with radius, and other factors are possibly interfering such as coordination number (also H-bonding), steric effects and the extent of semi-crystallinity. Likewise, for Na-alginate, the data on $Tg$ over glycerol concentration was also reflecting a charged, but slightly heterogeneous structure. We have also explored the water vapor diffusion of polyelectrolyte alginate films (alkali cations and the polyatomic $NH_4^+$ and Guanidinium$^+$). The uptake capacity can largely be explained by an increasing trend in the hydrodynamic radius (free volume). The water diffusion kinetics over a broad change in humidity (1-80% RH) shows convoluted phenomena. However, the sorption profile of polyelectrolytes can be modelled by assuming a material with a hydrated shell and dry core, in which the penetrating humid shell intrudes at a continuous velocity (Penetrating Shell model). Even though there was gradual diffusion, we note the appearance of an ion-specific inflection point, which can be related to the lowering of the glass transition temperature by moisture uptake. As expected, for polyelectrolytes the polymer relaxation time was seemingly decreasing with counterion radius. This was also observed in the averaged water-diffusion uptake velocity.

Alginates with multivalent counterions clearly showed changes in the mechanical and water barrier properties corresponding to ionomer-like systems. The data is better understood assuming the idea of ionic aggregation (ion-pair associations and the aggregation of pairs). The mechanical and water-diffusion properties were not marked by changes in radius and valency of polyvalent cations. Instead, they showed indications of specific nano- and microstructures arising from ion-macromolecule complex ligand interactions. Trends in $E'$ are not clear but might be understood by exploring the idea of a lower effective charge density arising from spherical ionic clusters. Following this rationale, the role of the range of Coulombic electrostatic interactions should be further investigated. We propose this theory for charged polymers to be explored through analogy with the ionic lattice energy (Born-Landé expression). For the plasticized films, the groups of alkaline earth and transition metals both showed lower $Tg$ values, which was more pronounced for the latter. The descriptive $Tg$ fits, via the Generalized Mean linear model, also suggest higher morphological heterogeneity for transition > alkaline earth > alkali metals. The idea of ionic aggregate inclusions is further supported by water vapor diffusion since moisture-induced relaxation is more inhibited in the crosslinked systems. Additional ion-specific interactions might explain the dynamics found in

ionomer-like alginate films. The ionomeric systems need more dedicated studies to elucidate on the nature, strength, and extent of counterion ligand complexation in alginates from the nano to the microscale.

**3**

## Supporting information

The complete supporting information is available at DOI: 10.5281/zenodo.8078037

## Supporting Text S3.1. Film synthesis and solvation theory

In the synthesis of ion-exchanged alginate films, the required conditions for the exchange reaction were explored. For polyvalent ions, the key parameters were the used metal salt, solvent dielectric constant, and reaction time. During reaction, there was an optimum between the dissociation of the used metal salt and hydration and swelling of the polymer. Thus, the ion-exchange greatly depended on the dielectric constant of solvent ($\varepsilon$), ionic salt lattice energy, and the swelling of the hydrogel. The ion-exchange solvent seemingly defined the rate of counterion exchange. Too high solvent polarity caused the hydrated film to partially solubilize, wrinkle and thickness became uneven. Too low solvent polarity has led to insolubility of the inorganic salt and virtually no polymer swelling or ion-exchange. For the plasticized films, the solvent dielectric constant was equality important, not only for good film formation, but to minimize the appearance of cavities and delamination as glycerol moved in- and out-side of the alginate membrane. In general, a dielectric constant of 66 or higher was necessary in the coagulation bath for the static ion-exchange of Na-alginate to happen (after ~4h). This working methodology is valid with some reservation since salt solvation and exchange conditions are in principle ligand specific.

The ionic salt lattice energy is relevant since this binding energy will determine the enthalpy of solvation. This concerns to the energetic balance between breaking of the crystal lattice over the hydration of the ions. The thermodynamic value can help explain the observed differences in solubility and relates to the extent of reaction time to fully ion-exchange the fabricated hydrogels. The model proposed by Born-Landé-Ephraim-Fajans-Bjerrum[20] for enthalpy of solution scales with the radius and charge of ions composing the lattice according to:

$$\Delta H_S^0 = -N_A \left(\frac{e^2 Z_+^2}{2r_+} + \frac{e^2 Z_-^2}{2r_-}\right)\left(1 - \frac{1}{\varepsilon}\right) + \frac{N_A A e^2 Z_+ Z_-}{r_+ r_-}\left(1 - \frac{1}{n}\right) \quad (S3.1)$$

where $N_A$ is Avogadro's number, $e$ the electron charge, $Z_+$ and $Z_-$ the charges of the cation and anion, respectively, $r_+$, and $r_-$ the radii of the cation and the anion, respectively, $\varepsilon$ the medium electric constant, $A$ the structural constant of Madelung constant, and $n$ the Born coefficient.

This expression links the solvation energy of the ions in a dielectric medium (first term) and the ionic network reticular energy (second term) from Born-Landé theory[21]. This is useful to understand the metal salt dissolution and the ion pairing in alginate-counterions, even though omitting entropic factors.[20] For instance, note that the water solubility of the monovalent NaCl is lower than trivalent $FeCl_3$, while the values of lattice energy are NaCl: - 760 to 790 kJ/mol and $FeCl_3$: - 5364 to 5436 kJ/mol.

## Supporting Text S3.2. Film fabrication methods and appearance

Ultimately, a good quality alginate film is hereby defined by a high or complete degree of ion-exchange, maintenance of film dimensions, and flatness. The achieved ion-exchange was monitored via SEM-EDS and TGA analyses (complete supporting information). However, the formation of wrinkles and hydrogel shrinking made some of the fabricated films impossible for tensile mechanical analysis (thick and brittle samples). To deal with polymer swelling effects, the practical solution was to lower the solvent quality (and exchange rate)[22] using either ethanol or glycerol to a ε dielectric constant baseline value around 60 to 70. Parallel to that, custom-made clamps were used to fixate the film during the reaction time (Figure S3.1). Even so, the films with multivalent ions (alkaline earth, transition, post-transition) still showed some degree of wrinkling and high shrinking levels (around 15 to 40%) (Figure S3.2). This has made the mechanical analysis challenging. Furthermore, the fabricated Fe(II)-alginate films showed a color change approaching that characteristic of Fe(III)-alginate (complete supporting information). It is possible that pH and light exposure changed part of the iron species in these samples.[5] For alkali alginates, neutralization of the alginic acid was the preferred working method. Overall, this method gave good film quality, with a few samples showing excess neutral salt crystallization ($K^+$ and $Rb^+$). The dialysis methodology also has produced high-quality films of Mg-alginate and Guanidinium-alginate.

The degree of plasticizer incorporation varied considerably for the films of multivalent ions (complete supporting information). This is likely a combined effect from the chosen ion-exchange procedure and crosslinked material properties. Even though there was obvious glycerol movement from the initial membranes, it was necessary to start with plasticized Na-alginate films to retain higher concentrations. In those, the osmotic flow of glycerol unfortunately often caused cavities and delamination in the final films. Furthermore, not all plasticized films retained detectable amounts of the small molecule,

3

*e.g.*, for Fe(III)-alginate. Post-plasticization generally produced better films but was possible only for a few alginate-counterion systems with sufficient swelling. Curiously, the retained percentage of glycerol, respective to the fixed mass in coagulation bath, followed an almost linear trend for alkaline earth metals, while for transition ions this amount decreased. This observation can be attributed to a characteristic alginate network formed in each type of complexed ligand, for which the hydrogel mesh dimensions and mobility between junctions are ion-specific.

## Fabrication of flattened films

Custom-made Teflon-coated metallic clamps were used to keep the initial Na-alginate film as flat as possible during the exchange time with 25 v/v% ethanol/water solvent ion-exchange (Figure S3.1). This was applied to cation-alginate films from the metals $Ca^{2+}$, $Ba^{2+}$, $Fe^{2+}$, $Co^{2+}$, $Cu^{2+}$, $Zn^{2+}$, $Al^{3+}$, and $Fe^{3+}$. This step was not deemed necessary for glycerol ion-exchanged films.
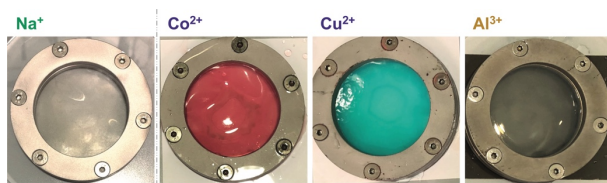


**Figure S3.1.** A Na-alginate film is straightened inside Teflon-coated metallic clamps (left-side). As prepared cation-alginate films – $Co^{2+}$, $Cu^{2+}$, $Al^{3+}$ – made by ethanol/water solvent ion-exchange from a Na-alginate film (right-side). The metal clamp inner diameter was 5.5 cm.

## Film shrinking
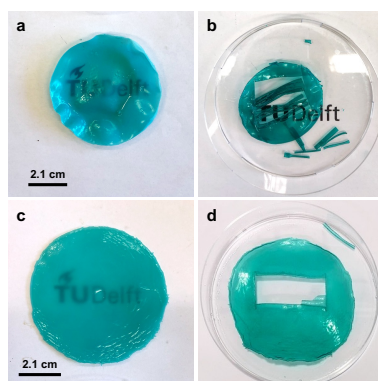


**Figure S3.2.** Cu-alginate films after 25 v/v% ethanol/water (a, b) and 35 v/v% glycerol/water (c, d) solvent ion-exchange processing starting with films of Na-alginate and Na-alginate-(35 wt.% glycerol), respectively. The films on the left-side are still humid and right-side shows the appearance after drying at ambient conditions.

# Supporting Text S3.3. Penetrating shell model for water sorption

The water vapor diffusion through a thin film can be simplified to the case of a spherical particle in which the shell gets wetted from the outside. The dry shell on the inside does not experience any effect of the wet shell on the outside. Therefore, the water vapor diffusion only depends only on the (constant) velocity of the diffusing water through the hydrated shell layer. The model is referred to as Penetrating Shell model.

## Penetrating shell model derivation

First, let's assume the material of interest to be a sphere of volume $V_{sphere} = \frac{4}{3}\pi r^3$. The extent of the dry matter is contained within a radius $r = a - x$, where $a$ and $x$ are the radius of entire particle and of dry core respectively.

Thus, the inner dry volume is $V_{dry} = \frac{4}{3}\pi(a - x)^3$ and outer wet volume becomes $V_{wet} = V_{total} - V_{dry} = \frac{4}{3}\pi a^3 - \frac{4}{3}\pi(a - x)^3$. The mass of incorporated water is then

$M_{water}(t) = c * V_{wet} = c * \left(\frac{4}{3}\pi a^3 - \frac{4}{3}\pi(a-x)^3\right)$. Since $c = \frac{M_{max}}{V_{max}} = \frac{M_{max}}{\frac{4}{3}\pi a^3}$, the mass over time is:

$$M_{water}(t) = M_{max} - \frac{M_{max}}{a^3}(a-x)^3 = M_{max}\left(1 - \frac{(a-x)^3}{a^3}\right) \qquad (S3.2)$$

Considering a constant velocity and the time to cover the distances $x$ and $a$ to be, respectively, $t = \frac{x}{v}$ and $\tau = \frac{a}{v}$:
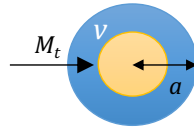
$$M_{water}(t) = M_{max}\left(1 - \frac{(a-vt)^3}{a^3}\right) = M_{max}\left(1 - \frac{v^3\left(\frac{a}{v}-t\right)^3}{a^3}\right) = M_{max}\left(1 - \frac{v^3}{a^3}(\tau - t)^3\right) \qquad (S3.3)$$

This expression can be further simplified to:

$$M_{water}(t) = M_{max}\left(1 - \frac{1}{\tau^3}(\tau^3 - 3\tau^2 t + 3\tau t^2 - t^3)\right) = M_{max}\left(1 - \left(1 - 3\frac{t}{\tau} + 3\frac{t^2}{\tau^2} - \frac{t^3}{\tau^3}\right)\right)$$

$$(S3.4)$$

Or:

$$M_{water}(t) = M_{max}\left(3\left(\frac{t}{\tau}\right) - 3\left(\frac{t}{\tau}\right)^2 + \left(\frac{t}{\tau}\right)^3\right) \qquad (S3.5)$$



**Figure S3.3.** Schematic of the Penetrating shell model for diffusion into a sphere, with $M_t$ as the diffusing mass, $v$ as the velocity, and $a$ as the average particle radius.

# Supporting Figures and Tables

## Metal salt solutions

**Table S3.1**. Metal salt solutions used in the Na-alginate ion-exchange experiments

| Counter cation | Metal salt solution | Concentration (wt.%) |
|:---:|:---:|:---:|
| $Ca^{2+}$ | $CaCl_2$ | 1.54 |
| $Al^{3+}$ | $Al(NO_3)_3.9H_2O$ | 3.48 |
| $Zn^{2+}$ | $ZnNO_3.7H_2O$ | 4.10 |
| $Cu^{2+}$ | $CuCl_2$ | 1.87 |
| $Fe^{2+}$ | $FeSO_4.7H_2O$ | 3.86 |
| $Fe^{3+}$ | $FeCl_3.6H_2O$ | 3.76 |
| $Mg^{2+}$ | $MgSO_4.7H_2O$ | 3.42 |
| $Ba^{2+}$ | $BaCl_2. 2H_2O$ | 3.39 |
| $NH^{4+}$ | $NH_4OH$ | 29.00 |
| $Ag^+$ | $AgNO_3$ | 4.71 |
| $Co^{2+}$ | $CoCl_2$ | 1.80 |

3

# References

(1)     European Commission. A European Strategy for Plastics in a Circular Economy, 2018. www.europarc.org/wp-content/uploads/2018/01/Eu-plastics-strategy-brochure.pdf.

(2)     Li, Z. J.; Srebnik, S.; Rojas, O. J. Revisiting Cation Complexation and Hydrogen Bonding of Single-Chain Polyguluronate Alginate. *Biomacromolecules* **2021**, *22* (9), 4027–4036. https://doi.org/10.1021/acs.biomac.1c00840.

(3)     Li, J.; He, J.; Huang, Y.; Li, D.; Chen, X. Improving Surface and Mechanical Properties of Alginate Films by Using Ethanol as a Co-Solvent during External Gelation. *Carbohydr. Polym.* **2015**, *123*, 208–216. https://doi.org/10.1016/j.carbpol.2015.01.040.

(4)     Hecht, H.; Srebnik, S. Structural Characterization of Sodium Alginate and Calcium Alginate. *Biomacromolecules* **2016**, *17* (6), 2160–2167. https://doi.org/10.1021/acs.biomac.6b00378.

(5)     Narayanan, R. P.; Melman, G.; Letourneau, N. J.; Mendelson, N. L.; Melman, A. Photodegradable Iron(III) Cross-Linked Alginate Gels. *Biomacromolecules* **2012**, *13* (8), 2465–2471.

(6)     Draget, K. I.; Skjåk-Bræk, G.; Stokke, B. T. Similarities and Differences between Alginic Acid Gels and Ionically Crosslinked Alginate Gels. *Food Hydrocoll.* **2006**, *20* (2-3 SPEC. ISS.), 170–175. https://doi.org/10.1016/j.foodhyd.2004.03.009.

(7)     Russo, R.; Malinconico, M.; Santagata, G. Effect of Cross-Linking with Calcium Ions on the Physical Properties of Alginate Films. *Biomacromolecules* **2007**, *8* (10), 3193–3197. https://doi.org/10.1021/bm700565h.

(8)     Agulhon, P.; Robitzer, M.; David, L.; Quignard, F. Structural Regime Identification in Ionotropic Alginate Gels: Influence of the Cation Nature and Alginate Structure. *Biomacromolecules* **2012**, *13* (1), 215–220.

(9)     El-Shatoury, S. A.; Hassan, R. M.; Said, A. A. Alginate Polyelectrolyte Ionotropic Gels-XVI. Kinetics and Chemical Equilibria Studies for Heterogeneous Ion Exchange of Polyvalent Metal Ions in Alginate Gel Complexes. *High Perform. Polym.* **1992**, *4* (3), 173–179. https://doi.org/10.1088/0954-0083/4/3/005.

(10)    Eisenberg, A.; Rinaudo, M. Polyelectrolytes and Ionomers. *Polym. Bull.* **1990**, *24* (6), 671–671. https://doi.org/10.1007/BF00300165.

(11)    Enokida, J. S.; Hu, W.; Fang, H.; Morgan, B. F.; Beyer, F. L.; Winter, H. H.; Coughlin, E. B. Modifying the Structure and Dynamics of Ionomers through Counterion Sterics. *Macromolecules* **2020**, *53* (5), 1767–1776. https://doi.org/10.1021/acs.macromol.9b02116.

(12)    Eisenberg, A. Clustering of Ions in Organic Polymers. A Theoretical Approach. *Macromolecules* **1970**, *3* (2), 147–154.

(13)    Chen, Q.; Bao, N.; Wang, J.-H. H.; Tunic, T.; Liang, S.; Colby, R. H. Linear Viscoelasticity and Dielectric Spectroscopy of Ionomer/Plasticizer Mixtures: A Transition from Ionomer to Polyelectrolyte. *Macromolecules* **2015**, *48* (22), 8240–8252. https://doi.org/10.1021/acs.macromol.5b01958.

(14)    Ju, L.; Pretelt, J.; Chen, T.; Dennis, J. M.; Heifferon, K. V.; Baird, D. G.; Long, T. E.; Moore, R. B. Synthesis and Characterization of Phosphonated Poly(Ethylene Terephthalate) Ionomers. *Polymer* **2018**, *151*, 154–163. https://doi.org/10.1016/j.polymer.2018.07.065.

(15)    Aziz, E. F.; Ottosson, N.; Eisebitt, S.; Eberhardt, W.; Jagoda-Cwiklik, B.; Vácha, R.; Jungwirth, P.; Winter, B. Cation-Specific Interactions with Carboxylate in Amino Acid and Acetate Aqueous Solutions: X-Ray Absorption and *Ab Initio* Calculations. *J. Phys. Chem. B* **2008**, *112* (40), 12567–12570. https://doi.org/10.1021/jp805177v.

(16)    Ouwerx, C.; Velings, N.; Mestdagh, M. M.; Axelos, M. A. V. Physico-Chemical Properties and Rheology of Alginate Gel Beads Formed with Various Divalent Cations. *Polym. Gels Netw.* **1998**, *6* (5), 393–408. https://doi.org/10.1016/S0966-7822(98)00035-5.

(17)    Izgorodina, E. I.; Bernard, U. L.; Dean, P. M.; Pringle, J. M.; MacFarlane, D. R. The Madelung Constant of Organic Salts. *Cryst. Growth Des.* **2009**, *9* (11), 4834–4839. https://doi.org/10.1021/cg900656z.

(18)    Espíndola, S. P.; Norder, B.; Koper, G. J. M.; Picken, S. J. The Glass Transition Temperature of Heterogeneous Biopolymer Systems. *Biomacromolecules* **2023**, *24* (4), 1627–1637.

(19)    Topuz, F.; Henke, A.; Richtering, W.; Groll, J. Magnesium Ions and Alginate Do Form Hydrogels: A Rheological Study. *Soft Matter* **2012**, *8* (18), 4877–4881.

(20)    Fernández–d'Arlas, B.; Huertos, M. Á.; Müller, A. J. Ion-Macromolecule Interactions Studied with Model Polyurethanes. *J. Colloid Interface Sci.* **2018**, *509*, 102–112.

(21)    Born, M.; Landé, A. The Absolute Calculation of the Crystal Properties with the Help of Bohr's Atomic Model. *Sitzungsberichte Koniglich Preuss. Akad. Wiss.* **1918**, 1048–1068.

(22)    Hermansson, E.; Schuster, E.; Lindgren, L.; Altskär, A.; Ström, A. Impact of Solvent Quality on the Network Strength and Structure of Alginate Gels. *Carbohydr. Polym.* **2016**, *144*, 289–296. https://doi.org/10.1016/j.carbpol.2016.02.069.

**3**

# 4

# Systematic study of the nanostructures of exfoliated polymer nanocomposites

*"Thermodynamics, correctly interpreted,*

*does not just allow Darwinian evolution; it favors it."*

*– Ludwig Boltzmann*

# Systematic study of the nanostructures of exfoliated polymer nanocomposites

## Abstract

*High-performance bioinspired materials have shown rapid development over the last decade. Examples are brick-and-mortar hierarchical structures, which are often achieved via solvent evaporation. Although good properties are claimed, most systems are composed of stacked or intercalated platelets. Exfoliation is a crucial step to give ultimate anisotropic properties, e.g., thermal, mechanical and barrier properties. We propose a general framework for all the various types of micro-scale structures that should be distinguished for 2D-filler nanocomposites. In particular, the exfoliated state is systematically explored by the immobilization of montmorillonite platelets via (gelatin) hydrogelation. Scattering techniques were used to evaluate this strategy at the level of the particle dispersion and the regularity of spatial arrangement. The gelatin/montmorillonite exfoliated nanostructures are fully controlled by the filler volume fraction since the observed gallery d-spacings perfectly fall onto the predicted values. Surprisingly, X-ray analysis also revealed short- and quasi long-range arrangement of the MMT at high loading.*

**4**
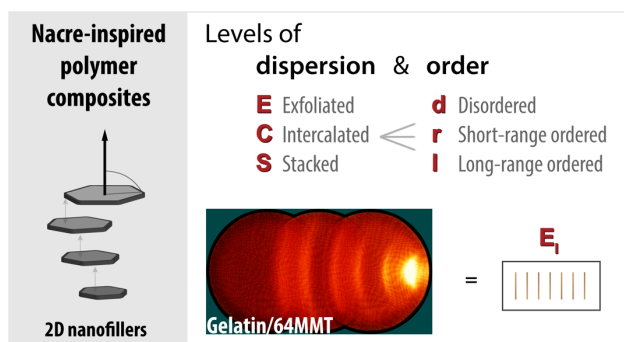
## 4.1. Introduction

Natural materials are intriguing as they can display complex, highly regular nano- to macro-architectures, which are fabricated at ambient conditions.[1] A common example is the "brick-and-mortar" micro-structure of nacre, which inspired the design of polymer composites for the past decades.[2] In essence, the hybrid nacre-like materials consist of highly ordered inorganic platelets which are bound in a lamellar manner. Several mimetic and bioinspired materials have been constructed either from suspension/melt mixing (top-down) or in-situ techniques (bottom-up).[2–4] The design of hierarchically structured composites from 2D nanoparticles has already been extended to clay silicates, (reduced) graphene oxide, boron nitride, MXenes, dichalcogenides, among others.[5–8] In general, the anisotropic materials show desired thermal, mechanical, conductive, and barrier properties. For instance, they combine excellent stiffness and toughness.[4,9,10] Nevertheless, in order to achieve tailored structural properties, the right choice of building blocks and fabrication strategy become important.

Processing conditions can dramatically influence the obtained hierarchical structure. Several processes have been reported, such as suspension casting, doctor blading, vacuum-assisted self-assembly, melt compounding, in-situ polymerization, etc.[2,11] About a decade ago, bioinspired polymer nanocomposites saw much advance with water-based and large-scale methodologies, akin to paper-making.[9,10,12,13] Since then, the focus has shifted to the optimization of polymeric core-shell particles, followed by solvent removal.[5,6,14] The ideal conditions to realize aligned assemblies have been extensively adjusted. Nevertheless, these often are formed by intercalated structures, with restacking still observed at higher filler concentrations.[2,15–20] Above all, these efforts have led to a great number of mechanisms being proposed for polymer-particle association and (re)organization.

The main drive behind new technologies is the same: surpassing the limits of measured anisotropic properties over the in-plane arrangement. As a strategy, the logical approach should be to keep the high aspect ratio of 2D filler (exfoliated state) and, if feasible, aim for high loadings. This would ensure the nanoscale properties, and functionalities, to be translated as much as possible to the bulk material. However, as previously discussed, composites do not frequently achieve the formation of exfoliated nanostructures, with limited polymer insertion in between the particles, although an exception might be made for samples from Layer-by-Layer or multilayer deposition approaches[21,22], which however are mainly of scientific interest. Furthermore, many applied studies exclusively

**4**

investigate whether there is polymer intercalation onto the integral layers of the 2D filler, which is accompanied by a synergetic improvement of properties. High filler contents, i.e., above 20 wt.%, are equally unexplored. Thus, the quality of (nano)dispersion needs more systematic evaluation, guiding the way to better methods and ultimate properties from all exfoliated samples.

Finally, there is still lack of consensus about the classification of composite micro-structures, where the difference between intercalated and exfoliated states remains elusive. For instance, highly interlocked systems can also show a certain level of regularity due to the particles' flat geometry. In other words, there can be a positional order-disorder transition with filler concentration. So far, we have seen not seen a complete overview of the combined effects of the level of 2D material dispersion and associated positional order to the (nano)structure. In Chart 4.1, we illustrate how this coupling (dispersion and regularity) will lead to many more composite nano- to meso-phases. The orientational order of dispersed phase is for now ignored, even though alignment will clearly have an influence on the anisotropic properties. Thus, we introduce a general framework on all the possible phases of dispersion and positional order present in polymer/platelet composites.

## 4.1.1. Nanostructure classification based on 2D particle dispersion and positional order

### Particle dispersion

Depending on the level of initial dispersion and system compatibility, 2D materials (platelets or sheets) can yield exfoliated ($E$), intercalated ($C$) or stacked ($S$) composite structures. Restacking into aggregates, or tactoids, is one of the most frequently addressed issues in nanocomposite preparation and processing.[23–26] When platelets are stacked ($S$) they are phase separated from the polymer matrix, indicating chains do not diffuse in between the individual layers, which remain immiscible. In X-ray diffraction, the gallery d-spacing, $d_{001}$, corresponds to the initial bulk material. In the specific case of sheets, additional phenomena such as wrinkling and fold-overs also come into play.[27] Further on, when the 2D-filler is considered intercalated ($C$), there is still aggregation, but an increase in the d-spacing between integral layers is observed. This is attributed to polymer

diffusion or expansion of the gallery. The distance between 2D units is enlarged and, most importantly, fixed. In the case of exfoliation (*E*), sometimes also called delamination, there is not a fixed length between the single layers but an average spacing value. This also means the net interparticle force between the individual colloids is repulsive. A point often overlooked is that the truly dispersed state, *E*, only happens when there is homogeneous distribution of the 2D material in the polymer matrix. Therefore, the mean spacing of 2D units must be dictated by the total volume of separated particles. In this context a criterion for exfoliation based on some required distance is not appropriate, as the distance depends on the filler volume fraction.

## Positional order-disorder

In addition to the dispersion, nacre-like composites with high aspect ratio particles can also develop a degree of periodicity. Considering samples from suspension or melt mixing, this is rare in contrast to the commonly attainable orientational order of anisotropic particles. Nevertheless, regularity can happen in a few systems, especially if there are self-assembling molecules and particularly towards higher 2D-filler fractions. When a structure is disordered (*d*), there is no regular correlation between the position of individual 2D particles, however delaminated or within a stack. Short-range ordered (*r*) systems will show some localized structural positioning. The extent of periodicity is determined by a correlation length, calculated from fitting a Lorentz-type function over scattering profile. This length is distinct from the platelet gallery spacing (dispersion). For the special cases of (quasi) long-range order (*l*), the materials' structure will resemble that of a 1D crystal. In practice, these long range ordered structures will have a finite size or have a finite correlation length domain length, representing the extent of periodicity of a pile of regularly spaced platelets. The finite domain length is commonly fitted to a Gaussian distribution function. In X-ray diffraction, short- and (quasi) long-range order can also be studied from the shape of the peak width of multiple {00*l*} reflections in the scattered intensity profile.[28] The more narrow these peaks are, the higher is the probability of finding a scatterer at a position that matches that of a crystal lattice plane. Regardless of the degree of order in the system (d, r, l), it is imperative to notice that this distinction is relevant irrespective of the dispersion quality (E, C, S).

# Systematic study of the nanostructures of exfoliated polymer nanocomposites

**Chart 4.1.** The structure classification of polymer nanocomposites based on level of 2D-filler dispersion and positional order-disorder. The length of 2D materials is typically between 100 and 5000 nm and exfoliated thickness around 1 to 10 nm
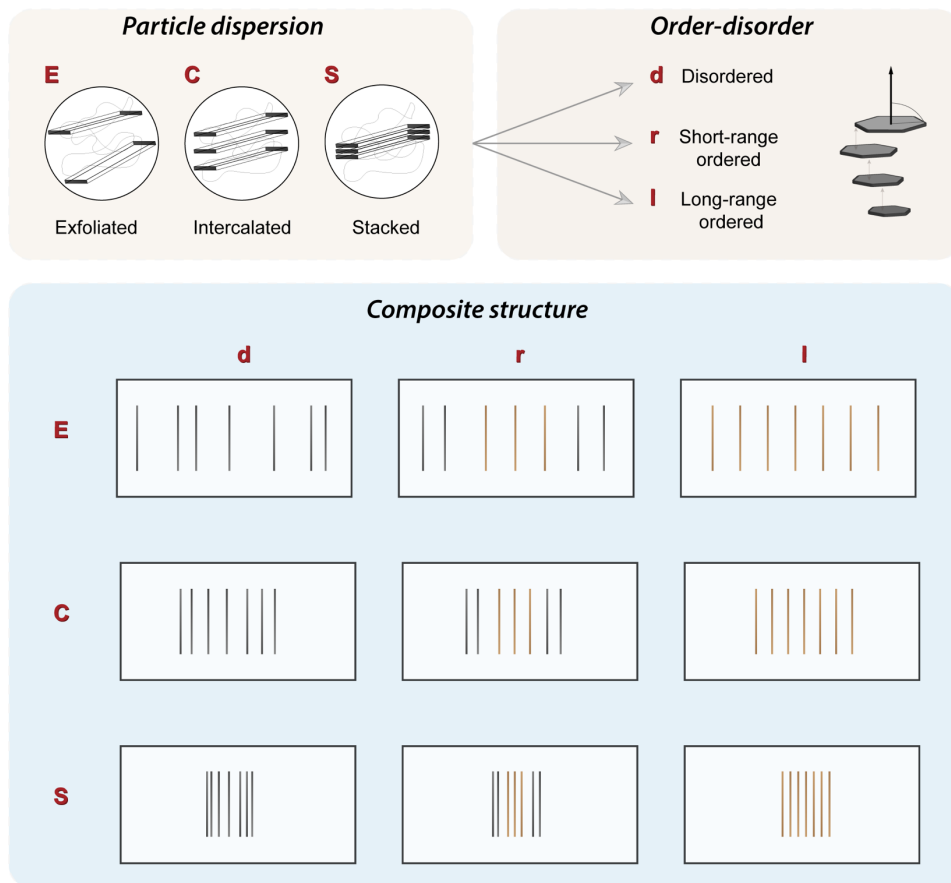


In the field of high-performance nacreous materials, the mechanisms to actively achieve nanoparticle exfoliation and hierarchical structure features are still missing. Therefore, the focus herein is on a strategy to fabricate exfoliated nanostructures, even at high loading, by preventing reaggregation. We hypothesize that an earlier immobilization of platelets would enable us to preserve, initially, the exfoliated system. To test this, we have investigated a water-based system using montmorillonite clay (MMT), up to a high fraction of 80 wt.% on composite basis, in a thermo-reversible gelatin network. The fast-gelling reaction should immobilize the platelets early enough to ensure less or no virtual

stacking during solvent evaporation. Therefore, a network formation that prevents filler relaxation would result in exfoliated structures and keep the MMT high aspect-ratio. The study is a systematic investigation of the evolving structures from exfoliated platelets locked in a hydrogel matrix. The underlying goals are two-fold: to reiterate the importance of achieving exfoliated nanostructures (level of dispersion) in the design of functional, nacre-like composites; and to clarify the nomenclature of 2D material organization. We refrain from addressing particle alignment here since this topic shall be discussed more extensively in Chapter 5.

## 4.2. Materials and Methods

### 4.2.1. Materials

Gelatin from porcine skin (Type A, 78-80 mM free COOH/100 g protein, 50,000−100,000 Da, gel strength 300, relative density 1.3 g cm$^{-3}$) was obtained from Sigma Aldrich and used as received. Sodium montmorillonite (Na-MMT), CLOISITE-Na+, with $D_{50}$ particle size <25 μm, basal spacing d001 of 11.7 Å, and density 2.86 g cm$^{-3}$ was supplied by BYK Chemie GmbH, Germany, and used without further purification or surface treatment. The aspect ratio length over thickness) of the dispersed Na-MMT is typically reported as ranging from 10 to 1000 nm. All chemicals used were of analytical grade.

### 4.2.2. Gel suspensions and film casting

A gelatin stock solution (3 w/v % solids content) was initially prepared by dissolving the powder in deionized water at 50 °C for 1 h using a magnetic stirrer. The pH of gelatin solution was 5.2 ± 0.1 at 50 °C, which is below its reported isoelectric point of 7 – 9.5. Na-MMT was mixed in deionized water under vigorous stirring for at least 24 h to achieve a 3 w/v % delaminated dispersion. The pH of Na-MMT suspension was 8.2 ± 0.1 at 50 °C.

Film-forming suspensions of protein/clay were prepared by carefully mixing (pre-calculated) wet ratios of the gelatin stock solution and Na-MMT suspension at 70 °C. This thermal treatment to the Na-MMT slurry was necessary to avoid lumps and re-agglomeration in the mixtures with protein due to temperature influence on its solubility.[39] All the Na-MMT was dispersed, without any remaining visual agglomerates. The protein/MMT suspensions were further mixed at 400 rpm for 2 hours at 70 °C to allow for gelatin-clay interaction. The pH at 50 °C of the casting gel suspensions ranged

from 5.4 up to 7.7, increasing in value with higher Na-MMT addition. The hot dispersion was carefully poured into a 9 x 2 cm polystyrene petri dish and dried at ambient conditions (20 °C, 50% RH) to form a thin film. The drying step lasted around 4 days and free-standing films were obtained by peeling off the new layer. Subsequently, the films were vacuum-dried at 40 °C for 1 day to remove excess humidity. The final thickness was designed to be in the range of 200 μm, what was confirmed using a digital micrometer at five random locations.

The study aimed at a wide range of filler loadings ranging from 1 to 80 wt. % Na-MMT, on the composite weight basis. In solid-state, this should be equivalent to up to 65 vol.% Na-MMT. Two replicates were performed for samples in region of interest, containing high clay content, where we aimed to achieve 30 and 60 vol. % MMT. The MMT content was later confirmed via thermal gravimetric analysis (TGA) (Supporting Text S4.1). Throughout this study, the composite clay content is expressed as volume percentage (vol. %). The samples are denoted as *X*MMT, where *X* is the volumetric MMT fraction percentage in the composite.

For the following characterization analyses, the films were additionally conditioned for a week in a desiccator containing silica gel at room temperature. This step was necessary to ensure there was absence of freely bound water, as the gelatin polymer has a hydrophilic nature.

## 4.2.3. Focused ion beam scanning electron microscopy (FIB-SEM)

Focused ion beam scanning electron microscopy (FIB–SEM) experiments were performed in FEI Helios G4 CX microscope. A conductive thin layer of Au (~10 nm thickness) and a protective thin layer of W (0.3 μm thickness) were deposited on the cross-sectional surface of specimens using a sputter coater and gas injection system respectively. The focused beam was operated at 30 kV and 2.5/0.24 nA used respectively to carve a trench and perform slicing up to a nominal depth of 10 μm. After correcting for the tilt angle between specimen and SEM detector, a series of micrographs were recorded of the polished cross-sections exposed, with a secondary electron detector operated at 10 kV. When possible, the average filler size and inclination of around 50 filler particles were identified and measured (Supporting Text S4.2). The technique allowed to

investigate micro-arrangement of MMT particles within the gelatin matrix. Image enhancement was needed, i.e. solving for "curtaining" effect in the milling direction and resolution, which was possible with the *polishEM* software tool[40]. Measurements and analysis of the micrographs were performed by *Gwyddion* software.

## 4.2.4. Wide-angle (WAXS) and Bragg-Brentano X-ray scattering

Wide-angle X-ray scattering (WAXS) was used to determine the composite nanostructure. Transmission mode X-ray diffraction was performed using a Bruker AXS D8 Discover with a VÅNTEC 2D detector and using Cu Kα radiation ($\lambda = 1.54184$ Å) at 50 kV and 1 mA. A point collimator of 0.3 mm was used, and the sample−detector distance was 30 cm parallel (incident beam at a glancing angle) and perpendicular to the film surface. Additional measurements were done with the detector shifted by $2\theta = 11.5°$ in order to obtain 2D patterns at higher angles while avoiding background noise.

Experiments were also conducted with a Bruker D8 Advance diffractometer (2theta-theta scan, often called Bragg-Brentano or focusing geometry) with Co Kα source ($\lambda = 1.7889$ Å, 35 kV and 40 mA) with Lynxeye position sensitive detector. The measurement range on a motorized varied divergent slit was set from 4 to 50 degrees with step size of 0.02 mm. A measuring time of 0.1 second per step was employed. For basic interpretation and data curation of the X-ray diffraction (XRD), Bruker software (DiffracSuite.EVA version 5.1, Bruker, USA) was used.

To normalize for the different X-ray sources ($\lambda$), the XRD data is shown over the scattering vector $q = (4\pi / \lambda) \sin \theta$, where $2\theta$ is the scattering angle. The layer d-spacing was calculated from Bragg's law.

## 4.2.5. Correlation or Domain length

In general, information on the size of ordered domains in composites can be extracted from the line shape of X-ray peaks. If we consider crystals with a three-dimensional lattice, the probability to find the center of mass of a molecule at a position $r$ with respect to a test molecule ($r = 0$) can be described by a distribution function $D(r)$. True dimensional positional order results in a series of Dirac delta functions along the $r$ values. However, for quasi long-range and short-range order systems, such as nanocomposites,

this distribution displays an algebraic decay with distance r, e.g., $D(r) \propto r^{-\eta}$ or $D(r) \propto e^{-\frac{r}{\xi}}$. The Fourier transform of the exponential decay corresponds to a Lorentzian expression, which is one of the distribution functions commonly fitted to the radially integrated X-ray profiles.[28]

In our case, the nanoplatelets will show a high aspect ratio if exfoliated, what favors the development of 1D ordered systems upon drying. Hence, distribution functions also can be fitted to estimate a correlation or domain length ($\xi$ or $L$) as a measure for the degree of positional order.[41] To calculate this length, we applied the Scherrer equation, which is originally derived for a 1D finite stack of lattice planes:

$$\xi \; or \; L = \frac{K \, \lambda}{FWHM \; \cos\theta} \qquad (S4.1)$$

where $\xi$ or $L$ are the average correlation length or domain size, $\lambda$ is the wavelength of X-ray source, FWHM is the peaks' full width at half maxima and $\theta$ the diffraction angle (radians), respectively. The empirical proportionality factor (K) was assumed to be 0.89. A Gaussian fit was chosen to obtain the FWHM, since we observed quasi long-range order and possible convoluted instrumental broadening of the scattered image. The Gaussian statistical goodness-of-fit was estimated by the probabilistic parameter of Efron's pseudo-$R^2$. The equivalent number of platelets within the period was estimated from the relationship: length over 00$l$ d-spacing.

## 4.2.6. Differential scanning calorimetry (DSC)

Differential scanning calorimetry (DSC) experiments were performed to characterize the thermal behavior of gelatin/MMT composites. First, snippets from the film samples were acclimated to a 33% relative humidity environment using $MgCl_2$ saturated salt solution. The water uptake capacity at the end of two weeks was measured gravimetrically. The DSC method consisted of heating the sample from 223 to 425 K, at rate of 3 K min$^{-1}$, on a PerkinElmer Pyris diamond instrument with two 1 g furnaces and calibrated with indium. Nitrogen gas was used to purge the thermal analyzer at 50 mLmin$^{-1}$. Stainless steel pans with o-ring seals were used for hermetically encapsulating the equilibrated samples (20 mg). An identical empty reference pan was used. The pans were sealed according to supplier instructions (PerkinElmer). Data visualization was carried out by

Python, in which the y-axis refers to endothermic transitions. Each thermogram was analyzed for the melting (or denaturation) event.

## 4.3. Results and Discussion

### 4.3.1. Quality of dispersion

The gelatin A/MMT bionanocomposites were prepared by solvent casting 3% solids suspensions at RT. The formation of an unfragmented hard gel network, like in pristine gelatin, was visually observed in hybrids up to a 20 wt.% MMT content (Figure S4.4). The final filler mass was determined by thermogravimetric analysis (TGA, Supporting Text S4.1). and converted to a composite volume fraction percentage $X$, herein denoted as $X$MMT. Curiously, the obtained films showed high translucency up to sample 11MMT, while volume fractions above 33 to 64% had increasing haziness (Figure S4.5). Because the aligned nanostructures are less scattering the visible light, transparency is often taken as an identifying feature of a homogeneous and well-dispersed phase. It is true transparency that can indicate the absence of 2D-filler aggregation but at times homogenous systems, for instance locally crystalline (spherulites in semicrystalline polymers) or anisotropic arrangements (nematic fluids), can show opacity.

We further examined the gelatin/MMT samples with focused ion beam scattering electron microscopy (FIB-SEM). Because of the large difference between soft/hard phases, the ion milling step was slightly uneven in the vertical direction and image treatment was necessary (Supporting Text S4.2). The obtained micrographs allow for inspecting the morphology of film cross-section. All the bionanocomposite samples showed the expected in-plane orientation. No large-scale aggregation or restacking was observed up to 64MMT. In Figure 4.1, we show a very diluted sample, containing only 0.4% MMT in volume. At this unique regime we could see MMT platelets separately and measure their lateral dimension, of roughly 130 to 270 nm. To investigate the 2D material thickness, electron scattering techniques should not be relied upon, due to charge density and contrast blurring effects. However, they can provide for a qualitative estimation of particle width, degree of separation, and extent of exfoliation.[29] The 0.4MMT sample can be classified as exfoliated disordered (*Ed*), because homogeneous spreading of nanosized particles is observed, but without any observable periodicity. Only a global evaluation the particle dispersion could be done for higher platelet fractions, 11MMT and 64MMT, because charging effects hindered discrete particle visualization (Figure S4.2). In general, we note the absence of clay aggregates based on uniform scattering. For these samples,

exfoliated or intercalated phases are probable, considering the uniform distribution of densely layered structures.
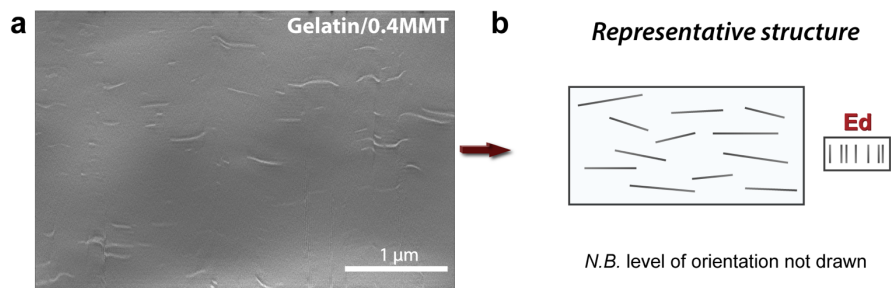


**Figure 4.1.** FIB-SEM cross sectional image of Gelatin/0.4MMT composite (a) and its representative nanostructure (b), classified as exfoliated disordered (*Ed*).

Wide angle X-ray scattering (WAXS) was used to investigate the basal spacing of MMT (Figure 4.2). The patterns were obtained with the incident beam at a glancing angle parallel to the film surface, as shown in Figure 4.2a. The angle applied was iterated to ensure the scattering vector properly intersects the Ewald sphere. This transmission mode is very sensitive to the local 2D material arrangement and the rather high level of in-plane orientation. We could observe distinct trends between sample groups 0.4 to 11MMT and 33 to 64MMT. A clear streak was observed up to 5MMT, while for 11MMT an ill-defined wedge shape appeared. At higher filler volume fractions, from 33MMT, there were clear equatorial arcs, typical of anisotropic MMT layers. The first detection of a basal 001 reflection was at 11MMT, corresponding to an average spacing of $d_{001}$ = 120 Å. Remarkably, a gradual change in the peak position of clay reflection was observed with increasing clay content (Figure 4.2b). With this, the corresponding d-spacings decreased down to 18 Å. These distances are larger than the back calculated pure MMT basal spacing of 12 Å (Figure 4.2c), which confirms that there was gelatin intercalation into the clay galleries for all samples. Additionally, the orientation seen in the pristine Na-MMT film likely developed from flocculation (edge-face attraction), yielding an arrangement like in a random pile of cards.[30]

In a defined two-dimensional space, if we consider perfectly aligned 2D nanoparticles that are not allowed to interact, the volume fraction can be defined by the summed

thickness of all particles over the determined space length. By analogy, the concentration of particles should be proportional to the thickness of particles over the inter-particle spacing (Figure 4.2d). For this reason, the apparent d-spacing is inversely proportional to the MMT volumetric content, decreasing with filler concentration. This volumetric rule is what truly defines an exfoliated structure and is valid to any form of 2D platelet/sheet nanocomposite. Within the realm of colloid science, the progression of the mean interparticle separation in correlation with the volume fraction is named the swelling (or dilution) law. Therefore, all the studied concentrations for gelatin/MMT seemed to follow the exfoliated regime. From 11MMT up to 64MMT, there is an excellent agreement between experimental and theoretical exfoliated d-spacings derived from the integrated 001 reflections ($R^2 = 0.993$). Despite unusually high clay fractions, there is virtually no re-stacking and phase separation over a wide concentration range (up to 64 vol.%). This is encouraging because examples of perfect exfoliation are limited, with often high temperature and pressure required.[26] In comparison, other successful 2D silicate bionanocomposites have been reported, usually at lower loadings, and, even so, fall inside the intercalated regime (Figure 3.2c).[18,31]

**4**

# Systematic study of the nanostructures of exfoliated polymer nanocomposites
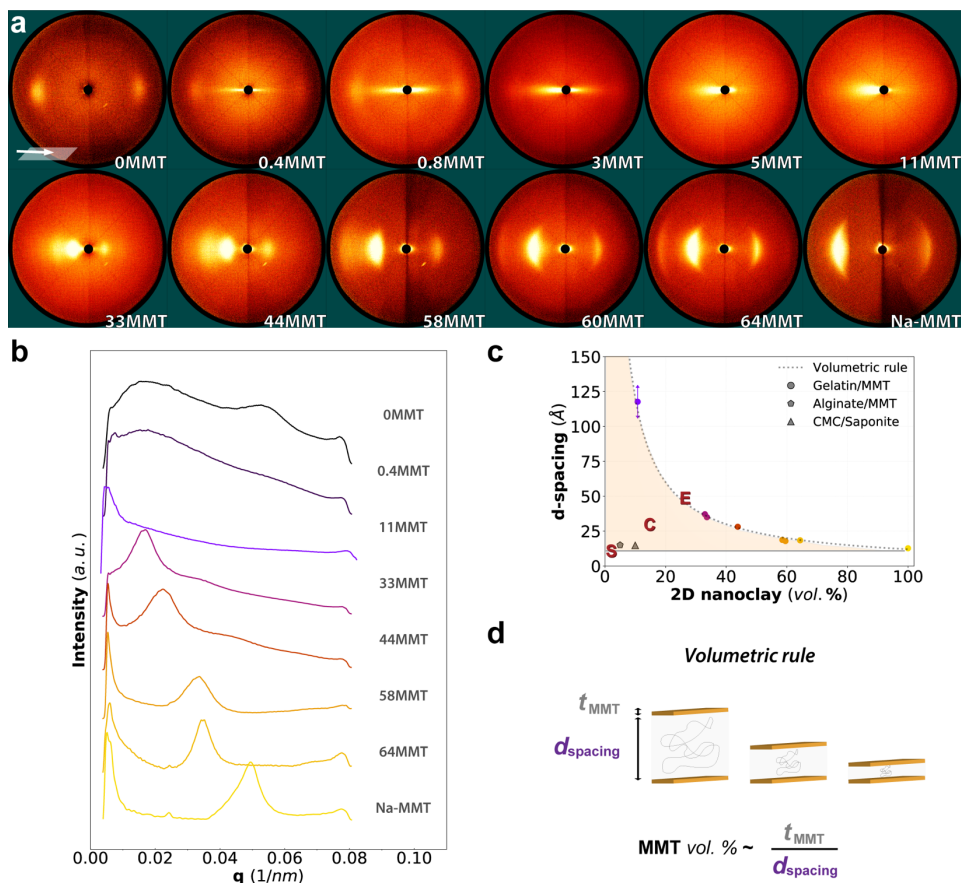


**Figure 4.2.** a) 2D transmission X-ray scattering images of gelatin/MMT samples with varying volumetric MMT composite content at beam inclination parallel to the plane of the films (90.5 to 94° range of glancing angle). The scattering patterns reveal anisotropy and a progressive change in basal reflections with increasing clay loadings. b) Wide-angle X-ray diffractograms depict a peak shift of $d_{001}$ MMT reflections towards higher angles starting from sample 11MMT. c) Comparison between experimental and calculated d-spacings derived from the $d_{001}$ MMT reflection. The thickness of a delaminated Na-MMT platelet was obtained by reciprocal fit of $d_{001}$ lengths and extrapolating to origin (virtual zero concentration). Alginate and carboxymethyl cellulose (CMC) composite data respectively from Zlopasa *et al.*[31] and Ebina and Mizukami[18]. d) Illustration depicting the theoretical basis for calculating d-spacing, where a reciprocal volumetric rule of concentration of MMT is assumed; $t_{MMT}$ is the thickness of a single platelet and $d_{spacing}$ is the platelet interspace.

## 4.3.2. Level of order

The WAXS diffraction patterns were also obtained at higher $q$ scattering vectors by moving the detection setup (Figure 4.3a). Interestingly, for neat gelatin the scan showed structural arrangement that is derived from the crystallization of collagen-like helices ($q$ 0.05 nm$^{-1}$) and a broad peak related to the peptide bonds.[32] The WAXS patterns showed that samples 33MMT and higher have additional reflection peaks (also broad [002] and [003] features), corresponding to higher orders of the MMT lamellar planes (Figure S4.7). Surprisingly, the sample 64MMT showed many additional reflections, all the way up to [006]. To investigate this further the layered bionanocomposites could also be studied in X-ray analysis in Bragg-Brentano geometry, allowing for higher intensity levels (Figure 4.3b). The 1D diffractograms are used to better detect the presence of higher order clay reflections [00$l$]. Additional lattice reflections ([002], [003]) were confirmed for samples 33MMT and higher around $q$ range 0.05 – 0.20 nm$^{-1}$, which can be interpreted as evidence of improved layer regularity. The sample 64MMT showed remarkable quasi long-range order and six reflection peaks. However, due to polydispersity in the particle's width, this should not be confused with a real one-dimensional lattice. The periodic systems were modelled by a Gaussian distribution function over $q$. The correlation length or (para)crystal domain size were calculated via the Scherrer equation[33] for both 001 and 003 reflections, which were observed using different scattering geometries (Table 4.1). In the case of gelatin/MMT composites, the length $L$ translates into the relative extent of short- or long-range positional order. We note that the platelet arrangements might be paracrystalline, since $\xi$ seemed to depend on the X-ray reflection. For 64MMT, a substantial length of L = 198 Å is found for the $d_{001}$ reflection (18 Å d-spacing). In other words, the 64MMT sample had a 001 polymer/clay (para)crystallite of $L$ ~200 Å, of which around 11 platelets were inside. This unexpected regularity at high particle content supports the findings of a closely packed lamellar structure.

Altogether, the various gelatin/MMT compositions resulted in exfoliated structures of different lamellar spatial arrangement (regularity), as previously illustrated in Chart 4.1. We could identify exfoliated disordered (up to 33MMT), short-range ordered (up to 44MMT), quasi long-range ordered at 64MMT (Figure 4.3b). Furthermore, the calculated equivalent number of platelets within periodic length ($n$) increased from the short-range to quasi long-range ordered composites – regardless of the scattering geometry (Table 1). This regularity is highly unexpected, since water-based polymer composites reinforced with high aspect ratio nanoparticles can easily present long-range orientational order (high orientation factor or $<P_2>$ value), but seldom show a significant degree of positional

order. In fact, to the best of our knowledge, positional order has been only reported in silicates modified by quaternary ammonium cations and host-guest additives.[26]

## 4.3.3. Hydrogel strategy

Our exfoliation strategy depends on the formation of a continuous network to immobilize the 2D material and develop yield stress. However, the extent of gelation or network density seemed to decrease with higher MMT loadings. The thermo-reversible gelation process is not a percolative one but it is caused by aggregation of helices into a collective fibrous network.[34] In the X-ray diffractions, we observed the appearance of equatorial diffraction arcs up to 5MMT at $q$ 0.06 nm$^{-1}$, which were from the gelatin component (Figure 4.2 and 4.3). This nanoscale organization comes from the aggregation of renatured supramolecular helices. The crystallization was evidently hampered at elevated MMT content[32,35,36], above 11 vol%, in which additions also slowly increased the pH of the system closer to the protein isoelectric point. Clay negative interference on renaturation was also supported by differential scanning calorimetry (Figure S4.8). This can be linked to the macroscopic breakdown of the gelatin-based physical network in the casting of gels (Figure S4.4). It is plausible that strong electrostatic and H-bonding interactions[36,37] and, particularly, the decreased amount of loose chain ends disturbed the cooperative joining of helices. At elevated MMT fractions, the macroscopic gelatin cross-linking was heavily suppressed. We speculate that by introducing the clay, there is gelatin absorption on the clay surface, thereby preventing thermal gelation. Despite the formation of weaker gels, the network in these MMT samples was apparently sufficient to avoid clay stacking and phase separation.

Curiously, the fact that the samples at elevated filler content show quasi long-range order could be linked to a platelet-driven nanoconfinement of gelatin chains. As the system settles from water evaporation, the mobility of gelatin decorated MMT is reduced. The locked gelatin molecules will progressively get confined in the interlayers and lose the ability to form secondary structures. One could consider the typical length of gelatin random coil as a radius of gyration ($Rg$) in the order of 50 to 100 Å[38], coming from the rough estimate that $Rg \sim aN^{1/2} \sim (10 \text{ Å})(100 \text{ units})^{1/2}$. This radius range is reasonably close to the increment in d-spacing at 58 to 64 vol.% MMT, indicating protein confinement. We propose that the gelatin specific binding is sufficient to prevent clay restacking and

instead we observe colloid positional order caused by steric repulsion from the confined gelatin coils.
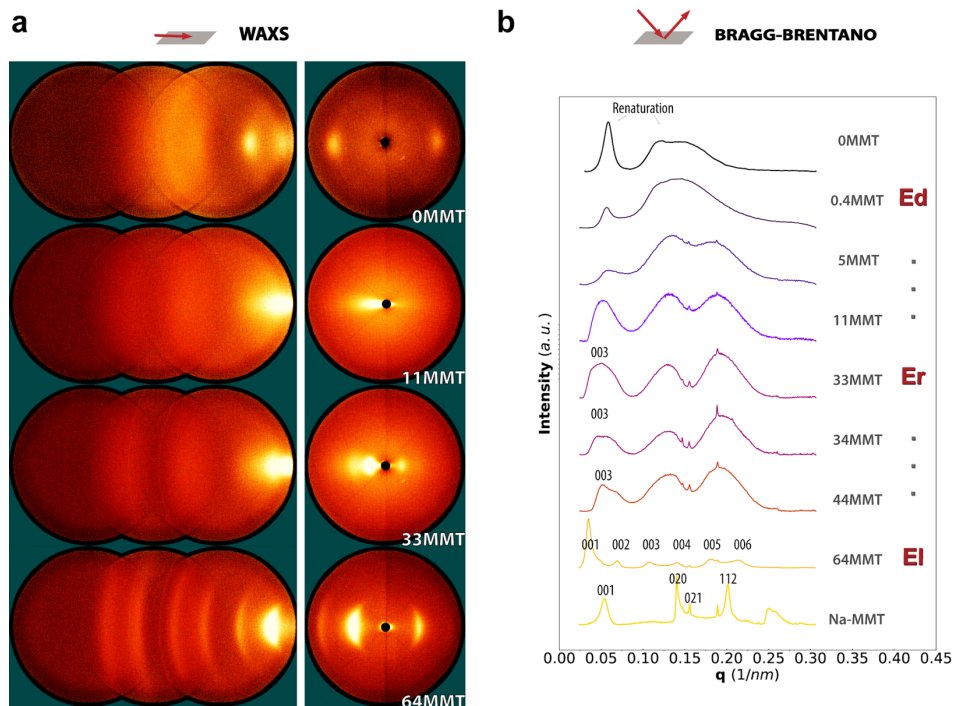


**Figure 4.3.** a) 2D transmission X-ray scattering images at higher scattering vectors $q$ of gelatin/MMT samples with varying volumetric MMT composite content at beam inclination parallel to the plane of the films (90.5 to 94° range of glancing angle). b) Bragg-Brentano X-ray diffractograms on films show a decrease in gelatin renaturation and appearance of multiple MMT reflections with increasing loading fractions. Multiple reflections are key to identify regularity (positional order).

**Systematic study of the nanostructures of exfoliated polymer nanocomposites**

**Table 4.1.** Equivalent correlation ($\xi$) or domain length ($L$) and number of platelets ($n$) estimated using the 1D Scherrer equation on 001 (from WAXS) and 003 (from Bragg-Brentano) basal reflections of gelatin/MMT composites.

| Sample | 001 | | | | | 003 | | | | |
|---|---|---|---|---|---|---|---|---|---|---|
| | $q$ (1/nm) | $a$ (Å) | Length (Å) | $n$ (L/a) | Efron's pseudo-$R^2$ gaussian | $q$ (1/nm) | $a$ (Å) | Length (Å) | $n$ (L/a) | Efron's pseudo-$R^2$ gaussian |
| 33MMT | 0.017 | 37.5 | **216.8** | **5.8** | 0.996 | 0.051 | 12.2 | **42.1** | **3.4** | 0.935 |
| 44MMT | 0.023 | 27.8 | **156.7** | **5.6** | 0.992 | 0.056 | 11.2 | **50.6** | **4.5** | 0.820 |
| 64MMT | 0.035 | 18.2 | **197.6** | **10.9** | 0.990 | 0.107 | 5.9 | **87.5** | **14.9** | 0.970 |

$q$: center of basal reflection; $a$: periodicity estimated from $q$; $\xi$ or $L$: equivalent correlation or domain length: $n$: equivalent number of platelets within periodic length; Efron's pseudo-$R^2$ gaussian: the Efron's pseudo-$R^2$ estimated for the Gaussian fit used to obtain full width at half maxima.

## 4.4. Conclusions

In conclusion, we hereby report on an easily attainable 2D material exfoliation strategy by implementing a hydrogel matrix with rapid network formation. If applied to solvent-based processes, this rationale can lead to controlled all-exfoliated systems for a wide loading range, as opposed to most reported results on nacre-like composites. For the thermo-reversible gelatin/MMT nanocomposites, we report filler loadings as high as 64% volume fraction. In addition, controlled hydrogelation becomes a suitable alternative to laborious processes such as multilayer deposition, in situ polymerization, external field alignment, etc. The high level of exfoliation and alignment of the clay platelets allows for precise tuning of the sample d-spacing through the hereby described volumetric rule. Nevertheless, the extent of gelation needs to provide enough particle immobilization during the drying phase. The locking mechanism needs to sustain time scales higher than that of filler relaxation. Hence, the strategy should be applied to other systems on a case-by-case basis. Another reason for this is that the system properties are still dependent on initial polymer-particle compatibility, polymer-penetration energy, and interfacial interactions. Remarkably, particle order-disorder transitions were found to develop from these nanostructures, which requires further attention. For instance, the composites 33MMT to 64MMT were found to form very ordered phases, with crystallite sizes about

200 Å long. The next chapter shall explore the proposed hydrogelation strategy with regards to the platelet orientation mechanism and its effect on anisotropic properties.

**4**

## Supporting information

## Supporting Text S4.1. Thermogravimetric Analysis

The composite samples were cut to snippets and analyzed using a thermogravimetric analyzer (TGA 8000, Perkin Elmer, USA) from 30 to 900 °C using a heating rate of 10 °C min$^{-1}$. The sample weight was in the range of 4 to 6 mg. Corundum crucibles were used and air as a purge gas at a flow rate of 20 mL min$^{-1}$. The method included isothermal steps at 105 and 900 °C for water removal and final weight equilibration, respectively.

In Figure S4.1, the thermal mass loss of gelatin, clay, and hybrids samples casted from 3 w/v % mixtures are shown. The first gelatin weight loss occurs at 270 °C, due to gelatin decomposition, and the second one around 500 °C region, due to combustion of residual organics. For the nanocomposite samples up to 5MMT, it can be clearly observed that the secondary onset thermal decomposition of the composites, around 530 to 610 °C, is higher than that of the neat protein. It can also be noted that the thermal rate of decomposition of hybrids is obviously reduced with clay concentration, specially at higher MMT loadings (> 11MMT). Thus, the well-dispersed clay inhibited the weight loss of gelatin, effectively acting as a barrier element, and because of its high thermal decomposition. Due to the usage of oxidative environment and negligible ash content of gelatin, the final residue represents the weight percentage of MMT. These concentrations were later converted into vol. % MMT, as presented in caption of Figure S4.1, ranging from 0.4 to 64%.

4
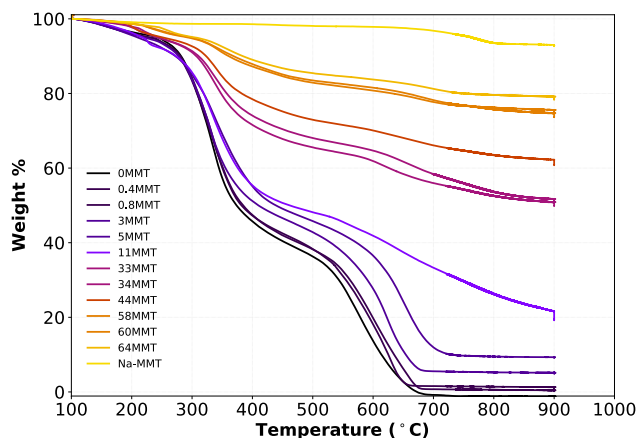
**Figure S4.1.** TGA of gelatin and gelatin/MMT composites fabricated from 3 w/v % suspensions at different filler loadings, shown in volume fraction.

## Supporting Text S4.2. FIB-SEM Image Treatment and Particle Analysis

The FIB-SEM sample images were first treated to remove typical ion beam streak artifacts or "curtaining" (Figure S4.2). The curtaining in the ion milling direction depends on the sensitivity of the material, being common in composites of hard and soft materials, and arising from uneven milling. This image treatment was done via 2D Fast Fourier Transformation (*polishEM* software tool).

In the case of sample Gelatin/0.4MMT, due to the low loading of MMT clay and its electron density, it was possible to observe the internal particle dispersion and composite structure. The MMT nanoplatelets are possible to be visualized only due to the high electron density contrast between the organic matrix and silicate filler. Because of the same phenomena, the visible particles are actually a blurred image of the real nanosized structure, which can only be further resolved with X-ray analysis.

Unlike previous, the FIB-SEM image of sample 11MMT was too convolved, a result from high charging interference. However, a dense and layered structure was observed, which was also free of clay aggregate traces. At 11MMT, the mean layer spacing was measured roughly 76 to 181 nm. The nanoparticles cannot be observed individually already at this volumetric content (Figure S4.2b and c). At high volume fraction (64MMT), the layered sample shows undulation features but it is also predominantly free of stacking.

No gelatin orientation was observed in any of the studied samples. However, during ion milling temperatures can shortly reach the onset melting point of solid gelatin ($\geq$ 87 °C or 360 K)[35], what hampers the observation of possible gelatin layers from the crystallization of helices.
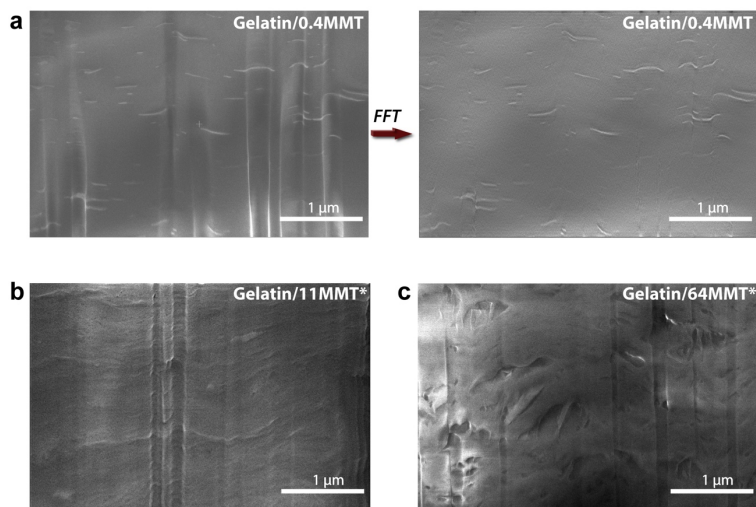


\* nanoparticles cannot be resolved with FIB-SEM

**Figure S4.2.** FIB-SEM images of gelatin/MMT nanocomposites: (a) 0.4MMT unprocessed (left) and with curtaining removed via 2D FFT (right); (b) unprocessed 11MMT and (c) unprocessed 64MMT.

## Length of Na-MMT Particles

The average particle length was estimated from three micrographic pictures belonging to the 0.4MMT sample (Figure S4.3a). Image analysis resulted in 212 ± 97 nm as average length of dispersed particle (Figure S4.3b). Furthermore, the (in-plane) inclination angle of particles coarsely tends to zero, suggesting sample anisotropy along this direction (Figure S4.3b and c).
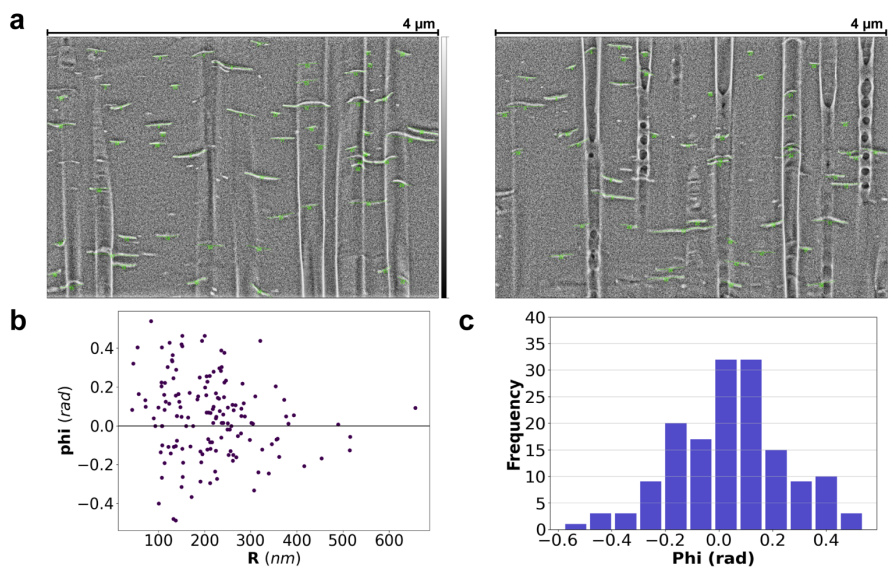
**Figure S4.3.** (a) FIB- SEM images of gelatin/0.4MMT showing imaging software particle identification and data. (b) R: total planar distances of particles, in nm; and Phi: inclination angle of particles, in radians. (c) The frequency distribution of inclination angle of MMT particles, Phi.

## Supporting Figures and Tables
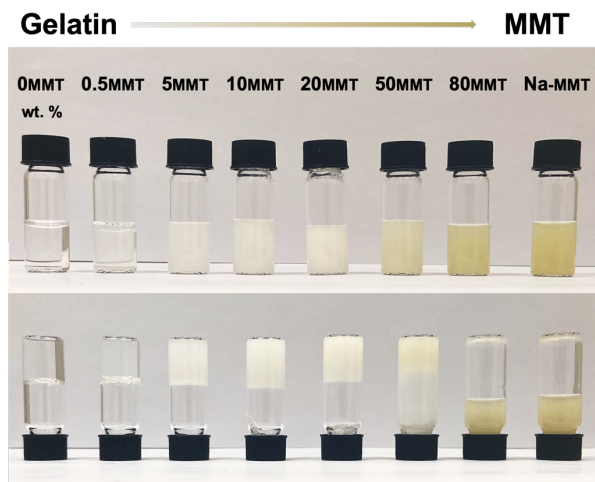


**Figure S4.4.** Vials containing gelatin/MMT film-forming suspensions (3 w/v % total solids). The notation $X$MMT classifies the suspension in terms of aimed MMT mass fraction ($X$%), on a gelatin/MMT basis. The inverted vials, at equilibrium, indicate that the hydrogel network starts to collapse at MMT loadings higher than 20 wt.%, which are gels resulting in composites with filler fractions above 11 vol. %.



**Figure S4.5**. Images of gelatin/MMT nanocomposite films. The film thickness was around 0.2 mm. The notation $X$MMT classifies the composite film in terms of the determined MMT volume fraction ($X$%), on a gelatin/MMT basis.
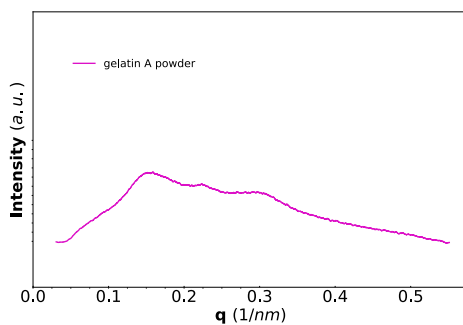
**Figure S4.6.** Powder XRD of the commercial gelatin type-A used in this study. The diffractogram shows that the *as is* gelatin is amorphous before processing into a solvent-casted film.
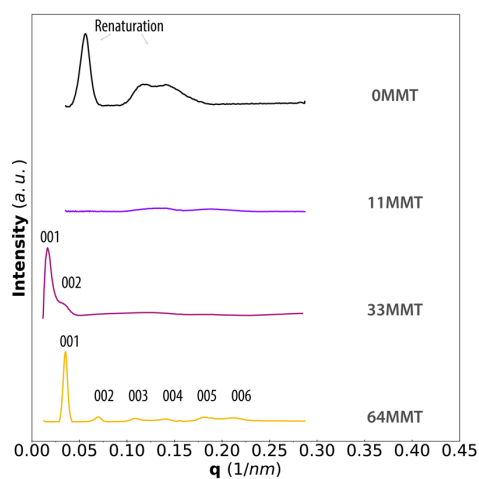


**Figure S4.7.** WAXS radial 1D integration of gelatin/MMT composites at higher *q* range and from a parallel glancing angle.

# Systematic study of the nanostructures of exfoliated polymer nanocomposites



**Figure S4.8.** DSC analysis of the temperature dependance of heat capacity (endo up) of gelatin/MMT films equilibrated to a 0.33 water activity ($a_w$). The equilibrium water uptake for each sample was measured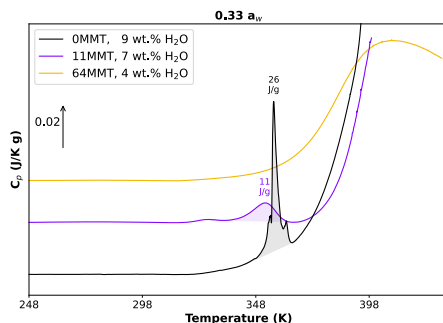 gravimetrically and is shown in legend. The blurred area assigned to the denaturation temperature $T_{Hel}$ was suppressed with increasing clay content, as observed via absent or decreased corresponding energetic barrier (J/g) at transition. This suggests that more amorphous gelatin structures were formed with increasing clay volume fraction. Above 373 K, the DSC pan seal integrity is broken and we observe sample water loss.

**Table S4.1**. Equivalent correlation ($\xi$) or domain length ($L$) and number of platelets ($n$) estimated using the 1D Scherrer equation on 001 (from WAXS) and 003 (from Bragg-Brentano) basal reflections of all gelatin/MMT composites.

| Sample | 001 | | | | | 003 | | | | |
|---|---|---|---|---|---|---|---|---|---|---|
| | $q$ (1/nm) | $a$ (Å) | Length (Å) | $n$ (L/a) | Efron's pseudo-$R^2$ gaussian | $q$ (1/nm) | $a$ (Å) | Length (Å) | $n$ (L/a) | Efron's pseudo-$R^2$ gaussian |
| 33MMT | 0.017 | 37.5 | **216.8** | **5.8** | 0.996 | 0.051 | 12.2 | **42.1** | **3.4** | 0.935 |
| 34MMT | 0.018 | 34.6 | **216.7** | **6.3** | 0.999 | 0.054 | 11.7 | **46.1** | **3.9** | 0.941 |
| 44MMT | 0.023 | 27.8 | **156.7** | **5.6** | 0.992 | 0.056 | 11.2 | **50.6** | **4.5** | 0.820 |
| 58MMT | 0.033 | 18.9 | **148.1** | **7.8** | 0.998 | n.a. | n.a. | **n.a.** | **n.a.** | n.a. |
| 60MMT | 0.035 | 18.1 | **144.1** | **8.0** | 0.960 | n.a. | n.a. | **n.a.** | **n.a.** | n.a. |
| 64MMT | 0.035 | 18.2 | **197.6** | **10.9** | 0.990 | 0.107 | 5.9 | **87.5** | **14.9** | 0.970 |

$q$: center of basal reflection; $a$: periodicity estimated from $q$; $\xi$ or $L$: equivalent correlation or domain length: $n$: equivalent number of platelets within periodic length; Efron's pseudo-$R^2$ gaussian: the Efron's pseudo-$R^2$ estimated for the Gaussian fit used to obtain full width at half maxima.
n.a. Experiment not available.

# References

(1)     Wegst, U. G. K.; Bai, H.; Saiz, E.; Tomsia, A. P.; Ritchie, R. O. Bioinspired Structural Materials. *Nat. Mater.* **2015**, *14* (1), 23–36. https://doi.org/10.1038/NMAT4089.

(2)     He, H.; Guan, L.; Le Ferrand, H. Controlled Local Orientation of 2D Nanomaterials in 3D Devices: Methods and Prospects for Multifunctional Designs and Enhanced Performance. *J. Mater. Chem. A* **2022**, *10* (37), 19129–19168. https://doi.org/10.1039/d2ta01926d.

(3)     Huang, C.; Cheng, Q. Learning from Nacre: Constructing Polymer Nanocomposites. *Compos. Sci. Technol.* **2017**, *150*, 141–166. https://doi.org/10.1016/j.compscitech.2017.07.021.

(4)     Yang, H. M.; Jo, S.; Oh, J. H.; Choi, B. H.; Woo, J. Y.; Han, C. S. Strong and Tough Nacre-Inspired Graphene Oxide Composite with Hierarchically Similar Structure. *ACS Nano* **2022**, *16* (7), 10509–10516. https://doi.org/10.1021/acsnano.2c01667.

(5)     Mianehrow, H.; Lo Re, G.; Carosio, F.; Fina, A.; Larsson, P. T.; Chen, P.; Berglund, L. A. Strong Reinforcement Effects in 2D Cellulose Nanofibril-Graphene Oxide (CNF-GO) Nanocomposites Due to GO-Induced CNF Ordering. *J. Mater. Chem. A* **2020**, *8* (34), 17608–17620. https://doi.org/10.1039/d0ta04406g.

(6)     Zheng, X.; Xu, M.; Yang, S.; Omonov, S.; Huang, S.; Zhao, J.; Ruan, H.; Zeng, M. Novel Bio-Inspired Three-Dimensional Nanocomposites Based on Montmorillonite and Chitosan. *Int. J. Biol. Macromol.* **2020**, *165*, 2702–2710. https://doi.org/10.1016/j.ijbiomac.2020.10.070.

(7)     Li, Q.; Xue, Z.; Zhao, J.; Ao, C.; Jia, X.; Xia, T.; Wang, Q.; Deng, X.; Zhang, W.; Lu, C. Mass Production of High Thermal Conductive Boron Nitride/Nanofibrillated Cellulose Composite Membranes. *Chem. Eng. J.* **2020**, *383* (July 2019), 123101–123101. https://doi.org/10.1016/j.cej.2019.123101.

(8)     Plantzopoulou, A.; Stergiou, A.; Kafetzi, M.; Arenal, R.; Pispas, S.; Tagmatarchis, N. One-Step Covalent Hydrophobic/Hydrophilic Functionalization of Chemically Exfoliated Molybdenum Disulfide Nanosheets with RAFT Derived Polymers. *Chem. Commun.* **2022**, *58* (6), 795–798. https://doi.org/10.1039/D1CC06195J.

(9)     Walther, A.; Bjurhager, I.; Malho, J. M.; Pere, J.; Ruokolainen, J.; Berglund, L. A.; Ikkala, O. Large-Area, Lightweight and Thick Biomimetic Composites with Superior Material Properties via Fast, Economic, and Green Pathways. *Nano Lett.* **2010**, *10* (8), 2742–2748. https://doi.org/10.1021/nl1003224.

(10)    Das, P.; Schipmann, S.; Malho, J. M.; Zhu, B.; Klemradt, U.; Walther, A. Facile Access to Large-Scale, Self-Assembled, Nacre-Inspired, High-Performance Materials with Tunable Nanoscale Periodicities. *ACS Appl. Mater. Interfaces* **2013**, *5* (9), 3738–3747. https://doi.org/10.1021/am400350q.

(11)    Guo, H.; Zhao, H.; Niu, H.; Ren, Y.; Fang, H.; Fang, X.; Lv, R.; Maqbool, M.; Bai, S. Highly Thermally Conductive 3D Printed Graphene Filled Polymer Composites for Scalable Thermal Management Applications. *ACS Nano* **2021**, *15* (4), 6917–6928. https://doi.org/10.1021/acsnano.0c10768.

(12)    Putz, K. W.; Compton, O. C.; Palmeri, M. J.; Nguyen, S. B. T.; Brinson, L. C. High-Nanofiller-Content Graphene Oxide-Polymer Nanocomposites via Vacuum-Assisted Self-Assembly. *Adv. Funct. Mater.* **2010**, *20* (19), 3322–3329. https://doi.org/10.1002/adfm.201000723.

(13)    Wu, L.; Ohtani, M.; Takata, M.; Saeki, A.; Seki, S.; Ishida, Y.; Aida, T. Magnetically Induced Anisotropic Orientation of Graphene Oxide Locked by in Situ Hydrogelation. *ACS Nano* **2014**, *8* (5), 4640–4649. https://doi.org/10.1021/nn5003908.

(14)    Kochumalayil, J. J.; Morimune, S.; Nishino, T.; Ikkala, O.; Walther, A.; Berglund, L. A. Nacre-Mimetic Clay/Xyloglucan Bionanocomposites: A Chemical Modification Route for Hygromechanical Performance at High Humidity. *Biomacromolecules* **2013**, *14* (11), 3842–3849. https://doi.org/10.1021/bm400883e.

(15)    Li, J.; Liu, X.; Feng, Y.; Yin, J. Recent Progress in Polymer/Two-Dimensional Nanosheets Composites with Novel Performances. *Prog. Polym. Sci.* **2022**, *126*, 101505. https://doi.org/10.1016/j.progpolymsci.2022.101505.

(16)    Hegde, M.; Yang, L.; Vita, F.; Fox, R. J.; van de Watering, R.; Norder, B.; Lafont, U.; Franceschangeli, O.; Madsen, L. A.; Picken, S. J.; Samulski, E. T.; Dingemans, T. J. Strong Graphene Oxide Nanocomposites from Aqueous Hybrid Liquid Crystals. *Nat. Commun.* **2020**, *11* (1), 830–830. https://doi.org/10.1038/s41467-020-14618-0.

(17)    Sanchis, M. J.; Carsí, M.; Culebras, M.; Gómez, C. M.; Rodriguez, S.; Torres, F. G. Molecular Dynamics of Carrageenan Composites Reinforced with Cloisite Na+ Montmorillonite Nanoclay. *Carbohydr. Polym.* **2017**, *176*, 117–126. https://doi.org/10.1016/j.carbpol.2017.08.012.

(18)    Ebina, T.; Mizukami, F. Flexible Transparent Clay Films with Heat-Resistant and High Gas-Barrier Properties. *Adv. Mater.* **2007**, *19* (18), 2450–2453. https://doi.org/10.1002/adma.200700162.

(19)    Wan, C.; Qiao, X.; Zhang, Y.; Zhang, Y. Effect of Different Clay Treatment on Morphology and Mechanical Properties of PVC-Clay Nanocomposites. *Polym. Test.* **2003**, *22* (4), 453–461. https://doi.org/10.1016/S0142-9418(02)00126-5.

(20)    Wan, C.; Chen, B. Reinforcement and Interphase of Polymer/Graphene Oxide Nanocomposites. *J. Mater. Chem.* **2012**, *22* (8), 3637–3646. https://doi.org/10.1039/C2JM15062J.

(21)    Gao, W.; Wang, M.; Bai, H. A Review of Multifunctional Nacre-Mimetic Materials Based on Bidirectional Freeze Casting. *J. Mech. Behav. Biomed. Mater.* **2020**, *109*, 103820. https://doi.org/10.1016/j.jmbbm.2020.103820.

(22)    Doblhofer, E.; Schmid, J.; Rieß, M.; Daab, M.; Suntinger, M.; Habel, C.; Bargel, H.; Hugenschmidt, C.; Rosenfeldt, S.; Breu, J.; Scheibel, T. Structural Insights into Water-Based Spider Silk Protein-Nanoclay Composites with

**4**

Excellent Gas and Water Vapor Barrier Properties. *ACS Appl. Mater. Interfaces* **2016**, *8* (38), 25535–25543. https://doi.org/10.1021/acsami.6b08287.

(23)        Shi, G.; Araby, S.; Gibson, C. T.; Meng, Q.; Zhu, S.; Ma, J. Graphene Platelets and Their Polymer Composites: Fabrication, Structure, Properties, and Applications. *Adv. Funct. Mater.* **2018**, *28* (19), 1706705. https://doi.org/10.1002/adfm.201706705.

(24)        Kim, H.; Abdala, A. A.; Macosko, C. W. Graphene/Polymer Nanocomposites. *Macromolecules* **2010**, *43* (16), 6515–6530. https://doi.org/10.1021/ma100572e.

(25)        Suter, J. L.; Groen, D.; Coveney, P. V. Mechanism of Exfoliation and Prediction of Materials Properties of Clay–Polymer Nanocomposites from Multiscale Modeling. *Nano Lett.* **2015**, *15* (12), 8108–8113. https://doi.org/10.1021/acs.nanolett.5b03547.

(26)        Kakuta, T.; Baba, Y.; Yamagishi, T.; Ogoshi, T. Supramolecular Exfoliation of Layer Silicate Clay by Novel Cationic Pillar [5] Arene Intercalants. *Sci. Rep.* **2021**, *11* (1), 1–9. https://doi.org/10.1038/s41598-021-90122-9.

(27)        Zhang, Y.; Wang, S.; Tang, P.; Zhao, Z.; Xu, Z.; Yu, Z.-Z.; Zhang, H.-B. Realizing Spontaneously Regular Stacking of Pristine Graphene Oxide by a Chemical-Structure-Engineering Strategy for Mechanically Strong Macroscopic Films. *ACS Nano* **2022**, *16* (6), 8869–8880. https://doi.org/10.1021/acsnano.1c10561.

(28)        De Jeu, W. H. *Basic X-Ray Scattering for Soft Matter*; Oxford University Press, 2016.

(29)        van Es, M. A. Polymer-Clay Nanocomposites : The Importance of Particle Dimensions. PhD thesis, Delft University of Technology, 2001.

(30)        Holder, C. F.; Schaak, R. E. Tutorial on Powder X-Ray Diffraction for Characterizing Nanoscale Materials. *Acs Nano* **2019**, *13* (7), 7359–7365.

(31)        Zlopasa, J.; Norder, B.; Koenders, E. A. B.; Picken, S. J. Origin of Highly Ordered Sodium Alginate/Montmorillonite Bionanocomposites. *Macromolecules* **2015**, *48* (4), 1204–1209. https://doi.org/10.1021/ma502147m.

(32)        Panzavolta, S.; Gioffrè, M.; Bracci, B.; Rubini, K.; Bigi, A. Montmorillonite Reinforced Type A Gelatin Nanocomposites. *J. Appl. Polym. Sci.* **2014**, *131* (11), 1–6. https://doi.org/10.1002/app.40301.

(33)        H. J. Kouwer, P.; F. Jager, W.; J. Mijs, W.; J. Picken, S. The Nematic Lateral Phase: A Novel Phase in Discotic Supramolecular Assemblies. *Macromolecules* **2001**, *34* (22), 7582–7584. https://doi.org/10.1021/ma011007j.

(34)        Pelc, D.; Marion, S.; Požek, M.; Basletić, M. Role of Microscopic Phase Separation in Gelation of Aqueous Gelatin Solutions. *Soft Matter* **2014**, *10* (2), 348–356. https://doi.org/10.1039/c3sm52542b.

(35)        Rao, Y. Q. Gelatin-Clay Nanocomposites of Improved Properties. *Polymer* **2007**, *48* (18), 5369–5375. https://doi.org/10.1016/j.polymer.2007.06.068.

(36)        Zheng, J.; Gao, S.; Li, H.; Yao, K. Effects of Reaction Conditions on Intercalation between Gelatin and Montmorillonite: Thermodynamical Impact. *J. Appl. Polym. Sci.* **2013**, *128* (1), 54–59. https://doi.org/10.1002/app.38129.

(37)        Xu, S. W.; Zheng, J. P.; Tong, L.; De Yao, K. Interaction of Functional Groups of Gelatin and Montmorillonite in Nanocomposite. *J. Appl. Polym. Sci.* **2006**, *101* (3), 1556–1561. https://doi.org/10.1002/app.23435.

(38)        Novikov, D. V.; Krasovskii, A. N. Density-Density Correlations on a Gelatin Films Surface. *Phys. Solid State* **2012**, *54* (8), 1688–1692. https://doi.org/10.1134/S1063783412080239.

(39)        Zheng, J. P.; Xi, L. F.; Zhang, H. L.; Yao, K. D. Correlation between Reaction Environment and Intercalation Effect in the Synthesis of Gelatin/Montmorillonite Hybrid Nanocomposite. *J. Mater. Sci. Lett.* **2003**, *22* (17), 1179–1181. https://doi.org/10.1023/A:1025332029976.

(40)        Fernandez, J. J.; Torres, T. E.; Martin-Solana, E.; Goya, G. F.; Fernandez-Fernandez, M. R. PolishEM: Image Enhancement in FIB-SEM. *Bioinformatics* **2020**, *36* (12), 3947–3948. https://doi.org/10.1093/bioinformatics/btaa218.

(41)        Yoshizawa, A.; Kato, Y.; Sasaki, H.; Takanishi, Y.; Yamamoto, J. Optically Isotropic Homochiral Structure Produced by Intercalation of Achiral Liquid Crystal Trimers. *J. Phys. Chem. B* **2016**, *120* (21), 4843–4851.

**4**

# 5

# Hydrogel affine deformation alignment in bioinspired nanocomposites

*"It is not the strongest of the species that survives,*

*not the most intelligent that survives.*

*It is the one that is the most adaptable to change."*

*– Charles Darwin*

# Hydrogel affine deformation alignment in bioinspired nanocomposites

## Abstract

*Tailoring order in hierarchical structures is a key goal of bioinspired nanocomposite design. Recently, nacre-like materials have been developed by solvent evaporation methods that are scalable and attain advanced functionalities. However, understanding the alignment mechanisms of 2D-fillers, nanosheets or platelets, remains challenging. This work explores the possible pathways for nanocomposite ordering via orientation distribution functions. We demonstrate how the immobilization of 2D-materials via a (pseudo)-network formation is crucial to alignment based on evaporation. We show a modified affine deformation model that describes such evaporative methods. In this, a gel network develops enough yield stress and uniformly deforms as drying proceeds, along with the immobilized particles, causing in-plane orientation. Herein, we tested the dominance of this approach by using a thermo-reversible gel for rapid montmorillonite (MMT) particle fixation. We researched gelatin/MMT as a model system to investigate the effects of high loadings, orientational order, and aspect ratio. The nacre-like nanocomposites showed a semi-constant order parameter ($<P_2>$ ~0.7) over increasing nanofiller content up to 64 vol.% filler. This remarkable alignment resulted in continuously improved mechanical and water vapor barrier properties over unusually high filler fractions. Some variations in stiffness and diffusion properties were observed, possibly correlated to the applied drying conditions of the hybrid hydrogels. The affine deformation strategy holds promise for developing next-generation advanced materials with tailored properties even at (very) high filler loadings. Furthermore, a gelling approach offers the advantages of simplicity and versatility in the formulation of the components, which is useful for large-scale fabrication methods.*

5
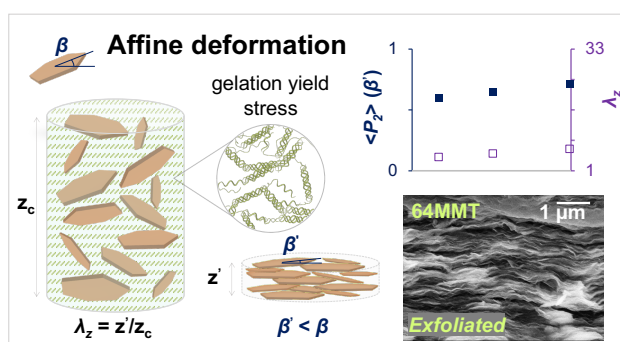
## 5.1. Introduction

The precise control and prediction of order in nanocomposite materials remain a crucial objective in the design of advanced nanomaterials. In recent years, materials inspired by the hierarchical structures found in nature gained substantial popularity.[1–3] Many methodologies have emerged trying to translate to man-made materials the exceptional property profiles of naturally formed hierarchical structures, such as the ones found in wood, bone, enamel, and nacre.[4–8] In particular, the thermal, mechanical, and permeability properties of in-plane oriented nacre-like materials have been intensively investigated.[9] Nacre is found in the inner shell of mollusks and mussels. Their main feature to be reproduced is the "brick-and-mortar" microstructure, where a high content of mineral aragonite tablets (95 wt.%) is decorated by an elastic organic biopolymer. This architecture results in many intriguing properties, from good polymer adhesion to distinct structural colors.[9,10] In turn, polymer nacre-like materials are lightweight and combine multiple properties, like high stiffness and toughness, via synergistic effects acting between the components of the composite. Good gas barrier properties have also been reported for these composites, which are again linked to the high in-plane orientation of well-distributed platelets.[11,12] Material optimization has been based on tailoring components, 2D-materials, and processes for engineering functional and structural applications (membranes, insulators, electromagnetic shielding material, sensing, biomedical, and aerospace devices, etc.).[2,6,13] However, an in-depth understanding of the possible alignment mechanisms in place would facilitate the successful application of the structure-property relationships found in highly ordered nanocomposites. Especially considering the scalability of the alignment method, it becomes a necessity to better understand the mechanism of alignment.

First, it is important to realize that the 2D-fillers in bioinspired composites will have consolidated order structures determined by the mobility in the environment they are produced. The layered "brick-and-mortar" structures are realized by a *dynamic* interplay of soft and hard phases. Ordered nacre-like materials are usually made from suspension/melt mixing or *in-situ* approaches.[14,15] For instance, they are produced via casting[16,17], vacuum filtration[18], and layer-by-layer assembly (L-b-L)[19,20] methods to achieve high-performance materials.[9] For some years now, a major development has been the implementation of water-based nanocomposites and large-area fabrication via solvent evaporation, akin to paper-making[18,21–23]. After that, building block formation, including cross-linking techniques and drying conditions, has been extensively optimized to realize nano- and mesoscopic assemblies of clay silicates, (reduced) graphene oxide,

**5**

MXenes, boron nitride, dichalcogenides, etc.[22,24–28] Most reports follow the rationale that a polymeric core-shell formation and subsequent particle alignment by directed or evaporative self-assembly mechanism preserve the high aspect ratio of platelet or sheet fillers.[7,8,18] However, the colloidal ordering principle is seldom explained nor explored in any detail. Some point out excluded volume associations[18,29,30], as in an Onsager-like treatment[31]. In any case, better criteria should be used to evaluate the structural ordering, ideally with the evaluation of an orientational distribution function (ODF).[15,24,32,33]

The role of the preferential orientation of 2D-materials on the properties of a wide range of composites is well-established.[30] In traditional particle-reinforced polymer composites, orientational order is usually studied by fitting a distribution function over experimental structural data, such as crystallite diffraction patterns. Unfortunately, unlike in nacre mimetics, this essentially covers composites with low filler loading[10] – up to 5 vol.%. This work focuses on a new perspective and strategy for the structural ordering of lamellar nanocomposites up to high loadings. We consider a common waterborne system in which an entangled network or hydrogel formation rapidly restricts 2D-nanofiller mobility. In particular, the effect of a frozen-in environment on the composite alignment is evaluated. The ordered nanostructures are tested over a wide range of 2D-nanofiller fractions, surpassing the polymer content and going into the highly confined polymer regime. Since we aim to understand the underlying dynamics of alignment in nacre-like lamellar systems, we scrutinize the consistency of an ODF, the modified affine deformation model, to describe each produced hydrogel system. This is of special importance in identifying the triggers to structural ordering and associated mechanical and transport property enhancement. Despite the focus on 2D-nanomaterials and nacre-inspired research, we expect this to extend to other types of grain morphologies (tubes, rods, and short fibers) and other solvent systems. Our theoretical perspective on nanoparticle movement restriction in waterborne methods should also be relevant to industrial scalability. In general, a network-based orientation should allow for less energy- and time-intensive methods. More importantly, meticulous control of preferred hierarchical ordering is crucial to the development of consistent large-area and large-volume manufacturing.

In summary, our study attempts to shed light on the alignment mechanism of nacre-like materials and providing insight into the design and optimization of high-load advanced nanomaterials with improved properties.

5

## 5.2. Orientation model

Several high aspect ratio 2D-nanofillers can reinforce and functionalize composite materials with "brick-and-mortar" structures. Even though numerous studies have proved that highly anisotropic nacre-inspired structures develop from initially isotropic hydrocolloidal suspensions, the exact orientation mechanism is often unsolved. Here, we will first explore the assumptions for a certain nano-structuration and possible alignment mechanisms (self-assembly *vs.* affine deformation). Next, we apply this to a hydrogel model system that should be ruled by affine deformation. In this, we research the influence on properties of parameters that are crucial to structural ordering, *i.e.*, the 2D-nanomaterial concentration, aspect ratio, and average order parameter, *e.g.*, $<P_2>$. The variables involved are extensively explored to establish how they influence the anisotropic mechanical stiffness and gas permeability properties of the nanocomposite. The main goal is to test the affine deformation alignment strategy up to very high loadings using facile fabrication methods.

### 5.2.1. 2D-nanocomposite alignment

Figure 5.1 classifies current waterborne nacre-like composite fabrication methods as mechanisms driven by self-assembly or affine deformation. Many nacre-inspired reports have focused on optimizing precursors and conditions via L-b-L deposition or a so-called self-assembly mechanism. Nevertheless, the required conditions for forming 2D-material assemblies must be contemplated. In systems where the order is formed through assembly, an externally induced or spontaneous process causes the randomly oriented 2D-materials to align along a preferred axis or director. For instance, a nematic environment can develop by applying an external field or through excluded volume interactions, which depend on a high particle concentration and aspect ratio (Figure 5.1a). The already aligned system is then consolidated by an external field, dense network formation, and/or drying. Only when this happens spontaneously, normally through localized interactions in a mobile phase, should the mechanism be termed self-assembly. Typical examples are thermotropic or lyotropic liquid crystal formation.[34] In such composites, the orientational distribution function is usually quite well described by a mean-field theory, *i.e.*, either the Maier-Saupe or the Onsager models.[31,35,36] Theoretically, Onsager-like nematic phases could develop from repulsion between the hard-core nanoparticles. However, it is fair to assume that most accounts on nacre-like materials do not exceed the required critical particle concentration. Usually, the lyotropic particles

described by Onsager's formula have a monodisperse character, a trait not so easily found in the employed 2D-nanoparticles. On the other hand, the Maier-Saupe model (eq 1) was initially proposed based on soft-core attraction forces. The theory assumes a molecular or particle long-range distribution that determines a nematic mean-field potential or influence on the basal angle of an individualized particle. The Maier-Saupe model might be considered for the specific cases of an externally directed flow (*e.g.*, electromagnetic polarization) or a very controlled L-b-L deposition. Nevertheless, both Onsager and Maier-Saupe ODFs functions will adopt a Gaussian shape at a high level of orientational order (high $<P_2>$).[37] A point often overlooked is that the nanoparticles can frequently get immobilized in a hydrogel or entangled network, in which case one must exclude the possibility of them further aligning via mean-field spontaneous self-assembly.

We have previously implemented an alternative theoretical framework to waterborne nacre-like nanocomposites, *e.g.*, based on nanoclay, graphene, or calcite.[15,24,32] The modified affine deformation model (eq 2) describes an orientation mechanism in which a (pseudo)network is formed in the matrix phase, developing enough yield stress to immobilize the nanoparticles while drying (Figure 1b). Here, the word affine infers that the local deformation is the same as the deformation in the global system, a term adapted from studies of the junction networks in ideal rubbers (Kuhn and Grun, 1942[38]). A uniform gelling matrix shrinkage drives in-plane alignment to the entrapped particles. More specifically, the structural ordering is controlled by the drying-induced vertical strain ($\lambda_z$) experienced by the network. One advantage of such mechanism comes from nanoparticle immobilization with the aid of an appropriate matrix solvent, thus, initially preventing loss of filler aspect ratio. This translates to nanostructures that are effectively exfoliated/intercalated and well-aligned[39], which is crucial for final material properties, *e.g.*, gas transport and mechanical properties. Even though this mechanism serves as a separate nacre-inspired strategy, many studies have resulted in a similar composite preparation method via trial and error. Those include gelation mechanisms and evaporation-induced (EISA) or vacuum-assisted self-assembly (VASA).[8,26,40,41] To name a few, Wu et al. (2014)[23] used an *in-situ* hydrogelation mechanism to lock magnetically-aligned graphene oxide platelets. The orientation mechanism described resulted in functionalized soft-materials with good order parameter values ($<P_2>_{Maier-Saupe}$ = 0.8). Zheng et al. (2020)[42] also reported high-performance bio-composites from chitosan/nanoclay cross-linked by either glutaraldehyde or $Pd^{2+}$ cations in water. Thus, cross-linking agents should also result in affine deformation of network-embodied nanoplatelets. Recently, Zhou et al. (2022) combined an oil-spreading shear-flow

alignment of alginate/MXene with divalent ion-induced cross-linking. This fast hydrogelation efficiently immobilized the aligned 2D-filler in the matrix before dry-settling, resulting in outstanding mechanical properties (elastic modulus 60 GPa). As shown above, the affine deformation mechanism can be an effective pathway to attain very highly oriented structures in nanocomposites, but it has mostly been explored implicitly.
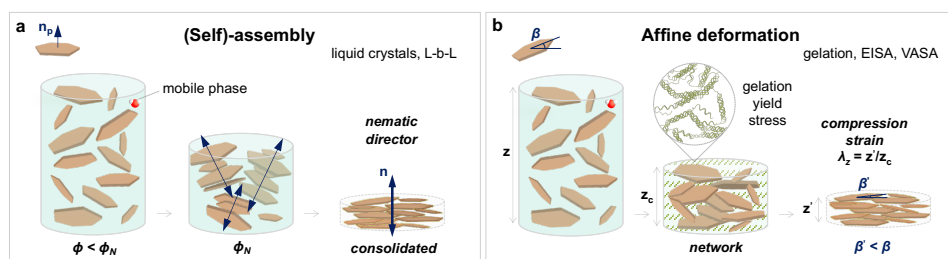


**Figure 5.1.** Schematic illustration of the nacre-inspired nanocomposites preparation via (self)-assembly methods (a), such as liquid crystals and layer-by-layer (L-b-L), or hydrogel affine deformation methods (b), such as gelation, evaporation-induced self-assembly (EISA), and vacuum-assisted self-assembly (VASA). In assembly mechanisms (a), starting at the critical concentration, $\phi_N$, a preferred orientation of particles with respect to the film plane develops and the nematic-like uniaxially aligned structure is consolidated by solvent removal. In affine deformation (b), yield stress builds from network formation or (pseudo)gelation and immobilizes the 2D-particles until the composite is fully immobilized by solvent evaporation (critical concentration represented by gel height $z_c$). The vertical strain, $\lambda_z$, is the factor that induces the orientational order in (b). This strain is assumed to result in an affine compression, *i.e.*, the local deformation is equal to the global deformation. The average angle between platelet and film normal, $\beta$, decreases with particle alignment either by excluded volume (a) or shrinkage (b) effects.

## 5.2. Materials and Methods

### 5.2.1. Chemicals

Porcine skin gelatin (Type A, 78-80 mM free COOH/100 g protein, 50,000−100,000 Da, gel strength 300, relative density 1.3 g cm$^{-3}$), MgCl$_2$ and KNO$_3$ were purchased from Sigma Aldrich and used as is. Sodium montmorillonite (Na-MMT), CLOISITE-Na$^+$, with D$_{50}$ particle size <25 μm, basal spacing d$_{001}$ of 11.7 Å, and density 2.86 g cm$^{-3}$ was obtained from BYK Chemie GmbH, Germany, and used without purification or surface treatment.

The platelet aspect ratio (length over thickness) of this dispersed Na-MMT is commonly reported within the range of 10 to 1000 nm but is typically 100-500 nm. The Na-MMT thickness is 1 nm. We have indirectly measured, via focused ion beam scanning electron microscopy (FIB-SEM), the average length of 212 ± 97 nm of dispersed nanoparticles in composite cross-section.[39] All chemicals used were of analytical grade.

## 5.2.2. Fabrication of nacre-inspired nanocomposites

The fabrication of nacre-like gelatin/MMT composites was done according to our previously reported method.[39] In short, a warm pre-dispersed MMT suspension (3 w/v %) was added to a hot gelatin A solution (3 w/v %, 50 °C) according to the desired MMT volume fractions. Film-forming suspensions of protein/clay were prepared by vigorously mixing wet ratios at 70 °C. The pH of stock and film forming solution was monitored. The dispersion was carefully poured into a polystyrene petri dish and dried at ambient conditions to form a thin film.

The study aimed at a wide range of filler loadings ranging from 1 to 80 wt. % Na-MMT, on the composite weight basis. In solid-state, this should be equivalent to up to 65 vol.% Na-MMT. This was measured via thermogravimetric analysis (TGA). Throughout this study, the composite clay content is expressed as volume percentage (vol. %). The samples are denoted as $XMMT$, where $X$ is the volumetric MMT fraction percentage in the composite.

For the following characterization analyses, the films were additionally conditioned for a week in a desiccator containing silica gel at room temperature. This step was necessary to ensure there was absence of freely bound water, as the gelatin polymer has a hydrophilic nature.

## 5.2.3. Characterization

### Thermogravimetric analysis (TGA)

The nanocomposite samples were cut to snippets and analyzed using a thermogravimetric analyzer (TGA 8000, Perkin Elmer, USA) from 30 to 900 °C using a heating rate of 10 °C min$^{-1}$. The sample weight was in the range of 4 to 6 mg. Corundum crucibles were used and air as a purge gas at a flow rate of 20 mL min$^{-1}$. The method included isothermal steps at 105 and 900 °C for water removal and final weight

equilibration, respectively. Due to the usage of oxidative environment and negligible ash content of gelatin, the final residue represents the weight percentage of MMT. These concentrations were later converted into vol. % MMT, ranging from 0.4 to 64%.

## Fourier-transform infrared spectroscopy (FTIR)

FTIR spectra were recorded using a Nicolet 6700 (Thermo Fisher Inc., USA) spectrometer from with a frequency range from 4000 to 600 $cm^{-1}$, at resolution of 2 $cm^{-1}$. The acquired spectrum of dry films was an average of 128 scans.

## Flame resistance test

The resistance of films to flame exposure using a (propane/butane) blue oxidizing torch was tested. When possible, the samples were exposed to the flame from both sides of the film until ignition and/or material radiation emission was observed (up to 30 s). Scanning electron microscopy (SEM) images were also taken of the burned specimens. Prior to flame tests the films, the dried films were conditioned for 2 days at 50% RH, RT.

## Scanning electron microscopy (SEM)

The cryo-fractured surface of the film samples was imaged with a JSM-6010LA JEOL (JEOL Ltd, Tokyo, Japan) scanning electron microscope at accelerating voltage of 8 kV and close working distance (7-9 mm). Measurements and image transform analysis of the micrographs were performed by *Gwyddion* software (1D FFT filter).

## Wide-angle X-ray scattering (WAXS)

Wide-angle X-ray scattering was performed using a Bruker AXS D8 Discover with a VÅNTEC 2D detector and using Cu Kα radiation (λ = 1.54184 Å) at 50 kV and 1 mA. A point collimator of 0.3 mm was used, and the sample to detector distance was 30 cm parallel (incident beam at a glancing angle) and perpendicular to the film surface. For basic interpretation and data curation of the X-ray diffraction, Bruker software (DiffracSuite.EVA version 5.1, Bruker, USA) was used. From the obtained 2D-XRD results, the radial integrations and particle dispersion analysis thereof can be found at Espíndola et al. (2023)[39].

## Orientation distribution functions and $<P_2>$ order parameter

The alignment in nacre-like nanocomposites was studied by means of orientation distribution functions. Applying orientation models is useful to understand which alignment mechanisms might be in place. The following functions were fitted to the WAXS azimuthal intensity profile data at maximum intensity region and are well-established for quantifying the orientation order parameter $<P_2>$.

### *Maier-Saupe model*

The Maier-Saupe model describes long-range contributions of a nematic environment on the orientation of a single particle along one direction[35,36]. Thus, the model is often used in liquid crystal theory in the self-assembly of nematic polymeric crystallites. Eq 5.1 describes the shape of the ODF resulting from this model:

$$f(\beta) = I_0 + A e^{\alpha \cos^2(\beta)} \quad (5.1)$$

where $I_0$ is the intensity baseline, $A$ is a normalization constant, $\alpha$ is the width of the curve and is directly related to order parameter $<P_2>$, and $\beta$ is the azimuthal angle.

### *Affine deformation model*

The affine deformation model, originally coming from the field of ideal rubber elongation[38], has been modified to describe orientational order in liquid crystals and composite systems[24,32,55,56]. In an affine deformation, due to cross-linking and development of yield stress, local deformations are equal to global deformations. Therefore, with the model, external deformation forces like shrinkage can be linked to the extent of alignment. Using the modified model, one finds that the orientational order can be developed from particle immobilization, via a (pseudo)network formation, and subsequent vertical consolidation over drying. Eq 5.2 describes the ODF predicted by this model:

**5**

$$f(\beta) = I_0 + A\frac{1}{2}\lambda^2 \frac{\cos^3(\tan^{-1}(\lambda\tan(\beta)))}{\cos^3(\beta)} \qquad (5.2)$$

where $I_0$ is the intensity baseline, $A$ is a normalization constant, $\lambda$ is a degree of (vertical) compression and is directly related to order parameter $<P_2>$, and $\beta$ is the azimuthal angle, which corresponds to the platelet angle with respect to the $z$-axis.

### $<P_2>$ order parameter

The sample degree of orientation derives from the fitted orientation models by calculating the order parameter $<P_2>$, using eq 5.3:

$$\langle P_2 \rangle = \frac{\int_{-1}^{1} P_2(\cos\beta) f(\beta)\ d\cos(\beta)}{\int_{-1}^{1} f(\beta)\ d\cos(\beta)} \qquad (5.3)$$

where $P_2(\cos\beta)$ is a second-order Legendre polynomial of $\cos(\beta)$: $P_2(\cos\beta) = \frac{1}{2}(3\cos^2(\beta) - 1)$. Analytical solutions for the $<P_2>$ calculation have also been previously demonstrated[57]. The fit-optimized values of width $\alpha$ and degree of consolidation $\lambda$ were used for Maier-Saupe and Affine deformation regression functions respectively. For randomly oriented samples $<P_2> = 0$, while for complete anisotropy $<P_2> = 1$. For a liquid crystal nematic phase, $<P_2>$ typical values lie in between 0.3 to 0.7.

The orientation functions were fitted to the experimental data by running code in Python language software and the modules *Scipy* and *Numpy*. Integrals were calculated using the *scipy.integral.quad* built-in function. The regression goodness-of-fit for orientation models was evaluated with reduced chi-squared statistics, where Efron's pseudo-$R^2$ coefficient of regression is reported.

## Dynamic mechanical thermal analysis (DMTA)

Dynamic Mechanical Thermal Analysis (DMTA) was performed on a PerkinElmer DMA-7e (Perkin-Elmer, USA). DMTA experiments were performed in a tensile mode at a frequency of 1 Hz from -50 to 300 °C temperature range at a heat rate of 5 °C min$^{-1}$, with film dimensions of roughly 10.0 x 3.0 x 0.15 mm. The thickness of the films was measured with the aid of a digital micrometer. Prior to this analysis, the films were extensively dried for 1 day at 40 °C.

DMA was also performed at constant temperature (30 °C) but varying relative humidity, using a DMA Q800 (TA Instruments, USA) with a controlled humidity chamber

accessory (HumiSys, InstruQuest Inc., USA). This allowed to monitor the moduli of films at varying humidity or water activity, $a_w$ = 0.01, 0.20, 0.40, 0.60 to 0.90.

To better understand the influence of nanoplatelet addition to mechanics, we used a semi-empiric composite theory taking into consideration the individual contributions of matrix and filler ($<P_2>$ order parameter, aspect ratio, volume fraction, and modulus). The Halpin-Tsai model is widely used to estimate the reinforcement effect of filler in polymer clay composites (Halpin and Kardos (1976))[58] which can be written in the following closed form:

$$E_c = E_m \frac{E_f(1+\zeta\phi)+E_m(\zeta-\zeta\phi)}{E_f(1-\phi)+E_m(\zeta+\phi)} \qquad (5.4)$$

where $E_c$, $E_m$, and $E_f$ are the moduli values of the nanocomposite, matrix, filler, respectively; $\phi$ and $\zeta$ are the volume fraction and shape factor of the filler. The latter depends on filler geometry, orientation, and aspect ratio ($\alpha$). The value for $E_f$ is hereby assumed to be 172 GPa for a perfect mica crystal, based on Shell and Ivey (1989).[59] Since gelatin renaturation was found to be decreasing with filler incorporation, we assumed a $E_m$ value based on a solvent-casted amorphous film (4 GPa).

Based on the filler shape factor, $\zeta$, this model reduces to series or parallel contributions to modulus, which can be used as boundary conditions for real application composites.[47] If the shape factor, and aspect ratio, is much lower than the modulus ratio of the filler and polymer matrix ($\zeta << E_c/E_m$), the model converges to the series model:

$$E_c = \left(\frac{1-\phi}{E_m} + \frac{\phi}{E_f}\right)^{-1} \qquad (5.5)$$

In the opposite case, the filler shape factor, and aspect ratio, is much higher than the modulus of the filler and the polymer matrix ($\zeta >> E_c/E_m$), the Halpin-Tsai model converges to the parallel version:

$$E_c = (1-\phi)E_m + \phi E_f \qquad (5.6)$$

**5**

Using eq 5.4, we can also calculate the effective modulus for composites containing perfectly anisotropic and isotropic platelets. Furthermore, by incorporating the previously obtained order parameter $<P_2>$ values from WAXS we can correct the composite modulus based on orientation applying eq 5.7.[60]

$$E_c = \left( \frac{<P_2>}{E_{\parallel}} + \frac{1-<P_2>}{E_{\perp}} \right)^{-1} \quad (5.7)$$

where $E_{\parallel}$ and $E_{\perp}$ are tensile moduli values of the composite in the radial direction of the platelets (unidirectional) and perpendicular to the platelets (random), respectively. For the moduli components, Van Es et al. (2001)[61] has previously derived the shape factors, $\zeta$, for $E_{\parallel}$ and $E_{\perp}$ to be equal to $2/3\alpha$ and 2, respectively.

## Dynamic water vapor sorption (DVS) and kinetic models

The effect nanoplatelets incorporation on water vapor capacity and kinetics was studied by dynamic water vapor sorption (DVS). DVS was performed in a TA Instruments Q5000 SA (TA Instruments, USA) by measuring the increment in mass from water vapor of the gelatin/MMT films or ground powder. The isotherms were collected by employing a method with 4 steps by varying the water activity ($a_w$) from equilibrated 0.01 to 0.20, 0.40, 0.60, and 0.80. Humidity was maintained in the sample environmental chamber by a laminar flow with a wet-dry vapor mixing at constant flow rate with feedback control. The time at each $a_w$ was iterated until a mass plateau was reached for most samples.

To interpret the water sorption kinetics, we use a Crank derivation to calculate the diffusion coefficient assuming complete Fickian behavior, infinite sheet geometry, and a constant initial concentration throughout the sample and surface[62]:

$$\frac{\Delta M_t}{\Delta M_{inf}} = 1 - \frac{8}{\pi^2} \sum_{n=0}^{\infty} \frac{e^{\left[ \frac{-D(2n+1)^2 \pi^2 t}{4l^2} \right]}}{(2n+1)^2} \quad (5.8)$$

where $\Delta M_t$ and $\Delta M_{inf}$ represent the water mass uptake at time $t$ and at equilibrium, respectively. $D$ is the effective diffusion coefficient over a specific concentration interval, and $l$ is the half thickness of the film.

Nevertheless, there is a lag phase before Fickian diffusion takes place in almost all samples, visualized by a curvature convex to the time axis before the actual Fickian regime. This lag is related to time necessary for attaining equilibrium saturation at the polymer/water-vapor interface ($\tau_S$), what is mostly reported to be a step from

instrumental anomaly and not a material property.[63] Hence, to calculate the diffusion coefficient from these sigmoidal sorption curves we applied exponential time-dependent boundary conditions, including $\tau_S$, derived by Long and Richman (1960)[64]. In addition, anomalous non-Fickian relaxations are also possible within the gelatin/MMT system due to morphological changes. Hence, the used solution of a time-dependent term coupled to the Fickian expression is given by the expressions 5.9a-b, with a non-Fickian term as proposed by Berens and Hopfenberg (1978)[63]. The original Fickian term is recovered if $\tau_S$ = 0 and $\tau_R$ tends to $\infty$.

$$M_t = M_{inf}\left[\phi_F\left(\frac{\Delta M_t}{\Delta M_{inf}}\right) + (1-\phi_F)(1-e^{-\frac{t}{\tau_R}})\right] \qquad (5.9a)$$

$$\frac{\Delta M_t}{\Delta M_{inf}} = 1 - e^{-\frac{t}{\tau_S}}\sqrt{\frac{D\tau_S}{l^2}}\tan\sqrt{\frac{l^2}{D\tau_S}} - \frac{8}{\pi^2}\sum_{n=0}^{\infty}\frac{e^{\left[\frac{-D(2n+1)^2\pi^2 t}{4l^2}\right]}}{(2n+1)^2\left\{1-(2n+1)^2\left[\frac{D\pi^2\tau_S}{4l^2}\right]\right\}} \qquad (5.9b)$$

where $\Delta M_t$ and $\Delta M_{inf}$ represent the water mass uptake at time $t$ and at equilibrium, respectively. $D$ is the effective diffusion coefficient, and $l$ is the half thickness of the film. $\tau_S$ is the characteristic time for attaining saturation at the polymer/water-vapor interface, what is mostly reported to be a step from instrumental anomaly and not a material property. The time $\tau_R$ is related to non-Fickian relaxations and is separated from the Fickian phenomena by the weighing factor $\phi_F$. Curve fitting was done in Python language software and the initial boundaries for $D$ parameter were set to match the Fickian slope in linear region (normalized mass uptake over $t^{0.5}$).

A reduction in diffusion coefficient is attributed to the tortuous path imposed to the penetrating water vapor by the incorporation of high aspect ratio platelets.[65,66] Hence, it can be directly linked to the nanostructure in composites and effective filler aspect ratio. A few models have been in use to describe the effects of incorporating impenetrable platelets to diffusion, based on concentration, aspect ratio, overlapping and order.[60] Nielsen (1967)[65] defined a simple model by assuming perfectly oriented and overlapped monodisperse platelets:

$$\frac{D_c}{D_m} = \frac{1-\phi}{1+\frac{1}{2}\alpha\phi} \qquad (5.10)$$

where $D_c$ and $D_m$ represent, respectively, the diffusion coefficient of composite and matrix, $\alpha$ is the width to thickness aspect ratio, and $\phi$ is the volume fraction of platelets.

To include the effect of orientational order on diffusion, via order parameter, we use the modified Nielsen model proposed by Bharadwaj (2003)[66]:

$$\frac{D_c}{D_m} = \frac{1-\phi}{1+\frac{1}{2}\alpha\phi\frac{2}{3}(<P_2>+\frac{1}{2})} \qquad (5.11)$$

where $D_c$ and $D_m$ represent, respectively, the diffusion coefficient of composite and matrix, $\alpha$ is the width to thickness aspect ratio, $\phi$ is the volume fraction of platelets, and $<P_2>$ is the composite order parameter, *e.g.*, calculated from affine deformation ODF.

In addition, other descriptive models were investigated, *i.e.,* Cussler[67], Fredrickson[54], Brydges[68], and modified Brydges[53].

### Differential scanning calorimetry (DSC)

Differential scanning calorimetry (DSC) experiments were performed to characterize the thermal behavior of nanocomposites. First, film snippets were acclimated to different relative humidity environments (0, 33, 93 %RH) using silica gel and saturated salt solutions ($MgCl_2$, $KNO_3$). The water uptake capacity at the end of two weeks was also measured gravimetrically. The DSC method consisted of heating the sample from -50 to 150 °C, at rate of 3 °C $min^{-1}$, on a PerkinElmer Diamond instrument with two 1 g furnaces and calibrated with indium. Nitrogen gas was used to purge the thermal analyzer at 50 mL $min^{-1}$. Stainless steel pans with o-ring seals were used for hermetically encapsulating the equilibrated samples (20 mg). An identical empty reference pan was used. The pans were sealed according to supplier instructions (PerkinElmer). Data visualization was carried out by *Python* script, in which the *y*-axis refers to endothermic transitions. Each thermogram was analyzed for the melting (or denaturation) event.

## 5.3. Results and Discussion

### 5.3.1. Characterization of hydrogel-based nanocomposites

According to this concept, our experimental design starts with selecting a compatible and versatile nacre-like hydrogel system. Due to the thermal transitions in gelatin (type A) and the high aspect ratio of the montmorillonite (Na-MMT), we have chosen the well-miscible gelatin/MMT composites to study this theory. In conjunction to that, we have explored the possibility of high loadings, going as far as 80 wt.% MMT composite fraction. We can control the mobility and total strain applied on both nanoplatelets and gelling matrix during film casting through simple solvent evaporation. In theory, we test the

effect of a (uniform) network deformation using a thermo-reversible gel for rapid 2D-particle immobilization as the exfoliated suspension cools to room temperature.

The gelatin/MMT nanocomposite films were easily fabricated under ambient conditions. The exact MMT composition content was confirmed by thermogravimetric analysis (TGA, Figure 5.2a), and the MMT volume fraction $X$ is herein abbreviated as $X$MMT. The thermal stability and degradation behavior were observed an under oxidative atmosphere. Figure 5.2b shows composites' thermal mass loss derivative curves, DTG, close to the gelatin oxidative pyrolysis interval. We observe the main degradation of gelatin around 340 °C, in which the DTG intensity represents the degradation rate. We note that the DTG intensity decreased with increasing MMT loadings. This is likely from the lower polymer mass; however, gas entrapment is also expected.

In Figure 5.2c, the FTIR spectrograph is shown for the gelatin and gelatin/MMT composite dry films. We can observe in the gelatin amide region (1800 to 1000 cm$^{-1}$) an overall reduction of amide absorption bands (C=O stretching at 1635 cm$^{-1}$, N-H deformation and C-N stretching at 1539 cm$^{-1}$ and 1226 cm$^{-1}$) with increasing nanoclay fractions. This might indicate strong protein-nanoclay associations, imparting changes in the gelatin triple helix supramolecular structures. A relatively steady increase in the inorganic MMT peak is also observed around 1000 cm$^{-1}$ (stretching of Si–O and Al–O). Up to high loadings, 64 vol.% MMT, we observe no aggregation phenomena, and a uniform dense lamellar structure is observed via cross-sectional SEM (Figure 5.2d and Figure 5.3d-f). In fact, the composites show a nacre-like structure in which MMT platelets are oriented perpendicular to the direction of hydrogel drying. In addition, our previous WAXS and FIB-SEM analysis shows that the polymer is homogeneously distributed within the lamellae, resulting in exfoliated nanostructures.[39]

A flame resistance test was performed for a few nanocomposites after 50% RH equilibration, Figure 5.2e and Figure S5.5. This test provides a rapid way to assess nanocomposite flame retardancy. The unfilled gelatin A film instantaneously melts and produces smoke. On the other hand, as expected from clay-based materials, the composite with very high filler loading keeps its integrity even after very high-temperature exposure (~1000 to 1970 °C) while not producing smoke. The flame exposure causes a spot of blackbody radiation glow from the front side (red spot), while that is almost not detected from the rear side, indicating an enormous thermal gradient in the sample in the order of 3000 K/mm (Figure S5.5). We also note that the gelatin/MMT nanocomposites possess a beneficial intumescent behavior, as supported

**5**

by the SEM of the char, where the film expands to a mesoporous structure but sinters to a structurally similar (lamellae) material. The films were around 0.1 to 0.2 mm thick, and the volumetric expansion is related to the localized formation of $CO_2$, $CO$, and $H_2O$ gases from the organic fraction decomposition. The non-flammability and heat-shield behavior presumably must come from a high level of orientation in the system at high loading, which diminishes the oxygen and low molar mass volatile component's diffusion through the films.
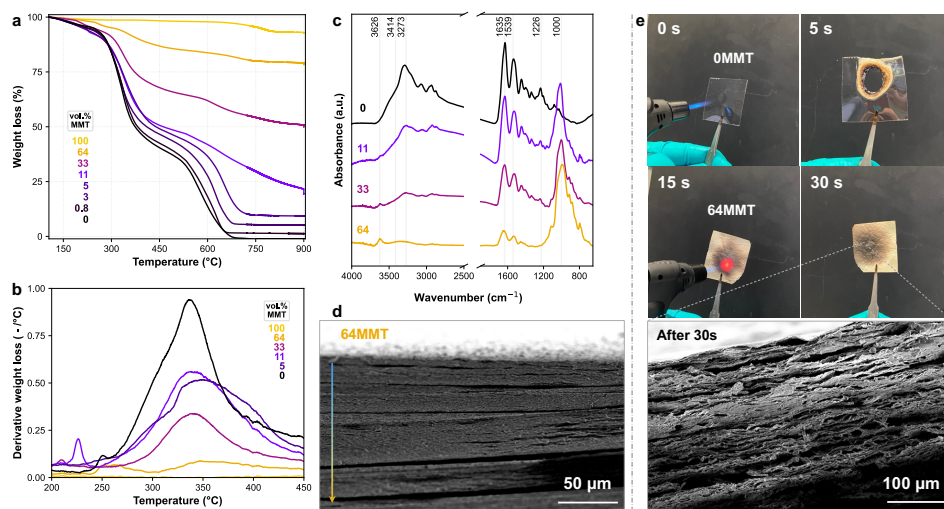


**Figure 5.2.** Characterization of nacre-inspired nanocomposites of gelatin/MMT cast from 3 wt.% suspensions. (a) TGA scan of neat gelatin type A (black), clay-based composites up to high volume fraction (64 vol.%), and pure clay (bright yellow). (b) The respective DTG for the same film materials at gelatin oxidative pyrolysis interval. (c) FTIR spectra of dried neat gelatin type A (black) and clay-based composites. (d) SEM cross-section image of gelatin/MMT composite with high loading shows homogenous lamellar structure without clay aggregates (arrow indicates the film drying direction). (e) Oxidizing flame test of the gelling matrix and 64 vol.% MMT composite (thickness 0.1 mm), including cross-sectional SEM after burning.

## 5.3.2. Origin of high orientational order

An orientation distribution function is a suitable tool to investigate which alignment mechanism is in place. In natural clay-rich materials, like shale rock or soil crust, ODFs are also fitted to X-ray scattering data to obtain the degree of "single platelet" orientation.[33] Clay system coordinates are usually defined by a frame coinciding with the

axis of symmetry (*i.e.*, the *z*-axis in Figure 5.1). The orientation distribution function describes the probability density that a particle is found between stepwise-changing orientations, defined over the platelet basal angle (*i.e.*, *β* angle in Figure 5.1). The ODF applied to this angular framing is analyzed as an infinite series of Legendre's polynomial functions or momenta. It is common to limit the extent of orientation analysis to the second moment $<P_2>$ (eq 3), also known as "Hermans orientation factor f" or "the order parameter S". For a perfectly aligned material, it should be that $<P_2>=1$, and for a perfectly isotropic material, $<P_2>=0$.

From the preferred orientation of MMT nanoplatelets, the X-ray [001] reflection can be evaluated as a function of the azimuthal angle. The development of [001] features in WAXS analysis at a glancing angle of the film surface, perpendicular to the drying direction, confirms the orientational order at the nanoscale (see Figure S5.2). When the analysis is performed perpendicular to the film surface, parallel to the drying direction, we observe an absence of features, indicating axial symmetry (Figure S5.2). The integrated azimuthal profiles at the highest intensity are fitted to the Maier-Saupe and affine deformation ODFs (Figure 5.3a-c). Due to X-ray instrument broadening effects, we fitted the affine deformation convoluted to a Gaussian function (Figure S5.3). The modified affine deformation model well describes the azimuthal intensity profiles of the films (Efron's pseudo-$R^2$ values > 0.96 and lower chi-squared statistics, Table 5.1). These results confirm that the anisotropic films result from affine compression during the fibrous network drying phase. Curiously, the neat gelatin also showed a highly layered and smooth microstructure, typical of a brittle material fracture[43] (Supporting Text S5.1, Figure S5.1). The gelatin matrix showed a degree of ordering resulting from aggregates of renatured triple-helices[44]. In addition, fast Fourier transforms (FFTs) of the SEM images also confirmed hierarchical anisotropy in the composites, showing high in-plane microscale orientation (Figure 5.3d-f, insets).

Table 5.1 shows the full width at half maximum (FWHM) coefficients of orientation functions, which are directly related to the order parameter. In affine deformation, the fitted variable $\lambda_z$ represents an equivalent vertical compressive strain. By inverting the value of $\lambda_z$, we have estimated the critical total solid concentration needed for the film-forming suspension to achieve particle immobilization. Generally, the nanocomposites developed yield stress already in the 22% to 11% solids regime. By comparison, intercalated alginate/MMT composites previously showed a critical concentration range for immobilization between 60% to 28% solids for samples with 5 to 50 wt.% MMT respectively[32]. The gelatin/MMT composites were initially cast at 3% solids. If the yield

stress had developed immediately upon casting, the maximum degree of vertical compression should have been 33 ($\lambda_{z\,max}$). The lower experimental $\lambda_z$ values indicates that the hybrid gels were not completely affinely deformed from the outset. A degree of non-affinity is inevitably present in hydrogels and arises from a fibrous filament bending and/or micro inhomogeneities in a determined sample.[45] A variation in gel dynamics was also observed, with the macroscopic gels formed above 11 vol.% MMT seeming to consist of fragmented networks.[39] In addition, these MMT concentrations led to gels that contracted and displayed lower adhesion to the substrate during drying, causing lateral shrinkage. The presence of a radial strain, $\lambda_r$, obviously lowered the amplitude of the uniaxial compression, $\lambda_z$, and the resulting anisotropy (Table 5.1). By analogy, the MMT particles served as tracer particles to the hydrogel affine deformation.

The <$P_2$> order parameter was calculated from the fit parameters extracted from Maier-Saupe (over WAXS) or affine deformation models (over WAXS and SEM) (Figure 5.3h). From WAXS, the <$P_2$>$_{Maier-Saupe}$ values ranged from 0.87 to 0.99 and the <$P_2$>$_{Affine}$ from 0.59 to 0.77. These values are well above the ones found for most oriented composites. Note that, from the theoretical formalism, <$P_2$>$_{Affine}$ values always will be lower than <$P_2$>$_{Maier-Saupe}$. The high order parameter found for filler fractions up to 5MMT may be linked to unresolved WAXS structures (streak features are unresolved a priori), which gives uncertainty in <$P_2$> determination. In general, the absolute values for each nanocomposite are more difficult to compare due to instrument broadening, radial film shrinkage ($xy$-plane), and the influence of high MMT fractions on the smoothness of the particles. Nevertheless, <$P_2$>$_{Affine}$ estimated from the layered microstructures follows a similar trend with nanoclay concentration as for the values calculated from diffraction data. This is clear evidence that the hydrogel compression history is the dominant factor. The overall trend of <$P_2$>$_{Affine}$ up to high MMT loadings (33 to 64MMT) indicates that the degree of orientation was at least maintained (no significant differences can be claimed, $p>0.05$). This semi-constant affine order parameter oscillated around the high value of 0.7.

Notably, ordering can be found at the global meso- and microscales and, simultaneously, at the nanoscale. These two levels of ordering are entirely independent. Hence, ODFs can also show a convoluted signal from an Onsager-like nanoscale orientation (from excluded volume). In our system, it is plausible to interpret this as the cause of change in ODF shape at elevated 2D-filler loadings (Figure S5.3). The Onsager-like orientation mechanism should yield a Gaussian-like function, which is indeed observed in azimuthal profiles above 33MMT fractions. In this, excluded volume interactions inflicted

nanoscale order in the cases of concentrated 2D-nanomaterial. This could be linked to the apparently increasing trend in $<P_2>_{Affine}$ in the high filler region. This observation is made in analogy to the orientation theory commonly applied to nematic liquid crystals. The director field describes the long-range orientation (micro-scale), whereas, at the molecular director level, the structures can be random or oriented from (flow-induced) orientation correlation.[46] Thus, for instance a relatively low level of alignment via affine deformation is possible while locally very highly ordered nanosized 'truncated' domains are formed. This result was highly unexpected, since the hydrogel network should limit nanoparticle mobility, thereby preventing structures to form. Thus, it makes sense to assume that excluded volume interactions are acting at the nanoscale, which ultimately results in a considerable regularity in the particle spacing.

**5**
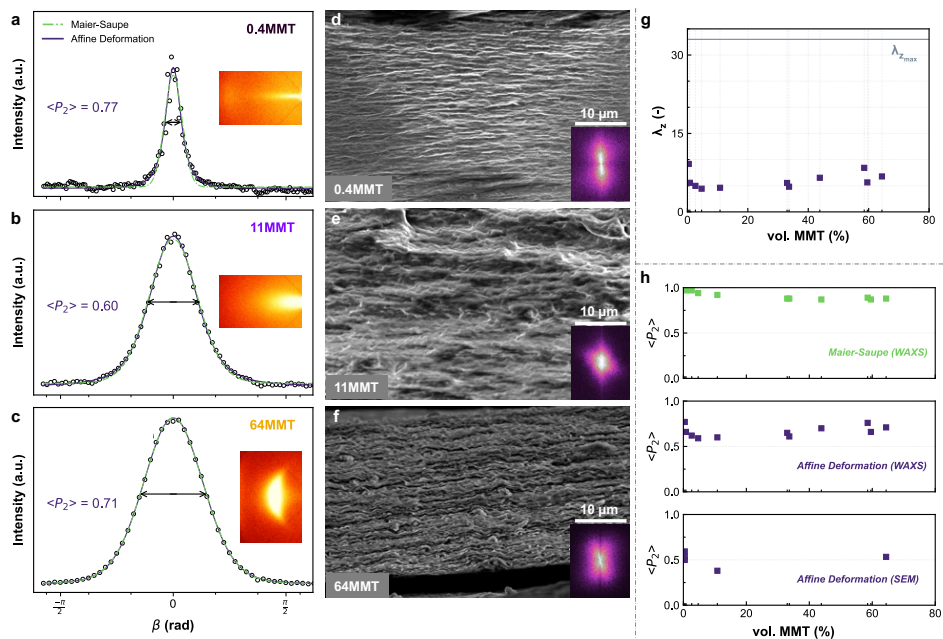
**Figure 5.3.** WAXS showing *001* Bragg reflections, azimuthal intensity profiles of the primary diffraction peak, and calculated orientation distribution functions of affine deformation (dark purple solid lines) and Maier-Saupe (light green dashed lines) for nacre-inspired nanocomposites 0.4MMT (a), 11MMT (b) and 64MMT (c). The $<P_2>$ values depicted in the images were determined via affine deformation ODF. SEM cross-section image of nanocomposites 0.4MMT (d), 11MMT (e) and 64MMT (f), where insets show corresponding fast Fourier transforms (FFT) of the images for peak integration. (g) Degree of compression, $\lambda_z$, obtained via affine deformation fits (WAXS). (h) Order parameter $<P_2>$ values estimated from orientation distribution functions of Maier-Saupe on WAXS data (top), affine deformation on WAXS data (middle), and affine deformation on SEM data (bottom).

**Table 5.1.** Obtained parameters from orientation distribution functions applied to gelatin/MMT azimuthal profiles and effect of final sample geometry on strain

| Sample | Measured radial strain ($\lambda_r{}^2$) | Maier-Saupe | | | Affine Deformation (Gaussian convoluted) | | | | |
|---|---|---|---|---|---|---|---|---|---|
| | | $\alpha$ | RSS | Efron's pseudo-$R^2$ | Vertical strain ($\lambda_z$) | Critical total solids ($100/\lambda_z$, wt.%) | RSS | Efron's pseudo-$R^2$ | Ideal uniaxial strain ($\lambda_{uniaxial}$ $= \lambda_z{}^*\lambda_r{}^2$) |
| 0.4MMT | 1 | 75.7 | 0.308 | 0.946 | 9.2 | 11 | 0.213 | 0.963 | 9.3 |
| 11MMT | 2.2 | 10.2 | 0.015 | 0.997 | 4.6 | 22 | 0.008 | 0.998 | 10.1 |
| 33MMT | 1.3 | 7.0 | 0.005 | 0.9996 | 5.5 | 18 | 0.004 | 0.9996 | 7.2 |
| 64MMT | 1.3 | 6.7 | 0.003 | 0.9998 | 6.8 | 15 | 0.002 | 0.9998 | 9.1 |

$\lambda_r{}^2$: degree of measured area shrinkage or strain in radial direction; $\alpha$: FWHM parameter in Maier-Saupe; $\lambda_z$: vertical strain in z-direction calculated from FWHM parameter in Affine Deformation; $\lambda_{uniaxial}$: expected ideal uniaxial strain via volumetric correction of an incompressible rubber ($\lambda_x\lambda_y\lambda_z = \lambda_r\lambda_r\lambda_z = 1$); RSS: residual sum of squares; Efron's pseudo-$R^2$: fit probabilistic pseudo-$R^2$.

## 5.3.3. Mechanical structure-properties

The gelatin system allowed us to push the system boundaries in MMT loading with highly oriented samples even at 64 vol.% filler. Similar composites fabricated with synthetic polymers traditionally go to low volume fractions, around 0.5 to 5 vol.%, to prevent 2D-particle aggregation.[14,47,48] Only recently, solvent-cast composites with higher loadings, roughly above 30 vol.%, have been presented.[21,22,49] From Figure 5.4, it is evident that the mechanical properties of films are positively affected by an increasing fraction of MMT platelets. In Figure 5.4a, a general increase in thermal stability with MMT fraction is also observed, probably a sign of decreased chain mobility. In addition, the highest fraction, 64MMT, shows clear sintering and high modulus at elevated temperatures (above 240 °C). Probably, the samples went through complete dehydration (denaturation) and browning reaction in the low oxygen atmosphere of testing. The enhanced thermomechanical properties are attributed to a synergetic effect of the highly ordered nacre-like structure and the strong electrostatic interactions between MMT and gelatin

matrix.[44,50] However, the highly ordered alignment of nanoplatelets is the main factor ruling the good mechanical properties, even at elevated humidity (Figures 4a and 4e). We observed a monotonic dependence of dry elastic modulus with clay content all the way to 64 vol.% MMT. We conclude this from the almost perfectly linear reinforcement efficiency of the matrix in the dry state (Figure 5.4b). This exceptional trend in the reinforcement was kept even for the higher ranges of relative humidity (up to 60% RH, Figure 5.4f). In a saturated water environment, the modulus of the gelatin matrix changed dramatically due to solvent plasticization (Figure 5.4e), while this effect is much less pronounced for the highly loaded composites, which kept their mechanical stiffness (Figure 5.4f).

## 5.3.4. Mechanical aspect ratio

The mechanical data is better understood by using the rationale of Halpin Tsai's composite theory. The Halpin Tsai model, eq 4, converges into a series or parallel model by changing the filler shape factor, which depends on geometry, orientation, and aspect ratio. The model converges to a series form if the shape factor is much lower than the modulus fraction composite/matrix due to a low aspect ratio (eq 5). If the aspect ratio is high, the model converges to a parallel rule-of-mixing type of reinforcement (eq 6). In Figure 5.4c, we plot the nanocomposite modulus within the Halpin-Tsai boundaries. The modulus of dry specimens from experimental and order-parameter corrected (eq 7) methods are depicted together. We observed a continuous increase in composite modulus with filler volume fraction. Although, at high loadings, there was a disparity between experimental and actual $<P_2>_{Affine}$-based values. This cannot be attributed to a lowered aspect ratio due to particle stacking, which would have been present in WAXS and SEM data.[39] Since all the composites were exfoliated, the main contribution to modulus should have been the orientational order.

In Figure 5.4d, we monitor the evolution of aspect ratio with particle concentration, back-calculated from Halpin-Tsai (eq 4). We have found at least a two-fold decrease in *effective* aspect ratio, initially predicted ~200 nm. Some decrease was expected since $<P_2>$ is lower than 1. However, this significant decay might be an artifact of gelatin specific binding and indirect MMT-MMT interactions, such as wrinkling phenomena. Hence, $\alpha$ could be interpreted as from the not entire particle but the averaged rigid parts of a nanoplatelet. In accordance with that, we have observed structural undulations due to MMT waviness from multiple data (*e.g.*, Figure 5.3f). The Halpin Tsai equation is based on the filler being

monodisperse and totally rigid, *e.g.*, ceramic discs, being typically demonstrated for low-volume fractions. Thus, based on a degree of 2D-material waviness, the real $E_f$ could decay by at least a factor of 2 or more. This has been observed before in fiber reinforcement, *e.g.*, in aramid fibers, $E_f$ goes from 240 GPa to ~80 GPa due to pleated sheet structure, even when there is a high $<P_2>$.[51,52] Therefore, particularly at low d-spacings as from 33MMT[39], the Halpin Tsai model couples the effects of high filler concentrations with aspect ratio.
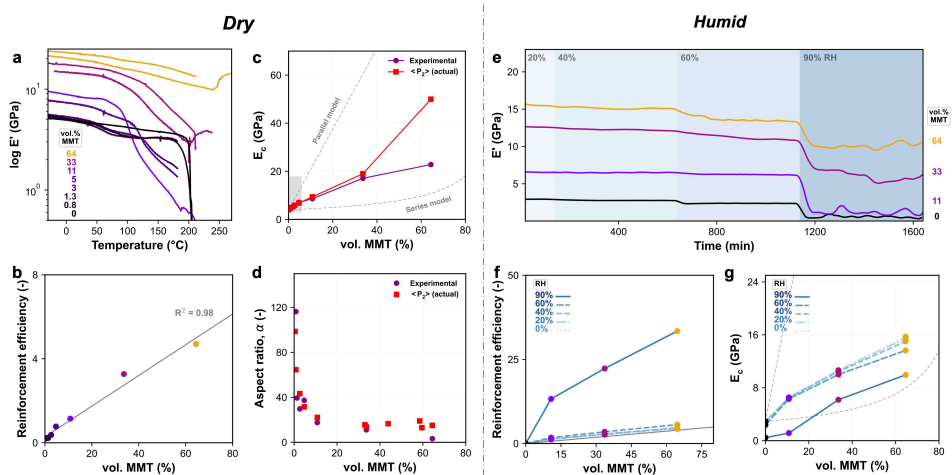


**Figure 5.4.** Mechanical properties of nacre-inspired nanocomposites with varying nanoclay loading acclimated to dry or humid conditions. (a) DMTA analysis of gelatin and gelatin/MMT nanocomposites. (b) Reinforcement efficiency based on dry storage modulus $((E_c - E_m)/E_m)$ for a wide range of MMT loading. (c) Dry storage modulus via experiments and $<P_2>$ based calculations. The boundaries (dashed lines) are set by Halpin-Tsai in parallel or series models. Gray rectangle is a guide for a typical concentration range of MMT in conventional composites. (d) Back-calculated effective aspect ratio, $\alpha$, of the MMT using Halpin Tsai (eq 4) for the various MMT loadings. (e) DMA analysis of gelatin and gelatin/MMT nanocomposites at 30 °C and varying relative humidity (RH) intervals. (f) Reinforcement efficiency based on humid storage modulus $((E_c - E_m)/E_m)$ for a wide range of MMT loading. (g) Humid storage modulus via DMA/RH experiments. The boundaries (dashed lines) are set by Halpin-Tsai in parallel or series models.

### 5.3.5. Transport structure-properties

Enhancing gas barrier properties by adding nanoplatelets and sheets to polymer membranes is well-established.[11,12,53] We have tested the influence of incorporating nanoplatelets with a high aspect ratio and surface area on the water vapor barrier properties. The MMT platelets significantly reduced the slope in water vapor sorption kinetics, particularly at low water activities ($a_w$) (Figure 5.5a-b). The impermeable filler's high aspect ratio increased the tortuous path for water vapor molecules through the composite. In addition, the nanocomposites show reduced water sorption capacity as the gelatin mass decreased, with an averaged drop of 62±5% in 64MMT (Figure 5.5c). Up to $a_w$=0.4, a further decrease in capacity can be attributed to the strong interactions between gelatin/MMT components, increasing hydrophobicity. However, adding platelets will also influence the free volume of the matrix polymer, increasing sample variation in water uptake (Table S1), especially in the case of gelatin, which can show supramolecular thermo-reversibility. In all samples, the equilibrium isotherms also show a clear step around $a_w$ 0.6 to 0.8 (Figure 5.5c), possibly due to water plasticization, *i.e.*, increased segmental mobility and clustering phenomena.

By fitting the kinetic sorption curves (eq 9), the Fickian diffusion parameter, $\phi_F$, also changes with water concentration (Figure 5.5d). We observe that the addition of MMT has shifted the non-Fickian transition from $a_w$=0.4 to higher humidity ($a_w$=0.6 to 0.8), a sign of anomalous diffusion that is loading-dependent. We have determined the diffusion coefficients ($D$) of gelatin and nanocomposites (Figure 5.5e). The eq 9 fits agreed well with experimental data ($\chi^2$ statistics, $p<0.05$). In general, $D$ increased with $a_w$, from the hydrophilic gelatin content. The global decrease in $D$ for nanocomposites with increasing MMT content reflects the tortuosity hypothesis. This phenomenon should scale with nanoplatelets' concentration, orientation ($<P_2>$), aspect ratio, and overlap factor. However, we find that the $D$ in composites was higher than expected and not following the $<P_2>$ of high-aspect-ratio exfoliated nanoplatelets.

### 5.3.6. Transport aspect ratio

The *effective* aspect ratio, $\alpha$, of nanoplatelets was back-calculated from the diffusion coefficients using the modified Nielsen model proposed by Bharadwaj (2001), eq 11. This simple model considers the orientational order parameter $<P_2>$, which we have obtained from WAXS results. The calculated $\alpha$ values started at the $a_w$-averaged value of 185 nm (Figure 5.5f). However, for the higher MMT loadings (33 and 64MMT), we observed an

apparent decline in $\alpha$, which did not follow the expected trend in $<P_2>$. This is explained by contradictions with the assumptions made by the descriptive Nielsen's model in eqs 10 and 11. Nielsen's model assumes that platelets are monodisperse in size and perfectly overlapped (*i.e.*, not stacked). Those were not the system conditions, and we expect random overlapping in a labyrinth effect, causing $\alpha$ underestimation (Figure 5.6a). Moreover, the models assume a constant value of $D$ for the matrix polymer. Curiously, the renaturation of gelatin supramolecular architectures has led to increased $D$ values, likely, from providing a 'highway' for water diffusion (Figure S5.4). In our system, we have found that gelatin A presented different degrees of the triple helices with increasing MMT loadings (Figures 5f-g). DSC also showed that the renaturation temperature of aggregates was dramatically influenced by MMT filler at a determined water uptake (Figure 5.5g). For 64MMT, the matrix renaturation point is so much suppressed in the confined gel that it only shows a residual 'melting' peak. On top of that, we imagine there might have been anomalous diffusion from interfacial phenomena at very high loadings (33-64MMT), as polymer confinement in the interphase can lead to properties different from the bulk, creating mobile water channels. This is substantiated by a possibly higher free volume in MMT-loaded samples, as shown by the degree of gelatin-based swelling (Table S1). Overall, we propose that the amorphous gelatin structure changes dramatically near a particle, be it a gelatin helix or an MMT platelet. These dynamic changes in matrix coefficient ($D_m$) with increasing MMT incorporation prevent a very reliable $\alpha$ determination using the established theoretical framework. To circumvent this, future work should be done on measuring the barrier properties of nanocomposites for other gases, such as $O_2$, methanol vapor, and $CO_2$, which plausibly are not very good plasticizers.

We further elaborate on the theoretical grounds for $\alpha$ determination via transport properties. It is important to restate that the effect of filler volume fraction has been somewhat described up to a semi-dilute regime (Figure 5.6a). The concentrated regime, including polymer confinement, edge extension, and (indirect) filler-filler interactions, is yet to be explored. In Figure 5.6b, we demonstrate how the adopted $\alpha$ model can dramatically influence the order of magnitude of the required diffusion ratios. Note the dramatic difference between the models, varying almost 50%, at the expected value for our studied MMT, $\alpha$=200 nm. Hence, the lack of comparative $\alpha$ models remains challenging in the filler-concentrated regime of (dynamic) polymer nanocomposites, certainly, if we are to test the effects of structural order on properties.
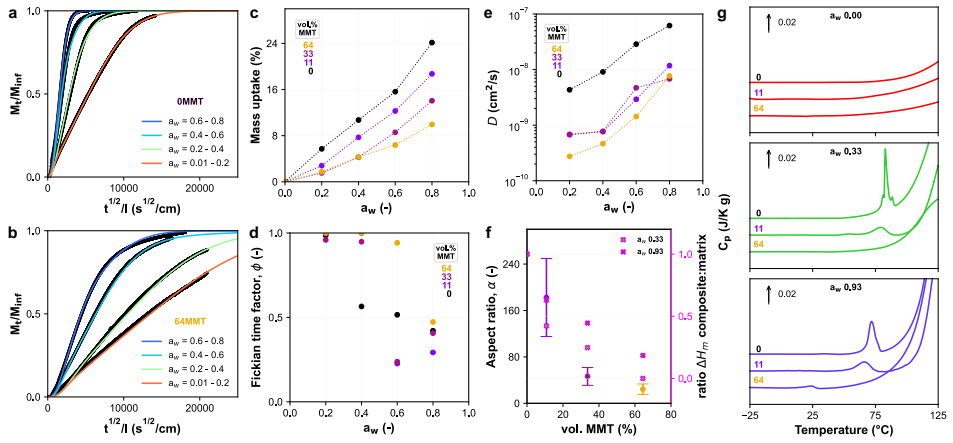
**Figure 5.5.** Kinetic water sorption at different water activities of (a) gelatin and (b) 64MMT nanocomposite at 30 °C. (c) Equilibrium water vapor sorption isotherms of matrix and nanocomposites. (d) Fickian time factor, $\phi_F$, a weighing parameter for the extent of Fickian type of diffusion in eq 9a, for matrix and nanocomposites. (e) Water diffusion coefficient, $D$, calculated with eq 9b from the kinetic sorption curves of matrix and nanocomposites. (f) Aspect ratio, $\alpha$, of the MMT backcalculated from $D$ for various MMT loadings, where the reported value is an average of the studied water activities ($a_w$ = 0.2 to 0.8). Error bars represent the standard deviation in aspect ratio. (g) DSC scans of matrix and nanocomposites previously equilibrated at different water activities ($a_w$).
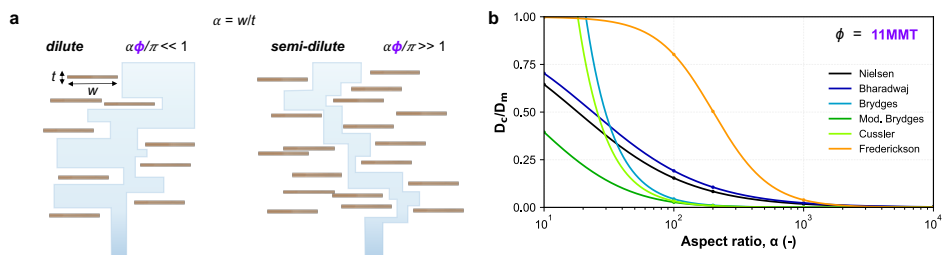
**Figure 5.6.** (a) Schematic depicting the tortuous path for gas diffusion through platelet reinforced nanocomposites in the dilute ($\alpha\phi/\pi$ <<1) and semi-dilute ($\alpha\phi/\pi$ >>1) concentration regimes, where $\alpha$ and $\phi$ are, respectively, particle aspect ratio and volume fraction, as previously proposed by Fredrickson and Bicerano (1999)[54]. The particle aspect ratio, $\alpha$, is defined by width, $w$, over thickness, $t$. Dilute regime: the platelet centers are spaced by a mean distance that exceeds their radius. Semi-dilute regime: the platelets overlap strongly imposing higher tortuosity. (b) Diffusion coefficient ratio between composite ($D_c$) and matrix ($D_m$) for a specific volume fraction, 11 vol.% MMT, covering several orders of magnitude in $\alpha$, as proposed by varying theoretical transport models.

We have demonstrated via mechanical and transport properties that a hydrogel affine deformation strategy can achieve continuous reinforcement and enhanced barrier properties through nanofiller immobilization and orientation. Future work shall extend this strategy to other compatible polymer nanocomposites by varying the individual components, shape, and aspect ratio of nanofillers, gelling or network conditions (cross-linking), and exploring how to prevent nanoparticle wrinkling phenomena. In addition, special attention should be given to rheological studies in which the actual degree of affine deformation, network strength, and filler relaxation times might be determined. A key goal would be to design scalable hybrid systems that achieve close to perfect affine compression and very high levels of orientation, preferably at high loadings. In an ideal scenario, this would be combined with green processing for large-area fabrication of advanced bioinspired materials with consistent and reproducible properties.

## 5.4. Conclusions and Perspectives

In this study, we propose that the orientation in many well-established waterborne nacre-mimetics methodologies cannot be achieved by the 2D-material assembly. Instead, it is often formed via a network that undergoes compressive affine deformation. This is based

on the premise that any mean-field assembly process requires mobility to result in nanoparticle alignment, which is inevitably absent in crosslinked systems. We hereby investigated the affine network mechanism with a hydrogel system consisting of gelatin/MMT and solvent casting to produce nanocomposite films. The experimental design was set to establish comprehensive relationships among the alignment mechanism, structure, thermomechanical and barrier properties as a function of filler loading, orientational order ($<P_2>$ parameter), and aspect ratio.

Gelatin/MMT nacre-like composites were successfully fabricated under facile ambient conditions and formed dense lamellar structures up to exceptionally high MMT loadings, studied up to 64 vol.%. First, the orientational order distribution in exfoliated nanocomposites was studied via wide angle X-ray scattering (nanostructure) and electron microscopy (microstructure). Indeed, we find that the orientation distribution function of affine deformation, in contrast to the Maier-Saupe theory, is suitable for the azimuthal intensity profiles in all nanocomposites. The affine deformation FWHM factor, representative of the compressive strain $\lambda$, allows us to estimate the solids concentration in which particle-immobilizing yield stress develops ($1/\lambda$). We find that the gelatin/MMT networks are, in reality, pseudo-affine since deformation does not occur until later in the evaporative process ($1/\lambda_z > 1/\lambda_{z\,max}$). Remarkably, for a wide range of nanoplatelet volume fractions, up to 64 vol.%, we find an almost constant degree of compression ($\lambda_z$) and respective order parameter $<P_2>$. This means a compatible hydrogel strategy is efficient in avoiding 2D-material stacking at high loadings and can ensure an excellent degree of orientational order via immobilization (in our case, $<P_2>_{affine}$ is scattered at about 0.7).

Next, we have verified the influence of these exfoliated nanostructures, containing a high aspect ratio filler, on stiffness, increased heat resistance, and lower gas permeability. The constantly high orientational order is also reflected in the monotonic increase of reinforcement efficiency from modulus. Increased mechanics is kept even at very high relative humidity (90%). The MMT aspect ratio, $\alpha$, was further investigated via Halpin-Tsai composite theory. From the exfoliated state, we know that structurally there must be a constant $\alpha$ - predicted around 200 nm - over MMT volume fraction. However, Halpin-Tsai's findings did not meet expectations, which we imagine might be due to platelet wrinkling. Thus, the $<P_2>$-based $\alpha$ values decreased with filler concentration from 99 to 13 nm. For the same reason, the experimental modulus does not improve accordingly, with 23 GPa for 64MMT. The $\alpha$ parameter was also examined through water vapor diffusion. We observe a remarkable reduction in sorption kinetics and diffusion coefficients with increasing MMT loading and diffusion tortuosity. However, for

**5**

gelatin/MMT nanocomposites, we also observe that the matrix diffusion, $D_m$, was altered by strong interactions with the clay component (reducing the level of gelatin renaturation). This also influenced the calculated $\alpha$, estimated from water diffusion data, which changed from about 200 to 60 nm. In addition, the models for estimating diffusion-based aspect ratio are yet to be translated for high volume fractions (high overlapping and labyrinth case), adding to underestimating this important morphological feature. Therefore, adjustments to the composite reinforcement and permeation theories are still needed to properly describe the high filler concentration regimes.

To conclude, we propose that the affine deformation mechanism is rather suitable to understand and indeed tailor nacre-inspired nanocomposites to a high level of orientational order and alignment, even at exceedingly high filler loading levels, which allows the development of advanced structure-property relationship based optimized materials. The predictive power of the affine deformation model should allow for tuning the degree of compressive strain (uniaxial drying) and associated alignment experienced by the entangled or immobilized 1D or 2D filler components. More importantly, because of the easy scalability potential of hydrogel affine deformation methods, this might broaden the scope for practical application of advanced bioinspired nanocomposite materials.

.

5

# Supporting information

The complete supporting information is available at DOI: 10.26434/chemrxiv-2023-99lv2

## Supporting Text S5.1. Affine deformation of renatured gelatin

Gelatin renaturation of collagen-like triple helices has been observed via X-ray scattering (WAXS) and scanning electron microscopy (SEM) (Figure S5.1). Gelatin consists of single or multi-stranded polypeptides, with possible proline helix conformations. The coil renaturation is expected to appear with the formation of a helical secondary structure and subsequent aggregation of the helix joints. In this, the network appears from H-bonding of intra- or inter-chain interactions between hydroxyl and carbonyl groups. The aggregates form a fibrous network which can uniaxially deform during evaporation, consolidating into an anisotropic gel.
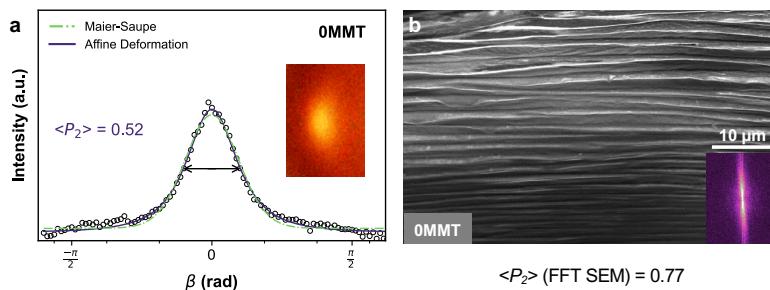


**Figure S5.1.** (a) WAXS feature, azimuthal intensity profile, and calculated orientation distribution functions of affine deformation (dark purple solid lines) and Maier-Saupe (light green dashed lines) for renatured gelatin A film (helical aggregates). The renaturation is observed by the appearance of equatorial diffraction arcs. (b) SEM cross-section image of gelatin A film (0MMT), where inset shows corresponding fast Fourier transforms (FFT) of the image for peak integration. The $<P_2>$ values depicted in images were determined via affine deformation ODF.

## Supporting Figures and Tables

## WAXS frames
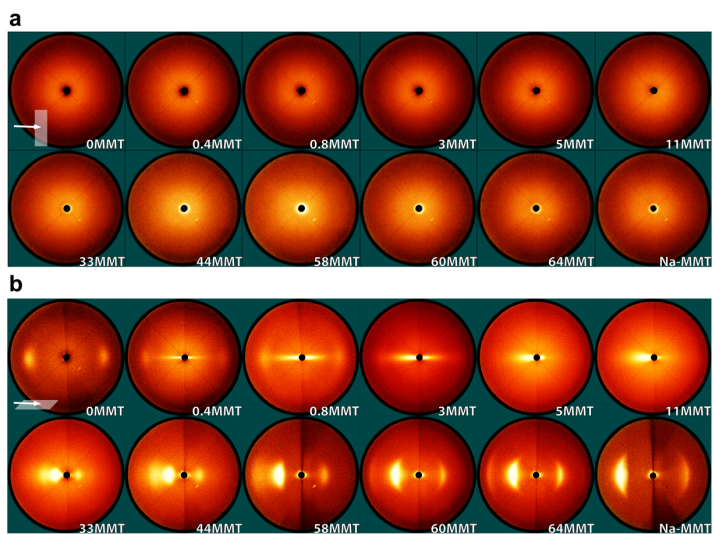


**Figure S5.2.** 2D transmission X-ray scattering images of gelatin and gelatin/MMT samples with varying MMT content at beam inclination (a) perpendicular and (b) parallel (at a glancing angle) to the plane of the films. The scattering patterns in (b) reveal anisotropic peaks (reproduced with permission from Espíndola et al. (2023)[39]).

## ODF Gaussian convolution

*Gaussian Convolution*
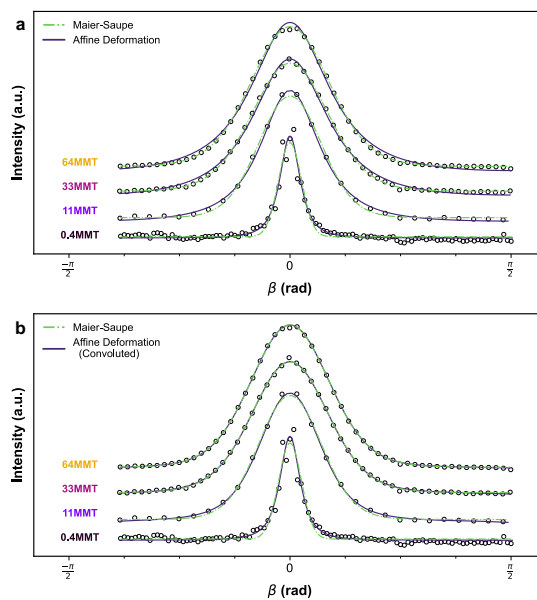


**Figure S5.3.** Azimuthal intensity profiles corresponding to the $d_{001}$ reflection at different MMT volumetric loadings. The lines are the curve fit results for the Maier-Saupe (light green) and affine deformation (dark purple) models convoluted to a Gaussian function.

**5**

## DVS amorphous and renatured gelatin
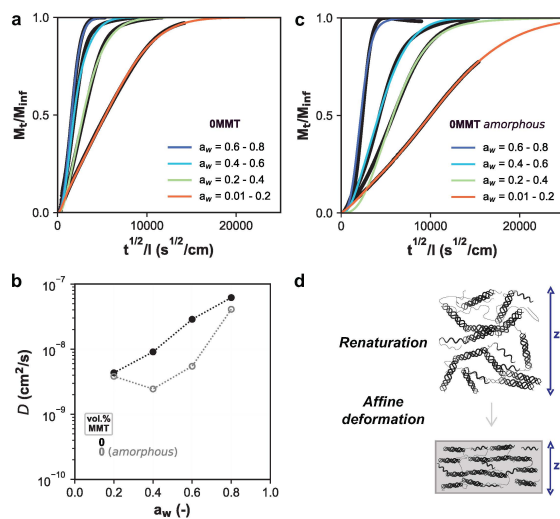


**Figure S5.4.** Kinetic water sorption of renatured gelatin (a) and amorphous gelatin (c) at 30 °C. (b) Water diffusion coefficient, $D$, calculated with eq 9 from the kinetic sorption curves for the different gelatins. (d) Schematic illustration of renaturation and affine deformation of renatured triple helix aggregated domains, creating a different microstructure.

## Flame resistance test
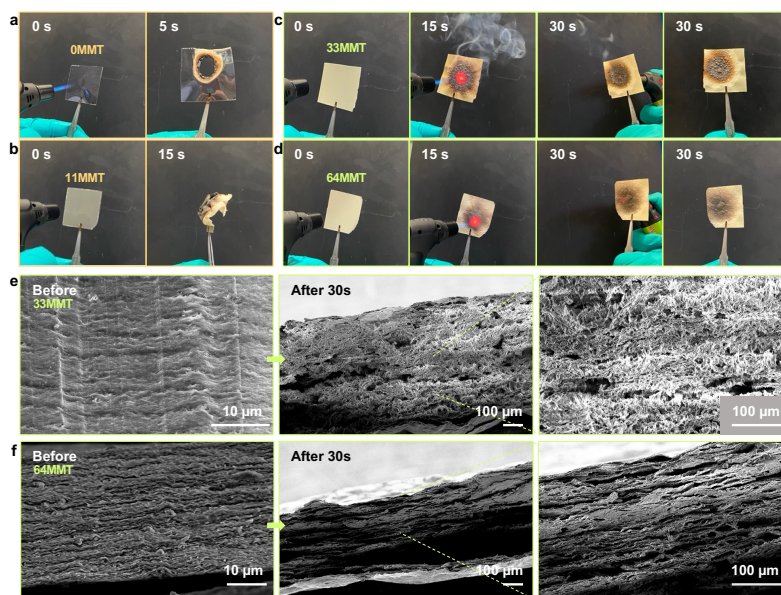


**Figure S5.5.** Flame resistance tests of gelatin and gelatin/MMT nanocomposites: 0 MMT (a), 11MMT (b), 33MMT (c), 64MMT (d). The corresponding SEM micrographs for 33MMT (e) and 64MMT (f) before and after flame exposure.

# References

(1)　　Bhushan, B. Biomimetics: Lessons from Nature - an Overview. *Philos. Trans. R. Soc. Math. Phys. Eng. Sci.* **2009**, *367* (1893), 1445–1486. https://doi.org/10.1098/rsta.2009.0011.

(2)　　Liu, S.; Wang, S.; Sang, M.; Zhou, J.; Zhang, J.; Xuan, S.; Gong, X. Nacre-Mimetic Hierarchical Architecture in Polyborosiloxane Composites for Synergistically Enhanced Impact Resistance and Ultra-Efficient Electromagnetic Interference Shielding. *ACS Nano* **2022**, *16* (11), 19067–19086. https://doi.org/10.1021/acsnano.2c08104.

(3)　　Yu, Y.; Kong, K.; Tang, R.; Liu, Z. A Bioinspired Ultratough Composite Produced by Integration of Inorganic Ionic Oligomers within Polymer Networks. *ACS Nano* **2022**, *16* (5), 7926–7936. https://doi.org/10.1021/acsnano.2c00663.

(4)　　Tan, G.; Zhang, J.; Zheng, L.; Jiao, D.; Liu, Z.; Zhang, Z.; Ritchie, R. O. Nature-Inspired Nacre-Like Composites Combining Human Tooth-Matching Elasticity and Hardness with Exceptional Damage Tolerance. *Adv. Mater.* **2019**, *31* (52), 1904603. https://doi.org/10.1002/adma.201904603.

(5)　　Wang, Y.; Zhang, Y.; Zhang, Z.; Li, T.; Jiang, J.; Zhang, X.; Liu, T.; Qiao, J.; Huang, J.; Dong, W. Pistachio-Inspired Bulk Graphene Oxide-Based Materials with Shapeability and Recyclability. *ACS Nano* **2022**, *16* (2), 3394–3403. https://doi.org/10.1021/acsnano.2c00281.

(6)　　Park, K. H.; Seo, J. G.; Jung, S.; Yang, J. Y.; Song, S. H. Quaternary Artificial Nacre-Based Electronic Textiles with Enhanced Mechanical and Flame-Retardant Performance. *ACS Nano* **2022**, *16* (4), 5672–5681. https://doi.org/10.1021/acsnano.1c10638.

(7)　　Gorur, Y. C.; Francon, H. S.; Sethi, J.; Maddalena, L.; Montanari, C.; Reid, M. S.; Erlandsson, J.; Carosio, F.; Larsson, P. A.; Wågberg, L. Rapidly Prepared Nanocellulose Hybrids as Gas Barrier, Flame Retardant, and Energy Storage Materials. *ACS Appl. Nano Mater.* **2022**, *5* (7), 9188–9200. https://doi.org/10.1021/acsanm.2c01530.

(8)　　Lossada, F.; Hoenders, D.; Guo, J.; Jiao, D.; Walther, A. Self-Assembled Bioinspired Nanocomposites. *Acc. Chem. Res.* **2020**, *53* (11), 2622–2635. https://doi.org/10.1021/acs.accounts.0c00448.

(9)　　He, H.; Guan, L.; Le Ferrand, H. Controlled Local Orientation of 2D Nanomaterials in 3D Devices: Methods and Prospects for Multifunctional Designs and Enhanced Performance. *J. Mater. Chem. A* **2022**, *10* (37), 19129–19168. https://doi.org/10.1039/d2ta01926d.

(10)　　Lossada, F.; Zhu, B.; Walther, A. Dry Processing and Recycling of Thick Nacre–Mimetic Nanocomposites. *Adv. Funct. Mater.* **2021**, *31* (30), 2102677.

(11)　　Doblhofer, E.; Schmid, J.; Rieß, M.; Daab, M.; Suntinger, M.; Habel, C.; Bargel, H.; Hugenschmidt, C.; Rosenfeldt, S.; Breu, J.; Scheibel, T. Structural Insights into Water-Based Spider Silk Protein-Nanoclay Composites with Excellent Gas and Water Vapor Barrier Properties. *ACS Appl. Mater. Interfaces* **2016**, *8* (38), 25535–25543. https://doi.org/10.1021/acsami.6b08287.

(12)　　Kochumalayil, J. J.; Bergenstråhle-Wohlert, M.; Utsel, S.; Wågberg, L.; Zhou, Q.; Berglund, L. A. Bioinspired and Highly Oriented Clay Nanocomposites with a Xyloglucan Biopolymer Matrix: Extending the Range of Mechanical and Barrier Properties. *Biomacromolecules* **2013**, *14* (1), 84–91. https://doi.org/10.1021/bm301382d.

(13)　　Gao, W.; Wang, M.; Bai, H. A Review of Multifunctional Nacre-Mimetic Materials Based on Bidirectional Freeze Casting. *J. Mech. Behav. Biomed. Mater.* **2020**, *109*, 103820. https://doi.org/10.1016/j.jmbbm.2020.103820.

(14)　　Huang, C.; Cheng, Q. Learning from Nacre: Constructing Polymer Nanocomposites. *Compos. Sci. Technol.* **2017**, *150*, 141–166. https://doi.org/10.1016/j.compscitech.2017.07.021.

(15)　　Palin, D.; Style, R. W.; Zlopaša, J.; Petrozzini, J. J.; Pfeifer, M. A.; Jonkers, H. M.; Dufresne, E. R.; Estroff, L. A. Forming Anisotropic Crystal Composites: Assessing the Mechanical Translation of Gel Network Anisotropy to Calcite Crystal Form. *J. Am. Chem. Soc.* **2021**, *143* (9), 3439–3447. https://doi.org/10.1021/jacs.0c12326.

(16)　　Kawasumi, M. The Discovery of Polymer-Clay Hybrids. *J. Polym. Sci. Part Polym. Chem.* **2004**. https://doi.org/10.1002/pola.10961.

(17)　　Rao, Y. Q. Gelatin-Clay Nanocomposites of Improved Properties. *Polymer* **2007**, *48* (18), 5369–5375. https://doi.org/10.1016/j.polymer.2007.06.068.

(18)　　Walther, A.; Bjurhager, I.; Malho, J. M.; Pere, J.; Ruokolainen, J.; Berglund, L. A.; Ikkala, O. Large-Area, Lightweight and Thick Biomimetic Composites with Superior Material Properties via Fast, Economic, and Green Pathways. *Nano Lett.* **2010**, *10* (8), 2742–2748. https://doi.org/10.1021/nl1003224.

(19)　　Tang, Z.; Kotov, N. A.; Magonov, S.; Ozturk, B. Nanostructured Artificial Nacre. *Nat. Mater.* **2003**, *2* (6), 413–418. https://doi.org/10.1038/nmat906.

(20)　　Finnemore, A.; Cunha, P.; Shean, T.; Vignolini, S.; Guldin, S.; Oyen, M.; Steiner, U. Biomimetic Layer-by-Layer Assembly of Artificial Nacre. *Nat. Commun.* **2012**, *3* (1), 966.

(21)　　Ebina, T.; Mizukami, F. Flexible Transparent Clay Films with Heat-Resistant and High Gas-Barrier Properties. *Adv. Mater.* **2007**, *19* (18), 2450–2453. https://doi.org/10.1002/adma.200700162.

(22)　　Putz, K. W.; Compton, O. C.; Palmeri, M. J.; Nguyen, S. B. T.; Brinson, L. C. High-Nanofiller-Content Graphene Oxide-Polymer Nanocomposites via Vacuum-Assisted Self-Assembly. *Adv. Funct. Mater.* **2010**. https://doi.org/10.1002/adfm.201000723.

**5**

(23)     Wu, L.; Ohtani, M.; Takata, M.; Saeki, A.; Seki, S.; Ishida, Y.; Aida, T. Magnetically Induced Anisotropic Orientation of Graphene Oxide Locked by in Situ Hydrogelation. *ACS Nano* **2014**, *8* (5), 4640–4649. https://doi.org/10.1021/nn5003908.

(24)     Vilcinskas, K.; Norder, B.; Goubitz, K.; Mulder, F. M.; Koper, G. J. M.; Picken, S. J. Tunable Order in Alginate/Graphene Biopolymer Nanocomposites. *Macromolecules* **2015**, *48* (22), 8323–8330. https://doi.org/10.1021/acs.macromol.5b01380.

(25)     Zhou, T.; Zhao, C.; Liu, Y.; Huang, J.; Zhou, H.; Nie, Z.; Fan, M.; Zhao, T.; Cheng, Q.; Liu, M. Large-Area Ultrastrong and Stiff Layered MXene Nanocomposites by Shear-Flow-Induced Alignment of Nanosheets. *ACS Nano* **2022**, *16* (8), 12013–12023. https://doi.org/10.1021/acsnano.2c02062.

(26)     Li, Q.; Xue, Z.; Zhao, J.; Ao, C.; Jia, X.; Xia, T.; Wang, Q.; Deng, X.; Zhang, W.; Lu, C. Mass Production of High Thermal Conductive Boron Nitride/Nanofibrillated Cellulose Composite Membranes. *Chem. Eng. J.* **2020**, *383*, 123101. https://doi.org/10.1016/j.cej.2019.123101.

(27)     Chen, W. Y.; Jiang, X.; Lai, S.-N.; Peroulis, D.; Stanciu, L. Nanohybrids of a MXene and Transition Metal Dichalcogenide for Selective Detection of Volatile Organic Compounds. *Nat. Commun.* **2020**, *11* (1), 1302. https://doi.org/10.1038/s41467-020-15092-4.

(28)     Zhao, F.; Peydayesh, M.; Ying, Y.; Mezzenga, R.; Ping, J. Transition Metal Dichalcogenide–Silk Nanofibril Membrane for One-Step Water Purification and Precious Metal Recovery. *ACS Appl. Mater. Interfaces* **2020**, *12* (21), 24521–24530. https://doi.org/10.1021/acsami.0c07846.

(29)     Das, P.; Malho, J.-M.; Rahimi, K.; Schacher, F. H.; Wang, B.; Demco, D. E.; Walther, A. Nacre-Mimetics with Synthetic Nanoclays up to Ultrahigh Aspect Ratios. *Nat. Commun.* **2015**, *6* (1), 5967. https://doi.org/10.1038/ncomms6967.

(30)     Wang, Y.; Desroches, G. J.; Macfarlane, R. J. Ordered Polymer Composite Materials: Challenges and Opportunities. *Nanoscale* **2021**, *13* (2), 426–443.

(31)     Onsager, L. The Effects of Shape on the Interaction of Colloidal Particles. *Ann. N. Y. Acad. Sci.* **1949**, *51* (4), 627–659. https://doi.org/10.1111/j.1749-6632.1949.tb27296.x.

(32)     Zlopasa, J.; Norder, B.; Koenders, E. A. B.; Picken, S. J. Origin of Highly Ordered Sodium Alginate/Montmorillonite Bionanocomposites. *Macromolecules* **2015**, *48* (4), 1204–1209. https://doi.org/10.1021/ma502147m.

(33)     Dabat, T.; Hubert, F.; Paineau, E.; Launois, P.; Laforest, C.; Grégoire, B.; Dazas, B.; Tertre, E.; Delville, A.; Ferrage, E. A General Orientation Distribution Function for Clay-Rich Media. *Nat. Commun.* **2019**, *10* (1), 5456. https://doi.org/10.1038/s41467-019-13401-0.

(34)     Hegde, M.; Yang, L.; Vita, F.; Fox, R. J.; van de Watering, R.; Norder, B.; Lafont, U.; Francescangeli, O.; Madsen, L. A.; Picken, S. J.; Samulski, E. T.; Dingemans, T. J. Strong Graphene Oxide Nanocomposites from Aqueous Hybrid Liquid Crystals. *Nat. Commun.* **2020**, *11* (1), 830–830. https://doi.org/10.1038/s41467-020-14618-0.

(35)     Picken, S. J.; Aerts, J.; Visser, R.; Northolt, M. G. Structure and Rheology of Aramid Solutions: X-Ray Scattering Measurements. *Macromolecules* **1990**, *23* (16), 3849–3854. https://doi.org/10.1021/ma00218a021.

(36)     Maier, W.; Saupe, A. Eine Einfache Molekular-Statistische Theorie Der Nematischen Kristallinflüssigen Phase. Teil L1. *Z. Für Naturforschung A* **1959**, *14* (10), 882–889.

(37)     Odijk, T. Elastic Constants of Nematic Solutions of Rod-like and Semi-Flexible Polymers. *Liq. Cryst.* **1986**, *1* (6), 553–559.

(38)     Kuhn, W.; Grün, F. Beziehungen Zwischen Elastischen Konstanten Und Dehnungsdoppelbrechung Hochelastischer Stoffe. *Kolloid-Z.* **1942**, *101* (3), 248–271. https://doi.org/10.1007/BF01793684.

(39)     Espíndola, S. P.; Zlopasa, J.; Picken, S. J. Systematic Study of the Nanostructures of Exfoliated Polymer Nanocomposites. **2023**.

(40)     Das, P.; Mai, V. C.; Duan, H. Flexible Bioinspired Ternary Nanocomposites Based on Carboxymethyl Cellulose/Nanoclay/Graphene Oxide. *ACS Appl. Polym. Mater.* **2019**, *1* (6), 1505–1513. https://doi.org/10.1021/acsapm.9b00245.

(41)     Kochumalayil, J. J.; Morimune, S.; Nishino, T.; Ikkala, O.; Walther, A.; Berglund, L. A. Nacre-Mimetic Clay/Xyloglucan Bionanocomposites: A Chemical Modification Route for Hygromechanical Performance at High Humidity. *Biomacromolecules* **2013**, *14* (11), 3842–3849. https://doi.org/10.1021/bm400883e.

(42)     Zheng, X.; Xu, M.; Yang, S.; Omonov, S.; Huang, S.; Zhao, J.; Ruan, H.; Zeng, M. Novel Bio-Inspired Three-Dimensional Nanocomposites Based on Montmorillonite and Chitosan. *Int. J. Biol. Macromol.* **2020**, *165*, 2702–2710. https://doi.org/10.1016/j.ijbiomac.2020.10.070.

(43)     Zheng, J. P.; Li, P.; Ma, Y. L.; Yao, K. De. Gelatin/Montmorillonite Hybrid Nanocomposite. I. Preparation and Properties. *J. Appl. Polym. Sci.* **2002**, *86* (5), 1189–1194. https://doi.org/10.1002/app.11062.

(44)     Panzavolta, S.; Gioffrè, M.; Bracci, B.; Rubini, K.; Bigi, A. Montmorillonite Reinforced Type A Gelatin Nanocomposites. *J. Appl. Polym. Sci.* **2014**, *131* (11), 1–6. https://doi.org/10.1002/app.40301.

(45)     Wen, Q.; Basu, A.; Janmey, P. A.; Yodh, A. G. Non-Affine Deformations in Polymer Hydrogels. *Soft Matter* **2012**, *8* (31), 8039. https://doi.org/10.1039/c2sm25364j.

(46)     Picken, S. J. Orientational Order in Aramid Solutions. *PhD Thesis Utrecht* **1990**.

**5**

(47)     Vlasveld, D. P. N.; Groenewold, J.; Bersee, H. E. N.; Mendes, E.; Picken, S. J. Analysis of the Modulus of Polyamide-6 Silicate Nanocomposites Using Moisture Controlled Variation of the Matrix Properties. *Polymer* **2005**, *46* (16), 6102–6113. https://doi.org/10.1016/j.polymer.2005.04.087.

(48)     Kornmann, X.; Berglund, L. A.; Sterte, J.; Giannelis, E. Nanocomposites Based on Montmorillonite and Unsaturated Polyester. *Polym. Eng. Sci.* **1998**, *38* (8), 1351–1358.

(49)     Yao, K.; Huang, S.; Tang, H.; Xu, Y.; Buntkowsky, G.; Berglund, L. A.; Zhou, Q. Bioinspired Interface Engineering for Moisture Resistance in Nacre-Mimetic Cellulose Nanofibrils/Clay Nanocomposites. *ACS Appl. Mater. Interfaces* **2017**, *9* (23), 20169–20178. https://doi.org/10.1021/acsami.7b02177.

(50)     Zheng, J.; Gao, S.; Li, H.; Yao, K. Effects of Reaction Conditions on Intercalation between Gelatin and Montmorillonite: Thermodynamical Impact. *J. Appl. Polym. Sci.* **2013**, *128* (1), 54–59. https://doi.org/10.1002/app.38129.

(51)     Picken, S. Applications of Liquid Crystal Polymers: Part 1: Fibre Spinning. *Liq. Cryst. Today* **1996**, *6* (1), 12–15.

(52)     Dobb, M.; Johnson, D.; Saville, B. Supramolecular Structure of a High-modulus Polyaromatic Fiber (Kevlar 49). *J. Polym. Sci. Polym. Phys. Ed.* **1977**, *15* (12), 2201–2211.

(53)     Vlasveld, D. P. N.; Groenewold, J.; Bersee, H. E. N.; Picken, S. J. Moisture Absorption in Polyamide-6 Silicate Nanocomposites and Its Influence on the Mechanical Properties. *Polymer* **2005**, *46* (26), 12567–12576.

(54)     Fredrickson, G. H.; Bicerano, J. Barrier Properties of Oriented Disk Composites. *J. Chem. Phys.* **1999**, *110* (4), 2181–2188. https://doi.org/10.1063/1.477829.

(55)     Picken, S. J.; Aerts, J.; Doppert, H. L.; Reuvers, A. J.; Northolt, M. G. Structure and Rheology of Aramid Solutions: Transient Rheological and Rheooptical Measurements. *Macromolecules* **1991**, *24* (6), 1366–1375. https://doi.org/10.1021/ma00006a023.

(56)     Picken, S. J.; van der Zwaag, S.; Northolt, M. G. Molecular and Macroscopic Orientational Order in Aramid Solutions: A Model to Explain the Influence of Some Spinning Parameters on the Modulus of Aramid Yarns. *Polymer* **1992**, *33* (14), 2998–3006. https://doi.org/10.1016/0032-3861(92)90087-D.

(57)     Fan, S. M.; Luckhurst, G. R.; Picken, S. J. A Deuterium Nuclear Magnetic Resonance Investigation of Orientational Order and Director Kinetics in Aramid Solutions. *J. Chem. Phys.* **1994**, *101* (4), 3255–3267. https://doi.org/10.1063/1.467573.

(58)     Halpin, J.; Kardos, J. Polym. Eng. Sci. **1976**.

(59)     Shell, H. R.; Ivey, K. H. *Fluorine Micas*; US Department of the Interior, Bureau of Mines, 1969.

(60)     Zlopaša, J. Exploring the Structure, Properties, and Applications of Highly Ordered Bionanocomposites. *Delft Univ. Technol.* **2017**. https://doi.org/10.4233/uuid:e47bfa54-4d58-4c82-829f-3cb2ceb6cfc7.

(61)     Van Es, M.; Xiqiao, F.; Van Turnhout, J.; Van der Giessen, E.; Al-Malaika, S.; Golovoy, A. Specialty Polymer Additives: Principles and Applications. *Malden MA Blackwell Sci.* **2001**.

(62)     Crank, J. Diffusion in a Sphere. *Math. Diffus.* **1975**, 89–103.

(63)     Burgess, S. K.; Mikkilineni, D. S.; Yu, D. B.; Kim, D. J.; Mubarak, C. R.; Kriegel, R. M.; Koros, W. J. Water Sorption in Poly(Ethylene Furanoate) Compared to Poly(Ethylene Terephthalate). Part 2: Kinetic Sorption. *Polymer* **2014**, *55* (26), 6870–6882. https://doi.org/10.1016/j.polymer.2014.10.065.

(64)     Long, F.; Richman, D. Concentration Gradients for Diffusion of Vapors in Glassy Polymers and Their Relation to Time Dependent Diffusion Phenomena1, 2. *J. Am. Chem. Soc.* **1960**, *82* (3), 513–519.

(65)     Nielsen, L. E. Models for the Permeability of Filled Polymer Systems. *J. Macromol. Sci. Part - Chem.* **1967**, *1* (5), 929–942. https://doi.org/10.1080/10601326708053745.

(66)     Bharadwaj, R. K. Modeling the Barrier Properties of Polymer-Layered Silicate Nanocomposites. *Macromolecules* **2001**, *34* (26), 9189–9192. https://doi.org/10.1021/ma010780b.

(67)     Cussler, E.; Hughes, S. E.; Ward III, W. J.; Aris, R. Barrier Membranes. *J. Membr. Sci.* **1988**, *38* (2), 161–174.

(68)     Brydges, W.; Gulati, S.; Baum, G. Permeability of Glass Ribbon-Reinforced Composites. *J. Mater. Sci.* **1975**, *10*, 2044–2049.

(69)     Xu, S. W.; Zheng, J. P.; Tong, L.; De Yao, K. Interaction of Functional Groups of Gelatin and Montmorillonite in Nanocomposite. *J. Appl. Polym. Sci.* **2006**, *101* (3), 1556–1561. https://doi.org/10.1002/app.23435.

(70)     Nagarajan, M.; Benjakul, S.; Prodpran, T.; Songtipya, P. Characteristics of Bio-Nanocomposite Films from Tilapia Skin Gelatin Incorporated with Hydrophilic and Hydrophobic Nanoclays. *J. Food Eng.* **2014**, *143*, 195–204. https://doi.org/10.1016/j.jfoodeng.2014.06.03

**5**

# 6

# Assays on a novel biopolymer from wastewater sludge: Kaumera®

*" 'What is the secret of life', I asked.*

*'I forget', said Sandra.*

*'Protein', the bartender declared. 'They found out something about protein.'*

*'Yeah,' said Sandra, 'that's it.' "*

*– Kurt Vonnegut Jr, Cat's Cradle*

# Abstract

*A novel biopolymer material can be recovered from wastewater sludge, which is a large byproduct (~ 30% of solids) of the water cleaning service. This bio-based material has been extracted since 2019 in pioneer factories in the Netherlands and commercialized under the name Kaumera*. In this study, we explore a few chemical and physical properties of Kaumera® polymeric substances from the perspective of a black box, focusing on the development of sustainable applications. A few assays illustrate the current scientific insights and provide a roadmap toward a directed functional group and charge property characterization. This includes discussions concerning sample purification and fractionation, classification of Kaumera® polymers between polyelectrolyte or polyampholyte behavior, ionizable charge analysis, and its related solubility phase diagram. Remarkably, the purified Kaumera® EPS is a polymeric mixture that can fully pH-transition throughout the cationic/zwitterionic/anionic charge regimes. This unique feature may find applications in several fields and certainly can be used to tune materials. Moreover, the topics of heterogenous plasticization, blending, and bionanocomposites are also superficially discussed. We could conclude that more attention needs to be paid to the protein fractions in Kaumera® biopolymers (positive charges, isoelectric point, salt dependence, conformations, complexation, phase diagram). This is important to explore bio-based material applications, such as a binder, a flocculant, an absorber, and bio(nano)composites.*

Kaumera: Bio-based polymers from sludge

6
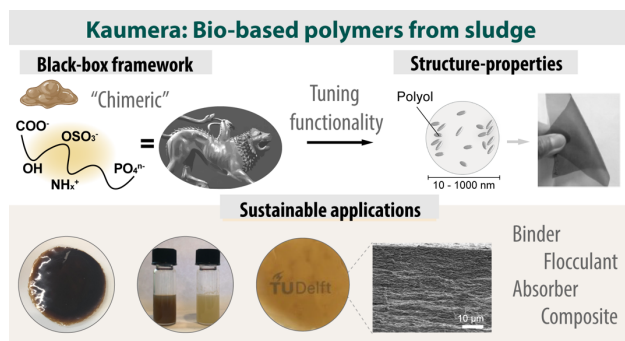
## 6.1. Introduction

In wastewater treatment plants, considerable amounts of excess sludge are formed as a byproduct of the water cleaning service.[1,2] The sludge contains biopolymers which are microbially synthesized as extracellular structural and binding material, also known as extracellular polymeric substances (EPS).[3,4] In particular, aerobic granular sludge has the advantage of containing a large concentration of gelling structural biopolymers, which can be extracted as a new raw material source.[5–7] In the Netherlands, novel sludge biopolymer extraction plants have operated since 2019. The product is extracted in a hot alkaline process and commercialized under the name Kaumera®, targeting sustainable applications.[1,2]

The chemical composition of Kaumera® EPS is intrinsically dynamic, as the microbial producers and their survival needs can vary according to the substrates and environment they are placed in.[3,4] Hence, multiple types of biopolymers and organic substances can be extracted, such as proteins (glycoproteins, lipoproteins, amyloids), polysaccharides (glycolipids, lipopolysaccharides, uronates, neutral sugars), nucleic acids, lipids, and humic substances.[4,8–10] However, the occurrence of each of these components is little understood, as the quest for mapping EPS chemical composition is only in its infancy.[9] On top of the complexity of the chemical nature, the operational nuances in biopolymer extraction can create selective barriers and change the balance in extracted biopolymers, *e.g.*, change the ratio of protein to polysaccharide-like monomers. Post-processing conditions varying solvent polarity, pH, ionic strength, and temperature should also directly affect the measured structure-property relationships of EPS.

Recently, Kaumera® and similar EPS have been proposed to have a predominant fraction of charged glycoproteins, *i.e.*, a protein backbone that is glycosylated.[4,10] Biological examples of such glycan-conjugated proteins are many, like mucin, collagen, and silk. Irrespective of this working hypothesis and the actual dynamic biopolymer composition, it mostly contains amino-acids (50-70% BSA equivalent) and sugars (circa 25% on glucose equivalent) as monomers, which can be bonded covalently or through electrostatic interactions.[11] In those, multiple functional groups are expected to occur, such as amines ($-NH_x$), hydroxyl (-OH), carboxylic ($-COO^-$), sulfate half esters ($-OSO_3^-$), and phosphates ($-PO_4^{n-}$). Taking a black-box approach, one could model and tune the possible electrostatic interactions from group contributions to study their influence on the biopolymer's physicochemical properties. Since this EPS is extracted under alkaline conditions, based solely on solubility, the material should be predominantly a net anionic

6

polymer. Herein, we investigate a few physicochemical properties, processing, and potential applications by means of short case studies. The work should be seen as an integration of the biopolymer research within this thesis to this novel class of polymeric material, shaping the resource recovery development.

## 6.2. Assays

The Kaumera® samples studied in the following experiments were collected from the large-scale (up to 400 tons/year) biopolymer recovery facility in Zutphen, the Netherlands. This factory handles the waste sludge from aerobic granular technology fed on the industrial effluent of a dairy producer.

### 6.2.1. Physicochemical characterizations

#### Solubility and fractionation

First, the Kaumera® EPS is evaluated for the biopolymer(s) solubility at different pH, salt levels, and temperatures. The as-extracted acidic Kaumera® generally consists of an amorphous gel phase at pH 2.2 and quite a high conductivity value (16-25 mS/cm). We have measured about 17% of this material to be inorganic. Upon dissolving the acidic gum to pH > 8, a large part of the material appears to solubilize. However, even after increasing the pH to 11 or applying high temperature (80 °C, 30'), we have observed that the polymer does not fully solubilize, and a gel pellet remains upon centrifugation.

To briefly evaluate the effect of salts on solubility, we have explored purification and fractionation routes starting from the extracted EPS (Figure 6.1). With dialysis of H-Kaumera® against ultrapure water, the conductivity could be lowered significantly (0.3 to 1 mS/cm). Hence, we have been able to remove excess salts significantly, *e.g.,* KCl is a byproduct of extraction, but likely also low molecular weight organic material (<3.5 kDa MWCO). Alternatively, washing-centrifuging cycles using tap or demi water can also be used (Figure 6.1b), resulting in dense gel aggregates (pH 2.5, 2.5 mS/cm) and about 41.5% mass loss on a raw Kaumera® basis. This purification step shall greatly impact composition since not only inorganic electrolytes are being removed but also loosely bound oligo- and polymeric components. Furthermore, dialyzed and "washed" H-Kaumera® gels are dynamic and tend to expel water over time (spontaneous syneresis). The low-salt Kaumera® samples could then be brought to alkaline pH (9 to 11) and fractionated by

6

centrifugation (Figure 6.1a) into soluble (supernatant) or aggregated/precipitated phases (hydrogel pellet). For the dialyzed Kaumera® sample, we have found the gel pellet to be about 30% of the initial mass. The same dialyzed-alkaline sample was also subjected to thermal treatment (80 °C, 30'), for which we found a lower percentage of the aggregated phase (17% of the initial mass). Curiously, this alkaline thermal step also formed a fat-like layer on top of the vial along with a pH drop from 10 to 9.4, an observation that still needs further investigation. On the other hand, for the "washed" Kaumera® sample, we observed that the alkaline-soluble fraction was somewhat hazy and that the gel pellet was more dominant, which composed 44% of the initial sample mass (at alkaline pH 11). As shown above, we note an overlooked influence of salt (and temperature) on the phase diagram of Kaumera® samples. These effects are considered during the following sample processing and physicochemical characterization.

6
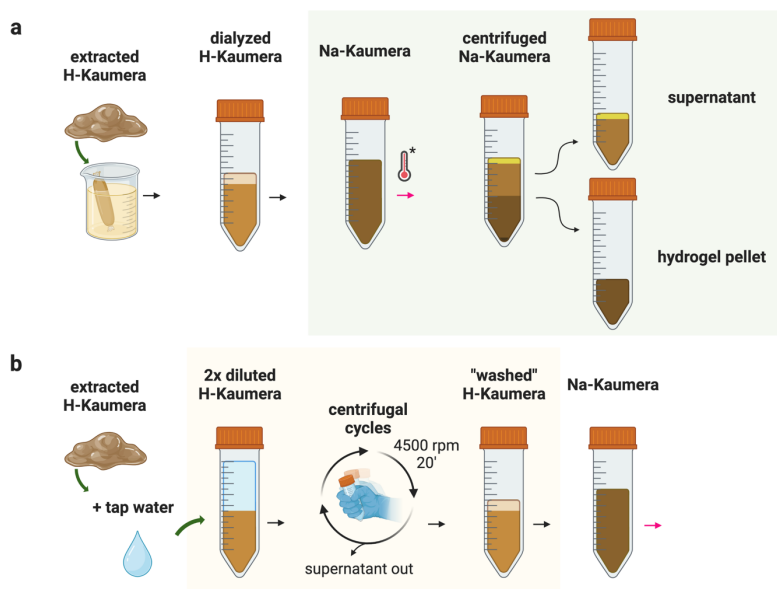
**Figure 6.1.** Post-processing of extracted Kaumera® EPS for purification and/or fractionation prior to analytical tests. a) Schematic showing steps of fractionation of a dialyzed acid Kaumera® (H-Kaumera®). The low-salt polymeric mixture is solubilized by NaOH addition (Na-Kaumera®) to a 3 wt.% mixture and subsequently centrifuged (5000 rpm, 20') to inspect aggregated/precipitated phases. Often, an amorphous hydrogel pellet is found. A thermal step (*) can also be included prior to fractionation to study the effect of temperature. b) Schematic showing an alternative method to purify the extracted EPS via washing-centrifuging cycles. The concentrated acidic biopolymer (8 wt.%) is mixed on a 1:1 ratio with clean tap or demi water. The supernatant phase is removed, and the washing step is repeated until low conductivity is achieved (around 4x). Often, this method resulted in a slight increase in H-Kaumera® concentration (9 wt.%). Figure created with BioRender.com.

## FTIR and elemental composition

We proceed to investigate reference functional groups in the following types of Kaumera® samples: unprocessed (raw), dialyzed, and "washed" H-Kaumera®. We have used Fourier Transform Infrared spectroscopy (FTIR) combined with qualitative elemental analysis (SEM-EDX). Figure 6.2a shows the ATR-FTIR spectra of ambient-dried Kaumera® samples, normalized by the amide peak (C=$O_v$ at 1626 cm$^{-1}$). The general spectra of Kaumera® confirmed the idealized profile of a mixture of proteins (NH$_{x,v}$ at 3500-3300 cm$^{-1}$ and secondary amide bonds at 1626 and 1530 cm$^{-1}$), polysaccharides (OH$_v$ at 3274 cm$^{-1}$ (broad), C=$O_v$ at 1750-1626 cm$^{-1}$, and O-$C_v$ at 1230 and 1030 cm$^{-1}$), lipids (CH$_{x,v}$

150

2922 cm$^{-1}$), and nucleic acids (P=O$_v$ at 1167 cm$^{-1}$ and P-OR$_v$ esters at 1050-900 cm$^{-1}$). These phosphated groups can also be an indication of phosphorylated proteins, sugars, and phospholipids. In addition, the peaks mentioned close to 1230 and 1250-970 cm$^{-1}$ can also overlap with the amide III band and alcohols/phenols, respectively. Unfortunately, the presence of sulfated compounds via FTIR is complicated since it lies in a lower-resolution region (700-900 cm$^{-1}$) and can overlap with aromatic ring-bending vibrations. However, we note that the highest FTIR signals matched those of peptide bonds - bands at 1626 cm$^{-1}$ (amide I, C=O$_v$ of peptides), 1530 cm$^{-1}$ (amide II, NH$_{2,\delta}$), and saccharides (OH$_v$ and O-C$_v$). Moreover, elemental analysis on unprocessed Kaumera$^*$ confirmed a general fraction of phosphates (0.60 P atom% or 0.01 P:C) and sulfates (0.16 S atom% or 0.003 S:C).

From previous reports[4,11], we also know the general composition of amino-acids and sugar monomers in hydrolyzed Zutphen H-Kaumera$^*$. With regards to amino-acids composition, glutamic and aspartic acids have been found, containing anionic carboxylic groups (-COO$^-$). Amino-acids that can be commonly phosphorylated (*e.g.*, Ser, Thr, Tyr, His) or, on occasion, sulfated (*e.g.*, Tyr) have also been detected. Although this functionalization is highly dependent on the amino-acid sequence. As for cationic amino-acids, lysine (1$^{ry}$ amine) and histidine (1$^{ry}$ and 2$^{ry}$ amines) were also present. There were, of course, also net neutral and even hydrophobic groups, like Gly, Ala, Val, Leu, Ile, Pro, and Phe residues. The sugar composition analysis has shown the likely presence of neutral -OH, anionic -COO$^-$, and cationic -NH$_3^+$ functional groups. Also, from previous microscopy staining and elemental analysis, we expect that sugars can also have -OSO$_3^-$ and PO$_4^{n-}$ functionalities.[4,12] Nucleic acids would also bring mostly -PO$_4^{1-}$ but also -PO$_4^{2-}$ groups. Hence, although both techniques are inconclusive, the FTIR and high-throughput monomer analyses are in general agreement with a polymeric mixture of proteins and (poly)saccharides and/or glycoproteins.

Applying the salt-removing processes on H-Kaumera$^*$ substantially changed the chemical composition (Figure 6.2a). If we compare the raw material to the dialyzed one, we observed major changes in the peaks around 2922, 1718, and 1167 cm$^{-1}$, which can be attributed, respectively, to lipids, acids (*e.g.*, H-bonded C=O$_v$ in acetic acid), and phosphates. There was also a minor decrease of the 1626 cm$^{-1}$ peak in comparison to the broad 3274 cm$^{-1}$ feature (ratio of acids and amides over -OH groups). On the other hand, for the "washed" Kaumera$^*$, we noticed a large relative increase of the overlapping area around the broad peak 3274 cm$^{-1}$, attributed to OH$_v$, and the amine bands (3500-3300 cm$^{-1}$). This is accompanied by large changes in the signals referring to lipids (2922 cm$^{-1}$),

acids (1718 cm$^{-1}$), saccharides (1626-1750, 1030 cm$^{-1}$), and phosphates (1167, 1050-900 cm$^{-1}$). Again, some amides might also have been washed out (ratio of 1626 and 1530 cm$^{-1}$ peaks to 3274 cm$^{-1}$). Furthermore, when the dialyzed or "washed" samples were subjected to alkaline fractionation (Figure 6.1a), the resulting soluble/insoluble fractions showed a similar FTIR peak assignment to each type of purified Kaumera® but with different intensity profiles. This directed FTIR analysis is useful in identifying the ratio of functional groups before and after processing; however, the quantity and chain distribution of (ionic) groups can be just as relevant to the material properties.

6
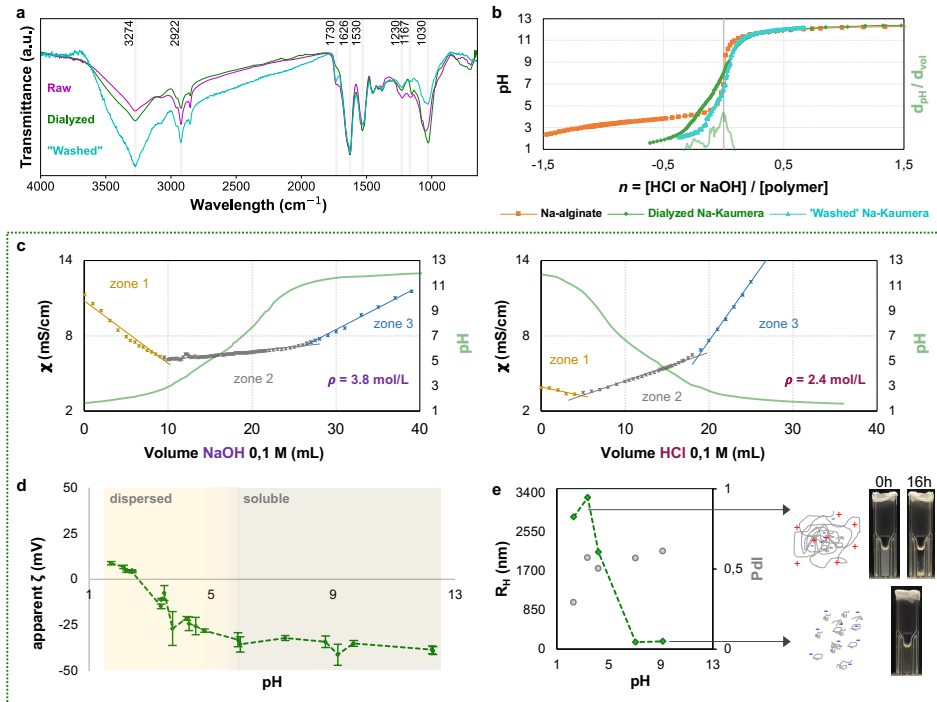
**Figure 6.2.** Multiple analytical and optical tes EPS. a) FTIR spectra of H-Kaumera* normalized to t 5 cr les after purification methods (dialysis and "washing"). b) Acid/Base titrations of Na-alginate and dialyzed/"washed" alkaline-soluble Kaumera* samples at RT and saline conditions (~10 mS/cm). For conciseness, the results of alkaline gel pellet samples are not depicted. The axis $d_{pH}/d_{vol}$ refers to the first derivative of pH, here shown for the dialyzed sample (green line). Box containing figures (c) to (e) show results with regards to the Na-Kaumera* sample dialyzed and alkaline-soluble (fractionation supernatant). c) Ion conductometric titration via strong base or acid. Conductivity ($\chi$) zones 1, 2, and 3 indicate the titration regimes of sample free $H^+/OH^-$ consumption, ion exchange of polymer backbone, and excess titrant (NaOH/HCl). d) Apparent zeta potential of dilute dialyzed Na-Kaumera* and observed region of sample solubility. e) The dynamic particle size (hydrodynamic radius, Rh) of dialyzed and alkaline-soluble samples obtained from dynamic light scattering. The polydispersity index, PDI, at pH value, is also given. A schematic shows the expected representations of the combined size and charge distribution of the structured/complexed Kaumera* sample at extremes of the pH range. Photographs of sample vials at different regimes confirm the change from dispersed or precipitated particles to a soluble polymeric complex.

## Acid/Base titrations

The acid/base titration of protons from ionizable groups in a polymer can be a useful tool to verify the composition and contribution of ionic compounds to structure(s). This can be done by precisely dosing standardized acid/base solutions to the polymer mixture of interest and monitoring the response to pH.[13–15] Acid/base titration of purified and fractionated Kaumera® samples was performed at polymer concentrations changing from an estimated 0.01 to 0.1 M (for the sake of comparison, the molar equivalent was set to alginate molecular weight: 216 g/mol). Influence from soluble $CO_2$ was minimized by $N_2$ stripping. As can be seen in Figure 6.2b for 0.1 M alkaline-soluble Kaumera®, the titration curve for adding a base is almost the mirror image of the curve for adding an acid, which was expected. The pH profile of Na-alginate is also given as a reference polysaccharide ($pK_a$ is 3.5-3.71, depending on ionic strength). In contrast, the results shown are very close to the pH profile of amino-acids, in which a zwitterion is formed at the neutral point (stoichiometric amount of acidic and basic units). These zwitterionic amino-acid residues are considered "neutral" due to balancing intrinsic charges.[16–18] The isoelectric point (p$I$) can be determined from the local maxima in the first derivative curve $d_{pH}/d_{vol}$. Stoichiometric zwitterion amino-acids usually have the p$I$ at pH 6.0 ± 0.6 from the synergism between carboxylic ($pK_a$ 2-4.8) and amine ($pK_a$ 8.5-11.3) groups. That was curiously similar to the case of our Kaumera® samples (alkaline-soluble and aggregated), in which the *apparent* pIs from maxima were at a range from 4 to 5, depending on sample processing. However, we know in advance that the origin of charges in Kaumera® can plausibly be from different biomolecules, not only proteins. In addition, no distinct (*apparent*) $pK_a$ regions could be defined using this titration method. On the contrary, it seems the profile matched that of multiple ionizing functional groups within the studied pH range of 1.6 to 12.5. The "washing" procedure resulted in a shift of *apparent* p$I$ for the "alkaline-soluble" sample from 4.18 ± 0.03 to 5.35 ± 0.21, a plausible sign that relatively more acidic groups have left the sample and/or more basic or hydrophobic groups were somehow selected in favor of acidic and polar components. A shift in p$I$ is commonly used to verify alterations in the amounts of charged groups of proteins/zwitterions and complexes thereof over changing solvent, salt, and functionalities.[19–21] Nevertheless, it is important to keep in mind that only proton titratable groups will be accounted for (*i.e.*, it excludes specifically bound metal-complexes and quenched polyionic interactions, which we here are implicitly taking to be negligible). Overall, the acid/base profile of Kaumera® samples confirms the predominant presence of multiple ionizable groups (weak acids/bases) with a strong resemblance to materials containing protein-like or

polyampholyte (mixed cationic/anionic) compounds. This means that these purified complex materials can be studied from the perspective of transitioning from cationic to zwitterionic to anionic behavior.

## Ion conductometric titrations and zeta potential

The charging behavior of purified Kaumera* samples can be investigated by employing ion conductometric titrations (ICT) and electrophoresis (zeta potential). ICT was performed on the different fractions of dialyzed and "washed" Kaumera*. As a reference, we have also analyzed Na-alginate. A home-build set-up and software (LabVIEW) were used to automate the experimentation based on calibrated automatic burette (765 Dosimat, Metrohm), pH meter (781 Metrohm, with Pt1000 probe), and conductometer (712 Metrohm, >100 µS/cm, with Pt1000 probe). The samples were again precisely titrated against standardized NaOH and HCl solutions. The drift in pH measurement was monitored until a pH plateau value was reached or, at the latest, after 3 min. Some of the titration curves were also performed at low and high ionic strengths (NaCl addition up to 15 or 33 mS/cm, which is, respectively, close to saline and half sea-water strength) to evaluate the salt-responsive behavior to titratable groups. Examples of the resulting titration curves for dialyzed alkaline-soluble Kaumera* are found in Figure 6.2c. The change in electrical conductivity from neutralization and ion exchanging reactions is monitored as strong acid (base) is added. The principle relies on the fact that if one of the ions is replaced by another, they will invariably have different mobility; *e.g.*, $Na^+$ is about 7 times less mobile than $H^+$. Hence, the method is also sensitive to chemical equilibria and the binding of counterions to the polymer backbone or network.[21] This is used in low-viscosity purified or deionized samples to observe marked differences in the conductivity rate over titrant volume, as these can be linked to the dissociation and half equivalence points.[22]

Kaumera* has proteins in its composition and behaves as a polyampholyte containing cationic and anionic groups. In Figure 6.2c, the left graph shows the titration of zwitterions and weak acids in dialyzed Kaumera* supernatant via a strong base. From this, we can calculate the charge density of acids. Similarly, the right graph shows the titration of zwitterions and weak bases via strong acid, allowing us to measure the charge density of bases. Based on ICT analyses, a table containing the predominant type and charge density of purified and alkaline-fractionated Kaumera* samples has been constructed (Table 6.1). The collection of ICT results indicates a net anionic character of dialyzed

Kaumera® biopolymer. However, about 40% of positively charged groups were still in this sample. With regards to the alkaline fractionation, it points out to a dialyzed gel pellet that is almost 2x more charged. Markedly, the measurable charge density of the respective alkaline supernatant increases by 18% in half sea-water conductivity. Furthermore, the charge density in "washed" Kaumera® samples was significantly lower and contained a polyacid/base charge distribution typical of a stoichiometric zwitterion or polyampholyte complex. The "washed" Kaumera® gel pellet seemed to have a slight positive charge surplus.

Hence, ICT is a suitable semi-quantitative method to estimate the ionizable groups in Kaumera®. In addition, it should be possible to monitor salt dependence and the formation of complexes via associative electrostatic interactions.

6

**Table 6.2**. Ion conductometric titration conditions and results for purified Kaumera[*] and Na-alginate samples

| Sample | Ionic strength (mS/cm or NaCl Meq) | Classification salinity level | Estimation anionic charge density, $\rho_-$ (mol/L) | Estimation cationic charge density, $\rho_+$ (mol/L) | pI *apparent* from acid/base titration |
|---|---|---|---|---|---|
| Dialyzed Na-Kaumera[*] (supernatant) | 11 or 0.10 | Highly saline | 3.78 | 2.44 | 4.18 ± 0.03 |
| Dialyzed Na-Kaumera[*] (supernatant) | 33 or 0.32 | Very highly saline (half sea-water level) | 4.46 | n/d | 4.11 ± 0.11 |
| Dialyzed Na-Kaumera[*] (pellet) | 15 or 0.14 | Highly saline | 6.35 | 4.40 | n/d |
| Washed Na-Kaumera[*] (supernatant) | 9 or 0.08 | Highly saline | 1.48 | 1.45 | 5.35 ± 0.21 |
| Washed Na-Kaumera[*] (pellet) | 8 or 0.07 | Highly saline | 2.09 | 2.97 | n/d |
| Na-alginate | 16 or 0.15 | Highly saline | 8.24 | n/a | n/a |

n/a: not applicable. n/d: not determined.

For zeta potential analysis, the dialyzed sample was stepwise diluted to obtain a suitable concentration (0.07 wt.%) and ionic strength (3 or 6 mS/cm), and the pH was varied systematically from 2-12. The samples were vigorously shaken just before the zeta potential reading, and particle size measurements were also taken via dynamic laser scattering (Malvern Zetasizer Nano) at 25 ºC. Figure 6.2d depicts the zeta-potential and mean particle size results for this alkaline-soluble fraction. This experiment confirmed the presence of positively charged ionic units in acidic Kaumera[*]. The zeta-potential curves show a common crossing point of zero charge (PZC)[21] at pH 2.6-3.0. This value should depend on the ionic nature (ionizable or quenched), the ratio of positive to negative charges, and the amount of co-adsorbed ions. Herein the PZC was apparently not so dependent on ionic strength considering small variations in conductivity to below

and above 4 mS/cm. Interestingly, the range of *apparent* p$I$ found by ICT does not coincide with the PZC observed by microelectrophoresis. However, one should note that the zeta-potential values are representative of a slipping plane between a mean coil/aggregate with regards to the solvent and not that of the actual biopolymer(s) backbone. Hence, it also depends on possible conformation (protein folding) and complexation (thermodynamics). The charge inversion observed is accompanied by aggregation and precipitation (clouding point) of the polymeric mixture with decreasing pH values starting from pH ~5. In theory, at the p$I$, a simple polyampholyte should form soluble (or dispersed) aggregates or might form a precipitate. Therefore, polymer chain mobility should decrease rapidly within the pH region 5 to 3 from electroneutrality and anticipated conformational changes. Considering the gel pellet sample, the sample remained aggregated for the whole pH range ($R_H$ = 0.9 to 2.7 μm). The average radius measured, even at alkaline-soluble conditions ($R_H$ = 160 nm), is rather large but cannot be explained if only protein secondary/tertiary structuring is assumed (typically 1-100 nm). This serves as an indication that this processed Kaumera® has aggregated subunits. Putting it into context, flexible mucin glycoproteins can form globular aggregates with sizes as large as >1 μm.[23] Alternatively, we can have aggregated complexes or coacervated proteins and polysaccharides/nucleic acids. The "washed" Kaumera® still needs electrokinetic characterization. Altogether, these results also support the idea that the as-extracted biopolymer is highly heterogeneous in composition/solubility, and one should expect to find mixed phases of solution, complex, and/or coacervate.

## Concluding remarks

Kaumera® contains significantly charged amphoteric biopolymers, *i.e.*, it can act as both a base and an acid. The typical charge density values around 3 to 6 mol/L lie in between that of charged proteins and polysaccharides, even if lower than the highly charged alginate polyelectrolyte (7 to 8 mol/L). The protein nature of the polymer should not be ignored, as well as the positive charges from amide/amine groups. We find a significant density of positive charges, with charge reversion from pH ~3 and what seems to be an *apparent* (global) p$I$ around 4 to 5. Indeed, the protein ampholyte nature in the extracted biopolymer(s) should induce a p$I$ resulting from synergistic electrostatic complexation. However, we do not know if the extracted polymers also contain separate polyelectrolytes that are not proteins, like anionic polysaccharides or oligo-sugars (phosphates), forming inter-complexes of a more dynamic nature (can have ion-hopping mechanisms).

Moreover, these complexes are expected to be mostly pH-ionized but also could bear a small fraction of strongly acidic/basic functional groups, like sulfate half esters or tertiary/quaternary amines. Until now, it remains unclear if the extracted biopolymers are predominantly of a glycoprotein nature (intra-complex) or a pool of complexed polysaccharides and proteins (inter-complex). This difference is key if we are to better interpret solubility results and the general material processing variables (miscibility, phase separation, syneresis, humidity-dependent behavior, environmental conditioning, plasticization/blending, etc.).

The extracted material has a complex solubility, which depends on pH, temperature, and ionic strength, like in proteins and polyampholyte complexes. For example, we initially expected solubility at alkaline pH 9-11, but a gel pellet was found upon centrifuging (about 30% of the initial mass). Depending on processing, a lipid-like top layer can also be observed. To understand the chemical nature influence, it is imperative to investigate the phase diagram and work with the separate phases (fractionation of solution, hydrogel, and precipitate at the condition). The thermo- and salt-sensitive behavior in solubility should be mapped in a phase diagram of the glycoprotein/coacervate[24].

Furthermore, for many zwitterions, a so-called anti-polyelectrolyte effect has been proposed, in which the polymer adopts a more expanded coil form with increasing salt levels due to better screening of intramolecular electrostatic attractions while also preventing aggregation.[28,29] The extracted Kaumera® EPS shows a similar anti-polyelectrolyte behavior, where it becomes more soluble with increasing salt content and the other way around. This is unexpected considering our working hypothesis of a charged, mostly amorphous, primarily anionic glycoprotein. One would have expected a polyelectrolyte effect or alginate-like salt dependence in a heavily charged glycosylated protein. In any case, the phase diagram of Kaumera® samples and ampholyte salt dependence requires more investigation.

Despite the intricate chemistry and behavior discussed above, in many cases, the physical and chemical evaluation of Kaumera® EPS can be largely simplified to obtain a set of desired properties for a given application, especially if the abovementioned effects of processing conditions on structure are considered.

6

## 6.2.2. Film formation through plasticization and blending

It has been previously observed that the extracted Kaumera® EPS has poor film-forming ability while also displaying fast crack propagation upon touch and high embrittlement (Figure 6.3a). Using plasticizers or blending to produce miscible polymer mixtures can improve film formation, pliability, and toughness (Chapter 2). In this assay, we have tested the possibility of improving the polymeric mix's cohesiveness and flexibility through i) the incorporation of polyol plasticizers or ii) a miscible polymer (binary blend).

Polyol-plasticized Kaumera® films were fabricated by mixing calculated volume fractions of the unprocessed polymer and plasticizer 'solutions'. The homogenous film-forming mixture, 3 wt.%, was cast in a PS petri dish and was allowed to be set via water evaporation. Both acidic and basic Kaumera® were tested, and the glass transition temperature of dried films was estimated by Dynamic Mechanical Thermal Analysis (DMTA). Only films with plasticizer content above 10 wt.% could be measured due to high brittleness (*i.e.*, spontaneous brittle failure during drying is not uncommon). The acidic/basic films with high plasticizer content, from 20 wt.%, were indeed more flexible and foldable. However, there was a tendency for the plasticizer to exudate from the film with applied pressure and/or over long storage times. The trend of polyol-induced plasticization (depression of the glass transition temperature, *Tg*) is depicted in Figure 6.3d, together with the curve fitting of the Generalized Mean model (see details in Chapter 2). Like semi-crystalline polysaccharides and proteins, the plasticized Kaumera® films also show a heterogenous behavior of *Tg* property (model constant $k_{GM} > 2$). More data is required. However, the $k_{GM}$ values are also seemingly higher for larger molecule polyols (arabitol and sorbitol), which we interpret as an indication of localized steric effects. To sum up, large amounts of plasticizer are required to achieve pliable Kaumera® films. Even though plasticization is easily achievable by incorporating polyols, at high plasticizer concentrations the stability through H-bonding is not enough to produce a stable heterogeneous mixture, and the system becomes immiscible over time. Other plasticizers and ternary mixtures shall be studied, aiming at higher stability and, preferably, excluding the high inorganic fraction in raw Kaumera®, using dialysis or "washing" procedures.
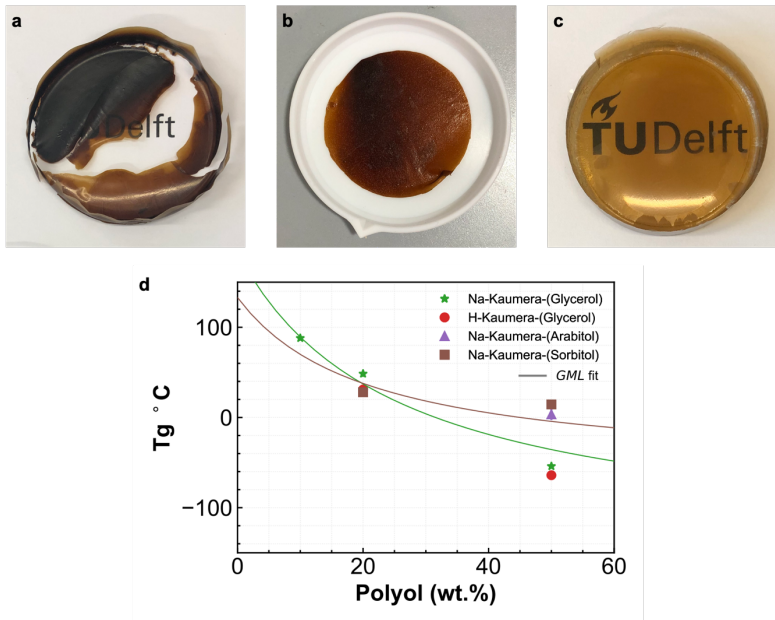
**Figure 6.3.** Solvent casting of Kaumera® materials from 3 wt.% solids: a) dialyzed K-Kaumera®. b) Plasticized Na-Kaumera®-(50 wt.% glycerol). c) Blend of Kaumera®-Gelatin A at 1:1 ratio at 9 mS/cm, pH 7.6. d) Effect of polyol plasticizers on the glass transition temperature, *Tg*, of acid and basic forms of Kaumera® polymer used as is. The Generalized Mean Linear model (*GML*) is fitted to Kaumera®-polyol *Tg* trends.

In general, we have observed that casting workable Kaumera® films without additives was impossible. The likelihood of strongly bound interchain (oppositely charged) ionic interactions and folding of rigid protein domains in Kaumera® EPS can be attributed to its brittle nature under dry conditions. Strongly bound ionic pairs might decrease the flexibility of polymer chains and be poor energy dissipators. Thus, improving film formation, toughness, and pliability of these materials might depend on charge screening effects and the degree of domains that are less or unavailable for plasticization (crosslinked and crystalline regions). A good example is the somewhat unexpected finding that Kaumera® and gelatin polymers are miscible and can form a cohesive film after hot solution processing (Figure 6.3c). The possibility of mixing the two polymers is remarkable and likely enabled by good ionic complexation (of a polyampholyte character), H-bonding, and hydrophobic interactions in this system. The complex miscibility is yet another indication of the protein-like nature of Kaumera®. This blend

6

needs further studying towards an actual structure and bonding, but we report on apparently tough and strong films without signs of phase separation.

The *Tg* of polyelectrolyte complexes and coacervates is also poorly understood, especially if combined with the influence of water. It has been previously related to changes in humidity (bound water), temperature, effective polyion pairing (intrinsic ion pairs), and sample history.[31–33] Interestingly, if the complex/coacervate is ionizable (pH-dependent), the *Tg* should present a higher sensitivity to the pH during fabrication and humidity history (annealing and storage conditions). This can lead to an unexpected antiplasticization regime, where the complex shows higher modulus/*Tg* with increasing water content, *e.g.*, through increased chain rigidity via H-bonding. Hence, a general recommendation is that relationships could be drawn from the presence of complexes in (plasticized/blended) Kaumera® EPS samples, hydration level, and the observed thermomechanical relaxations. Compatibility studies via the Generalized Mean model (Chapter 2) and solubility parameters should yield interesting results.

On the global mechanical properties, the effect of plasticizers (*e.g.*, polyols, citric acid, sugars) and blending components (*e.g.*, proteins, alginate, PVA) should be further investigated based on toughness and strength. Furthermore, the effects of ionic compatibilization and stabilization through coacervation and crosslinking steps should also be explored.

## 6.2.3. Nanocomposites

Nanofillers add to film reinforcement while conferring functionalities like mechanical, barrier, thermal, and optical properties. To this end, the degree of particle dispersion and alignment (order parameter) is crucial. We have tested the effects of filling a Kaumera®-based matrix with exfoliated montmorillonite nanoplatelets (MMT). The main goal was to apply the acquired knowledge on the positive effects of a gelling matrix to prevent MMT aggregation and promote orientational order (Chapters 4 and 5). A change in these features should yield better thermal and mechanical composite properties. In detail, we have used well-dispersed MMT composites with Na-Kaumera® and Kaumera®-Gelatin blend as matrices. This experimental design aimed at, respectively, a wet composite starting with a soft colloidal solution or with a thermo-reversible hardening gel network of polymers and colloidal nanoparticles (Figure 6.4a).

Na-Kaumera˙ was first centrifuged to remove possible large inorganic impurities, and all the supernatant was processed to a 3 wt.% stock solution at alkaline pH 9 and 16 mS/cm. To this, a complex was created using gelatin A (3 wt.%) at a mildly acidic pH 5. The complexed blend was a stable hot 'solution' at final pH 7.6 and brine conductivity 9 mS/cm and is hereby named Kau-Gel. The Na-Kaumera˙ and Kau-Gel stock solutions were used in film-forming suspensions were made containing ~50 wt.% clay loading and vigorously stirred at a high temperature, 70 °C, to allow for polymer-induced clay exfoliation. Films were produced by solvent casting at ambient conditions, Figure 6.3b, and dried using a vacuum oven at 40 °C for a day prior to analysis.

We have found lamellar nacre-like structures for both types of composite films with SEM (Figure 6.3c). Wide angle X-ray diffraction was used to monitor the $d_{001}$ basal spacing from MMT nanoplatelets, confirming good polymer intercalation (clay gallery d-spacings above 25 Å). The Kau-Gel/MMT film shows higher WAXS orientation (order parameter $<P_2> = 0.57$) than the non-gelling matrix Na-Kaumera˙ ($<P_2> = 0.42$). This is in accordance with the hydrogel affine deformation mechanism previously discussed in Chapter 5. Curiously, the XRD data for the Kau-Gel matrix showed no sign of gelatin renaturation via triple helix formation, which was probably hampered by interactions with the Kaumera˙. The storage modulus of composites was measured with DMA. The unfilled Kau-Gel sample had a modulus of 4.8 GPa. The modulus of Kaumera˙ itself cannot be measured but is expected to be ≥ 5 Gpa – from the many ionic group contributions. Even so, the ordered lamellar structure of Kau-Gel/MMT resulted in a slightly higher modulus E' = 17.0 Gpa, in contrast to Kaumera˙/MMT at 14.6 Gpa. This gives a factor 2 reinforcement efficiency for the Kau-Gel composite. These encouraging results, already for the raw biopolymer, highlight the potential of fabricating excellent Kaumera˙ based bionanocomposites using the affine deformation alignment strategy.

6
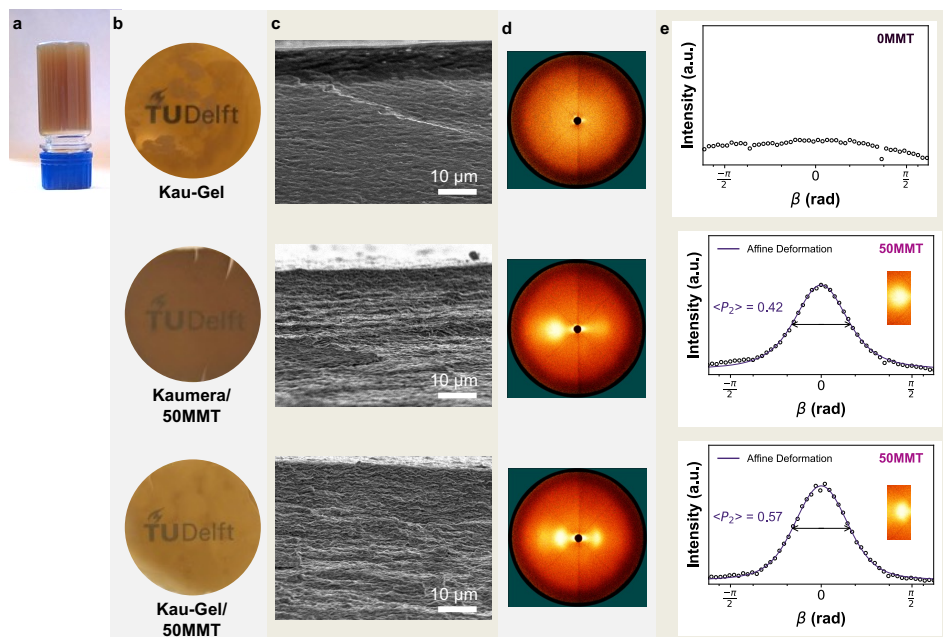
**Figure 6.4.** Nanocomposites based on Kaumera® and montmorillonite (MMT). a) Inverted vial showing the gel state of Kaumera®-Gelatin A blend, Kau-Gel, before processing with MMT. b) Images of Kau-Gel film and the nanocomposites of Kaumera® and Kau-Gel filled with 50 wt.% exfoliated MMT nanoparticles. c) SEM cross-section image of respective nanocomposites. d) 2D transmission X-ray diffraction pattern of each nanocomposite at beam inclination parallel to the film plane. E) The respective azimuthal intensity profiles of the primary diffraction peak and calculated orientation distribution functions of affine deformation and $<P_2>$ values.

Furthermore, the MMT nanomaterial is particularly interesting for its flame retardancy. Kaumera® EPS is also not toxic and also presents a non-flammable character in itself, which has been mostly attributed to the presence of phosphates enhancing char formation.[37] Thus, the combination of Kaumera®/MMT is desirable for the design of insulating foam material. We have also tested the possibility of lightweight, structured, self-standing insulating foam materials (Figure 6.5). This was achieved by appropriately mixing a Kaumera®-based binding matrix, a templating fiber-reinforcement phase (cellulose nanofibers, CNF), and well-dispersed MMT nanoclay. The Kaumera®-Gelatin complexed biopolymer blend, on a 1:1 ratio, was also evaluated. As a proof-of-concept, lightweight foams, $\rho \sim 0.027$ g/cm$^3$, were fabricated via suspension casting and freeze-drying. We report on promising properties for these open cell foams, as they can be

classified as fast self-extinguishing on a level comparable to polyurethane foams containing 25 wt.% ammonium polyphosphate[38] (94V-0 classification according to UL 94V vertical flammability test[39]). They also do not show dripping or glowing combustion, and the Kaumera®-Gelatin/CNF/MMT keeps better the specimen dimensions, possibly from the rapid sealing effect from ionic interactions[40]. These Kaumera®/CNF/MMT foams serve as an example of applied research towards sustainable bionanocomposite applications.



**UL94V test for Lightweight & Flame Retardant Foams**
**35Matrix/35CNF/30Na-MMT, 0.7 cm thick, ρ~ 0.027 g/cm³**
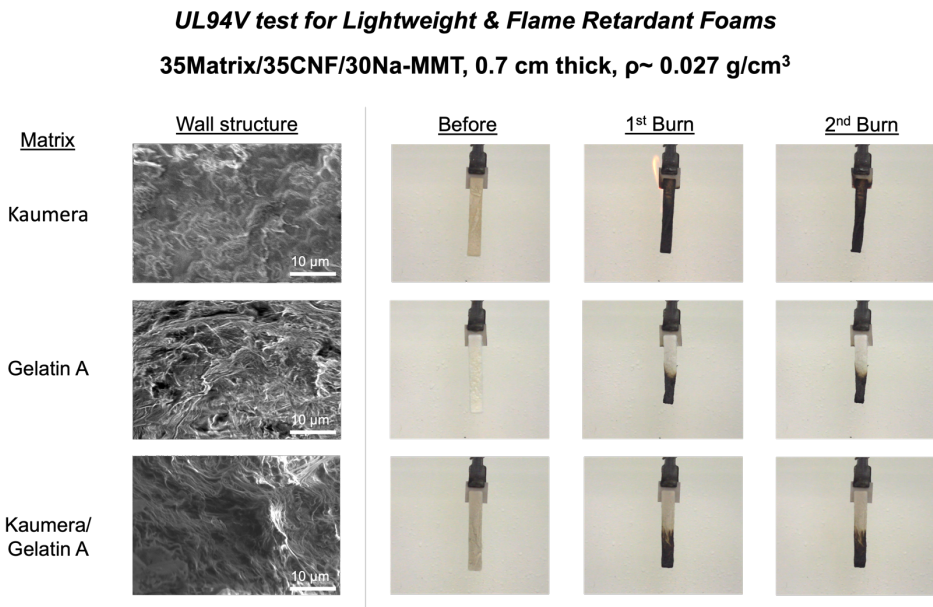
**Figure 6.5.** Aerogel foams based on 35 wt.% polymer matrix, 35 wt.% fiber reinforcement with cellulose nanofibers (CNF, produced by UMaine PDC), and 30 wt.% Na-montmorillonite nanoplatelets. The polymer matrix consisted of Na-Kaumera®, Gelatin type A, or a 1:1 mix thereof. The images show SEM micrographs of the open cell foam walls (left) and the test specimens before and after UL94V flammability test (right). The propane/butane flame distance to the specimen was 2 cm.

## 6.3. General Discussion and Outlook

## Order from chaos

The Kaumera® EPS material can be quite variable in composition and complex miscible phases depending both on the source of wastewater sludge, extraction method, and raw material processing techniques, can be found. Nevertheless, we still would like to have some level of control over how to process it for sustainable product design without having to solve the full picture of the chemical nature of each batch of raw material. In general, we have observed that there is a much higher influence of the protein or polyampholyte fraction(s) on the physicochemical properties than initially thought (the alginate-like exopolysaccharides framework[5]). We specifically note this based on the anomalous salt-dependent solubility and possible influence of temperature upon processing. In addition, the functionality and respective property profile are apparently that of a multifunctional polymeric mixture or maybe corresponding to a (set of) glycoprotein(s), as is evidenced by the appearance of several dissociation constants ($pK_a$ values) in comparison to commonly found amino-acids (ionizable amines, carboxylic) and sugar (ionizable carboxylic) functionalities. This points towards a polymeric mixture that can be called "chimeric" as an allusion to the multiheaded chimera beast from Greek mythology. Even though a multifunctional character can make research more challenging, this might be advantageous since it allows turning on/off certain charged groups for different applications, making it a versatile product from very humble waste origin. Hence, a new direction for Kaumera® EPS is to adjust the current black-box approach from alginate-like EPS to these recent insights on the protein influence and degree of multi-functionalities, for instance, by monitoring the degree of cooperative ionization through values of *apparent* p*I*. This already useful updated framework can certainly become even more refined by applying concepts borrowed from complex and coacervate formation, in particular between (poly)electrolytes and (poly)ampholytes. However, even though there is a focus on ionic groups, from a scientific viewpoint, the material scientist should be careful to at least consider the importance of other electrostatic interactions, the hydrophobic effect, and the formation of structures via renaturation (stereo complexes, helices, sheets, etc.).

All the assays above indicate that it is crucial to investigate the solubility phase diagram of Kaumera® samples, particularly the thermal and salt dependence. For that, the charge density, polymer concentration, pH, ionic strength, and non-polymeric impurities (*e.g.*, organic acids, surfactants, dyes) should be considered. For instance, it is known that the

addition of polyelectrolytes might polarize the polyampholyte, yielding different systems.[25] As for reference systems, it is curious that polyampholyte and polyelectrolyte complex mixtures, *e.g.*, proteins and DNA or hyaluronate, can also yield triphasic systems in which solution, gel, and precipitate co-exist. In addition, biopolymers with a more controlled chemical structure can be used as references, *e.g.*, gelatins and pectins. In such systems, not only ionic attractions but also H-bonding might play an important role. Likewise, if the dominant glycoprotein theory holds, the processing of analogous proteins like mucin and collagen can be further studied (H-bonding, hydrophobic, van der Waals). However, charge effects and supramolecular structures will make the interpretation of the physicochemical behavior (even) more difficult.

It is important to note that (glyco)protein folding and association to higher-order structures through self-assembly is a complex topic as it depends on the chemical nature and the environment. It is well known that peptides can organize into crystals, amorphous aggregates, colloids, super structures, fibrils, and amyloid-type fibrils. This could be studied in-depth for the purpose of interpretation of the discussed phase diagrams (biopolymer concentration, pH, T, ionic strength), for instance, via X-ray diffraction (XRD), spectroscopic methods (RAMAN, FTIR, fluorescence spectroscopy, and circular dichroism) or even scanning probe microscopy.[30] So far, we have observed only minor evidence of possible $\beta$-sheet arrangements from FTIR (amide peak at 1626 cm$^{-1}$) and XRD (amorphous broad peak at $2\theta = 22°$) peak identifications in Kaumera® samples. This is very important to know if protein structuring is affecting the thermomechanical profile of the polymeric materials, among other properties.

In connection with salt dependence, free ions can screen the charges of polyelectrolytes or polyampholytes in different ways. In a polyelectrolyte, a concentrated salt solution usually results in a screening of the backbone charges, lowering the uniform repulsive forces and resulting in coil contraction (equivalent to a non-polar polymer).[26] For ampholytes like proteins, however, the salting effect is less obvious, depending on the type and distribution of ionic groups within the structure.[27,28] Proteins might also be influenced by renaturation and the presence of hydrophobic units, which can induce packing depending on salt stabilization (*e.g.*, coil-to-globular transition). If excess salt is added, further increasing the ionic strength, a "salting out" effect might occur, where there is competition for solvent between the ionic species, *e.g.*, proteins in concentrated ammonium sulfate solution. For globular proteins, as an example, at the p*I*, the "core" can be forced out of solvent, creating a hydrophilic "edge". In fact, polyampholyte and/or polyelectrolyte complexes in nature are responsible for the self-organization of a few

types of proteins, e.g., intrinsically disordered proteins and fuzzy complexes.[27] Therefore, we recommend that the behavior of Kaumera® in solutions of varying conductivity and ionic strength be mapped under the salting in/out and anti-polyelectrolyte effect frameworks.

## Multiple Kaumera® polymers

The preliminary results on Kaumera® EPS group contributions indicate that these methods can be extended to EPS from different biological sources and processing. For example, the combination of straightforward techniques for group and elemental composition (FTIR and EDX or ICP) to analytical titrations (Acid/Base and Ion conductometric) shall yield quick results on functionality dominance and approximate quantification. This makes way to compare the bulk composition of extracted EPS from (brackish) sea-water, and domestic or industrial wastewaters. For instance, from a biologically-wired protective mechanism (Donnan potential), we expect the Kaumera® EPS from saline and domestic wastewaters to be relatively different in ionizable group content and thus charge density. Another example is related to the raw polymer processing since the dialyzed or "washed" polymer can be characterized based on the soluble or titratable functionalities. Likewise, if the raw material is bleached (*e.g.*, $H_2O_2$, in Figure 6.6) or denatured by salts (*e.g.*, urea or guanidinium), we would like to confirm if a similar character and number of functional groups remain after such chemical treatment.

To further elucidate the actual protein and polysaccharide ionic structures, size exclusion chromatography can be useful to possibly fractionate the polymeric mixture into protein-rich and polysaccharide-rich fractions. This high-end method could be coupled with qualitative and semi-quantitative analysis for charge characterization, *e.g.*, ion conductometric titration and zeta potential. In addition, if strong acids like sulfate half esters are to be characterized, it would be interesting to know if they can be measured via conductometric titrations and elemental analysis after treatment with cation exchange resin (full polymer protonation). Moreover, there is also a need for additional research on topics like protein purification methods (Hofmeister[27] and Irving–Williams series) and the influence of nucleic acids and humic-like substances on miscibility and properties.

With this chapter, we have shown that Kaumera® EPS can have a significant number of cationic charges that are able to pass through the alkaline selection barrier during

6

extraction. It remains unclear whether these charges are predominately from amino-acids (ionizable amines) or sugar monomers (*i.e.*, glucosamines like in chitosan). The zwitterion state is also relevant to study the possible antifouling property of the protein-like Kaumera® EPS.[29,34] In addition, it would be of commercial interest to investigate if an analogous but net cationic polymer material can also be extracted by starting with an acidic extraction[7] and subsequent alkaline precipitation. In other words, if a "chitosan-like" anti-Kaumera® material can be extracted from excess aerobic granular sludge.
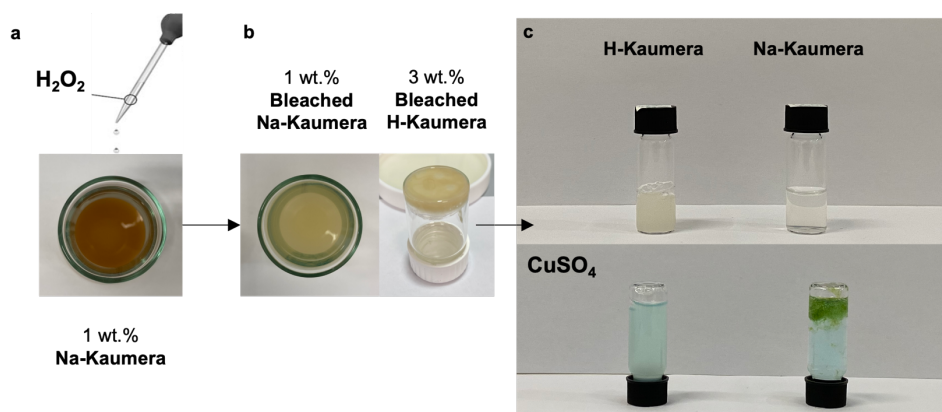


**Figure 6.6.** Kaumera® biopolymer extracted from Zutphen wastewater facility after successful $H_2O_2$-bleaching. Alkaline Kaumera® (pH 11, 1 wt.%) before (a) and after (b) bleaching with 2.5 wt.% $H_2O_2$. c) This bleached Kaumera® is tested for anionic polymer metal-ion crosslinking (40 mM $Cu^{2+}$ to 1 wt.% Kaumera®) via gelation of the acid (pH 2, HCl) and basic (pH 11, NaOH) forms. The expected Cu-Kaumera® gel formation is observed starting with the basic form. The bleaching method is still under development.

## Groundwork towards applications

This "chimeric" biopolymer can be the basis of many novel high-stiffness and lightweight materials. There is an increasing adoption of granular sludge wastewater technology[1], increasing the potential for global Kaumera® biopolymer extraction. With large-scale Kaumera® facilities, we hope several circular materials with unique properties, low environmental impact, and a lost cost can be made available in high volumes through water authorities. Consequently, fabricating high-performance (nano)composites using polymers recovered from wastewater opens avenues for creating novel lightweight, stiff, and functional products, including those with binding, adhesive, barrier, flame-retardant,

and ion-conductive properties. However, for the realization of circular Kaumera® materials, it is imperative not only to test the fabrication of composites but also to optimize the workability, toughness, strength, reactivity, and moisture-dependence of the matrix.

Currently, extensive efforts are underway to design and optimize various materials incorporating the Kaumera® biopolymer for future commercialization. For instance, the application of this biopolymer is being explored in the field of coatings for fertilizers and seeds, concrete curing, as a binding material for 3D-printing ink, and as a constituent of thermoset fiber-reinforced composites.[2,41,42] The potential for developing hydrogels, binders, absorbers, adhesives, coatings, composite membranes[43], and foams using safe and sustainable fabrication methods appears to be within reach. However, the success of these Kaumera® applications largely hinges upon achieving a high level of control over structure-properties, including rheological, thermomechanical, and barrier characteristics. Thus, there is an urgent need for a comprehensive set of tools that can rapidly characterize the chemical composition, hydrogel behavior, and solid-state properties of the polymers extracted from wastewater. Only then a myriad of materials, especially bionanocomposites, should become progressively available to supply the increasing societal demand for bio-based and circular materials.

6

# References

(1)     Kehrein, P. A. Towards Water Resource Factories: Designing and Planning Sustainable Circular Wastewater Treatment Processes, *Delft University of Technology*, **2021**. https://doi.org/10.4233/UUID:227A498C-52EE-4848-9E98-74FE0E7D2453.

(2)     The Rhine and IJssel Water Authority, the Vallei and Veluwe Water Authority, Delft University of Technology, RoyalHaskoningDHV and the Dutch Foundation for Applied Research in Water Management (STOWA(stichting ondersoek waterschappen)). *Kaumera*. https://kaumera.com/english/kaumera/ (accessed 2023-05-05).

(3)     Sutherland, I. W. Biofilm Exopolysaccharides: A Strong and Sticky Framework. *Microbiology* **2001**, *147* (1), 3–9. https://doi.org/10.1099/00221287-147-1-3.

(4)     Felz, S. Structural Extracellular Polymeric Substances from Aerobic Granular Sludge. *Delft University of Technology* **2019**, 115–115. https://doi.org/10.4233/uuid:93e702d1-92b2-4025-ab57-6d2c141ed14d10.4233/uuid:93e702d1-92b2-4025-ab57-6d2c141ed14d.

(5)     Lin, Y.; de Kreuk, M.; van Loosdrecht, M. C. M.; Adin, A. Characterization of Alginate-like Exopolysaccharides Isolated from Aerobic Granular Sludge in Pilot-Plant. *Water Research* **2010**, *44* (11), 3355–3364. https://doi.org/10.1016/J.WATRES.2010.03.019.

(6)     Lin, Y. M.; Sharma, P. K.; van Loosdrecht, M. C. M. The Chemical and Mechanical Differences between Alginate-like Exopolysaccharides Isolated from Aerobic Flocculent Sludge and Aerobic Granular Sludge. *Water Research* **2013**, *47* (1), 57–65. https://doi.org/10.1016/j.watres.2012.09.017.

(7)     Pronk, M.; Neu, T. R.; Van Loosdrecht, M. C. M.; Lin, Y. M. The Acid Soluble Extracellular Polymeric Substance of Aerobic Granular Sludge Dominated by Defluviicoccus Sp. *Water Research* **2017**, *122*, 148–158. https://doi.org/10.1016/j.watres.2017.05.068.

(8)     Flemming, H. Colloids and Surfaces B : Biointerfaces The Perfect Slime. *Colloids and Surfaces B: Biointerfaces* **2011**, *86* (2), 251–259. https://doi.org/10.1016/j.colsurfb.2011.04.025.

(9)     Seviour, T.; Derlon, N.; Dueholm, M. S.; Flemming, H.-C.; Girbal-Neuhauser, E.; Horn, H.; Kjelleberg, S.; van Loosdrecht, M. C. M.; Lotti, T.; Malpei, M. F.; Nerenberg, R.; Neu, T. R.; Paul, E.; Yu, H.; Lin, Y. Extracellular Polymeric Substances of Biofilms: Suffering from an Identity Crisis. *Water Research* **2019**, *151*, 1–7. https://doi.org/10.1016/j.watres.2018.11.020.

(10)    Lin, Y.; Reino, C.; Carrera, J.; Pérez, J.; van Loosdrecht, M. C. M. Glycosylated Amyloid-like Proteins in the Structural Extracellular Polymers of Aerobic Granular Sludge Enriched with Ammonium-oxidizing Bacteria. *MicrobiologyOpen* **2018**, *7* (6), e00616. https://doi.org/10.1002/mbo3.616.

(11)    Lin, Y. REACH Report Results for Kaumera EPS. Personal Communication., 2023.

(12)    de Graaff, D. R.; Felz, S.; Neu, T. R.; Pronk, M.; van Loosdrecht, M. C. M.; Lin, Y. Sialic Acids in the Extracellular Polymeric Substances of Seawater-Adapted Aerobic Granular Sludge. *Water Research* **2019**, *155*, 343–351. https://doi.org/10.1016/j.watres.2019.02.040.

(13)    Da Silva, B. C.; De Oliveira, M.; Ferreira, J. G. L.; Sierakowski, M. R.; Simas-Tosin, F. F.; Orth, E. S.; Riegel-Vidotti, I. C. Polyelectrolyte Complexes from Gum Arabic and Gelatin: Optimal Complexation PH as a Key Parameter to Obtain Reproducible Microcapsules. *Food Hydrocolloids* **2015**, *46*, 201–207. https://doi.org/10.1016/j.foodhyd.2014.12.022.

(14)    Bos, O. J. M.; Labro, J. F. A.; Fischer, M. J. E.; Wilting, J.; Janssen, L. H. M. The Molecular Mechanism of the Neutral-to-Base Transition of Human Serum Albumin. *Journal of Biological Chemistry* **1989**, *264* (2), 953–959. https://doi.org/10.1016/S0021-9258(19)85036-6.

(15)    Wen, S.; Xiaonan, Y.; Stevenson, W. T. Microcapsules through Polymer Complexation: I: Complex Coacervation of Polymers Containing a High Charge Density. *Biomaterials* **1991**, *12* (4), 374–384.

(16)    Xiao, S.; Zhang, Y.; Shen, M.; Chen, F.; Fan, P.; Zhong, M.; Ren, B.; Yang, J.; Zheng, J. Structural Dependence of Salt-Responsive Polyzwitterionic Brushes with an Anti-Polyelectrolyte Effect. *Langmuir* **2018**, *34* (1), 97–105. https://doi.org/10.1021/acs.langmuir.7b03667.

6

(17)     Singh, P. K.; Singh, V. K.; Singh, M. Zwitterionic Polyelectrolytes: A Review. *e-Polymers* **2007**, *7* (1). https://doi.org/10.1515/epoly.2007.7.1.335.

(18)     Johnson, K. M.; Fevola, M. J.; McCormick, C. L. Hydrophobically Modified Acrylamide-based Polybetaines. I. Synthesis, Characterization, and Stimuli-responsive Solution Behavior. *Journal of applied polymer science* **2004**, *92* (1), 647–657.

(19)     Rawel, H. M.; Kroll, J.; Hohl, U. C. Model Studies on Reactions of Plant Phenols with Whey Proteins. *Food / Nahrung* **2001**, *45* (2), 72–81. https://doi.org/10.1002/1521-3803(20010401)45:2<72::AID-FOOD72>3.0.CO;2-U.

(20)     Abramson, H. A. Electrokinetic Phenomena: VI. Relationship between Electric Mobility, Charge, And Titration of Proteins. *The Journal of general physiology* **1932**, *15* (5), 575.

(21)     Schulz, S.; Gisler, T.; Borkovec, M.; Sticher, H. Surface Charge on Functionalized Latex Spheres in Aqueous Colloidal Suspensions. *Journal of colloid and interface science* **1994**, *164* (1), 88–98.

(22)     Farris, S.; Mora, L.; Capretti, G.; Piergiovanni, L. Charge Density Quantification of Polyelectrolyte Polysaccharides by Conductometric Titration: An Analytical Chemistry Experiment. *Journal of Chemical Education* **2012**, *89* (1), 121–124. https://doi.org/10.1021/ed200261w.

(23)     Kruger, A. G.; Brucks, S. D.; Yan, T.; Cárcarmo-Oyarce, G.; Wei, Y.; Wen, D. H.; Carvalho, D. R.; Hore, M. J. A.; Ribbeck, K.; Schrock, R. R.; Kiessling, L. L. Stereochemical Control Yields Mucin Mimetic Polymers. *ACS Cent. Sci.* **2021**, *7* (4), 624–630. https://doi.org/10.1021/acscentsci.0c01569.

(24)     Sing, C. E.; Perry, S. L. Recent Progress in the Science of Complex Coacervation. *Soft Matter* **2020**, *16* (12), 2885–2914. https://doi.org/10.1039/d0sm00001a.

(25)     Kudaibergenov, S. E.; Nuraje, N. Intra-and Interpolyelectrolyte Complexes of Polyampholytes. *Polymers* **2018**, *10* (10), 1146.

(26)     Liu, G.; Parsons, D.; Craig, V. S. J. Re-Entrant Swelling and Redissolution of Polyelectrolytes Arises from an Increased Electrostatic Decay Length at High Salt Concentrations. *Journal of Colloid and Interface Science* **2020**, *579*, 369–378. https://doi.org/10.1016/j.jcis.2020.06.072.

(27)     Maity, H.; Baidya, L.; Reddy, G. Salt-Induced Transitions in the Conformational Ensembles of Intrinsically Disordered Proteins. *J. Phys. Chem. B* **2022**, *126* (32), 5959–5971. https://doi.org/10.1021/acs.jpcb.2c03476.

(28)     Gao, M.; Gawel, K.; Stokke, B. T. Polyelectrolyte and Antipolyelectrolyte Effects in Swelling of Polyampholyte and Polyzwitterionic Charge Balanced and Charge Offset Hydrogels. *European Polymer Journal* **2014**, *53*, 65–74. https://doi.org/10.1016/j.eurpolymj.2014.01.014.

(29)     Choi, W.; Park, S.; Kwon, J.-S.; Jang, E.-Y.; Kim, J.-Y.; Heo, J.; Hwang, Y.; Kim, B.-S.; Moon, J.-H.; Jung, S.; Choi, S.-H.; Lee, H.; Ahn, H.-W.; Hong, J. Reverse Actuation of Polyelectrolyte Effect for *In Vivo* Antifouling. *ACS Nano* **2021**, *15* (4), 6811–6828. https://doi.org/10.1021/acsnano.0c10431.

(30)     Pignataro, M. F.; Herrera, M. G.; Dodero, V. I. Evaluation of Peptide/Protein Self-Assembly and Aggregation by Spectroscopic Methods. *Molecules* **2020**, *25* (20), 4854. https://doi.org/10.3390/molecules25204854.

(31)     Lyu, X.; Clark, B.; Peterson, A. M. Thermal Transitions in and Structures of Dried Polyelectrolytes and Polyelectrolyte Complexes. *J. Polym. Sci. Part B: Polym. Phys.* **2017**, *55* (8), 684–691. https://doi.org/10.1002/polb.24319.

(32)     Nolte, A. J.; Treat, N. D.; Cohen, R. E.; Rubner, M. F. Effect of Relative Humidity on the Young's Modulus of Polyelectrolyte Multilayer Films and Related Nonionic Polymers. *Macromolecules* **2008**, *41* (15), 5793–5798. https://doi.org/10.1021/ma800732j.

(33)     Lalwani, S. M.; Batys, P.; Sammalkorpi, M.; Lutkenhaus, J. L. Relaxation Times of Solid-like Polyelectrolyte Complexes of Varying PH and Water Content. *Macromolecules* **2021**, *54* (17), 7765–7776. https://doi.org/10.1021/acs.macromol.1c00940.

(34)     Pfaff, N. M.; Dijksman, J. A.; Kemperman, A. J. B.; van Loosdrecht, M. C. M.; Kleijn, J. M. Rheological Characterisation of Alginate-like Exopolymer Gels Crosslinked with Calcium. *Water Research* **2021**, *207* (October), 117835–117835. https://doi.org/10.1016/j.watres.2021.117835.

6

(35)     Felz, S.; Kleikamp, H.; Zlopasa, J.; van Loosdrecht, M. C. M.; Lin, Y. Impact of Metal Ions on Structural EPS Hydrogels from Aerobic Granular Sludge. *Biofilm* **2020**, *2*, 100011. https://doi.org/10.1016/j.bioflm.2019.100011.

(36)     Collins, K. D. Ion Hydration: Implications for Cellular Function, Polyelectrolytes, and Protein Crystallization. *Biophysical Chemistry* **2006**, *119* (3), 271–281. https://doi.org/10.1016/j.bpc.2005.08.010.

(37)     Kim, N. K.; Mao, N.; Lin, R.; Bhattacharyya, D.; van Loosdrecht, M. C. M.; Lin, Y. Flame Retardant Property of Flax Fabrics Coated by Extracellular Polymeric Substances Recovered from Both Activated Sludge and Aerobic Granular Sludge. *Water Research* **2020**, *170*, 115344–115344. https://doi.org/10.1016/j.watres.2019.115344.

(38)     Ni, J.; Tai, Q.; Lu, H.; Hu, Y.; Song, L. Microencapsulated Ammonium Polyphosphate with Polyurethane Shell: Preparation, Characterization, and Its Flame Retardance in Polyurethane. *Polymers for Advanced Technologies* **2010**, *21* (6), 392–400.

(39)     UL, O. 94-Tests for Flammability of Plastic Materials for Parts in Devices and Appliances. *Underwriters Laboratories Inc* **1996**.

(40)     Zhang, L.; Huang, Y.; Sun, P.; Hai, Y.; Jiang, S. A Self-Healing, Recyclable, and Degradable Fire-Retardant Gelatin-Based Biogel Coating for Green Buildings. *Soft Matter* **2021**, *17* (20), 5231–5239. https://doi.org/10.1039/D1SM00435B.

(41)     Amsterdam Institute for Advanced Metropolitan Solutions. *COMPRO: Creating a fully circular and bio-based building material from wastewater resources*. Ams-Institute. https://www.ams-institute.org/urban-challenges/circularity-urban-regions/compro-composite-building-material-wastewater-resources/ (accessed 2023-05-05).

(42)     Spinnewijn, O. Sustainable Binders for the Creation of a Dredge-Based Tile, Utrecht University, 2021. https://studenttheses.uu.nl/handle/20.500.12932/191 (accessed 2023-05-05).

(43)     Zlopaša, J. Exploring the Structure, Properties, and Applications of Highly Ordered Bionanocomposites. *Delft University of Technology* **2017**. https://doi.org/10.4233/uuid:e47bfa54-4d58-4c82-829f-3cb2ceb6cfc7.

**6**

6

# 7

# Nanocellulose recovery from domestic wastewater

*"For an idea that does not first seem insane,*

*there is no hope."*

*– Albert Einstein*

This chapter was published as:

# Abstract

*Wastewater solids could be an attractive source of secondary raw cellulose, mainly originating from toilet paper. Cellulose can be recovered through sieving of raw wastewater, return sludge, or excess sludge. In particular, a large fraction of cellulose (13-15%) can be found in the excess sludge of the aerobic granular sludge produced by the* Nereda° *wastewater technology. A cellulose extraction method was developed during this study, allowing the recovery of a pulp with over 86 wt% purity. The wastewater derived cellulose fibres could be an excellent source for production of recovered cellulose nanocrystals (rCNC). Several pre-treatment steps needed in cellulose nanocrystals (CNC) production from wood pulp are already performed in the production of toilet paper. Here, the technical feasibility of such rCNC is studied. As reference materials, microcrystalline cellulose and toilet paper were also used. The rCNC were obtained by acid hydrolysis, with yields of ~30 wt% (pulp basis). The wastewater-based material was rod-like, with high aspect ratio (10-14), crystallinity (62-68%), and chemical structure similar to commercial CNC. The yield of rCNC per gram of cellulose recovered from the influent was 22%, while for excess sludge cellulose it was less (4%). Bio-nanocomposites of rCNC and alginate were also investigated. At 50 vol% loading of rCNC, there was a 50% relative increase in stiffness (18 GPa) compared to matrix (12 GPa). The characterization of rCNC and positive impact in composite materials confirms a suitable quality of wastewater derived CNC. Ultimately, the nanocellulose is a tangible example that recovery of high-end products from wastewater is possible, in line with a circular economy.*



| Wastewater Treatment Plant | CNC Nanocellulose | CNC films |

7
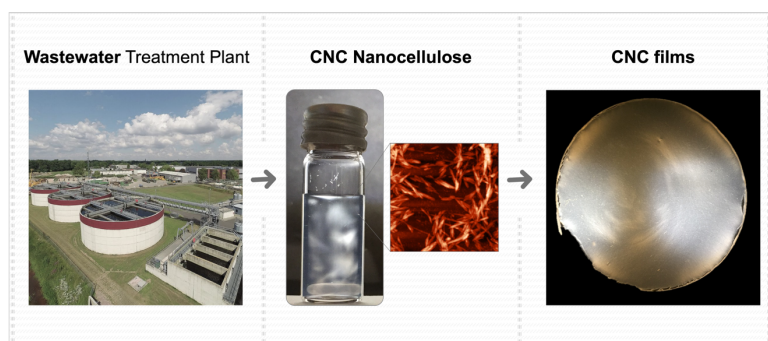
## 7.1. Introduction

For thousands of years, mankind process cellulose derived from plants in the production of pulp, paper, and derivatives. With the adoption of toilet paper in modern societies, cellulose fibres became, in many countries, a primary insoluble substrate entering sewage treatment plants (STP). They now compose 30 – 50% of the total solids in the sewage of western countries (Ghasimi et al., 2015a). A large fraction of this cellulosic matter is recalcitrant to current physicochemical and biological treatment technologies, resulting in extra surplus sludge production. Hence, more chemicals, aeration, and post-treatments are required to dispose of this urban waste. Although limited research has been conducted on the fate and recovery of cellulose in wastewaters (Chen et al., 2017; Ghasimi et al., 2016; Shun'ichi et al., 2002), the topic has lately gained the attention of water authorities.

Fine sieves have been proposed as alternative for primary clarifiers (Rusten and Odegaard, 2006), when applied at a higher loading rate mainly the cellulosic fraction is recovered from the wastewater (Ruiken et al., 2013). Recovery of the cellulosic fraction can contribute to a more circular economy and improvement of the wastewater treatment process as a whole (Reijken et al., 2018). In the last decade, a few sites have adopted this technology, mainly in Europe and North America (Nussbaum et al., 2014; Paulsrud et al., 2014; Ruiken et al., 2013; Rusten and Odegaard, 2006). Fine sieving before the biological treatment results in a fibrous mass of influent solids, which contains around 70 wt.% cellulose (Figure 7.1) (Ruiken et al., 2013). Due to the low biodegradability of cellulose, other common wastewater solids have a high cellulose content, such as primary and waste sludge (Shun'ichi et al., 2002). Interesting new opportunities could be opened by the widely deployed aerobic granular sludge technologies, like the Nereda® technology (Pronk et al., 2015). The suspended sludge fraction (containing the influent cellulose) has a low retention time in the granular reactors (Ali et al., 2019). Thus, resulting in a relative low biodegradation of the cellulose, which accumulates in the excess sludge (Figure 7.1) (Pronk, 2016).

7
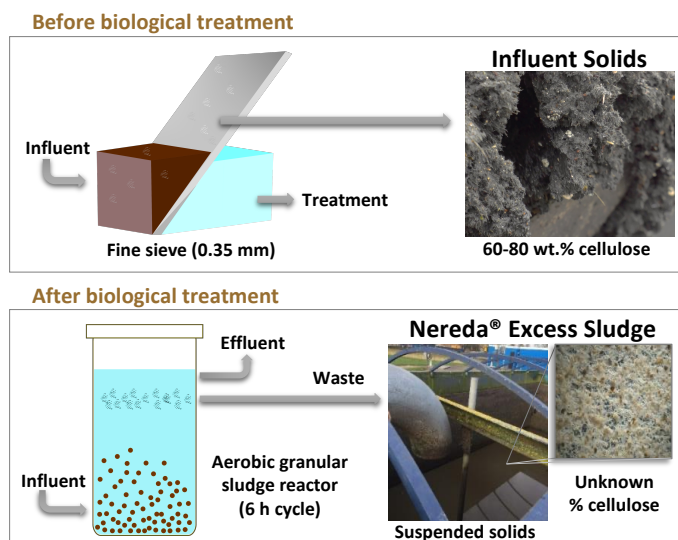
**Figure 7.1.** The generation of cellulosic wastewater solids before and after biological treatment. The upper scheme shows the (sieved) influent solids being harvested, with 20–30 wt. % total solids, of which around 60–80 wt.% is cellulose. The lower scheme indicates that the suspended sludge and solids, or excess sludge, produced at the end of an aerobic granular sludge treatment cycle (around 6 h), are potentially rich in cellulose fibres.

The development of materials from wastewater can improve the economy of the water sector and integrate it in the circular economy (Leeuwen, 2018). Cellulose is a well-known renewable constituent in the production of green materials. There are many possible valorisation routes for raw cellulose. Applications can be developed using the fibre itself - in the paper, construction, furniture, textile, and automotive industries; or producing valuable chemicals, such as bioethanol and bioplastics (Ghasimi et al., 2016; Zhou et al., 2019). An interesting application could be the conversion of the wastewater derived cellulose pulp into nanocellulose.

The cellulose fibre exhibits highly ordered crystalline domains separated by less ordered domains, called amorphous regions. There are two main routes for production of the nanocrystalline cellulose: *(i)* mechanically, to produce Cellulose NanoFibres, and *(ii)* chemically, to produce Cellulose NanoCrystals (CNC). These nanocellulose fibres are potentially interesting, due to their exceptional stiffness (on par with Kevlar®), high aspect ratio, low density, low thermal expansion, simple surface modification, and low toxicity. (Börjesson and Westman, 2015; Klemm et al., 2011; Rajinipriya et al., 2018). Such

properties, together with renewability and biodegradability, make nanocellulose an ideal sustainable material. There are numerous high-end applications of CNC in the composite, paper, filtration and separation, food, biomedical, automotive, and cosmetic industries (Charreau et al., 2020; Qin et al., 2020; Rajinipriya et al., 2018; Roy et al., 2018; Trache et al., 2020).

Nanocellulose as new bio-based material has gained momentum, and its production is now beyond scientific curiosity with a growing interest in research and development. Large-scale commercialization is already a reality, and there is increasing industrial interest (Mabrouk et al., 2020; Reid et al., 2017). During the past decade, the production of cellulose nanoparticles from lignocellulosic biomass, bacterial cellulose, paper and pulp industrial wastes have been extensively published (García et al., 2016; Jordan et al., 2019; Kumar et al., 2020; Rajinipriya et al., 2018; Reid et al., 2017). The potential of municipal solid waste paper for nanocellulose isolation has been recently mentioned (Hietala et al., 2018). However, the production of cellulosic nanomaterial from recovered toilet paper or wastewater solids has not been reported.

Cellulose from wastewater may be an interesting source of fibres for CNC production in comparison with the often-studied wood pulp or agricultural wastes, as several bleaching and purification steps can be avoided. These treatments have been performed in the production of the original cellulose toilet paper. Thus, recovered cellulose nanocrystals (rCNC) are explored as a new bio-based material for the valorisation of wastewater-based cellulosic material. The main goal of this study was to investigate the lab-scale production of rCNC from wastewater solids of Dutch treatment plants. The yield and the physical properties of rCNC were evaluated. Finally, bio-nanocomposites with rCNC and alginate polymer were manufactured. This had a two-fold purpose: *(i)* measuring the stiffness of commercial and lab-made rCNC for quality comparison and *(ii)* as a material concept that may be suitable for application.

## 7.2. Materials and Methods

### 7.2.1. Sampling of wastewater solids

Samples were collected either through sieving of raw wastewater or from the excess sludge of aerobic granule reactor.

## Sieved influent solids

Screened wastewater (mesh size 6 mm) was finely sieved by a rotating belt filter equipped with a <0.35 mm pore size sieve (Salsnes Filter, Norway) at the STP Blaricum, the Netherlands, operated by Waternet. Plant size was of 30,000 p.e. and maximum hydraulic capacity 1600 $m^3$ $h^{-1}$. The retained influent solids were collected in December 2016 and stored at 4 °C before analysis. The influent solids were mainly composed of toilet paper fibres and residual sand, hair, leaves, and undefined materials. When dried, the material resembles papier-mâché. The total solids content was 162 ± 8 g $kg^{-1}$, with 150 ± 9 g $kg^{-1}$ volatile, measured according to standard methods (APHA, 1998). Further information on fine sieving can be found in previous reports (Ghasimi et al., 2016; Ruiken et al., 2013).

## Nereda˚ excess sludge

Excess sludge samples were taken from a Nereda˚ plant operated on domestic wastewater by Royal HaskoningDHV in Utrecht, the Netherlands. The Nereda˚ aerobic granule reactor is operated in sequencing batch mode, with process cycles of ± 6 hours. Within these hours, approximately 1h is for anaerobic feeding in upwards plug-flow with simultaneous effluent withdrawal. The majority of remaining time is for aeration, followed by past settling (Giesen et al., 2013; Pronk et al., 2015). The prototype was in the start-up phase since 19th December 2016. Starting-up means the biomass concentration and granulation grade in the reactor are increasing over time. During the first sampling, cellulose fibres seemed to be building up in the reactor. The plant had a maximum hydraulic capacity of 125 $m^3h^{-1}$ and volume of 1,000 $m^3$. The reactor was fed with screened (6 mm) municipal wastewater. Sampling campaigns happened in January (sample NES 1) and March 2017 (sample NES 2), at the sludge buffer tank where this material is often discharged (Figure 7.1). The samples were concentrated on-site by settling and decanting off clear supernatant and further stored at 4 °C. Total suspended solids (TSS) and volatile suspended solids (VSS) were measured according to standard methods (APHA, 1998). For NES 1, TSS was 13.0 ± 0.2 g $L^{-1}$ and VSS was 11.7 ± 0.4 g $L^{-1}$. For NES 2, TSS was 14.0 ± 0.1 g $L^{-1}$ and VSS was 12.5 ± 0.3 g $L^{-1}$. The used excess sludge was a mixture of flocculent solids that remain on the surface of the granular sludge blanket after aeration, at times combined with some granular sludge that is less frequently removed. Granules larger than 0.2mm were mostly absent; but on the other hand, samples visibly contained seeds, sands, plastics, among other debris. For completeness, several excess sludge samples were also collected from full-scale Nereda˚ treatment plants across the Netherlands.

7

## 7.2.2. Cellulose extraction

A cellulose extracting method was developed based on a pulping process (blending and sieving in combination with the removal of water and alkaline-soluble compounds) and final bleaching treatment. The protocol is described in detail in Supporting Information (online).

### Extraction scheme

The standard cellulose extraction procedure is briefly described. The sample was dried, cut into 1x1 cm pieces and blended with demi water until forming a homogeneous suspension. It was then heated on a hot plate to 50 °C while stirring for removing water-soluble compounds. Next, the residue of filtration was placed in a beaker with an alkaline solution and heated to 80 °C. The mixture was sieved and washed thoroughly with demi water for removing alkaline-extracted compounds. This alkaline step was performed at least twice. Finally, the remaining residue was bleached with a $NaClO_2$ solution with a slightly acidic buffer. After a final sieving and washing step (until neutral pH), the resultant pulp was thoroughly dried at 60 °C. The yield of cellulose pulp was calculated based on the sample's initial solid content. All reagents were of analytical grade and used without further processing.

### Alkaline and bleaching tests

Influent solids and excess sludge cellulose extractions were tested using a 2 wt.% NaOH solution for alkalisation. Further, an extended alkaline treatment was tested for sludge due to its expected high microbial and polymeric content. Bleaching tests were performed by using a solution composed of equal parts of 1.7 wt.% $NaClO_2$ and acetate buffer (27 g NaOH and 75 mL glacial acetic acid in 1 L, pH 4.6). The minimum reaction time for each bleaching step was ~6 hours in a heating environment of 60 – 70 °C. More than one bleaching step was sometimes tested to ensure the samples were almost free of (coloured) impurities.

### Van Soest analysis

The method of Van Soest and Wine (1967), initially developed for estimating dietary fibre fractions, was used to obtain fractions of lignin, hemicellulose, and cellulose in samples. The method is based on the combined activity of detergents. With the assay, three fibre residues were obtained: neutral detergent fibre (NDF), acid detergent fibre (ADF) and acid detergent lignin (ADL), from which it is possible to evaluate the lignin (ADL),

celluloses (ADF–ADL) and hemicelluloses (NDF–ADF). The technique was applied to cellulosic pulp extracted from both influent solids and excess sludge to check for the validity of the extraction method. Recycled pulp toilet paper (TP, sampled from the university's lavatory) was also tested.

## 7.2.3. Nanocellulose (CNC) isolation

After obtaining the recovered pulp, a controlled acid hydrolysis was tested for nanocellulose isolation.

### Materials

Sulphuric acid 95–98 % was purchased from Sigma-Aldrich. For dialysis, cellulose acetate bags with 3,500 Da molecular weight cut off were purchased. Avicel PH101 Eur. microcrystalline cellulose was acquired from Sigma-Aldrich. TP was first cleaned by the cellulosic pulp extraction method (section 2.2.1). A commercial sample, CelluForce° NCC, was obtained via a donation from a current industrial producer (CelluForce, Montreal, Canada). CelluForce uses 64 wt.% sulphuric acid hydrolysis to produce CNC from bleached Kraft pulp. Following hydrolysis, this commercial CNC is commonly diluted, separated from residual acid, neutralised to sodium form, and spray dried. All chemicals were of analytical grade and used as received.

### Isolation procedure

The (r)CNC isolation was initially tested via controlled acid hydrolysis with sulphuric acid (64 wt.% $H_2SO_4$, 1:20 cellulose to acid ratio) at 45 °C. These conditions are commonly applied to paper and lignocellulosic sources (Rajinipriya et al., 2018). Following hydrolysis, quenching, centrifugation with demi water, glass fibre vacuum filtration, neutralisation with NaOH, dialysis (4 days) and ultrasonication steps were sometimes performed. The exact hydrolysis conditions had to be modified for each cellulose source and are described in detail in Supporting Text S7.1. The yield of isolated (r)CNC from the treated cellulose sources was determined gravimetrically by freeze-drying after ultrasonication.

### Cellulose sources

Several sources were tested for CNC isolation. As reference materials, microcrystalline cellulose and TP were used first to obtain a baseline method. Then, influent solids and excess sludge pulp were tested for rCNC production. The recovered pulp was milled

(mesh 0.5 mm, Fritsch mill D-55743, Germany) before hydrolysis to guarantee homogenous fibre digestion. In addition, key hydrolysis parameters were tested, and different conditions of centrifugation and washing steps, filtration, and neutralisation were applied.

## 7.2.4. Nanocellulose (CNC) characterization

### Birefringence and haze

Well-known optical properties of CNC suspensions were used to detect a significant presence of CNC nanoparticles in isolated samples. To assess whether there was self-assembly of nanocrystals in suspension and films, the samples were observed in between crossed polarizers with a background source of light. For suspensions, this was done after shaking and standing for 5' to observe flow birefringence. The presence of this refractive property under shear indicated a biphasic behaviour (isotropic and nematic liquid crystal phases of CNC). If samples display permanent birefringence (no flow, at rest) , the samples were considered to be in the chiral nematic regime (Habibi et al., 2010). The presence of haziness in dried films was also used for identification of chiral nematic phase formation.

### Atomic force microscopy (AFM)

Atomic force microscopy (AFM) was performed to determine the morphology and dimensions of the isolated and commercial CNC by using a Ntrega Prima NT-MDT scanning probe microscope (Moscow, Russia). Before the observations, a few drops of diluted aqueous suspension (mildly ultrasonicated) were placed on a Si wafer and allowed to dry for 20' at RT. The samples were scanned in tapping mode, using ETALON probes, at RT. The length and width of CNC were measured using Nova Px software by manually obtaining the values from at least three different pictures, of which 20 values were averaged.

### Fourier transform infrared spectroscopy (FTIR)

The surface chemistry of CNC were analysed by Fourier Transform InfraRed spectroscopy (FTIR) spectra. The samples were ground and mixed with KBr at a ratio of 1:100 (w/w) and pressed into thin pellets before analysis. A FTIR spectrometer (Nicolet 6700 from Thermo Fisher Inc., USA) was used from 400 to 4000 cm$^{-1}$ at a resolution of 2 cm$^{-1}$. The acquired spectrum was an average of 32 scans.

7

## X-ray diffraction (XRD)

XRD was performed on CNC with a Bruker D8 Advance diffractometer in Bragg-Brentano geometry ($\lambda$ = 1.78897 Å), with lynxeye position sensitive detector. A cobalt tube with iron filter scattered from 5° to 55° while the sample was spinning, using step size 0.05° and counting time 0.8 s per step. The crystallinity index (CrI) was estimated according to the equation: $CrI(\%) = (I_{200} - I_{am})/I_{200} \times 100$, where $I_{200}$ is referred to the maximum intensity of the 200 lattice diffraction peak at region around $2\theta$ = 26.1 ° and $I_{am}$ is the intensity of diffraction for the amorphous part at around $2\theta$ = 21.0 ° (Segal et al., 1959). The angle values were translated from Cu K$\alpha$ values to Co-equivalent by using Bragg's equation and d-spacing values for native cellulose (Poletto et al., 2014).

## Bio-nanocomposites for mechanical performance

Bio-nanocomposites were made by adding the isolated and commercial CNC to Na-Alginate polymer matrix. CNC from TP and influent solids were chosen as a reference for the wastewater-recovered material. Sodium Alginate (mannuronate/guluronate = 1.56, Mw = 150 kg mol$^{-1}$) was obtained from Sigma-Aldrich, and was used as received. Thin-films were prepared by mixing equal parts of 2 wt.% CNC suspensions with alginate solutions (2 wt.%). The CNC volume fraction used was 50 vol.% (density of both materials can be assumed as 1.5 g cm$^{-3}$). All mixtures were ultrasonicated for 5 min on ice prior and after mixing (Brandson ultrasonicator, 40 % duty cycle, microtip limit 3). No remaining agglomerates were visible. The resulting dispersions were dried (20°C, 50 % RH) in a Petri dish. The storage modulus of dried Na-Alginate-CNC films was assessed by Dynamic Mechanical Analysis (DMA, PerkinElmer Pyris Series DMA7e, USA)) using rectangular strips (around 0.25mm $\times$ 10mm $\times$ 85 μm) cut out from the films. Testing was done in the linear regime for 2 minutes using tensile clamps at 1 Hz and 2 mm amplitude. The reinforcement efficiency (RE) was obtained by: $RE = (E_c - E_m)/E_m$, where $E_c$ is the modulus of composite and $E_m$ is the modulus of matrix.

## 7.3. Results and Discussion

## 7.3.1. Cellulose extraction

For the sieved influent solids, standard cellulose extraction procedure, with two NaOH extraction steps and one bleaching step, was sufficient to remove sludge and most of the colour (Figure 7.2). Moreover, heating with demi water already eliminated some

turbidity, and a layer of scum was formed, indicating fat removal. On the other hand, for Nereda® excess sludge, after first alkaline treatment (2 wt.% NaOH), the samples were still viscous, and fibres presented a dark-brownish appearance. This was solved with more successive alkaline treatments - two times or more depending on wastewater solids characteristics - or even treatments with increased NaOH concentration (4–8 wt.%). In general, after three consecutive alkaline treatments with NaOH, the resulting pulp was similar to the pulp obtained from influent solids. Without these steps, the samples always caused clogging during sieving, even with 350 µm sieves. Overall, following the NaOH treatments, a gradual decolouration of the sample occurred, leaving mainly cellulosic fibres. Non-cellulosic coloured material are well known to be partially solubilized in high alkaline conditions (dos Santos et al., 2016). This explains the high colour removal efficiency at high pH (13). The procedure is similar to what is applied in the delignification and pulping used by the paper industry to remove as much as possible the non-cellulosic components, i.e., hemicellulose and lignin-like compounds (García et al., 2016).

The number of bleaching steps varied per wastewater solid investigated. For fibrous material that has been in contact with wastewater/sludge for a short time, such as influent solids, one bleaching step was sufficient to extract cellulose. The resulting fibres had a white appearance, which indicates low impurity (Figure 7.2). The bleaching needed for excess sludge also varied between the samples collected. For sludge samples from the Nereda® plant, one bleaching step was sufficient. The bleaching of cellulose is performed for obtaining a more homogeneous and decolorized pulp (dos Santos et al., 2016). The slightly acidic chlorite ($ClO^{2-}$) bleaching can be performed in single or multiple steps, depending on the cellulose source, without considerably altering the intrinsic cellulose percentage of the sample. However, this procedure is not ideal due to the formation of bleaching by-products. Other more eco-friendly (but maybe less efficient) bleaching methods, such as the use of ozone, hydrogen peroxide, and, more recently, oxygen delignification with bleach effluent recovery could be explored in future (dos Santos et al., 2016; García et al., 2016).

Depending on the wastewater source, a lot of other inert debris can be present that interfere in the extraction and measurement of cellulose. Thus, it is imperative that, for cellulose quantification, the analysis is only carried out on wastewater/sludge where the cellulose input is much higher than that of other inert solids, such as sands, plastics, and seeds. This is a limitation of the proposed method. Moreover, dry milling at 0.5 mm mesh size has also resulted in some purification of the extracted pulp via fractionation. Heavier

7

material deposit first, and the low-density (loosened) cellulose fibres remain on top, thus, can be separated.

With a defined method, the cellulosic content of wastewater samples could be determined, which can be found in Table 7.1. The cellulose of the influent solids was high, around 65 % (g g dry matter$^{-1}$). Excess sludge from the Nereda® reactor contained only 13 to 15 % (g g TSS$^{-1}$). The cellulosic content in wastewater solids can be interfered by varying human activity, seasonal changes, and pre-treatment (Ghasimi et al., 2015b).

As confirmed by the Van Soest method, both wastewater derived pulps showed a high cellulosic content (> 86 %), and low hemicellulose and lignin values (Table 7.2). In addition, a similar cellulose content, around 80 %, was obtained for the reference toilet paper with both the developed and Van Soest methods (Tables 7.1 and 7.2). This validates the proposed cellulose extraction. Nevertheless, the Van Soest method as an approach for measuring the cellulose content of wastewater samples should be used with caution, since polysaccharides, proteins, and divalent cations can affect the assay (Chai and Udén, 1998). The limitations of this method are also related to its impracticality and the fact that at least 10 g of dry solids are required for the experiment. In this sense, the newly developed alkaline-bleaching method is a useful alternative.

7
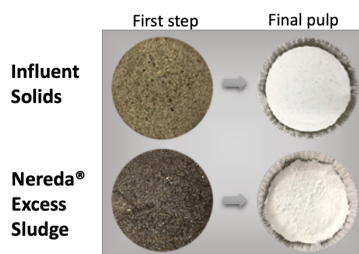
**Figure 7.2.** The residues collected on sieve after the first cellulose extraction step and the final pulp for sieved influent solids (upper scheme), and Nereda® excess sludge (lower scheme).

**Table 7.1.** The yield of cellulosic pulp on initial dry mass and back-calculated concentrations for toilet paper and wastewater solids

| Sample | Cellulosic pulp (wt.% on initial dry matter) | Cellulose concentration (g Kg$^{-1}$) |
|---|---|---|
| Toilet Paper | 84.7 | n.d. |
| Influent solids | 64.8 ± 6.6 | 105.1 ± 5.3 |
| Nereda® excess sludge 1 | 13.1 ± 0.4 | 10.1 ± 0.3 |
| Nereda® excess sludge 2 | 15.3 ± 1.3 | 11.0 ± 0.9 |

n.d., not determined.

**Table 7.2.** Van Soest analysis for toilet paper and extracted cellulosic pulp

| Sample | Cellulose (wt.%) | Hemicellulose (wt.%) | Lignin (wt.%) |
|---|---|---|---|
| Toilet Paper[*] | 80.3 | 9.2 | 4.2 |
| Influent solids pulp | 87.4 | 4.2 | 0.8 |
| Nereda® excess sludge pulp | 86.1 | 4.9 | 1.1 |

[*] Sample was analysed as is and might contain additives.

## 7.3.2. Nanocellulose (CNC) isolation

Controlled acid hydrolysis was tested for CNC isolation from reference (microcrystalline cellulose, toilet paper) and recovered cellulosic pulp. The procedure varied per cellulose source, as hydrolysis conditions are crucial for obtaining the nanocrystals (Börjesson and Westman, 2015). For microcrystalline cellulose, reaction times were higher (>100 min),

187

but all other conditions used were standard. Moreover, for microcrystalline cellulose, a direct strong acid addition (96.5 %) on wet cellulose resulted in good CNC isolation, in agreement with Bondeson et al. (2006). Microcrystalline cellulose has a highly crystalline structure composed of bundles of heterogeneous cellulose microfibril aggregates, which are strongly hydrogen-bonded (dos Santos et al., 2016). Thus, microcrystalline cellulose is intrinsically harder to hydrolyse. In contrast, slightly higher cellulose to acid ratio (1:30 or 1:55) and shorter reaction times (45 to 60 minutes) were better for the isolation of CNC from toilet paper and recovered cellulose. The addition of cold 60 % acid instead of 96.5 % was also imperative. These settings avoided fast cellulose degradation and often resulted in a deep yellow reaction mixture after hydrolysis (colour reflects release of residual impurities, e.g. lignin). An increase in temperature from 45 to 50 °C also induced faster kinetics.

Toilet paper was also studied for regular and longer reaction times (60' and 120' reaction time, respectively). The longest reaction time resulted in a dark hydrolysis liqueur, where yellow-brownish impurities were formed. This indicates over-hydrolysis of the cellulose, with by-products formation (polymers, sugars, salts) (Reid et al., 2017; Silvério et al., 2013). More specifically, caramelization has happened (formation of C double bonds due to dehydration). For such samples, longer centrifugation-washing and dialysis cycles were necessary.

However, part of the colour developed during hydrolysis remained in all isolated CNC (Figure 7.3), possibly because large sugars attached to the surface.

The CNC extraction procedure can include several post-treatment steps, such as washing, centrifugation, sonication, homogenization, dialysis, neutralization. For the CNC isolated from microcrystalline cellulose and toilet paper, neutralisation with NaOH was required due to inefficient dialysis, which could have caused adhesion of hydrolysis by-products on the nanocrystals (Reid et al., 2017). Neutralisation was also performed in previous studies by using 0.1 to 0.25 mM NaOH (Chen et al., 2016; Reid et al., 2017). Due to impurities of the wastewater-derived pulp, several centrifugation-washing cycles and filtration steps were also required to obtain CNC from influent solids and excess sludge cellulose. These impurities were still present in these pulp samples and were visible again at the bottom of the reaction flask after hydrolysis. Therefore, there is room for optimization in the rCNC production.

The yields of (r)CNC on a pulp basis were 38 %, 32.8 %, 33.4 ± 17.9 %, and 26.5 ± 8.2 % for microcrystalline cellulose, toilet paper (60' reaction time), influent solids, and excess

7

sludge pulps, respectively. This corresponds to 38 %, 26.2 %, 21.7 ± 11.6 %, and 4 ± 1.2 % (r)CNC per g source. The yield of CNC from microcrystalline cellulose is in accordance with literature (30 %) (Bondeson et al., 2006). For toilet paper CNC and rCNC, the yield on an extracted-pulp basis was similar, but with large variation for the latter. Hydrolysis conditions, especially the reaction time, strongly influence the yield of (r)CNC, reflecting a balance between the cleavage of fibre amorphous domains and by-product formation. The CNC yields based on starting material mostly agree with values previously reported for waste paper (1.5 – 64 %) and lignocellulosic wastes (26 – 77 %) (García et al., 2016; Kumar et al., 2020; Silvério et al., 2013).

## 7.3.3. Nanocellulose (CNC) characterization

After obtaining suitable CNC isolation for each cellulose source, the visual appearance was compared. In aqueous suspensions of lab-made CNC, haze and dynamic birefringent domains were observed (Figure 7.3), which is typical of CNC. In addition, a bluish-colour was observed for the CNC suspensions obtained from microcrystalline cellulose and influent solids. This bluish colour has also been reported for many types of CNC suspensions (Börjesson and Westman, 2015).

Chiral nematic CNC can reflect/transmit visible light depending on the length of the chiral pitch, where different wavelengths are reflected differently, and white light gets reflected emitting different colours. The chiral liquid crystal birefringence was more intense with higher CNC concentration in suspension and longer ultrasonication periods (dispersion of nanocrystals), as can be observed for the MCC sample. In very dilute regimes (<0.15 wt.%), the suspensions did not show haziness nor birefringence (Supporting information). In addition, the isolated CNC showed good colloidal stability in water (Supporting information). The stability in water of the isolated-CNC can be attributed to negative hydroxyl groups from the cellulose structure and sulphate half esters groups grafted on the surface of nanocrystals during hydrolysis (Rajinipriya et al., 2018). This structure also assists in the formation of liquid crystal phases and affects the CNC rheology. Finally, thin flakes were produced via freeze-drying (Fig. 3), with an appearance similar to commercial products.

7
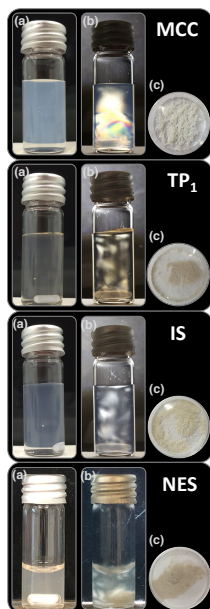
**Figure 7.3.** Suspensions of CNC isolated from different sources: microcrystalline cellulose (MCC), toilet paper with regular extraction time (TP₁), sieved influent solids (IS), and Nereda° excess sludge (NES). Concentrations are ~1 wt.% for MCC, and ~0.15 wt.% for TP₁, IS, and NES. (a) Under normal illumination. (b) Under cross polarisation and shear. (c) Freeze-dried CNC powder.

The isolated-(r)CNC samples show a rod-like morphology, similar in appearance to commercial CNC, as observed with AFM (Figure 7.4). The nanocrystals length and diameter could also be estimated, and a relatively high aspect ratio (L/D: 10 – 14) was observed for the isolated (r)CNC. This aspect ratio was in line with the commercial CNC sample, which had an L/D of 15. Typical CNC aspect ratios range from 1 to 100 (Börjesson and Westman, 2015; Reid et al., 2017). The average dimensions of CNC from microcrystalline cellulose and commercial CNC were in the same range, around 86 – 110 nm long and 7 nm wide. Interestingly, the (r)CNC isolated from toilet paper and wastewater-pulp had similar dimensions: lengths ranging from 111 to 134 nm and diameters from 10–14 nm. In a previous report, nanorods showed typical dimensions of 5 to 20 nm in diameter and 100 to 500 nm in length for several waste-recovered CNC (García et al., 2016). The morphology and dimensions are usually related to the hydrolysis conditions, such as acid to fibre ratio and acid concentration, hydrolysis time, temperature, in which extreme conditions can lead to shorter nanoparticles and higher dispersibility (Reid et al., 2017; Wang et al., 2019).
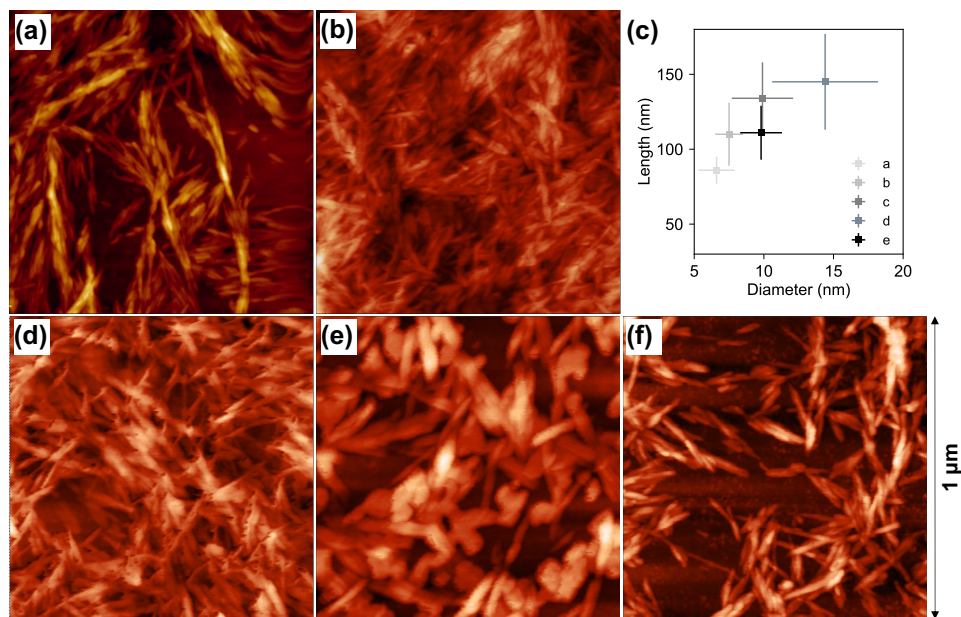
**Figure 7.4.** AFM images of CNC from different sources: (a) commercial and isolated from (b) microcrystalline cellulose, (d) toilet paper with regular extraction time, (e) influent solids and (f) Nereda® excess sludge. The area covered by the images is 1x1 μm. (c) The diameter and length of the CNC samples is shown.

FTIR spectra were obtained to assess changes in surface chemistry with cellulose and CNC isolation treatments. The spectra are shown in full and also with a focus on the fingerprint region, which is assigned to stretching vibrations in the $1800 – 700$ cm$^{-1}$ region (Figure 7.5). Some of the peaks observed can be attributed respectively to 1640 cm$^{-1}$: O-H bending vibration of absorbed water, 1428 cm$^{-1}$: CH$_2$ symmetric bending, 1160 cm$^{-1}$: C-O-C asymmetric stretching of cellulose, 1100 cm$^{-1}$: β-glucosidic ether linkages (C-O-C) of the anydroglucopyranose ring, 810 cm$^{-1}$: sulphonation. Features representative of cellulose I at 1428, 1160, and 1110 cm$^{-1}$ wavelengths (Chen et al., 2016) are present in all samples of nanocellulose. All the isolated CNC showed strong similarities to the FTIR spectrum for commercial CNC. At 3400 cm$^{-1}$ region, there is wrinkling in the spectra of MCC, TP$_2$, and TP$_1$. This can be related to the hydrophilic tendency of nanowhiskers. Furthermore, the appearance of a peak at 810 cm$^{-1}$ is due to sulphate half ester groups attached to the nanocrystals via esterification. It is estimated that by using 64 % sulphuric acid, around $0.5 – 2$ % sulphate half esters will be added to the CNC's surface (Börjesson

and Westman, 2015). The analysis supports that cellulose and nanocellulose have been produced from wastewater solids.
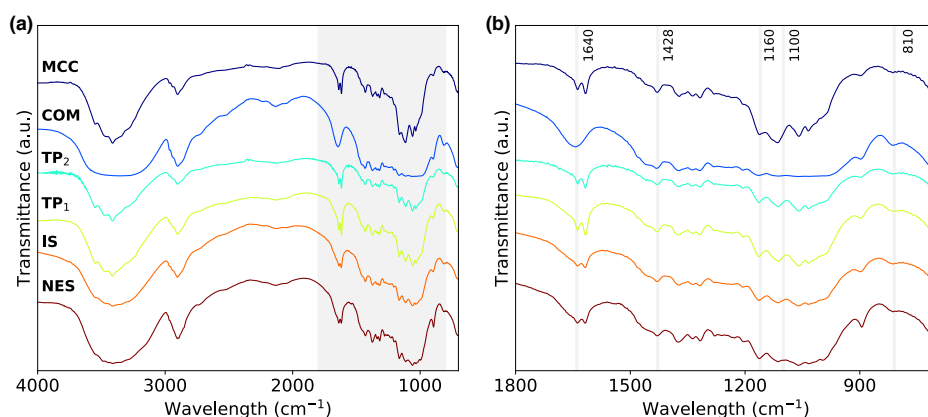


**Figure 7.5.** FTIR spectra of CNC from microcrystalline cellulose (MCC), commercial CNC (COM), toilet paper with long (TP$_2$) and regular extraction time (TP$_1$), sieved influent solids (IS), Nereda® excess sludge (NES) origin (top-down curves respectively). (a) Full-length spectra with a highlight in the fingerprint region. (b) Zoomed view of fingerprint region.

The diffraction peaks of the studied CNC, see Figure 6.6a, showed reflection peaks at 16.8 °, 18.6 °, 26.1 °, and 40.4 °, for all samples. These peaks are related to the crystal planes $1\bar{1}0$, 110, 200, and 040, respectively, which are commonly attributed to native cellulose I (Poletto et al., 2014). The major peak at 26.1 ° corresponds to the crystalline structure of cellulose I. These cellulose reflections are expected but also indicate that the primary crystal structure of the cellulosic source is preserved. The diffraction patterns of wastewater-extracted rCNC are similar to commercial CNC. However, for wastewater-rCNC, other extra peaks were observed at 13.6 °, 23.7 °, and 34 °. CNC from microcrystalline cellulose also showed many other peaks, with a major peak at 37.2 °. They are resulting from the mineralisation of compounds from the acid hydrolysis or neutralisation steps, like Na$_2$SO$_4$. Based on the diffraction peak 200 and the amorphous region, the crystallinity index of samples could be estimated (Figure 7.6b). CrI was similar among samples, ranging from 62 – 68 % for toilet paper-based CNC. Overall, CrI for toilet paper-based sources is comparable to the value of commercial CNC (73 %). Moreover, the crystallite size of CNC samples can also be estimated by using Scherrer's

192

equation (Das et al., 2009). The crystallite values ranged from 4 to 8 nm for all the isolated-CNC and had an average size of 4.6 nm for the toilet paper-based CNC. This is in accordance with previously reported for cellulose (5 nm) (Poletto et al., 2014). This value represents a relative estimation of the crystalline portions of the isolated nanostructures, and is complementary to AFM dimensions. It is important to note that cellulose crystallites also present imperfections and, thus, a significant portion of the nanocellulose edges can still be less ordered or amorphous.



| | CrI (%) |
|---|---|
| MCC | 80 |
| COM | 73 |
| TP$_2$ | 66 |
| TP$_1$ | 65 |
| FSF | 62 |
| ES | 68 |
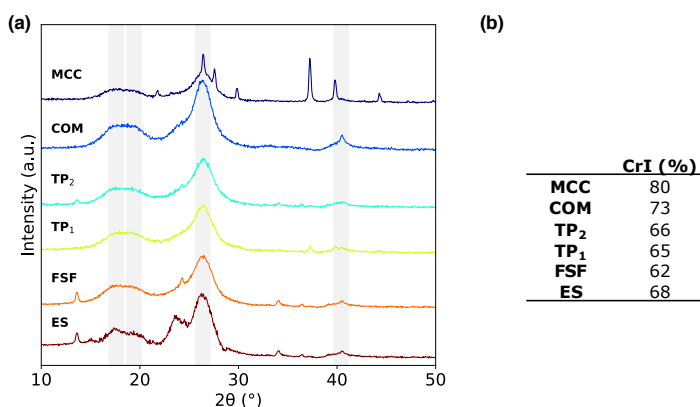
**Figure 7.6.** (a) X-ray diffractograms of CNC from microcrystalline cellulose (MCC), commercial CNC (COM), toilet paper with long (TP$_2$) and regular extraction time (TP$_1$), sieved influent solids (IS), Nereda® excess sludge (NES) origin (top-down curves respectively), with evidence on the peak's correspondent to the crystal lattice structure of native cellulose. (b) Crystallinity index of the samples obtained by the equation proposed by Segal et al.

Bio-nanocomposites were produced with Na-Alginate and CNC of both commercial and lab origin (Figure 7.7a). The films were opaque but translucent. In between polarizers, all films of Alginate-50 vol.% CNC displayed a few birefringent domains, typical of the chiral nematic phase of CNC. The storage modulus for the produced films is shown in Figure 7.7b. The modulus of a neat Na-Alginate film was 12 GPa, which by addition of 50 vol.% commercial CNC increased to 19 GPa, resulting in the reinforcement efficiency of 58 % for this filler. All isolated CNC increased the stiffness of alginate films to a similar value. The CNC from influent solids reinforced the modulus of alginate by 50 % (18 GPa). The other isolated CNC (microcrystalline cellulose, TP) showed a relative increase in the alginate modulus of 42 % and 83 % (or 17 and 22 GPa), respectively. This is on par with

7

the stiffness obtained using commercial CNC. The development of nanocellulose-reinforced composites takes advantage of the CNC's intrinsically high mechanical properties, aspect ratio, and surface area. In many studies, dramatic changes to the modulus of bio-nanocomposites are reported even at low CNC fraction (dos Santos et al., 2016; Wang et al., 2019). CNC have been used as a filler to reinforce composites with several biopolymers, such as cellulose acetate butyrate, chitosan, starch, and polylactic acid (Börjesson and Westman, 2015; Wang et al., 2019). Both optical and mechanical properties support the fact that the isolated toilet paper and wastewater-CNC have great potential as nanoparticle reinforcement agents.
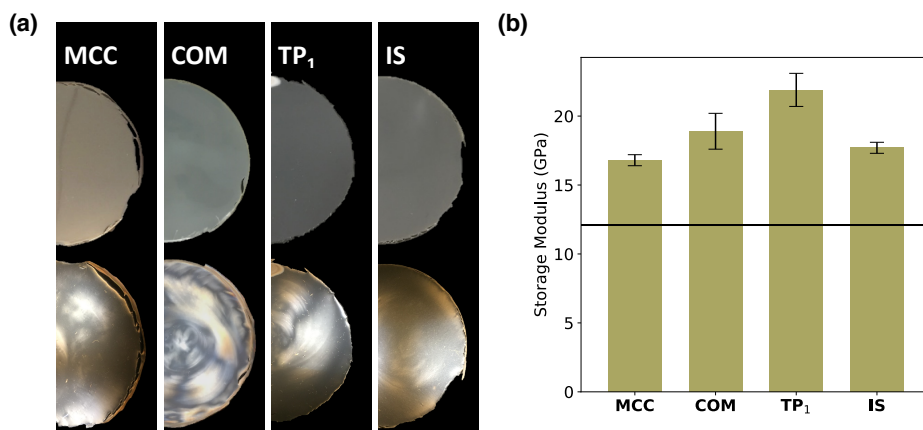


**Figure 7.7.** (a) Alginate bio-nanocomposites with 50 vol.% CNC from microcrystalline cellulose (MCC), commercial CNC (COM), Toilet paper (regular extraction time, $TP_1$), and sieved influent solids (IS) origin. Upper films are shown under normal illumination, whereas lower images are under cross polarisation. (b) Storage modulus of the bio-nanocomposites of Na-Alginate and CNC (50 vol.%). The modulus of Na-alginate is indicated by the black horizontal line.

Thus, the aspect ratio, morphology, chemical structure, crystallinity, and reinforcement of toilet paper-based CNC were convincingly similar to commercial CNC.

## 7.3.4. Nanocellulose from wastewater

The global production of household and sanitary paper (including toilet paper) was 36 million tons in 2018 (FAO, 2018). In the Netherlands only, it was estimated that toilet

paper consumption is around 1 kg per person per month (Ruiken et al., 2013), which can amount to over 200 kt annually. Cellulosic wastewater solids (e.g., influent solids or excess sludge) are mostly being incinerated, digested, or composted, increasing the costs of waste management facilities. Alternatively, other uses have already been proposed, such as a soil conditioner, substrate for bioenergy, chemicals, construction material, composites, etc. (Da Ros et al., 2020; Ghasimi et al., 2016; Palmieri et al., 2019; Zhou et al., 2019). The origin of such waste is still the main limitation for reuse opportunities due to its appearance and odour. The alkaline-bleaching method for extracting pulp from wastewater recovers high-quality cellulose. Hence, it could be applied for developing (sustainable) recovered cellulose applications. Instead of using the raw recovered matter, resource recovery could shift towards the production of high-end materials, including nanocellulose.

Secondary sources of cellulose, such as waste paper, have not been suggested for CNC production until recently (Hietala et al., 2018; Kumar et al., 2020). The cellulose fraction in agro-wastes is usually lower than in waste paper, with cellulose varying from 25 % (olive husks) to 56.5 % (sunflower shells) and lignin values as high as 50.4 % (García et al., 2016). Influent solids therefore showed to be a more attractive source for CNC production, with only a few pulping and bleaching steps required. This makes it an interesting source for CNC production due to its high cellulose content and abundance at a potentially low economical and energy cost. Nevertheless, other properties of wastewater-rCNC require research, such as thermal stability, charge density, etc.

The nanocellulose from wastewater could also be investigated by studying alternative pre-treatments and isolation techniques. The latter can be chemical, by using other acid forms, oxidative and ionic liquid reaction, mechanical, or even microbial (Rajinipriya et al., 2018; Wang et al., 2019). Greener and more efficient methods could be found. For instance, Cellulose NanoFibres could be obtained with no chemicals required (Nechyporchuk et al., 2016). Therefore, implementing cellulose recovery aligned to nanocellulose production can be considered as an option. Nanocellulose recovery could even be done by means of a smart waste management with concomitant production of high-value products.

Finally, recovered nanocellulose shows potential for making fully wastewater-based bio-nanocomposites in combination with extracellular polymers extracted from excess

7

sludges (Kaumera Nereda® Gum[1]) (Felz et al., 2016; Leeuwen, 2018). The need for alkaline conditions in both cellulose recovery and e.g., Kaumera® production gives options to integrate the recovery of both materials in a wastewater resource recovery facility. Nanocellulose composites have shown great mechanical and thermal properties while maintaining light transmittance and biodegradability (Wang et al., 2019). Bio-composites from wastewater-rCNC, possibly even in combination with other recovered materials, could result in novel and sustainable high-performance materials. Hence, the production of nanocellulose serves as an inspiring example of resource valorisation for the water sector in the broader context of a circular economy. For further information, the reader is referred to a public video (TU Delft TV/TU Delft, 2019).

## 7.4. Conclusions

A facile procedure for cellulose extraction and the determination of cellulose content in wastewater solids or sludge was demonstrated. The method is based on alkaline and bleaching treatments and, therefore, is source-specific. The studied sample only needs initial screening, however a cross-check by using the Van Soest method is recommended. This study covers extractions for sieved influent solids and excess sludge wastes, which can yield pulp with high cellulose fractions (>86 wt.%).

Controlled acid hydrolysis can be used to isolate Cellulose NanoCrystals from toilet paper and wastewater derived cellulose. Wastewater-rCNC isolation is a feasible process since the yield based on cellulosic pulp can be above 30 %. Sieved influent forms an attractive cellulose source with a high overall yield rCNC (22 % g $g_{solids}^{-1}$) compared to Nereda® excess sludge (4 % g $g_{sludge}^{-1}$). All the suspensions of CNC show visible flow birefringence, typical of this material. The TP- and wastewater-CNC are rod-like, around 130 nm long and 10 nm wide (L/D ratio ranges from 10 to 14). The functional groups on CNC are mainly correlated to the cellulose origin and severity of the acid treatment. The rCNC's crystallinity is comparable to that of commercial (62–68 %). In addition, bio-nanocomposites of wastewater-CNC and Na-alginate can be produced via solvent-casting. It appears that wastewater-CNC is an attractive nanofiller, resulting in high stiffness bio-nanocomposites (18 to 22 GPa). The relative increment in stiffness by TP or

[1] Kaumera Nereda® Gum mainly consists of the polymeric substances, i.e., glycoproteins, extracted from aerobic granular sludge. Kaumera® was formerly known as alginate-like exopolymers due to similar properties with alginate biopolymers.

wastewater-CNC addition ranges between 50 and 83 %. This increment is remarkably similar to the commercial product (58 %). Therefore, the aspect ratio, morphology, chemical structure, crystallinity, and reinforcement of wastewater-CNC samples are convincingly similar to the current commercial standard.

## Supporting information

The complete supporting information is available at DOI: 10.1016/j.jclepro.2020.124507

## Supporting Text S7.1. Acid hydrolysis of MCC, toilet paper, and recovered cellulose

7

**Table S7.1.** Acid hydrolysis conditions applied for each cellulose source investigated

| Hydrolysis conditions | MCC | TP | IS pulp | NES pulp |
|---|---|---|---|---|
| Cellulose : acid ratio | 1 g: 20 mL | 1 g: 45 mL | 1 g: 50 mL | 1 g: 30 mL |
| Acid addition | $1^{st}$: addition 44.3 mL demi water. $2^{nd}$: 55.7 mL of 96.5% $H_2SO_4$ added dropwise, on ice, vigorous mixing. | $1^{st}$: addition 22.2 mL demi water. $2^{nd}$: 96.5% $H_2SO_4$ (22.8 mL) was slowly added, on ice (<20°C), stirring with a glass rod. | Cold 60% $H_2SO_4$ was slowly added, on ice (<20°C), stirring with a glass. | Cold 60% $H_2SO_4$ was slowly added, on ice (<20°C), stirring with a glass rod. |
| Acid concentration | 64% | 60% | 60% | 60% |
| Temperature | 45 °C – 50 °C | 45 °C – 50 °C | 50 °C | 45 °C |
| Time | 105'-120' | 60'($TP_1$) and 120'($TP_2$) | from 45'-60' | 45' – 50' |
| Centrifugation and washing | 3 x 10' at 10000 rpm, 4 °C, or until turbid supernatant[*] | 4 times of 20' at 4400 rpm 4 °C or until turbid supernatant[*] | 3 times of 20' at 4400 rpm 4 °C or until turbid supernatant | 3 times of 20' at 4400 rpm 4 °C or until turbid supernatant |
| Filtration | Not necessary | Several filtration steps with glass fibre vacuum filtration were performed | Several filtration steps with glass fibre vacuum filtration were performed | Many vacuum filtration steps with glass fibre filters were performed |
| Dialysis | 4 days, ultrapure water, changed every day | 4 days, ultrapure water, changed every day | 4 days, ultrapure water, changed every day | 4 days, ultrapure water, changed every day |
| Reference | Adapted from Bondeson et al. (2006) | This study | This study | This study |

MCC: microcrystalline cellulose; TP: recycled pulp toilet paper; IS: sieved influent solids; NES: Nereda[*] excess sludge
[*] NaOH drops were added to precipitate the CNC and neutralize mixture.

# References

1. Ali, M., Wang, Z., Salam, K.W., Hari, A.R., Pronk, M., Van Loosdrecht, M.C.M., Saikaly, P.E., 2019. Importance of species sorting and immigration on the bacterial assembly of different-sized aggregates in a full-scale Aerobic granular sludge plant. Environ. Sci. Technol. doi.org/10.1021/acs.est.8b07303

2. APHA, 1998. APHA: Standard Methods for the Examination of Water and Wastewater. Am. Public Heal. Assoc. Water Work. Assoc. Environ. Fed. 552.

3. Bondeson, D., Mathew, A., Oksman, K., 2006. Optimization of the isolation of nanocrystals from microcrystalline cellulose by acid hydrolysis. Cellulose 13, 171–180. doi.org/10.1007/s10570-006-9061-4

4. Börjesson, M., Westman, G., 2015. Crystalline Nanocellulose — Preparation, Modification, and Properties, in: Cellulose - Fundamental Aspects and Current Trends. doi.org/10.5772/61899

5. Chai, W., Udén, P., 1998. An alternative oven method combined with different detergent strengths in the analysis of neutral detergent fibre. Anim. Feed Sci. Technol. 74, 281–288. doi.org/10.1016/S0377-8401(98)00187-4

6. Charreau, H., Cavallo, E., Foresti, M.L., 2020. Patents involving nanocellulose: Analysis of their evolution since 2010. Carbohydr. Polym. 237, 116039. doi.org/10.1016/j.carbpol.2020.116039

7. Chen, R., Nie, Y., Kato, H., Wu, J., Utashiro, T., Lu, J., Yue, S., Jiang, H., Zhang, L., Li, Y.Y., 2017. Methanogenic degradation of toilet-paper cellulose upon sewage treatment in an anaerobic membrane bioreactor at room temperature. Bioresour. Technol. 228, 69–76. doi.org/10.1016/j.biortech.2016.12.089

8. Chen, Y.W., Lee, H.V., Juan, J.C., Phang, S.M., 2016. Production of new cellulose nanomaterial from red algae marine biomass Gelidium elegans. Carbohydr. Polym. 151, 1210–1219. doi.org/10.1016/j.carbpol.2016.06.083

9. Da Ros, C., Conca, V., Eusebi, A.L., Frison, N., Fatone, F., 2020. Sieving of municipal wastewater and recovery of bio-based volatile fatty acids at pilot scale. Water Res. doi.org/10.1016/j.watres.2020.115633

10. Das, K., Ray, D., Bandyopadhyay, N.R., Ghosh, T., Mohanty, A.K., Misra, M., 2009. A study of the mechanical, thermal and morphological properties of microcrystalline cellulose particles prepared from cotton slivers using different acid concentrations. Cellulose 16, 783–793. doi.org/10.1007/s10570-009-9280-6

11. dos Santos, F.A., Iulianelli, G.C. V, Tavares, M.I.B., 2016. The Use of Cellulose Nanofillers in Obtaining Polymer Nanocomposites: Properties, Processing, and Applications. Mater. Sci. Appl. 7, 257–294. doi.org/10.4236/msa.2016.75026

12. FAO, 2018. FAOSTAT Forestry Production and Trade [WWW Document]. FAO Yearb. For. Prod. URL http://www.fao.org/faostat/en/#data/FO (accessed April 2020).

13. Felz, S., Al-Zuhairy, S., Aarstad, O.A., van Loosdrecht, M.C.M., Lin, Y.M., 2016. Extraction of Structural Extracellular Polymeric Substances from Aerobic Granular Sludge. J. Vis. Exp. e54534. doi.org/10.3791/54534

14. García, A., Gandini, A., Labidi, J., Belgacem, N., Bras, J., 2016. Industrial and crop wastes: A new source for nanocellulose biorefinery. Ind. Crops Prod. 93, 26–38. doi.org/10.1016/j.indcrop.2016.06.004

15. Ghasimi, D.S.M., de Kreuk, M., Maeng, S.K., Zandvoort, M.H., van Lier, J.B., 2016. High-rate thermophilic bio-methanation of the fine sieved fraction from Dutch municipal raw sewage: Cost-effective potentials for on-site energy recovery. Appl. Energy 165, 569–582. doi.org/10.1016/j.apenergy.2015.12.065

16. Ghasimi, D.S.M., Tao, Y., de Kreuk, M., Abbas, B., Zandvoort, M.H., van Lier, J.B., 2015a. Digester performance and microbial community changes in thermophilic and mesophilic sequencing batch reactors fed with the fine sieved fraction of municipal sewage. Water Res. 87, 483–493. doi.org/10.1016/j.watres.2015.04.027

17. Ghasimi, D.S.M., Tao, Y., De Kreuk, M., Zandvoort, M.H., Van Lier, J.B., 2015b. Microbial population dynamics during long-term sludge adaptation of thermophilic and mesophilic sequencing batch digesters treating sewage fine sieved fraction at varying organic loading rates. Biotechnol. Biofuels 8, 171. doi.org/10.1186/s13068-015-0355-3

18. Giesen, A., de Bruin, L.M.M., Niermans, R.P., van der Roest, H.F., 2013. Advancements in the application of aerobic granular biomass technology for sustainable treatment of wastewater. Water Pract. Technol. 8, 47–54. doi.org/10.2166/wpt.2013.007

19. Habibi, Y., Lucia, L.A., Rojas, O.J., 2010. Cellulose nanocrystals: Chemistry, self-assembly, and applications. Chem. Rev. 110, 3479–3500. doi.org/10.1021/cr900339w

20. Hietala, M., Varrio, K., Berglund, L., Soini, J., Oksman, K., 2018. Potential of municipal solid waste paper as raw material for production of cellulose nanofibres. Waste Manag. 80, 319–326. doi.org/10.1016/j.wasman.2018.09.033

21. Jordan, J.H., Easson, M.W., Dien, B., Thompson, S., Condon, B.D., 2019. Extraction and characterization of nanocellulose crystals from cotton gin motes and cotton gin waste. Cellulose 26, 5959–5979. doi.org/10.1007/s10570-019-02533-7

22. Klemm, D., Kramer, F., Moritz, S., Lindström, T., Ankerfors, M., Gray, D., Dorris, A., 2011. Nanocelluloses: A new family of nature-based materials. Angew. Chemie - Int. Ed. 50, 5438–5466. doi.org/10.1002/anie.201001273

23. Kumar, V., Pathak, P., Bhardwaj, N.K., 2020. Waste paper: An underutilized but promising source for nanocellulose mining. Waste Manag. 102, 281–303. doi.org/10.1016/j.wasman.2019.10.041

24. Leeuwen, K. Van, 2018. The Energy & Raw Materials Factory : Role and Potential Contribution to the Circular Economy of the Netherlands. Environ. Manage. 786–795. doi.org/10.1007/s00267-018-0995-8

7

25. Mabrouk, A. Ben, Dufresne, A., Boufi, S., 2020. Cellulose nanocrystal as ecofriendly stabilizer for emulsion polymerization and its application for waterborne adhesive. Carbohydr. Polym. 229. doi.org/10.1016/j.carbpol.2019.115504

26. Nechyporchuk, O., Belgacem, M.N., Bras, J., 2016. Production of cellulose nanofibrils: A review of recent advances. Ind. Crops Prod. 93, 2–25. doi.org/10.1016/j.indcrop.2016.02.016

27. Nussbaum, B.L., Soros, A., Mroz, A., Rusten, B., 2014. Removal of Particulate and Organic Matter from Municipal and Industrial Wastewaters Using Fine Mesh Rotating Belt Sieves. Proc. Water Environ. Fed. 2006, 3052–3056. doi.org/10.2175/193864706783750907

28. Palmieri, S., Cipolletta, G., Pastore, C., Giosuè, C., Akyol, Ç., Eusebi, A.L., Frison, N., Tittarelli, F., Fatone, F., 2019. Pilot scale cellulose recovery from sewage sludge and reuse in building and construction material. Waste Manag. doi.org/10.1016/j.wasman.2019.09.015

29. Paulsrud, B., Rusten, B., Aas, B., 2014. Increasing the sludge energy potential of wastewater treatment plants by introducing fine mesh sieves for primary treatment. Water Sci. Technol. 69, 560–565. doi.org/10.2166/wst.2013.737

30. Poletto, M., Ornaghi Júnior, H.L., Zattera, A.J., 2014. Native cellulose: Structure, characterization and thermal properties. Materials (Basel). 7, 6105–6119. doi.org/10.3390/ma7096105

31. Pronk, M., 2016. Aerobic Granular Sludge: Effect of Substrate on Granule Formation. PhD Thesis, Delft University of Technology.

32. Pronk, M., de Kreuk, M.K., de Bruin, B., Kamminga, P., Kleerebezem, R., van Loosdrecht, M.C.M., 2015. Full scale performance of the aerobic granular sludge process for sewage treatment. Water Res. 84, 207–217. doi.org/10.1016/j.watres.2015.07.011

33. Qin, L., Gao, H., Xiong, S., Jia, Y., Ren, L., 2020. Preparation of collagen/cellulose nanocrystals composite films and their potential applications in corneal repair. J. Mater. Sci. Mater. Med. 31. doi.org/10.1007/s10856-020-06386-6

34. Rajinipriya, M., Nagalakshmaiah, M., Robert, M., Elkoun, S., 2018. Importance of Agricultural and Industrial Waste in the Field of Nanocellulose and Recent Industrial Developments of Wood Based Nanocellulose: A Review. ACS Sustain. Chem. Eng. 6, 2807–2828. doi.org/10.1021/acssuschemeng.7b03437

35. Reid, M.S., Villalobos, M., Cranston, E.D., 2017. Benchmarking Cellulose Nanocrystals: From the Laboratory to Industrial Production. Langmuir 33, 1583–1598. doi.org/10.1021/acs.langmuir.6b03765

36. Reijken, C., Giorgi, S., Hurkmans, C., Pérez, J., van Loosdrecht, M.C.M., 2018. Incorporating the influent cellulose fraction in activated sludge modelling. Water Res. doi.org/10.1016/j.watres.2018.07.013

37. Roy, S., Zhai, L., Van Hai, L., Kim, J.W., Park, J.H., Kim, H.C., Kim, J., 2018. One-step nanocellulose coating converts tissue paper into an efficient separation membrane. Cellulose 25, 4871–4886. doi.org/10.1007/s10570-018-1945-6

38. Ruiken, C.J., Breuer, G., Klaversma, E., Santiago, T., van Loosdrecht, M.C.M., 2013. Sieving wastewater - Cellulose recovery, economic and energy evaluation. Water Res. 47, 43–48. doi.org/10.1016/j.watres.2012.08.023

39. Rusten, B., Odegaard, H., 2006. Evaluation and testing of fine mesh sieve technologies for primary treatment of municipal wastewater. Water Sci. Technol. 54, 31–38. doi.org/10.2166/wst.2006.710

40. Segal, L., Creely, J.J., Martin, A.E., Conrad, C.M., 1959. An Empirical Method for Estimating the Degree of Crystallinity of Native Cellulose Using the X-Ray Diffractometer. Text. Res. J. 29, 786–794. doi.org/10.1177/004051755902901003

41. Shun'ichi, K.H., Naoyuki, M., Iwahori, Honda, S., Miyata, N., Iwahori, K., 2002. Recovery of biomass cellulose from waste sewage sludge. J. Mater. Cycles Waste Manag. 4, 46–50. doi.org/10.1007/s10163-001-0054-y

42. Silvério, H.A., Flauzino Neto, W.P., Pasquini, D., 2013. Effect of incorporating cellulose nanocrystals from corncob on the tensile, thermal and barrier properties of poly(vinyl alcohol) nanocomposites. J. Nanomater. 2013. doi.org/10.1155/2013/289641

43. Trache, D., Thakur, V.K., Boukherroub, R., 2020. Cellulose Nanocrystals/Graphene Hybrids—A Promising New Class of Materials for Advanced Applications. Nanomaterials 10, 1523. doi.org/10.3390/nano10081523

44. TU Delft TV/TU Delft, 2019. The hidden gems of wastewater. YouTube: youtu.be/cC0-LYWHoXg. (accessed April 2020), The Netherlands.

45. Van Soest, P.J.., Wine, R.H., 1967. Use of Detergents in the Analysis of Fibrous Feeds. IV. Determination of Plant Cell-Wall Constituents. J. A.O.A.C. 50, 50–55. doi.org/10.1016/j.ijhydene.2012.08.110

46. Wang, J., Liu, X., Jin, T., He, H., Liu, L., 2019. Preparation of nanocellulose and its potential in reinforced composites: A review. J. Biomater. Sci. Polym. Ed. 30, 919–946. doi.org/10.1080/09205063.2019.1612726

47. Zhou, Y., Stanchev, P., Katsou, E., Awad, S., Fan, M., 2019. A circular economy use of recovered sludge cellulose in wood plastic composite production: Recycling and eco-efficiency assessment. Waste Manag. doi.org/10.1016/j.wasman.2019.08.037

7

7

# 8

## Outlook

## 8. Outlook

The aim of this thesis was to develop structure-property relationships for biopolymers and nanocomposites thereof. To this end, research was conducted systematically evaluating solid-state properties of alginates, gelatin, and wastewater-recovered polymers, such as Kaumera® EPS and cellulose. Regarding nanocomposites, theoretical background and structural analysis on 2D materials (platelets and sheets) were given; robust strategies were explored for producing exfoliated and highly ordered bionanocomposites, even at a high level of nanofiller incorporation. This is a start towards the design of ultimate material properties directed to bio-based (natural and recovered resources) and nearly natural components. This section selected topics for an overarching or general discussion on understanding and tuning of bionanocomposites. For each topic, an outlook is given to guide future research efforts in this field.

## 8.1. Heterogeneity in biopolymer systems

**Chapter 2** deals with monitoring changes in the glass transition property, *Tg*, concerning the developed structures in solid-state biopolymer systems. A case study using polyols and Na-alginate as a rigid, semi-crystalline matrix indicated that plasticizers, typically small molecules, might partition into plasticizer-rich domains. This heterogenous miscibility is attributed to regio-specific interactions and possible steric effects. The data interpretation was much substantiated by a model developed during this thesis work, the Generalized Mean model. The linearized version of this thermodynamical model, *GML*, is versatile and can be applied to an extensive set of biopolymer systems (plasticized or in a blend). Another essential feature is the possibility of modeling the *Tg* profile of samples showing anti-plasticization behavior. The *GML* has proven useful as a descriptive model for the heterogeneity expected in many binary bio-based materials, including complex structures. For instance, in cases where polymer semi-crystallinity, crosslinking, induced segmental alignment, or simply sample history becomes relevant. This structure-property analysis is suitable for applied material research and selecting a stable plasticizer.

Considering the elaborated molecular morphology of biopolymers, we have concluded that most of these mixtures tend to have very heterogenous miscibility. Future research in this direction might include estimating the magnitude of the effect on *Tg* from structural parameters, such as polydispersity, chiral macromolecular arrangements (helices, sheets, globules), and crystallinity. Furthermore, exploring the overall impact of

8

a higher number of ionic or H-bonding interactions to specific binding and *Tg* could also be explored. This could be done via *GML* modeling (use of $k_{GM}$ partitioning constant) after accurately and systematically gathering data on a few biopolymer systems. Another important idea is to explore the application of the model for multi-component systems. This should be immediately relevant to sectors like food and biomedical technology, where many additives are commonly employed for bio-based and synthetic polymers. However, it is noteworthy to mention that the *Tg* model is not strictly applicable to biopolymers and has also been shown to function well for synthetic polymers. Considering that well-characterized and structurally controlled synthetic polymers can also be modeled, the predictive mode of the *GML* model for multi-component mixtures might also be further studied. From a thermodynamic point-of-view, it might also be curious to investigate the creation of a similar model for other polymer relaxations. For instance, beta-relaxations could potentially be theoretically described and have established importance to the physical aging of materials.[1]

## 8.2. Biopolymer ionomeric systems

In **Chapter 3**, the transient crosslinking of alginates with polyvalent metal counterions was investigated with regard to film fabrication, solid state mechanics, and water vapor diffusion. We have explored the hypothesis that the evident alginate gelation in neutral and ion-coordinated states is dominated by a transition from polyelectrolyte to ionomeric states. The structural effects from this transition were monitored through elastic modulus, *Tg*, and water diffusion properties. In short, when alginates were composed of monovalent cations, we observed high water solubility and typical polyelectrolyte behavior. On the other hand, in combination with a series of divalent and trivalent counterions (alkaline earth, transition, post-transition), the alginates formed insoluble hydrogels with mechanical and diffusion properties resembling ionomers (systems formed by ion-macromolecule complex ligand interactions). This general outcome is largely supported by mechanical data, in which the elastic modulus *E'* was coarsely decreasing with increasing counterion valency and possible chelation or aggregation of ionic pairs. Additionally, for the same complexing ions but including glycerol as a plasticizer, we have estimated a higher sample heterogeneity (the *GML* model was used). The water sorption profiles of dry films could be modeled using a novel model, the Penetrating Shell model. In this, a hydrated shell is assumed to advance to the materials core at a respective water diffusion velocity, which can be calculated from the isotherms.

8

In particular, the isotherms of multivalent alginates were interesting to model because an inflection point could be related to the polymer relaxation induced by water uptake. In turn, we estimate this marked event is possibly linked to a larger structural change in the polymer crosslinked by ionic aggregates (heterogenous morphology). We hope these indications of specific nano- and microstructures can be further elucidated by additional experiments, *e.g.*, diffraction at different length scales. From a fundamental standpoint, whether the effect on modulus caused by ion-aggregated 'spherical' clusters is indeed equivalent to a lower effective charge density (Coulombic electrostatic interactions) should be pursued.

We conclude that counterion-crosslinking in charged polymers is complex even for well-characterized and studied reference compounds, *i.e.*, alginate. Therefore, careful experimentation and systematic analysis are crucial for establishing dynamic and steady-state structure-property relationships. In general, more studies are needed to understand ionomer hydrogel properties at different levels better and, by extension, get to desired solid-state properties. For example, understanding the formation of ionic clusters and aggregates to rheological parameters in the hydrogel state might help elucidate the final properties of the solids. Investigating polyelectrolytes and ionomers composed of different charged groups (pendant or covalently attached to the backbone) and density would be ideal. In addition, the framework of ion-pair affinities – lyotropic phenomena related to ion-specific behavior observed in water or polar solvents – can also be useful for interpreting results. This might be easier to comprehend if able to study linear homopolymer polysaccharides. However, the palette of biopolymer structures found in nature is usually made of heteropolymers. For heteropolymers such as proteins, although not fully understood, it is common to resort to the Hofmeister and Irving-Williams series, which are vaguely dedicated to solvation energy phenomena like polarity-solubility and ion-coordination binding to transition metals, respectively. Notwithstanding, the challenges lie in the deconvolution of the electrostatic phenomena and supramolecular arrangements (denaturation and renaturation).

## 8.3. Highly ordered (bio)nanocomposites

In **Chapters 4 and 5**, fabrication strategies and methods for bioinspired and high-ordered nanocomposites were investigated. We showcased a facile hydrogelation strategy to achieve 2D nanomaterial exfoliation, even at high nanofiller volume fractions. This was done by systematic investigation of gelatin/MMT bionanocomposites, showing exfoliated

**8**

multiscale nacre-like architectures. We have discussed the essential features to measure the quality of nanoparticle dispersion (exfoliated, intercalated, or stacked) and the degree of positional order through scattering data. Remarkably, the studied system showed the desired exfoliated nanostructures all the way to very high nanofiller incorporation. This allowed us to study better the structural aspects of orientational order and related thermomechanical and barrier properties. We could explore the hydrogel 2D particle immobilization strategy using the framework of orientational distribution functions. The gelatin/MMT system followed the affine deformation theory to a large extent, resulting in a high level of control of structure formation with respect to the quality of dispersion and ordering. In sum, controlling the extent of hybrid hydrogel affine deformation has greatly impacted the final in-plane alignment and resulted in a semi-continuous increase of properties like mechanical reinforcement and gas barrier. Even though this methodology was demonstrated by bionanocomposites, the theoretical grounds and main parameters used for tailoring bioinspired composites shall also apply to synthetic polymers and nanomaterials (of 1D or 2D morphology).

Despite these significant findings on a competitive design for nacre-like materials, additional lines of experimentation are still needed for the proposed hydrogel affine deformation. For example, similar studies could be easily attainable by investigating the effect of varying the 2D material composition, aspect ratio, and possible wrinkling or undulation. This shall provide more insights into the effective aspect ratio from structure-property and better fabrication processes. With regards to the soft phase, it is important to achieve good polymer-particle interaction and interlocking prior to the material's macroscopic deformation. To this end, many more waterborne and compatible gelling systems could be screened. Hence, it is also recommended to investigate the use of non-toxic crosslinking agents and other nanoparticle fixation mechanisms, for instance, by controlling pH and specific interactions. The interfacial phenomena between the organic matrix and the inorganic building blocks also should be explored. This work could be assisted by examining the formation of coated hydrocolloid particles, *e.g.*, by AFM and other nanotechnology tools. Another important topic for investigation is the extent of affinity in hydrogels since improving the level of uniform deformation of the system's network would surely increase structural orientational order. With this intention, a better understating of the rheological properties (yield stress and gel strength) of hydrogel polymers and inorganic hybrids might be a useful direction. Furthermore, many currently proposed nacre-like fabrication strategies involve applying at least one step of vacuum-assisted filtration. It would be desirable to perform comparative studies using

8

the same 2D material hybrid systems and affine deformation as the primary mechanism (strain-induced alignment).

Concerning the general topic of bionanocomposites, the effect of charge on polymer and nanomaterial could be investigated. Following the abovementioned strategies, we do not expect this to play a major role in the alignment mechanism. However, the chemical structure shall be important, at least for composite combability, thermal stability, water uptake, and interfacial phenomena. One possible direction is the study of structure-property in charged polymers, *e.g.,* alginate, chitosan, gelatin (zwitterion), in combination with amphoteric fillers, such as gibbsite and boehmite. Following a similar rationale, alternative composite fabrication methods that can be combined to affine deformation could be explored, such as in situ polymerization and mineralization.

## 8.4. Role of structure-property relationships

This thesis reiterates the general importance of structure-property relationships to the design of tailored materials. This has been demonstrated at different levels, from nuances related to the molecular morphology (**Chapters 2 and 3**) to the micro- and mesostructures in composites (**Chapters 4 to 7**). Certainly, this approach has proven useful to generate guidelines for enhancing (solid-state) properties linked to the cohesive energy (thermal, mechanical, barrier) in a material and composite synergetic interaction. Following this approach, additional studies on the chief effects of a (controlled) biopolymer composition could be performed. For instance, one idea is to study functional group contributions and the assumption of a global chemical structure using well-characterized biopolymers; and to follow the effects on key properties. We envision that electrostatic interactions shall have a primary influence on properties like the elastic modulus or the onset of thermal degradation, among others. In particular, the effect of Coulombic interactions in charged biopolymers seems to play an important role in thermomechanical performance. Biological organisms tend to naturally produce biopolymers with ionic groups. Thus, a study on the tradeoff of properties in (bio)polymers could be further elucidated. Nowadays, analytical, thermal, and mechanical analysis techniques have advanced to great precision. Insights on this topic could benefit the design of novel bio-based materials since it extends the current knowledge on the importance of the chemical group and monomer functionalities and interactions to the desired material properties. Moreover, this study could be integrated into the previously discussed topics of polymer mixtures (**Chapter 2**) and charged

**8**

complexes (**Chapters 3 and 6**). Overall, some level of control over structure-property relations might encourage the usage of biopolymers in high-performance material applications.

## 8.5. Concluding remarks

The use of polymers has revolutionized modern materials science, with fossil-based polymers being the backbone of many industries for decades. Hence, fossil-based polymers have been extensively studied and optimized over decades. The high level of control of the chemical structure in synthetic polymers can offer good mechanical properties (*i.e.*, high strength and impact resistance), thermal stability, and versatility. However, their use could be more sustainable, and the characteristic resistance to chemical and biological degradation generates problems with waste management.

Biopolymers and biotechnology are crucial to establish a sustainable bio-based economy. Using their unique properties and versatile applications, biopolymers derived from renewable resources (biomass, agricultural and urban wastes) offer a promising alternative to conventional fossil-based materials such as plastics derived from crude oil or natural gas. Furthermore, the integration of biotechnology enables the development of innovative processes to improve the quality of life but also allows for the recovery of high-value bio-based chemicals and microbial biopolymers (**Chapters 6 and 7**). By harnessing the potential of biopolymers and biotechnology, we can close material cycles, lowering greenhouse gas emissions and preventing pollution to help foster a more environmentally friendly and economically viable future.

Bio-based polymers have observed significant progress in exploring mechanical properties, thermal stability, and processability in recent years. They are already widely used in applications such as food packaging, agriculture, textiles, and biomedical devices. However, there is still large resistance to implementation due to a general lack of control over processing, compatibility, and properties. Our efforts aimed at systematic examples of ways to overcome these shortcomings by employing structure-property relationships. The chemical nature of biopolymers and derivatives can be complicated and challenging to determine in detail. Analytical and characterization methods on this quest should be intensively promoted. Despite this, by unraveling important parameters to realize processes and products with consistent desired properties, the goal to increase biopolymer applications might become technologically and commercially feasible. In addition, other advances in bio-based polymer research, including novel processing

8

techniques, functionalization strategies, and polymer blends, have the potential to bridge the performance gap. Balancing performance, sustainability, and cost-effectiveness is a key challenge that requires continued research and innovation.

The development of tailored bio-based materials with improved properties will be crucial to realize a more sustainable and circular economy. The emerging field of bionanocomposites demonstrates how lightweight and high-performing materials can be designed using biopolymers and non-toxic fillers and additives. The thermal, mechanical, and barrier performance can be greatly improved by applying mechanisms and nanostructures inspired by biological systems, which have been perfected over millions of years of evolution. In this thesis, we have explored the fabrication of highly anisotropic nacre-like materials through bioinspired routes, resulting in a significant level of waterborne system control. This opens avenues for many tailored and (multi)functional applications and for expanding the framework to a wide range of polymer systems, including biopolymers recovered from agricultural and urban waste. Developing bioinspired composite materials holds immense promise for materials science while offering the additional advantage of employing biodegradable and sustainable components.

## References

(1)       Minguez, R.; Barrenetxea, L.; Solaberrieta, E.; Lizundia, E. A Simple Approach to Understand the Physical Aging in Polymers. *European journal of physics* **2018**, *40* (1), 015502.

8

# Acknowledgments

Here I am, almost 5 years later, drinking tea and trying to recollect all my memories of this PhD battle. Writing a thesis is no easy task but this emotional part feels even harder. There is so much to tell in a few pages. The mind wanders and I think of just how many teas and coffees where needed to get me here. Maybe that should be a first thank you. A recognition to early and morden civilizations for indulging hot beverages and its associated social rituals. Most of this work was done in some way powered by caffeine and many of the informal but crucial meetings happened over a cup of 'coffee'. The samurais of early-modern japan knew it better, as they would pour a cup of green tea and go in a meditative state *before* a battle. Preparation of the mind is key and certainly this was a hard lesson to me. And I surely had to learn to be kind to myself. So, let me take a break before continuiting to talk and thank you all for the good and challenging times.

Dear supervisors, thank you for supporting me throughout this journey and pretty much a carrier change from biotechnology to materials science. **Stephen**, you have been a great teacher to me, and I had never imagined how much your personalized lectures would change even the way I perceive the world around me. Notions on alginates, optics, cooking, and the microwave (bomb box) machine equation are just a feel examples of the topics of our fun and eye-opening discussions. Thank you for all the support on scientific and professional spheres and the confidence you have trusted on me. All this specially during life hardships, like family loss or the 2020 pandemic. **Jure**, since I've met you, I was very impressed with the complex science you can develop, how creative you can be, teaching skills, etc. However, over the years, I think what strikes me the most is how much you care about people and topics that are very dear to you. I think how passionate and sincere you are about education and science is very inspiring. And I wanted you to know that, even with all the ups and downs in your carrer and my supervision, the credits for these studies and my development are largely yours. Thank you (obrigada) for sticking to it. **Mark**, you have such a great power to motivate the students and communities around you. I've always felt that I could reach out to you. Our conversations were always very open and encouraging, thank you for that. In addition, I am also thankful to **Ger** and **Gabrie** for the nice projects together.

Dear **Ben**, you have been a great instructor, lab manager, and technician 'plus' during my project. You have also deposited a lot of trust in my learning skills since the beginning, thank you. Another big thanks for being available for consulation even after your retirement. It was essential. More than that, you have become a friend to me and Elmira. It was just so nice to count on you for a coffee together, bike ride, and even the nice dinner you and Mieneke prepared for us. Dear **Marcel**, **Xiaohui**, **Sasha** and **Sietse**, thank you very much for the lunches together, training, and the many discussions over experiments. **Bart**, a shoutout to you being open to develop 'Crazy Experiment' using your software engineering skills. That was both highly impressive and appreciated. Please, keep learning Portuguese. **Duco**, you have helped and 'rescued' me in the lab so many times I have lost count. Since the beginning of this project, you have been available to help and, even better, just to have a casual discussion about pretty much any scientific topic. Not to name your remarkable workshop and setup talents. Thank you, big time, for being present and directly aiding many of my projects, *e.g.,* the nanocellulose fiber spinning or flame torch tests.

Dear ASM colleagues, it took me some time to truly get to know most of you. But I am so very happy many bonds were formed. Caro **Eduardo**, obrigada por todas as conversas francas, passeios culturais, discussões politicas, e muito muito mais. Sempre pude contar que você entenderia meus pensamentos e divagações em instantes. A warm hug to all my 'early times' office mates **Peggy**, **Irene**, **Benjamin**, **Sarah**, **Reece**, **Tobias**, **Elmira**, **Mark,** **Guotai**, **Bowen**. But also, a shoutout to **Georgy**, **Çancel**, **Hendrik**, **Emma**, **Angie**, **Benni**, **Ardeshir**, **Jacqueline**, and **Tammar**. It was great to share with you many dinners after lab-cleaning, lunches, coffees, and so on. Extra tranks to the friends Peggy, Irene, Sarah, and Elmira for being with me throught thick and thin and encouraging me to go on. Irene and Sarah specially for aperol spritz and being my loving peroxide angels. Reece, thank you for all the coffee science, board games, and openness. Benjamin, thank you for being the social glue of the group and teaching me to say good morning. **Anand**, I wish you all the best with finishing your Kaumera thesis and biopolymer/rocket science and it was also fun to have before that the torched cookkie team. Dear EBT colleagues, it was also nice to have you around and to join in your group occasionally. **Danny, Simon** and **Jules** thanks for inspiring me to do a PhD. Also, many thanks to **Sergio**, **Chris**, **Yuemei**, **Jelmer**, **Philipp**, among others, for having me around and sometimes collaborating. Special thanks to Jelmer for introducing me to **Caetano**. Dear **Claire**, thanks for letting me use your Deltares lab at and meet nice people there.

Doing a PhD gives you the great opportunity to interact with and guide students. Superficially, it might seem that the PhD supervisor is streaming knowledge into the pupil's head. Often, it is actually such a mutual exchange this learning process. I had the opportunity to explore and learn a great deal together with **Amira**, **Vera**, **Sylvie**, **Charlie**, **Giovanna**, and others. Thank you for your patience, efforts, and, specially, curiousity and a fresh pair of eyes. This motivated me through every new beginning.

**Edward** and **Mario**, a.k.a. the ivy league, it has been a wonderful surprise to me that after working together at RHDHV we kept in touch pretty much all these years. You always had my back, and we can have interesting debates and jokes about everything. Thank you forever. From RHDHV, I also had the chance to also talk a great deal about Kaumera with **Eline**. The occasional fun catching up with also **Valerie** and **Pascalle**. Last but not least, I am thankful for the opportunity to work with ChainCraft (**Robbert** and **Maddalena**) and to be involved from a distance in the COMPRO project for a Kaumera-based resin and derivative materials.

My dear friends, you are luckily so many and, unfortunately to me, scattered around the globe… The first person that comes to mind when I think of this PhD and time in Delft is, of course, **Hugo**. You are a great person and showed me so many weird fun stuffs since the masters and also inspired me to do a PhD. Thanks a bunch for the nice activities. You are such an amazing friend. **Vanessa**, you have also been a great buddy and friend since the masters, love you. **Raluca** and **Marij**, you are very sweet and loving in your own special way. A thankful hug also to my architect friend **Joanna** and the nice talks about food, buildings, and work ethics. **Yuri**, for the Dutch lessons, philosophical discussions but also social and lively events together in A'dam. Also, for having my back many times. The best housemates ever from house 13 (**Alice**, **Tatiana**, **Heather**, **Iris**). Thank you for keeping in touch and being so kind, even during corona times. I don't like to think how it would have been without you. Dear **Baerritos**, you arrived later in my Dutch life, but you have been already such kind and supportive friends, thanks for always having the door open to me. Just as important are my Brazilian friends, who deserve a special thanks. **Rafael** e **Rayssa**, vocês são grande parte da minha razão para viver. E até neste contexto professional gostaria de dizer que vocês me ensinaram a buscar fazer o que amo. Sem vocês sou nada. Queria eu tê-los pertinho todos os dias. **Maísa**, você é amiga, quase-irmã, confidente, e rainha. Obrigada por poder contra com seu carinho e potência de pessoa. **Leandro** e **Tainá**, vocês tambem já há muitos anos ao meu lado e de um companheirismo infinito. Obrigada por todo esse amor e também àqueles que não tive como mencionar neste longo texto.

I would like to express the importance of ones who took care of my mental health, either via TU Delft or externally. So many thanks to **Paula**, **Michelle**, and **Ana Carolina**.

I also would like to thank my parents. It is with a lot of sadness that I write these lines, since my dad is not among us since Oct 2019. Thus, I'll write it the language that is closer to my heart. **Pai**, você sempre foi uma rocha, uma fortaleza, e, acima disso, um poço de inspiração. Sinto a sua falta todos os dias e levo você comigo em pensamento. Hoje choro por não estar mais conosco, mas só de me lembrar do seu rosto sempre sereno e palavras doces com as filhas me sinto suficiente e capaz de continuar e lutar pelos meus sonhos. **Mãe**, você sempre me fez acreditar que posso evoluir e me apoiou mais do que todos nestes anos de educação e esforco. Você tem uma força extraordinária. Guardo em mim um amor infinito por vocês. Irmãs **Isabela** e **Silvânia**, vocês são únicas, difíceis, mas, sempre ao fim, muito amorosas. O amor prevalece acima de tudo. Com relação a este trabalho, tenho muito a agradecer pelas discussões com **Silvânia**, que em momentos difíceis muito me ajudou a continuar e sempre procurar pelo melhor possível. Tio **Renato**, você é para mim como um segundo pai e porto seguro. Padrinhos **Solange** e **Tião**, a sua companhia sempre me alegra, até mesmo em tempos tempestuosos. Um grande abraço em vocês!

**Maurício**, my love and strange soulmate, as you have told me with some frequency during the past years: "*The best part of the PhD is that I got to meet you.*" I can also surely say you have become my best companion and I believe I only got the endurance needed to accomplish this and many other things because of you. So, if this isn't nice, I don't know what is.


Suellen Pereira Espíndola

Apr 2023

Delft

# List of publications

## A. Journals

**B.** **Espíndola, S. P.**; Zlopasa, J.; Picken, S. J. (2023) Affine deformation and self-assembly alignment in hydrogel nanocomposites. ChemRxiv. This content is a preprint and has not been peer-reviewed. https://doi.org/10.26434/chemrxiv-2023-99lv2 (*under review*)

**C.** **Espíndola, S. P.**; Zlopasa, J.; Picken, S. J. (2023) Systematic Study of the Nanostructures of Exfoliated Polymer Nanocomposites. https://doi.org/10.1021/acs.macromol.3c00575 (*accepted* in Macromolecules)

**D.** **Espíndola, S. P.**, Norder, B., Koper, G. J., & Picken, S. J. (2023). The Glass Transition Temperature of Heterogeneous Biopolymer Systems. Biomacromolecules, 24, 4, 1627–1637. https://doi.org/10.1021/acs.biomac.2c01356

**E.** **Espíndola, S. P.**, Pronk, M., Zlopasa, J., Picken, S. J., & van Loosdrecht, M. C. (2021). Nanocellulose recovery from domestic wastewater. Journal of Cleaner Production, 280, 124507. https://doi.org/10.1016/j.jclepro.2020.124507

## B. Conferences

**1.** Polymer Connect 2023 Conference, Rome, Italy (2023). The role of electrostatic interactions in the mechanics of biopolymers. *Oral presentation.*

**2.** Brightlands Polymer Days 2021, Veldhoven, the Netherlands (2021). "Plasticization of Alginate films: glass transition mechanisms and modelling." & "Effect of electrostatic interactions on the elastic modulus of (bio)polymers." *Poster presentations.*

**3.** NWO Closed Cycles Programme Day 2020, Utrecht, the Netherlands (2020). "Nature-inspired biopolymer nanocomposites towards a cyclic economy (Nanocycle)". *Oral presentation.*

**4.** Nature-Inspired Engineering 2019 Conference, Cetraro, Italy (2019). Structure-property relations of highly ordered bio-nanocomposites. *Oral presentation.*

**5.** Frontiers in Polymer Science 2019 Conference, Budapest, Hungary (2019). Unravelling the mechanisms behind the plasticization of Na-Alginate films. *Poster presentation.*

## C. Press

**1.** TU Delft TV and Espíndola, S. P. [TU Delft TV]. (2019, September 27). The hidden gems of wastewater [Video]. YouTube. https://youtu.be/cC0-LYWHoXg

**2.** TU Delft TV (2019, September 27). What can be made of your used toilet paper? You'll be surprised. Retrieved from https://www.delta.tudelft.nl/article/what-can-be-made-your-used-toilet-paper-youll-be-surprised

**3.** Espíndola, S. P. [TU Delft]. (2019, May 07). TU Delft - FameLab | Suellen Pereira Espindola [Video]. Youtube. https://youtu.be/luiuyq6t37Y

**4.** Prize: Delft University of Technology (2019, April 05). Suellen Pereira Espíndola (TU Delft) and Hans Huybrighs (ESA) winners of the Delfts FameLab heat. Retrieved from https://www.tudelft.nl/en/2019/tu-delft/suellen-pereira-espindola-tu-delft-and-hans-huybrighs-esa-winners-of-the-delfts-famelab-heat/

# Curriculum Vitae

Suellen Pereira Espindola was born on 18 January 1993 in Uberlândia, Brazil. She received her B.Sc. degree in Environmental Engineering (2015) from Federal University of Uberlândia, Brazil, and M.Sc. degree in Water Technology (2017) from Wageningen University, the Netherlands. Her master thesis was carried out in Delft University of Technology, where she studied the recovery and valorisation of resources from wastewater, such as cellulose. Around the same period, she was also an intern at Royal HaskoningDHV, learning about aerobic granular sludge wastewater treatment technology. In 2017-2018, she worked at the local water Department of Uberlandia (Brazil) and later as a biotechnologist consultant for Royal HaskoningDHV (placed in São Paulo, Brazil). In 2018, she shifted towards material science and started her Ph.D. in the Chemical Engineering department at the Advanced Soft Matter group of Delft University of Technology (the Netherlands). The doctorate topic was over physicochemical characterization and structure-property relationships of commercial and emerging bio-based polymers, and their incorporation into composite materials. In 2023, she started an entrepreneurial postdoc on bio-based polymer coatings for agriculture. The last works were performed in the group of Prof. Stephen J. Picken.